NOVEL THIAZOLIDINEDIONE DERIVATIVES AS CORROSION INHIBITORS FOR MILD STEEL AND ZINC IN 1 M HCl

By

Nhlalo M. Dube-Johnstone

(11625197)

A thesis submitted in fulfilment of the requirements for the degree of

Doctor of Philosophy

In the

Department of Chemistry

Faculty of Science, Engineering and Agriculture

University of Venda

Thohoyandou, Limpopo

South Africa

Supervisor

PROFESSOR LC MURULANA

Co-supervisor

PROFESSOR SS MNYAKENI-MOLEELE

DECLARATION

I, Nhlalo Michael Dube-Johnstone, hereby declare that the work in this thesis is my own and was under the supervision of Professor L.C. Murulana and Professor S.S. Mnyakeni-Moleele as my co-supervisor. The information derived from literature has been duly acknowledged in text and a list of references provided. This work is being submitted for the degree of Doctor of Philosophy in Chemistry at the University of Venda and has not been submitted before for any degree or examination at any other university.

Signature: 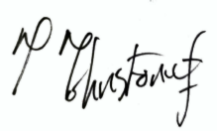

Date: 22/01/2024

DEDICATION

This thesis is dedicated to my late mother, Dr Bevelyn Dube, who as a PhD holder herself was not only a source of inspiration but always full of encouragement and as such would have loved to see this work completed.

TABLE OF CONTENTS

ACKNOWLEDGEMENTS

I would like to first start by acknowledging both my supervisor (Professor Lutendo C. Murulana) and my co-supervisor (Professor Simon S. Mnyakeni-Moleele) for all their tireless efforts in ensuring that this research project was brought to a successful conclusion. Their immense contribution has been indispensable to the success of this work.

I would also like to thank my colleagues in the University of Venda Drug Synthesis and Isolation (DSI) group, particularly Miss Unarine Tshishonga and Dr Tshiluka, for their assistance with the synthesis component of the research project. My colleagues in the Corrosion Science (CorroSci) research group, from whom I have learnt a lot over the years particularly from my good friend Dr Nesane, also deserve a very special thanks.

Finally, I would like to thank the National Research Foundation (NRF) for all the financial support that they rendered towards the completion of this research project. Without their financial support, this project would not have been completed.

ABSTRACT

Corrosion inhibition studies on mild steel (MS) and zinc in 1 M HCl were carried out at four temperatures (303.15 K, 313.15 K, 323.15 K, and 333.15 K) using eight novel thiazolidinedione derivatives (TZDs) codenamed: A1, A2, A3 (alaninates), B1, B2 (butanoates), G1, G2, and G3 (glycinates). After synthesis, the TZDs were characterized using nuclear magnetic resonance (NMR) spectroscopy. Specifically, two NMR techniques were employed: proton NMR (^{1}H NMR) at 400MHz and carbon 13 NMR (^{13}C NMR) at 100MHz. After characterization, five experimental techniques were employed to investigate the corrosion inhibition potential of the TZDs: weight loss (WL) analysis, potentiodynamic polarization (PDP), electrochemical impedance spectroscopy (EIS) and Fourier transform infrared spectroscopy (FTIR). The adsorption of the TZDs onto both metals was found to be best modelled by the Langmuir adsorption isotherm. Thermodynamic data showed that all TZDs adsorbed spontaneously onto both metal surfaces, transitioning from mixed type adsorption to chemisorption with an increase in temperature. However, WL analysis percentage inhibition (%IE_{WL}) and activation energy (E_a) data showed that all TZDs adsorbed onto zinc via chemisorption. Data obtained from PDP analysis showed that the TZDs inhibit corrosion on MS at both anodic and cathodic sites, with a prevalence of cathodic action. However, on zinc, all TZDs inhibit corrosion exclusively at anodic sites. Data from EIS analysis showed that the adsorption of the TZDs onto both metals is a charge transfer driven process. The significantly depressed semi-circles obtained from zinc EIS data shows that capacitance plays much less of a role relative to MS, explaining the much lower phase shift (n) values obtained. Spectra obtained from FTIR analysis show that carbonyl, amine, nitro, aliphatic and aromatic functional groups all take part in the formation of an adsorption film on both metal surfaces.

LIST OF ABBREVIATIONS

A1	Alaninate 1
A2	Alaninate 2
A3	Alaninate 3
B1	Butanoate 1
B2	Butanoate 2
C_{dl}	Double Layer Capacitance
CE	Counter Electrode
C_{inh}	Inhibitor Concentration
CPE	Constant Phase Element
C_R	Corrosion Rate
DCM	Dichloromethane
DMSO	Dimethyl Sulfoxide
E_a	Activation Energy
E_{corr}	Corrosion Potential
EIS	Electrochemical Impedance Spectroscopy
FTIR	Fourier Transform Infrared Spectroscopy
GDP	Gross Domestic Product
G1	Glycinate 1
G2	Glycinate 2
G3	Glycinate 3
i_{corr}	Corrosion Current Density
IE	Inhibition Efficiency

LAI	Langmuir Adsorption Isotherm
MS	Mild Steel
NMR	Nuclear Magnetic Resonance
PDP	Potentiodynamic Polarization
R_{ct}	Charge Transfer Resistance
RE	Reference Electrode
R_p	Polarization Resistance
R_s	Solution Resistance
SiC	Silicon-Carbide
THF	Tetrahydrofuran
TZD	Thiazolidinedione Derivative
TZD-K^+	Thiazolidinedione Derivative Potassium Salt
WE	Working Electrode
WL	Weight Loss

LIST OF FIGURES

LIST OF TABLES

CHAPTER ONE

INTRODUCTION

Chapter one summary

This chapter provides a brief background on corrosion and corrosion inhibition. In addition, chapter one highlights the reason for the study in the form of a study justification, along with the objectives that will be followed in fulfilment of the study's aim.

1.1 Background of the study

Corrosion is an electrochemical process that results in the degradation of a material's properties overtime due to interactions between the material and its environment [1]. For metals, corrosion can also be defined as a spontaneous process by which a metal oxidises from a high energy state to a lower more stable energy state, usually its oxide [2].

Metals are important for the proper functioning of a country's economy, for example, they are used extensively in food production [3]. However, the extraction of metals from their respective ores is costly as far as the global climate is concerned [4]. In addition, the mining of these ores very often leads to environmental degradation [5]. Loss of production output due to either frequent maintenance or replacement of corroded equipment can have a deleterious effect on a country's gross domestic product (GDP) [6]. Depending on the use of the metal, a catastrophic failure caused by corrosion can also lead to loss of life [7]. These important facts have led to many studies being carried out with the specific purpose of using corrosion inhibitors to prevent metal corrosion [8-10].

Corrosion inhibition studies make use of highly aggressive environments, usually acids and sometimes at different temperatures, to stress test corrosion inhibitors to ensure they can protect metals from corrosion in the harshest of environments [11-13]. Through a series of experimental techniques, corrosion inhibition studies allow the corrosion scientist to make an accurate determination as to whether a corrosion inhibitor can protect a metal from corrosion in a specific environment.

1.1.1 Corrosion inhibitors

Corrosion inhibitors reduce the rate of metallic corrosion when added to a corrosive environment in trace quantities, thereby extending the life of the metal [14]. Corrosion inhibitors can either be organic or inorganic [15]. Before 1960, inorganic corrosion inhibitors were extensively used due to their effectiveness at preventing corrosion (Table 1.1) [16]. Between 1960 and 1980, the cost of a corrosion inhibitor began to outweigh its efficiency as companies looked to further cut production costs and raise profits. In the decades after 1980, the negative impact corrosion inhibitors were having on the environment began to increasingly take precedence. This paved the way for

many studies that have used non-toxic organic corrosion inhibitors to protect metals from corrosion in aggressive environments. This research is a natural progression of this evolution in corrosion inhibitors as it makes use of non-toxic, novel organic compounds called thiazolidinedione derivatives (TZDs) as efficacious corrosion inhibitors for both Mild steel (MS) and zinc in 1 M HCl.

Table 1.1: Evolution of corrosion inhibitors [16].

Inhibitor type	**Time frame**	**Reason for use**
Chromates, phosphates, nitrates, borates, silicates, Zn compounds	<1960	Efficiency
Cations, polyphosphates, gluconates, vanadates, molybdates, phosphono acids, polyacrilates, soluble oils, carboxylates, surface active chelates	1960-1980	Economy
Tannins, natural compounds, surfactants, phosphono-organic, natural polymers, vitamins, ozone	1980-1995	Ecology
REM, multifunctional organic compounds, mixtures of REM inhibitors with organic/inorganic compounds for synergism, encapsulation of inhibitors	1995-Present	Environmentally friendly

1.1.2 Thiazolidinedione derivatives as effective corrosion inhibitors

Three corrosion studies were conducted using TZDs as corrosion inhibitors [17-19]. Through experimental techniques such as weight loss (WL) analysis, potentiodynamic polarization (PDP) and electrochemical impedance spectroscopy (EIS), these three studies demonstrated the effectiveness of TZDs as corrosion inhibitors for different metals in contrasting corrosive environments. For example, the highest WL analysis percentage inhibition efficiency (%IE) results obtained by Chaouiki *et al.* [17] for two TZDs codenamed MeOTZD and MeTZD, for carbon steel in 1 M HCl, were 94% and 83% respectively. Potentiodynamic polarization and EIS experiments conducted by Lgaz *et al.* [18] using TZDs codenamed MTZD and ATZD, on copper in NaCl, yielded %IE of 90%, 96% respectively (PDP) and 94%, 98% respectively (EIS). Alamry *et al.* [19] carried out WL analysis on MS in 5% HCl using TZDs codenamed TZD and AT, reporting %IE of 98% and 99.7% respectively at 60°C and an inhibitor concentration of 5×10^{-4} M.

1.2 Justification of the study

Food production is a key economic sector for every country. Unfortunately, it is vulnerable to the negative effects of corrosion. Corrosion of irrigation equipment and other implements such as tractors and combine harvesters can reduce productivity, negatively impacting on food production. In a study focusing on small holder farms in South Africa, it was determined that organic acids from roots and decomposing plant material corroded irrigation canal walls rendering them vulnerable to mechanical damage [20]. The water that is used for irrigation purposes is stored, in many cases, in metal tanks and carried from source to field by pipes that in many cases are also made of metal. Corrosion of this vital infrastructure results in unnecessary leakages and water wastage. In water scarce parts of the world such as South Africa, this water wastage is nothing short of unacceptable [21].

In the year 2019, every tonne of liquid steel produced resulted in 1.8 tonnes of CO_2 being released into the atmosphere, bringing the total CO_2 emissions for 2019 to 2.4 gigatonnes [22]. The act of mining the ore from which the metal is extracted can be itself a problem. Liu *et al.* [23] conducted a study to determine the impact of iron ore mining in five countries (Australia, Brazil, Canada, South Africa, and Ukraine). The

bulk of the negative effects of iron ore mining were seen in Brazil, with its marine environment bearing the brunt of these negative impacts. The order of impact, from the worst impacted country to the least impacted country, was as follows: Brazil>Australia>South Africa>Canada>Ukraine [23]. Developing effective corrosion inhibitors to protect MS from corrosion will prolong the useful life of steel structures, reducing the replacement frequency of corroded steel and thereby reducing demand for fresh steel products.

The negative effects of corrosion cost companies and governments large sums of money in lost output annually. One study estimated that the total annual direct impact of corrosion on the Canadian economy had a staggering $41 billion price tag, roughly 3% of Canada's GDP at the time [24]. Studies in several countries such as Japan, the United Kingdom and the United States have estimated corrosion losses to the national economy of these countries to be 5% of GDP [25]. The corrosion costs in the Indian pulp and paper industry were once estimated to reach £1.5 million annually [26].

Corrosion can also affect public safety. Corrosion of steel reinforcing bar (rebar) in concrete can proceed undetected and suddenly (or seemingly so) result in failure of a section of highway, the collapse of electrical towers, damage to buildings, parking structures and bridges. This results not only in significant repair costs but crucially it also endangers public safety. In 2019, the Himalaya Bridge in Mumbai collapsed due to corrosion resulting in loss of human life [27]. In the US state of Minnesota, the poorly designed gusset plates of the I-35W Bridge, significantly weakened by corrosion, collapsed on August 1st, 2007, leading to loss of life [28].

1.3 Aim and objectives of the study

The aim of the study is to synthesise, characterise and ascertain the corrosion inhibition potential of eight novel TZDs codenamed A1, A2, A3 (alaninates), B1, B2 (butanoates), G1, G2, G3 (glycinates) on MS, and Zn in 1 M HCl.

The objectives of the study are to:

- synthesise and characterise the TZDs with nuclear magnetic resonance (NMR) spectroscopy.

- carry out WL experiments at different temperatures to determine the kinetics of the corrosion process.
- use WL data to ascertain the adsorption isotherm and parameters that best describe the adsorption mechanism of the TZDs onto MS and zinc.
- use WL data to determine the activation parameters of the corrosion process.
- carry out electrochemical studies (PDP and EIS) to determine the inhibition potential of the TZDs.
- use Fourier transform infrared spectroscopy (FTIR) to establish the functional groups involved in the adsorption of the TZDs onto MS and zinc.

1.4 Hypothesis of the study

The determination of the corrosion inhibition potential of eight novel TZDs will lead to the discovery of effective corrosion inhibitors for MS and zinc not only in 1 M HCl but also in environments less aggressive than 1 M HCl.

CHAPTER TWO

LITERATURE REVIEW

Chapter two summary

This chapter highlights the problem of corrosion and the different forms in which it presents itself. The chapter then goes on to show different ways in which corrosion can be mitigated, especially using corrosion inhibitors. The chapter discusses the use of novel thiazolidinedione derivatives, a class of organic compounds, and their potential use as corrosion inhibitors for the protection of mild steel and zinc in 1 M HCl. Finally, the chapter elaborates on the corrosion studies that these novel compounds will be put through to determine their corrosion inhibition potential.

2.1 Hydrochloric acid induced corrosion of steel

Mild steel, sometimes referred to as plain-carbon steel, is widely used in industry [29]. It is used in construction, machinery, manufacture of chemical reactors and storage tanks [30-33]. Mild steel is extensively used in industry because it is strong and affordable to use at scale [34].

The problem arises when MS encounters HCl, which frequently happens in industrial settings [35, 36]. Industrial uses of HCl include acid pickling and descaling, well acidizing and electrochemical etching [37-39]. When contact between HCl and MS occurs, corrosion sets in leading to various negative effects. These negative outcomes can include reduction in the mechanical strength of the metal and fluid leakages in containers and pipelines made from MS [40-42].

In the petroleum industry, in a process called acidification, large amounts of HCl solution are pumped into silica-limestone rock formations through N80 steel tubes to aide in the extraction of fossil fuels [43, 44]. Iron and its alloys are also regularly cleaned using HCl, for example, iron manufactured by the Saudi Basic Industries Corporation (SABIC), called SABIC Fe, is regularly cleaned of any oils and fat deposits on it by HCl solutions [45]. However, this acid cleaning leads to corrosion [45]. Razali *et al.* [46] stated that carbon steels are susceptible to acidic corrosion by HCl since these acids frequently encounter carbon steels in industrial applications such as industrial cleaning, pickling, acid descaling, and oil well acidizing.

Figure 2.1 shows the process by which MS is corroded by HCl [47]. The oxidation half-reaction (Equations 1 and 2) occurs at the anodic sites on the MS surface [48]. This half-reaction results in the formation of either Fe^{2+} or Fe^{3+} cations, along with the loss of electrons. The Fe cations subsequently react with Cl^- ions to form iron chlorides. The electrons produced at the anode migrate to the cathodic sites on the MS surface, where they participate in the reduction half-reaction (Equation 3), producing $H_2(g)$ [48]:

$$Fe_{(s)} \rightarrow Fe^{2+}_{(aq)} + 2e^- \quad (1)$$

$$Fe_{(s)} \rightarrow Fe^{3+}_{(aq)} + 3e^- \quad (2)$$

$$2H^+_{(aq)} + 2e^- \rightarrow H_{2(g)} \quad (3)$$

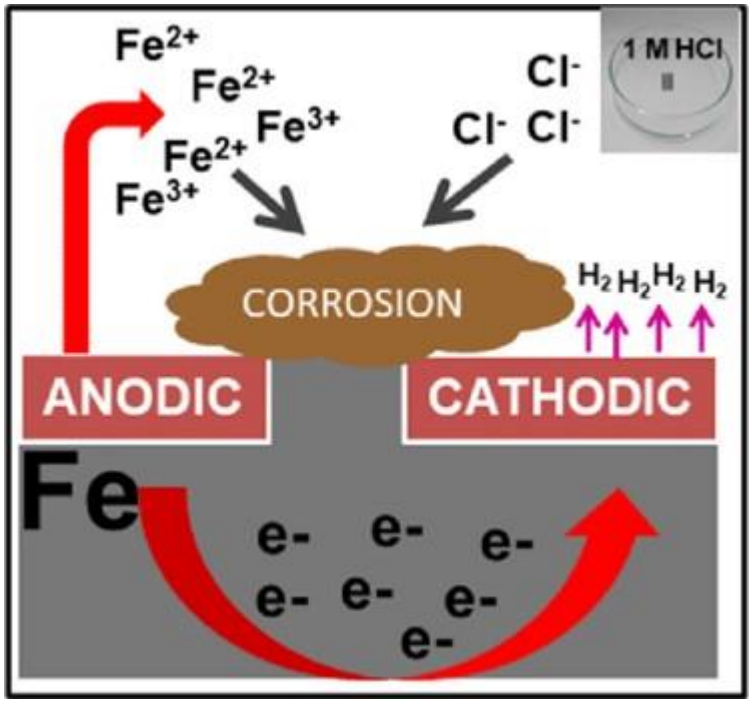

Figure 2.1: Corrosion of MS in HCl [47].

2.2 Types of corrosion

Noor *et al.* [49] noted that, after immersion into HCl solutions of concentrations ranging between 0.25 M to 2.5 M, MS showed susceptibility to pitting and general corrosion. Furthermore, it was shown that at higher concentrations of HCl, general corrosion became more prevalent [49].

2.2.1 Pitting corrosion

Pitting corrosion, also known as localized corrosion, is the relentless attack of a metal surface by corrosive species in the electrolyte at specific points on the metal surface [50]. Pitting corrosion is associated with metals that can form passive films, for example, stainless steel [51, 52]. Mild steel is generally unable to passivate therefore any pitting corrosion observed is most likely due to imperfections in the microstructure of the metal at those points where pitting is observed [50]. Depending on their concentration in the corrosive medium, the presence of halide ions (especially Cl^- ions) can facilitate pitting corrosion by reacting with metal ions in the metal oxide passive film, weakening and eventually breaking the metal oxide ionic bond [53]. Papavisanam

[54] identified seven types of pits that can form and propagate on a metal surface (Figure 2.2). Once a weak spot is found, the corrosive medium will continue to propagate the pit along the path of least resistance, therefore determining the overall shape and depth of the pit.

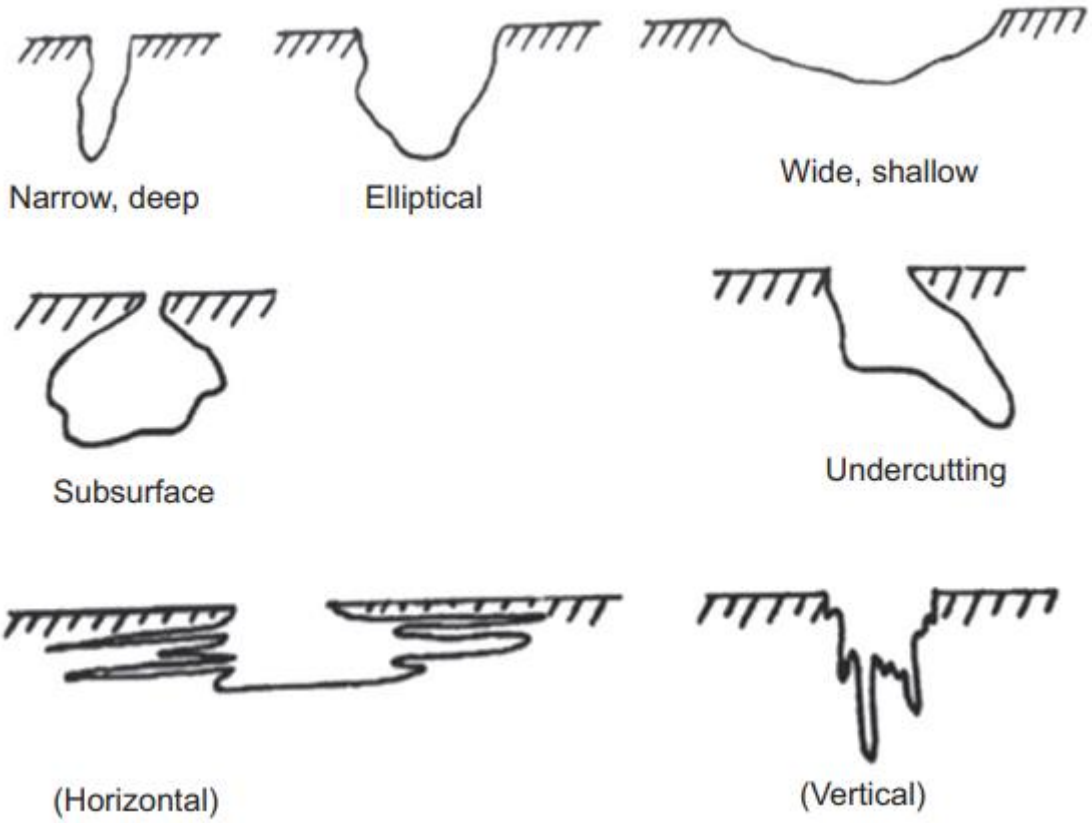

Figure 2.2: Different pit shapes caused by pitting corrosion [54].

Equation 4 implies that the time (t) over which corrosion of the metal surface is allowed to occur is the only determining parameter for pit depth (D). However, other factors such as the aggressive nature of the medium with which the metal is in contact, and the strength of the passive film formed surely play a role in pit depth.

$$D = \lambda t^{n} \qquad (4)$$

where λ and n are constants [50].

In metals that passivate, there are three main stages involved in pitting corrosion [55]:

1. Passivity breakdown
2. Pit development
3. Pit re-passivation

The ability of a metal to re-passivate, essentially repairing its surface, depends largely on the aggressive nature of the surrounding medium, in particular its Cl^- content [55]. The higher the Cl^- content, the more unlikely re-passivation is to occur.

2.2.2 General corrosion

General corrosion, also known as uniform corrosion, primarily affects most (if not all) of the surface of a steel structure without a passive film [56, 57]. If the steel structure is a pipe, general corrosion can affect the pipe both internally and externally, with the latter occurring due to inadequate coating [58]. Figure 2.3 shows a pipe that has suffered general corrosion on its exterior, eroding and thus weakening the external wall of the pipe, resulting in a rupture [58]. The visibly thin walls of the pipe show how destructive general corrosion can be.

Figure 2.3: Ruptured steel pipe gradually worn out by general corrosion [58].

Figure 2.4 shows yet another example of the destructive effects of uniform corrosion. A corroded gate valve used to regulate the flow of a chemical in a chemical transfer pipeline was corroded over its entire surface. The valve is so severely corroded that a component once attached to it, a gate pin, is missing [57].

Figure 2.4: Corroded gate valve of a chemical transfer pipeline [57].

Whilst many authors agree that general corrosion affects the entire metal surface uniformly [59-62], Mills *et al.* [63] disagrees with this notion, stating that the uniform distribution of corrosion is an oversimplification of the nature of the process. Lambert [64] seems to agree with Mills *et al.* [63] when he/she uses the phrase "general corrosion results in what at least appears to be a uniform attack on the metal surface." What is evident, however, is that general corrosion is a significant threat to steel structures.

2.3 Corrosion of steel: a case study of the petroleum industry

As outlined in Section 2.1, steel is extensively used in the petroleum industry for the extraction of fossil fuels. Crude oil naturally contains corrosive substances [65]. These corrosive substances are primarily $CO_{2(g)}$ and $H_2S_{(g)}$, with both gases accounting for approximately 60% of corrosion failures in the petroleum industry, with HCl and other corrosive species accounting for the remaining 40% [66]. $CO_{2(g)}$ and $H_2S_{(g)}$ cause sweet and sour corrosion respectively [67].

2.3.1 Sweet corrosion

$CO_{2(g)}$ induced corrosion is widely recognized as a common feature in the petroleum industry [68]. Whilst $CO_2(g)$ is not itself corrosive, it does result in the formation of carbonic acid when it dissolves in water (Equation 5), which then attacks the surface of the metal [69]. Carbonic acid facilitates both the oxidation and reduction half-reactions necessary for corrosion by dissociating into $H^+_{(aq)}$, $HCO_3^-{}_{(aq)}$ and $CO_3^-{}_{(aq)}$ ions [70-72]:

$$CO_{2(g)} + H_2O_{(l)} \leftrightarrow H_2CO_{3(aq)} \quad (5)$$

$$H_2CO_{3(aq)} \rightarrow H^+_{(aq)} + HCO^-_{3(aq)} \quad (6)$$

$$HCO^-_{3(aq)} \rightarrow H^+_{(aq)} + CO^{2-}_{3(aq)} \quad (7)$$

Sweet corrosion can often appear in the form of pitting corrosion, with sweet pitting corrosion in pipelines a key concern for the petroleum industry [73]. Figure 2.5 shows an oil and gas pipeline damaged by sweet pitting corrosion. The pipe shows the telltale signs of pitting corrosion in the form of small pits surrounding a much larger, deeper pit, all of which have severely eroded the pipe.

Figure 2.5: Sweet pitting corrosion on the internal lining of an oil and gas pipeline [74].

2.3.2 Sour corrosion

Whilst the corrosion mechanism of $H_2S_{(g)}$ is still not yet fully understood, it is generally accepted that sour corrosion is caused by $H_2S_{(g)}$ first dissolving in an aqueous environment according to the reaction mechanism shown below [75]:

$$H_2S_{(aq)} \leftrightarrow HS^-_{(aq)} + H^+_{(aq)} \quad (8)$$

$$HS^-_{(aq)} \leftrightarrow S^{2-}_{(aq)} + H^+_{(aq)} \quad (9)$$

Due to the myriad of factors influencing sour corrosion and their interconnectedness, it has been very difficult to understand the influence that one factor has on the process [74]. However, what is not in dispute is the damaging effect that sour corrosion has on metal structures in the petroleum industry. Figure 2.6 shows pipes damaged by sour corrosion [74]. Both Figure 2.6a and 2.6b show pipes whose internal lining has been severely damaged. The pipe in Figure 2.6a has been damaged to the point were a big chunk of it has broken off. The internal lining in Figure 2.6b seems to have been so badly eroded it has even begun to flake off.

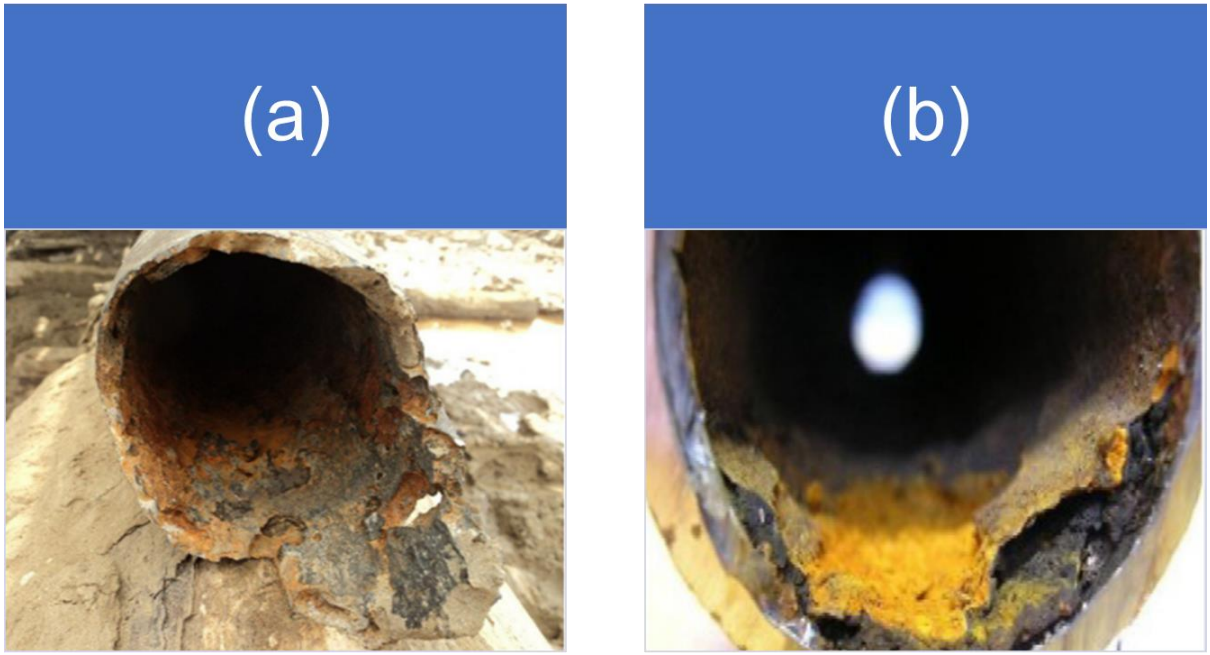

Figure 2.6: Two pipes severely corroded by sour corrosion [74].

2.4 Hydrochloric acid induced corrosion of zinc

Zinc is a non-ferrous metal widely used in industry [75]. Zinc is susceptible to corrosion by acidic media, particularly at a pH <6 [76-78]. When zinc encounters a solution of HCl, corrosion sets in in much the same way as with MS with the only difference being the metal involved in the oxidation half-reaction (Equation 10). The reduction half-reaction at the cathode remains unchanged.

$$\mathrm{Zn_{(s)}} \rightarrow \mathrm{Zn^{2+}_{(aq)}} + 2\mathrm{e^-} \qquad (10)$$

This susceptibility to acid corrosion makes zinc useful in protecting MS from acidic corrosion via a method called cathodic protection. Zinc has a much lower reduction potential than Fe (the primary component in MS), resulting in zinc corroding preferentially to MS [79]. Loto *et al.* [80] found that zinc sacrificial anodes performed well at protecting MS from HCl corrosion at temperatures of 27°C and 60°C. However, before steel can be protected by zinc, it must first be coated with zinc in a process known as galvanization [81]. This is just one of the many methods currently employed to protect steel from corrosion.

2.5 Methods for protecting steel from corrosion

2.5.1 Galvanization of steel

Zinc is primarily used in the production of galvanized Fe/steel [82]. Galvanized steel is produced either by “hot dipping” steel into molten zinc or the electrodeposition of zinc onto steel by making steel the cathode [83]. The former is a less efficient way of galvanizing steel as it produces an imperfect zinc layer on the steel surface due to the formation of Zn-Fe phases [84]. The addition of aluminium suppresses the formation of these phases by forming Zn-Al phases instead [85], thereby improving the quality of the overlying zinc protective layer. Figure 2.7 shows a schematic of how steel is galvanized using the hot dip method [86]. The technique consists of transporting steel pieces via a conveyer belt, through four sections, before being dipped in molten zinc. Excess molten zinc is blown off the freshly galvanized steel pieces by jet nozzles before being heated, cooled, and finally transported to a storage facility.

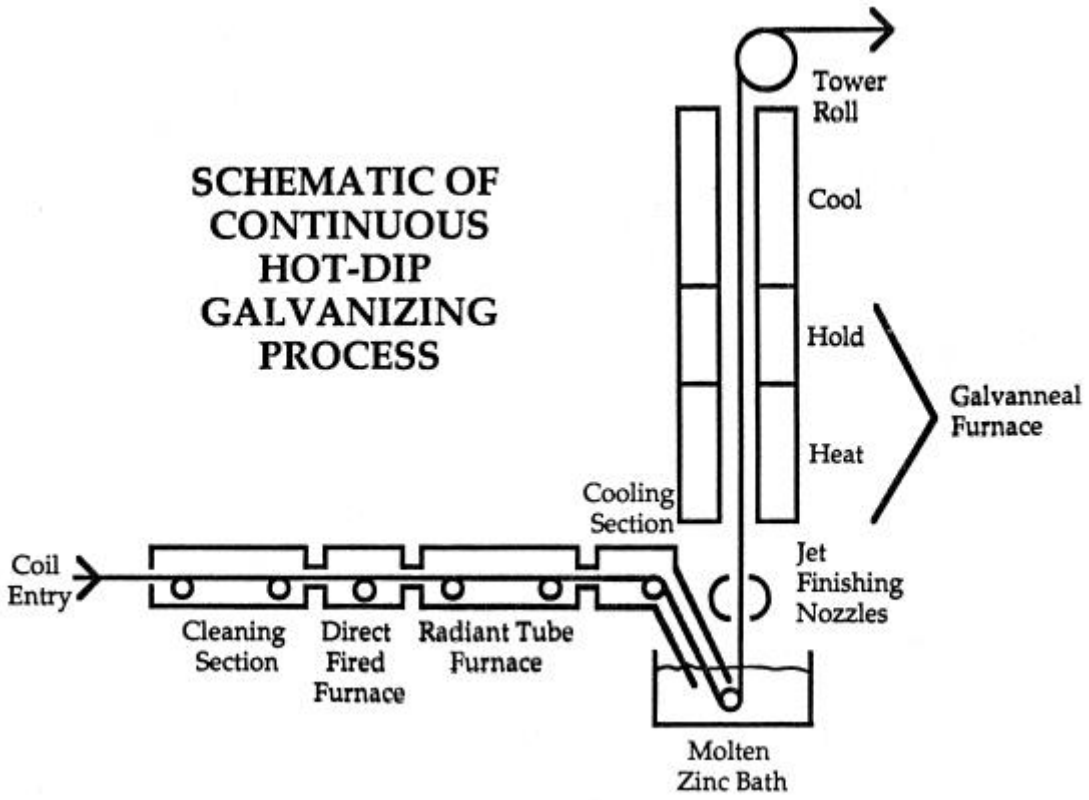

Figure 2.7: Schematic of hot-dip galvanizing process [86].

2.5.2 Material selection

Material selection is an important way to minimize corrosion by ensuring equipment is made up of metals suitable for the task at hand. This entails considering a wide range of factors such as the environmental conditions at the work site, pressure, temperature and if being used in the petroleum industry, the corrosiveness of the constituent chemicals in the oil and gas streams being extracted [87, 88]. Figure 2.8 shows the process that is undertaken when selecting suitable materials for use in a particular environment [89, 90]. The selection criteria are quite robust and consider important factors such as the corrosive environment in which the equipment will be operating, the most suitable equipment for that corrosive environment, its cost, and how best to protect the equipment from corrosion during service, thereby reducing repair and maintenance costs [89, 90].

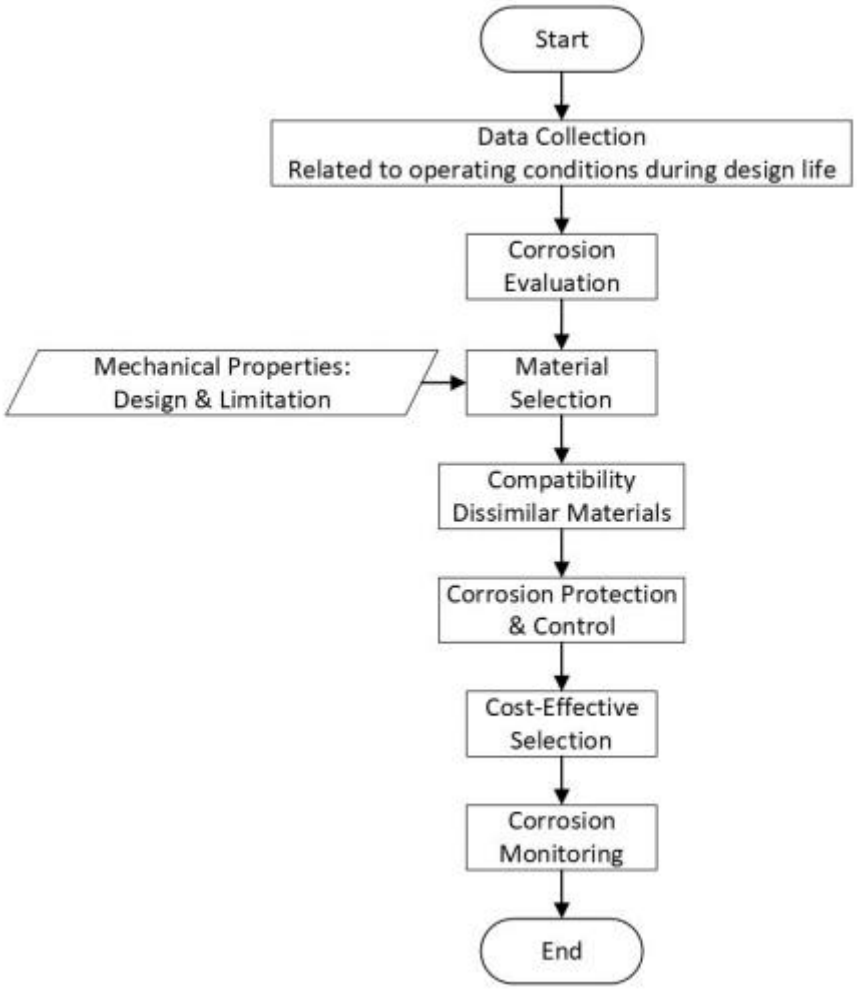

Figure 2.8: Selection process followed when selecting suitable materials for use in a corrosive environment [89, 90].

2.5.3 Corrosion inhibitors

Corrosion inhibitors are substances that reduce the rate of corrosion when added to a corrosive environment in trace quantities [91]. They achieve this through adsorption onto a substrate's surface thereby creating a protective film between the substrate and its corrosive environment [92]. Many industries make use of corrosion inhibitors: crude oil industry, chemical manufacture, heavy manufacturing, and water treatment [91]. Corrosion inhibitors can be either organic or inorganic [93].

2.5.3.1 Organic corrosion inhibitors

To be effective corrosion inhibitors, organic corrosion inhibitors must satisfy certain molecular structural requirements: they must have heteroatoms and multiple bonds [94]. The ability for heteroatoms and multiple bonds to donate electrons to the metal surface enables organic corrosion inhibitors to form adsorption films on the metal surface, rendering them useful in alleviating metallic corrosion [95-97]. The novel TZDs highlighted in this research all have the necessary structural requirements to be effective organic corrosion inhibitors for both MS and zinc in 1 M HCl.

2.5.3.1.1 Novel thiazolidinedione derivatives

Figure 2.9 shows the general molecular structure of the novel TZDs used in this research [98]. The TZD molecule consists of three distinct parts: a central TZD scaffold, an amino acid chain attached to the TZD scaffold by a two-carbon linker and an arylidene chain. The TZD scaffold is a ubiquitous moiety, enabling different functional groups to be attached to it. This is perhaps why it found extensive use in the synthesis of, at the time, new and revolutionary treatments for type 2 diabetes [99, 100].

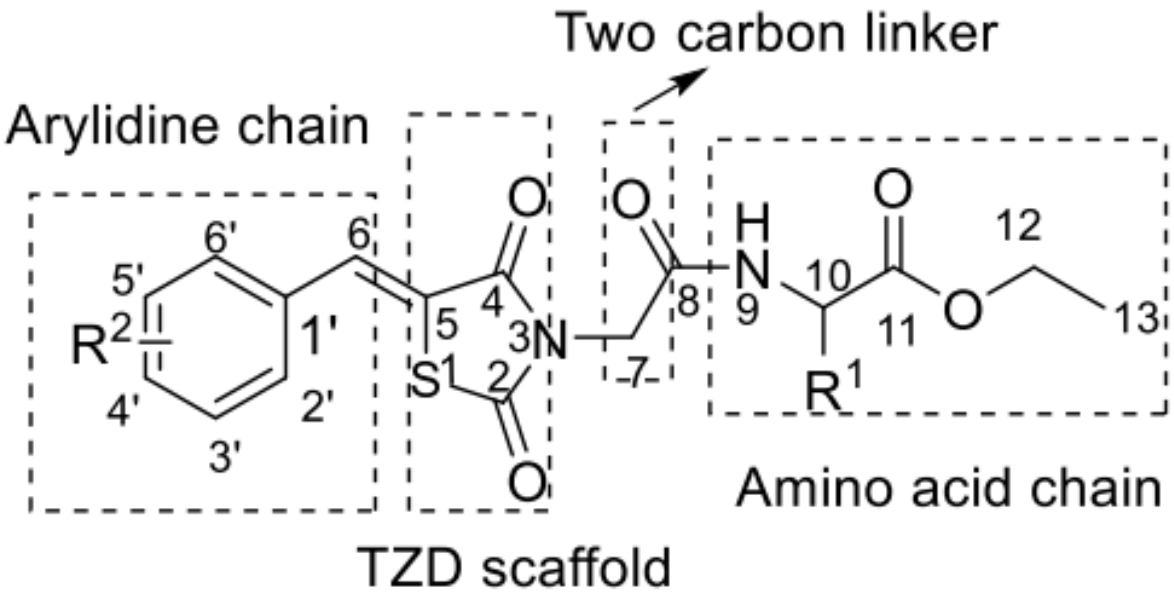

Figure 2.9: General molecular structure of novel TZDs [98].

However, a suitable molecular structure alone is not enough to conclude whether a corrosion inhibitor will be effective at protecting a metal from corrosion. To accurately assess the inhibition potential of a corrosion inhibitor, it must be subjected to a series of experiments, known as corrosion experiments/studies.

2.6 Corrosion experiments

2.6.1 Weight loss analysis

Weight loss analysis is the most basic experimental technique in corrosion studies. It is simple, easy to use and reliable [101]. Verma *et al.* [102] highlighted the significance of WL analysis when they noted its ability to bring together characteristics such as accuracy, simplicity, reliability, and precision. Verma *et al.* [103] emphasized the significance of WL analysis when they stated it is easy to use, precise, and reproducible. Thangarasu and Anand [104] described WL analysis as a cheap, easy to use and widely recognized experimental technique in corrosion research, spurring on numerous researchers to make use of it. All these attractive qualities of WL analysis have resulted in many researchers including it in their research [105-112].

Weight loss experiments can yield information on the kinetics of a corrosion reaction by varying the temperature of the aggressive environment (Equation 11) [113]. Additionally, WL analysis data can be used to calculate the surface coverage (θ) (Equation 12) and the %IE of a corrosion inhibitor (Equation 13) [113].

$$C_R = \frac{W_a - W_b}{A \cdot t} \tag{11}$$

$$\theta = \frac{w_o - w_i}{w_o} \tag{12}$$

$$\%IE = \theta \times 100 \tag{13}$$

were C_R, W_b, W_a, A, t, w_o and w_i are the metal corrosion rate, metal weight before immersion, metal weight after immersion, total metal surface area, immersion time and the weight loss values in the absence and presence of a corrosion inhibitor respectively [114-117].

In the case of the Langmuir adsorption isotherm (LAI), the most frequently encountered adsorption isotherm in corrosion studies, θ is utilised to obtain a parameter known as the adsorption equilibrium constant (K_{ads}) [118]. Once K_{ads} is known, the standard Gibbs free energy change of adsorption ($\Delta G°_{ads}$) can be calculated (Equation 14) [119]. The magnitude of $\Delta G°_{ads}$ reveals if adsorption proceeds via physisorption or chemisorption [120].

$$K_{ads} = \frac{1}{55.5} \cdot e^{\frac{-\Delta G^{\circ}_{ads}}{RT}} \quad (14)$$

where 55.5 is the concentration of water in $mol \cdot L^{-1}$, R is the universal gas constant and T is the temperature of the aggressive environment in Kelvin (K).

Through the van't Hoff equation (Equation 15), K_{ads} can also be used to calculate the standard enthalpy change of adsorption ($\Delta H°_{ads}$) and standard entropy change of adsorption ($\Delta S°_{ads}$) [121]:

$$\ln K_{ads} = \frac{-\Delta H^{\circ}_{ads}}{RT} + \frac{\Delta S^{\circ}_{ads}}{R} \quad (15)$$

Weight loss analysis data can also be used to derive other important thermodynamic data about the corroding metals. Information about activation parameters can be derived from both the Arrhenius (Equation 16) and transition state plots (Equation 17):

$$\mathrm{Log} C_R = \mathrm{Log} A - \frac{E_a}{2.303 \cdot R \cdot T} \quad (16)$$

where A and E_a are the frequency factor and activation energy respectively [122].

$$\log\left(\frac{C_R}{T}\right) = \left[\log\left(\frac{R}{Nh}\right) + \left(\frac{\Delta S^{\circ}_{act}}{2.303R}\right)\right] + \left(\frac{-\Delta H^{\circ}_{act}}{2.303R}\right)\left(\frac{1}{T}\right) \quad (17)$$

where N and h are Avogadro's and Planck's constants measured in mol^{-1} and J·s, respectively. Plotting $\log(C_R/T)$ vs 1/T yields a straight line with a slope equal to $(-\Delta H°_{act}/2.303R)$, from which the standard enthalpy change of activation ($\Delta H°_{act}$) can be calculated. The y-intercept is used to calculate the standard entropy change of activation ($\Delta S°_{act}$) [122].

All metal specimens used in WL analysis must be well prepared prior to commencement of experiments. These preparations entail wiping metal specimens with a clean dry cloth/tissue paper (even sandpaper were necessary), washing with

tap water, washing with distilled water, and degreasing with acetone to remove organic impurities [123]. After preparations are complete, metal specimens can be kept in a desiccator until commencement of WL experiments [124]. Initially, WL analysis involves three steps: weighing of metal coupons, their immersion in an aggressive environment and removal of metal coupons after a specified period. When metal coupons are removed from the corrosive environment, they are rinsed with distilled water and ethanol, degreased with acetone and air dried for a short period of time before being re-weighed [125]. This process is repeated at different inhibitor concentrations (C_{inh}) and temperatures. Weight loss analysis requires only basic apparatus: a thermostatic water bath, heating mantle (were necessary) and suitable glassware.

Weight loss analysis is an important technique in corrosion inhibition research and must therefore be utilized where possible. The fact that it is affordable, easy to set up, user friendly, accurate, reliable, and precise makes it an obvious starting point when carrying out corrosion research. Another advantage of WL analysis is that it can predict pseudo long term corrosion behaviour of a metal given that experiments are often conducted over many hours and sometimes many days as well.

2.6.2 Potentiodynamic polarization

Potentiodynamic polarization is a sensitive technique typically used to ascertain the corrosion current density (i_{corr}) of a metal in contact with a corrosive medium [126]. The i_{corr} can then be used to obtain the %IE of the corrosion inhibitor (Equation 18).

$$\%\mathrm{IE} = \left(1 - \frac{\mathrm{i}^{\mathrm{i}}_{\mathrm{corr}}}{\mathrm{i}^{\mathrm{o}}_{\mathrm{corr}}}\right) \times 100 \qquad (18)$$

where i^{o}_{corr} and i^{i}_{corr} are the corrosion current densities obtained for the uninhibited and inhibited solution respectively.

As an electrochemical technique, it requires a three-electrode set-up to function. Figure 2.10 shows such a set up: the working electrode (WE) which in corrosion studies represents the metal of interest (1), a reference electrode (RE) allowing for the accurate determination of the potential at the WE (2), and an inert counter electrode (CE) allowing for the completion of the circuit (3) [127]. A high impedance voltmeter

connects the WE and RE to keep the potential of the RE constant, allowing for the accurate measurement of the potential at the WE [127].

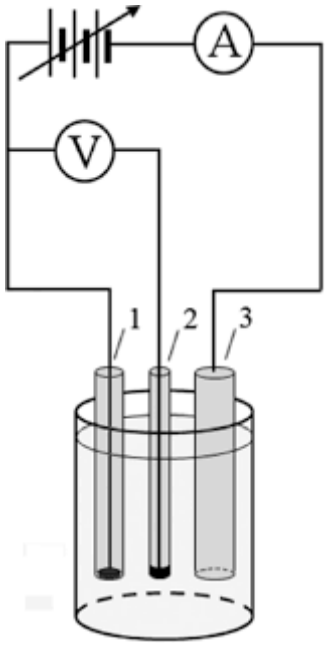

Figure 2.10: Typical three electrode set up for electrochemical analysis [127].

Using suitable software, tangents can be drawn to the cathodic and anodic curves in a Tafel plot (Figure 2.11), allowing for the calculation of β_a and β_c, the anodic and cathodic Tafel constants respectively [128]. The two tangents intercept at the corrosion potential (E_{corr}) and i_{corr} [128].

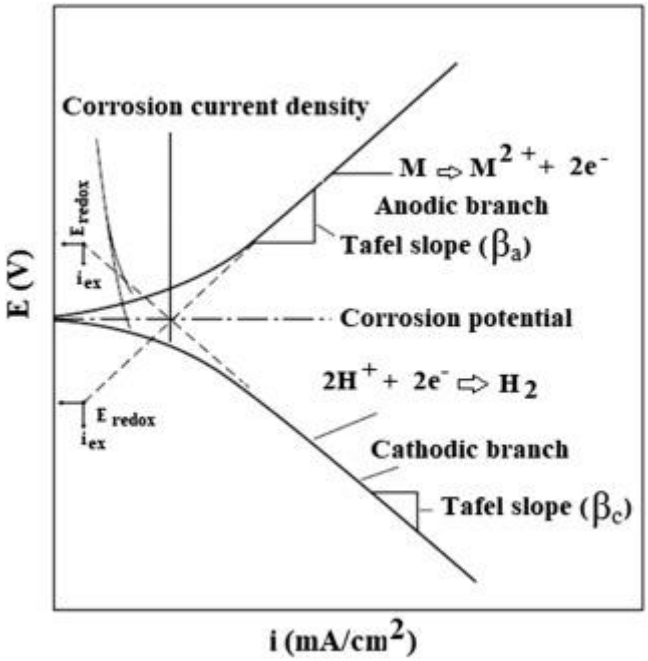

Figure 2.11: Tafel plots with tangents drawn showing Tafel constants, E_{corr} and i_{corr} [128].

When software automatically calculates i_{corr}, it does so by making use of the Stern-Geary equation (Equation 19) [128]. When calculating C_R, the software uses Equation 20:

$$i_{corr} = \frac{1}{2.303 R_p \cdot \left(\frac{\beta_a \cdot \beta_c}{\beta_a + \beta_c}\right)} \tag{19}$$

$$C_R = \left(\frac{i_{corr} \cdot t \cdot M}{F \cdot A \cdot d}\right) \tag{20}$$

where R_p, t, M, F, A, and d are the polarization resistance, immersion time, equivalent molar weight of the metal, Faraday's constant, WE surface area and metal density respectively [129, 130].

Whilst conceding that PDP is a sensitive and speedy technique, Obot *et al.* [131] state that it has some challenges such as errors inherent in manual extrapolation of Tafel constants and the destructive nature of the technique with regards to the surface of the WE, thus distorting i_{corr} data. A more accurate technique, they suggest, is electrochemical frequency modulation (EFM), a technique that allows for the determination of i_{corr} without the need to carry out a Tafel fit.

Despite the challenges faced in PDP analysis, it nonetheless provides important information regarding the active, passive, and trans-passive characteristics of a corroding metal [131]. This, along with its other essential qualities, ensures that PDP will continue to be an important tool in corrosion science research for many years to come.

2.6.3 Electrochemical impedance spectroscopy

Electrochemical impedance spectroscopy is a non-destructive, rapid technique in which a sinusoidal potential input signal is applied by the potentiostat, resulting in a sinusoidal current response [132]. The result is a spectrum known as a Nyquist plot which contains valuable information about the corroding metal such as charge transfer resistance (R_{ct}) and ohmic/solution resistance (R_Ω/R_s) [132]. Figure 2.12 shows an example of a Nyquist plot [133]. The gap between the imaginary axis and the semicircle is R_Ω whereas the diameter of the semi-circle is R_{ct} [133]. The apex of the semi-circle represents the maximum frequency (ω_{max}) of the potential signal, with frequency increasing from right to left on the plot.

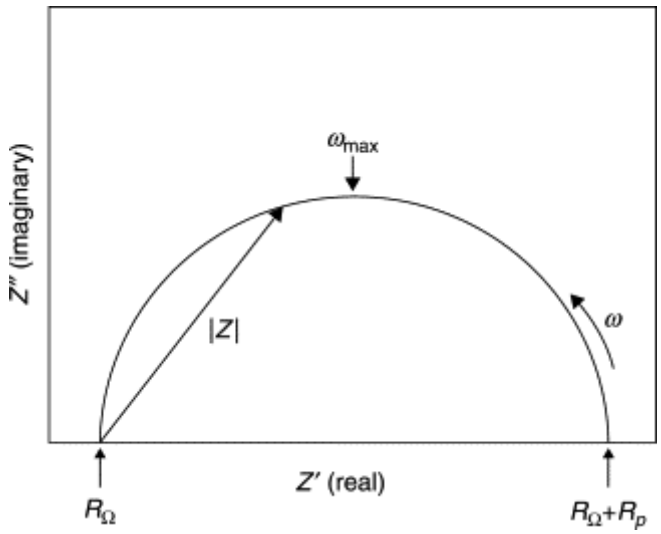

Figure 2.12: A Nyquist plot showing all its basic parameters [133].

The Nyquist plot in Figure 2.12 corresponds to a circuit known as a Randles circuit/cell (Figure 2.13). A Randles circuit consists of three basic components: two resistors (sometimes three if there's Warburg impedance (Z_d) involved) and a capacitor [134]. The three resistors shown account for R_{ct}, R_s and Z_d whilst the capacitor accounts for

the double-layer capacitance (C_{dl}) formed between the metal surface and the electrolyte [134].

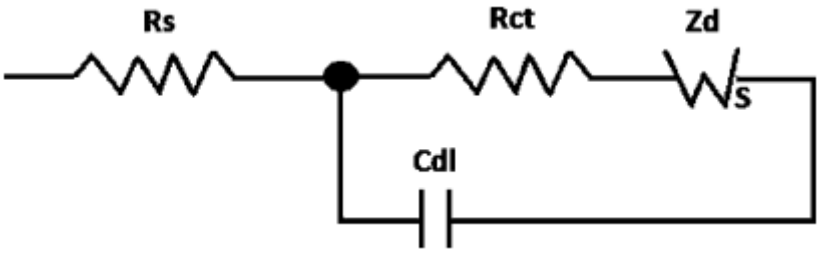

Figure 2.13: A Randles circuit and its basic components [134].

Like all experimental techniques, EIS is not without its faults. Poursaee [133] identified three major issues with Nyquist plots: details concerning the frequency are absent from the Nyquist plot, C_{dl} cannot be determined from the plot but must be calculated separately and only the largest impedance determines the nature of the plot regardless of whether there are smaller impedances present in the circuit. Whilst Bode plots are an alternative plot derived from EIS data, the Nyquist plot remains the simplest and most common form of representation of EIS data.

2.6.3.1 Bode plots

The major difference between a Nyquist plot and a Bode plot is that frequency data can be derived from the latter, along with any frequency dependent parameters of the electrochemical system, both of which cannot be determined from the Nyquist plot [135]. Figure 2.14 shows a typical Bode magnitude and phase angle plot, in which the frequency dependence of impedance and phase angle is shown [136]. As the frequency decreases, impedance increases, signifying corrosion inhibition. The direct proportionality relationship between impedance and C_{inh} also signifies corrosion inhibition is occurring [136]. As mid-frequency is approached from either direction, the phase angle approaches 90°, indicative of a perfect Nyquist plot and therefore ideal capacitance [136].

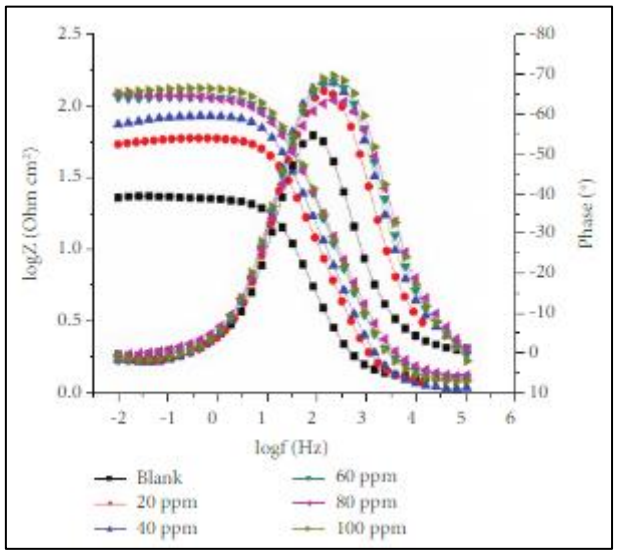

Figure 2.14: Bode magnitude and phase angle plot showing the inhibitive performance of different C_{inh} on MS in 1 M HCl [136].

2.6.4 Surface characterization techniques

There are many techniques that can reveal information regarding the chemical composition of the surface of a substrate some of which are: x-ray photoelectron spectroscopy (XPS), x-ray diffraction (XRD), surface enhanced Raman spectroscopy, and FTIR. The first three techniques make use of x-ray photons fired at the sample material [137-139]. In each technique, the different ways in which the photons interact with the sample material gives information about the chemical composition of the sample. For example, in XPS the incident photons will strike off electrons in the inner orbitals of the atoms in the sample sending them towards a detector, enabling the detector to measure their kinetic energies and workout the unique binding energy between the ejected electrons and their respective nuclei [140]. In XRD, the incident photons are deflected by the sample atoms such that Bragg's law is satisfied, causing constructive interference, and thus enabling the unique chemical signature of the sample to be identified [141]. In surface enhanced Raman spectroscopy, the difference in the frequencies (and therefore energies) of the incident and scattered photons is measured, allowing for the identification of the functional groups present in a sample [142].

2.6.4.1 Fourier transform infrared spectroscopy

Fourier transform infrared spectroscopy is a rapid, economical, easy, and non-destructive technique utilized in characterizing pure solids, liquids, and gases [143-147]. It can also be used for the investigation of surface and interfacial phenomena, its primary use in corrosion studies [148]. The technique works by directing infrared radiation toward the sample. A fraction of the radiation is absorbed whilst the remainder passes through [149]. Each chemical bond absorbs infrared energy at a specific frequency, providing information on the chemical composition of the sample [150].

Although an underrated surface characterization technique, FTIR not only provides information about the chemical composition of the surface of a substrate but, also provides visual proof, via the spectrum produced, that a corrosion inhibitor has indeed adsorbed onto a metal surface. In Figure 2.15, the red spectrum (unadsorbed extract) shows several peaks that are not present in the blue spectrum (adsorbed extract) [151]. The disappearance of these peaks shows that the extract did indeed adsorb onto the MS surface [151].

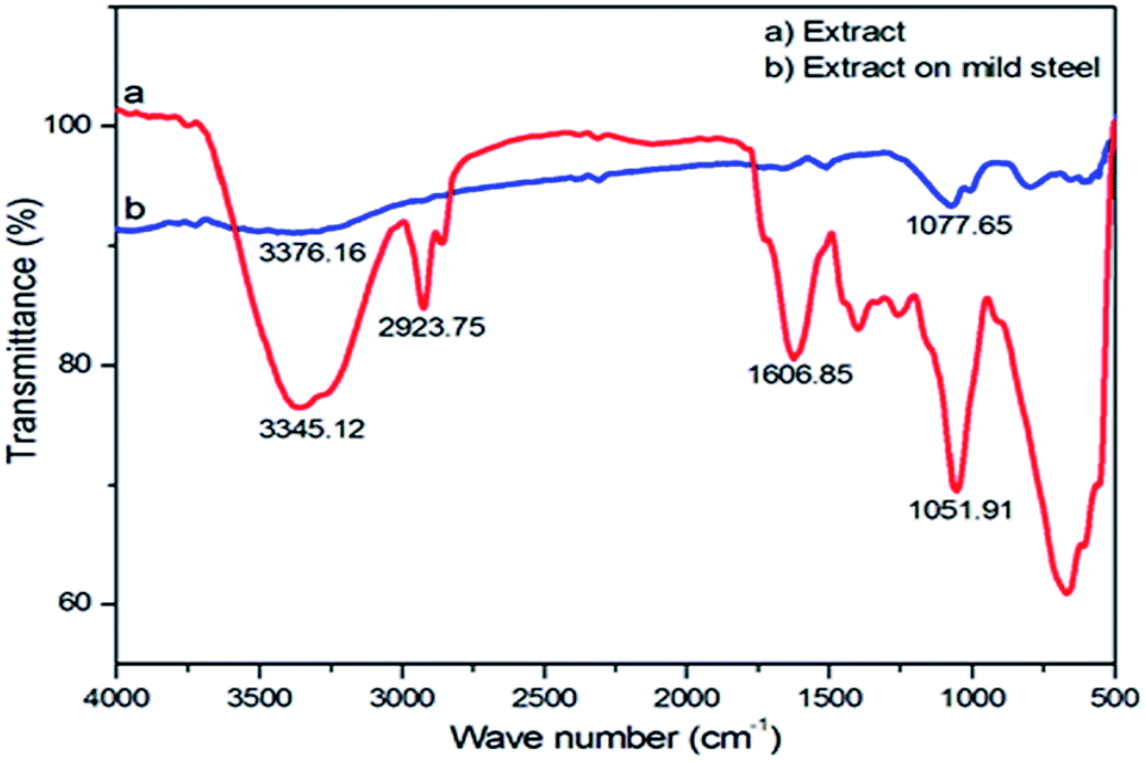

Figure 2.15: FTIR spectra for *Rhus verniciflua* on MS in 1 M H_2SO_4 [151].

CHAPTER THREE

METHODOLOGY

Chapter three summary

This chapter gives a detailed description of the synthesis of the novel TZDs by highlighting all the different reagents and reaction conditions used during the synthesis process. In addition, the chapter provides information about the different experimental techniques and instrumentation used to ascertain the corrosion inhibition potential of the novel TZDs.

3.1 Synthesis and characterization of corrosion inhibitors

All TZDs were synthesized as shown in Figure 3.1. Three types of TZD were synthesized: alaninates, butanoates and glycinates using alanine, α-amino butyric acid, and glycine as starting reagents, respectively.

In the first reaction (a), an amino acid was mixed with thionyl chloride in a 1:1 molar ratio. To this mixture was added 50 mL of ethanol. After refluxing the mixture for a minimum of 12 hours, the mixture was poured into a 20 mL ice/water mixture to precipitate the ester (compound 2). After filtration, the ester was dried and weighed.

In reaction b, a 1:1 molar ratio mixture of K_2CO_3 and the protected amino acid were added to a mixture comprising of 50 mL de-ionized water and 50 mL dichloromethane (DCM). When the mixture's temperature had been dropped to between 0°C and 5°C using an ice bath, bromoacetyl chloride was added dropwise to the mixture until a 1:1:1 molar ratio was achieved with both the protected amino acid and K_2CO_3. After being stirred at room temperature for a minimum of 12 hours, the DCM layer was separated from the aqueous layer using a separating funnel. $MgSO_4$ was then mixed with the DCM layer to absorb any leftover moisture. After filtering out the $MgSO_4$, the DCM was vapourised using a Buchi Labor-Technik AG R-210 rotavapor (Flawil, Switzerland), after which the acetamide ester was obtained and its mass recorded.

Reaction c was carried out by adding a commercially obtained TZD salt to KOH in a 1:1 molar ratio. To this mixture was added 50 mL of ethanol. After thoroughly mixing all the reagents, the mixture was refluxed for a minimum of 1 hour. Once the mixture had cooled to room temperature, it was further cooled in an ice bath to precipitate additional thiazolidinedione potassium salt (TZD-K^+). The TZD-K^+ salt was then filtered out, dried, and weighed.

In reaction d, the TZD-K^+ salt was mixed with the acetamide ester in a 1:1 molar ratio. To this mixture was added 50 mL of tetrahydrofuran (THF). The mixture was then refluxed, with magnetic stirring, for a minimum of 12 hours. After cooling to room temperature, the THF layer containing the TZD-acetamide ester was vapourised using a rotavapor, after which the TZD-acetamide ester was obtained and its mass recorded.

In reaction e, a Knoevenagel condensation, the TZD-acetamide ester and aldehyde were mixed in a molar ratio of 1:1. 50 mL of ethanol was then added to the mixture

together with 0.20 mL of piperidine. The overall mixture was refluxed for a minimum of 12 hours. After cooling to room temperature, the contents of the round bottom flask were poured into a beaker containing a 20 mL ice/water mixture to precipitate the TZD. The TZD was then filtered out and weighed after drying.

After purification of the TZDs through washing with hot methanol, each TZD was characterized using a Bruker Ultra Shield Plus NMR spectrometer (Billerica, United States). Specifically, ^{1}H NMR and ^{13}C NMR were used to characterize the TZDs.

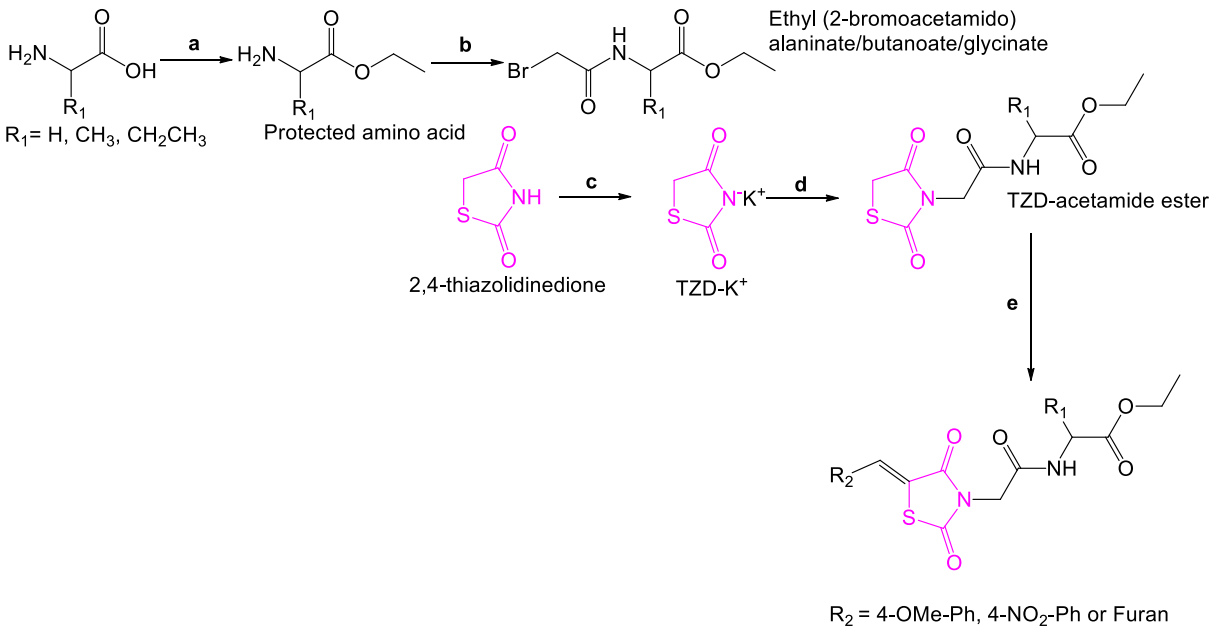

Figure 3.1: Synthesis of novel TZDs.

Reagents and conditions: **(a):** Thionyl chloride, EtOH, reflux for 12 hours; **(b):** DCM, H_2O, Bromoacetylchloride (0°C), K_2CO_3, magnetic stirring at rt for 12 hours; **(c):** EtOH, KOH, reflux for 1 hour; **(d):** Ethyl (2-bromoacetamido) alaninate/butanoate/glycinate, THF, reflux for 12 hours; **(e):** para-anisaldehyde/4-nitrobenzaldehyde/furfural, piperidine, EtOH, reflux for 12 hours

The assays of all the reagents used for the synthesis and characterization of the TZDs are shown in Table 3.1. All chemical reagents shown, apart from the NMR solvent used for characterization, were used in the synthetic steps shown above (see Figure 3.1). Only analytical grade quality reagents were used for synthesizing the TZDs.

Table 3.1: Reagent assays.

Reagents	Assay (%)
Bromoacetyl chloride	≥98
Dichloromethane	≥99.8
Dimethyl sulfoxide (anhydrous)	≥99.5
Dimethyl sulfoxide (NMR solvent)	99.9
DL-2-aminobutyric acid	99
Ethanol	95
Furfural	99
4-Nitrobenzaldehyde	98
Para-anisaldehyde	98
Piperidine	≥99
Potassium chloride	≥99
Potassium hydroxide pellets	≥85
Tetrahydrofuran	99.9
2,4-thiazolidinedione (Technical grade)	90
Thionyl chloride	≥99

Table 3.2 shows the molecular structures of the TZDs. Apart from B2 which was synthesized using furfural, all TZDs with the numbers 1, 2 and 3 as part of their code were synthesized using para-anisaldehyde, 4-nitrobenzaldehyde and furfural respectively.

Table 3.2: TZD molecular structures.

TZD	Molecular structure
A1	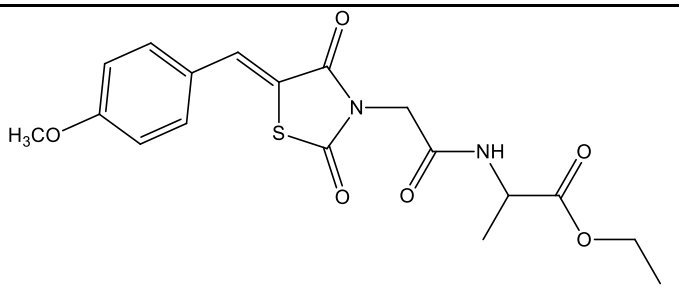
A2	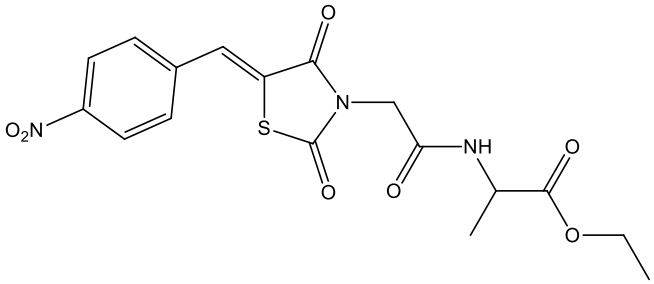
A3	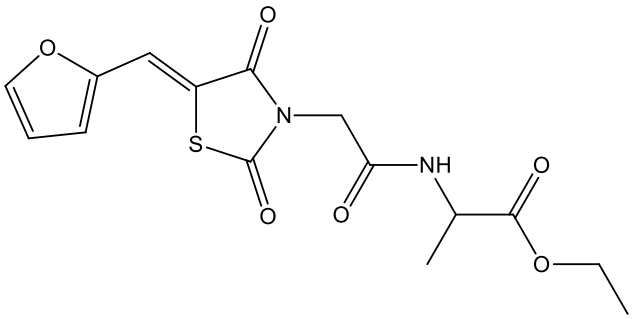
B1	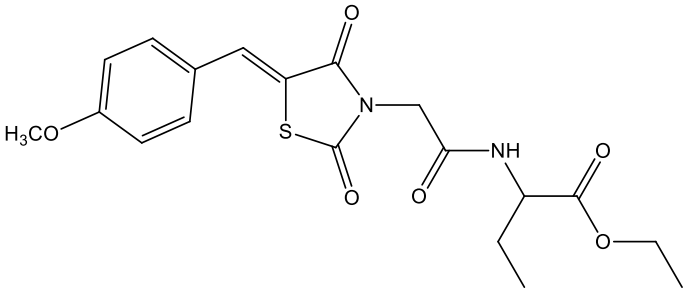
B2	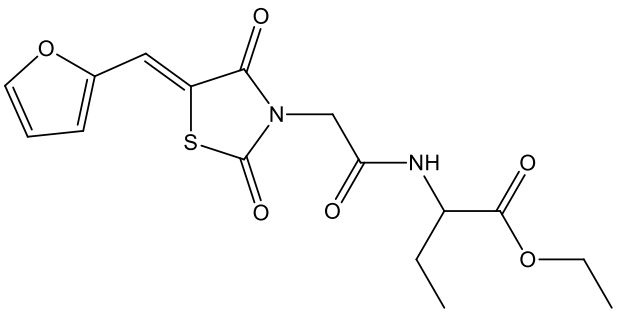

G1	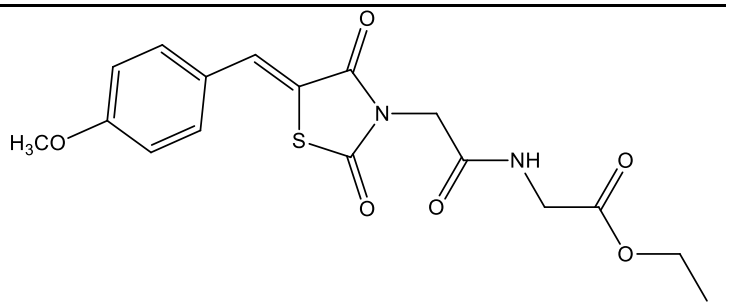
G2	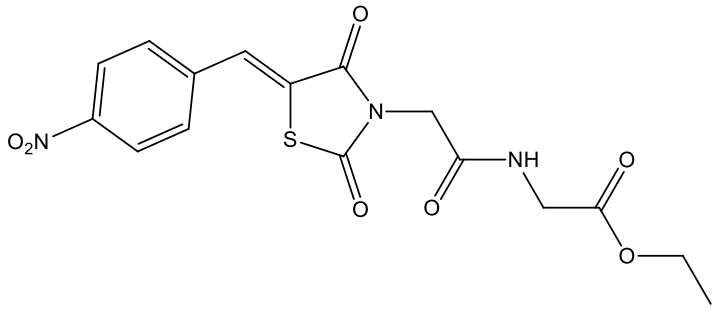
G3	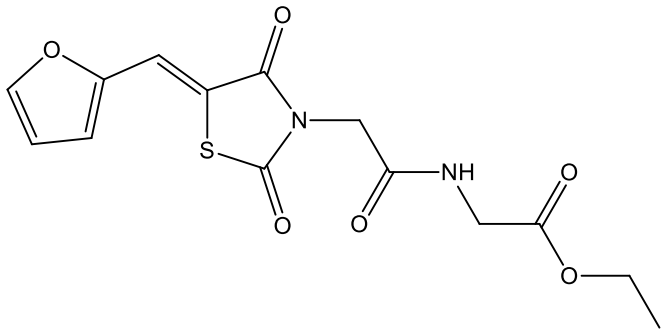

3.2 Corrosion studies

3.2.1 Metal coupons

Table 3.3 shows the elemental composition of all MS coupons used. All Zn coupons used had a 99.90 wt. % purity. Mild steel is an alloy of Fe and thus the bulk of its elemental composition will be Fe. All other elements are added to provide mechanical strength to the MS coupons.

Table 3.3: Elemental composition of MS coupons.

Element	Fe	C	Ni	Mn	S	P	Mo
wt. %	99.32	0.21	0.04	0.37	0.03	0.02	0.01

3.2.2 Solution preparation

All 1 M HCl solutions were prepared using fuming, 32% HCl and ultra-pure deionized water. The ultra-pure deionized water was obtained from a Suez purewater 300 laboratory water purifier (Thame, England). Due to the poor solubility of all the TZDs in water, an organic solvent called anhydrous dimethyl sulfoxide (DMSO), together with slight heating and magnetic stirring, were required to ensure solvation of TZDs before commencement of corrosion studies.

3.2.3 Weight loss analysis

Weight loss experiments were conducted from 303.15 K to 333.15 K with 10 K temperature increments. Memmert water baths (Buchenbach, Germany) were used for all WL experiments. All metal coupons were polished with silicon-carbide (SiC) paper before commencement of WL experiments. Once polished, the metals were washed with acetone, air dried, weighed and immersed in both a blank and TZD infused 1 M HCl solution. After 5 hours, metals were extracted from the caustic solutions. Once the brushing, re-rinsing (with acetone) and re-drying steps were completed, the metal coupons were re-weighed.

3.2.4 Electrochemical studies

All electrochemical analysis experiments were conducted at 303.15 K using an SP-150 Biologic potentiostat (Seyssinet-Pariset, France). All metal coupons used as WE had a total surface area of 1 cm^2. Before commencement of experiments, all WE were polished with abrasive SiC paper. To complete the electrochemical cell, two other electrodes were used: a Ag/AgCl RE and a graphite CE. Open circuit potential was reached after 30 minutes.

3.2.5 Fourier transform infrared spectroscopy

All FTIR experiments were conducted using a Bruker platinum 22 vector instrument (Billerica, United States). All metal coupons were prepared at 303.15 K. After pre-treatment of metal coupons (no weighing involved), each metal was immersed in both

a blank and TZD infused 1 M HCl solution. After 5 hours, metal specimens were extracted and granted sufficient time to corrode. Corrosion products were then scrapped off the metal surfaces and analysed using FTIR.

CHAPTER FOUR

RESULTS AND DISCUSSION

Chapter four summary

This chapter provides a detailed discussion of not only the results of the synthesis of the TZDs but also the results obtained from four experimental techniques: weight loss studies, potentiodynamic polarization analysis, electrochemical impedance spectroscopy and, Fourier transform infrared spectroscopy.

4.1 Synthesis of novel thiazolidinedione derivatives

Table 4.1 shows the percentage yields (%Y) of all eight TZDs. Some of the %Y are quite low, with the lowest %Y achieved being that for B1 (20%). The highest %Y achieved is that for A1 (52%). The low %Y may be because of the bulky nature of the reagents involved (see Figure 3.1), resulting in steric hinderance between the reagents, thus slowing down the reaction. This is even though all reactions were allowed to proceed for a minimum of 12 hours. However, since corrosion inhibitors are used in trace quantities, a low %Y is not necessarily a negative as there may still be more than enough compound to utilize in corrosion studies, as was the case in this research.

Table 4.1: Percentage yields obtained from the synthesis of novel TZDs.

TZD	Yield (%)
A1	52
A2	24
A3	38
B1	20
B2	31
G1	48
G2	21
G3	39

Figures 4.1 to 4.6 show the ^{1}H NMR spectra for the alaninates. All the ^{1}H NMR spectra consist of three regions: aliphatic, heteroatomic and aromatic. The ^{1}H NMR spectra have the same aliphatic region, consisting of two (-CH_3) group peaks at approximately 1.19 ppm and 1.30 ppm, attributed to H-1 (triplet) and H-5 (doublet), respectively. Moreover, all the ^{1}H NMR spectra have a doublet between 8.75 ppm and 8.79 ppm, ascribed to H-6 (a secondary amine proton). Due to the similarity of the molecular structures of A1 and A2, their aromatic regions are quite similar, with two doublets attributed to H-14 and H-15 whilst H-12 is consistently a singlet. The presence of a furan ring gives A3 a very different aromatic region. There are three doublets attributed to H-6 (8.76 ppm), H-14 (7.18 ppm) and H-16 (8.10 ppm). Proton H-15 in the ^{1}H-NMR spectrum of A3 is a doublet of a doublet (dd) (6.78 ppm). There is a lot more variation

between the alaninates in the heteroatomic region. The heteroatomic region of A1 shows H-17 (singlet), H-2 (dd), H-4 (multiplet) and H-8 (singlet). The heteroatomic regions of A2 and A3 are like that of A1, with only H-17 missing as A2 and A3 have a ($-NO_2$) group and furan ring, respectively.

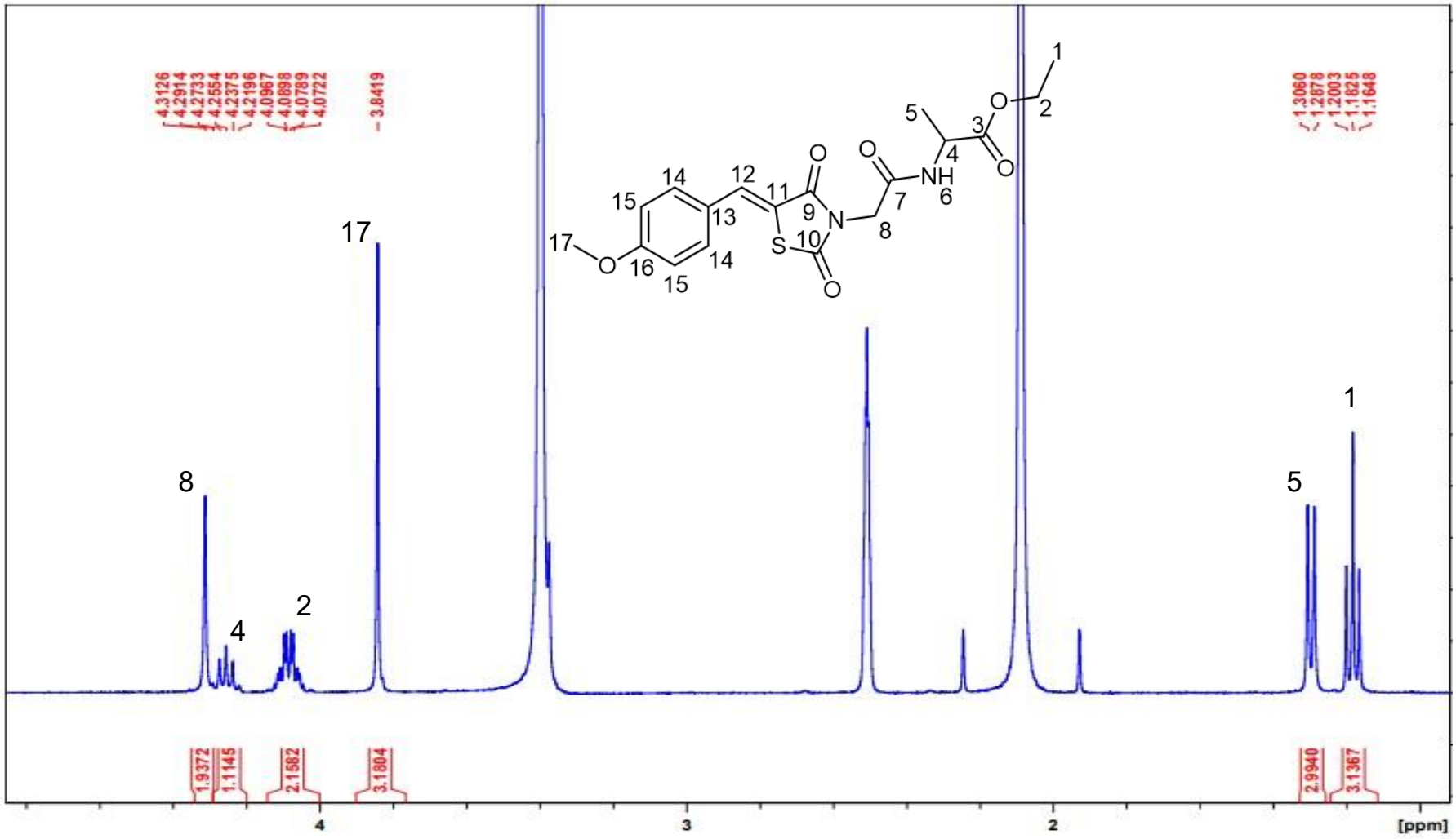

Figure 4.1: A1 ^{1}H NMR spectrum (aliphatic and heteroatomic regions).

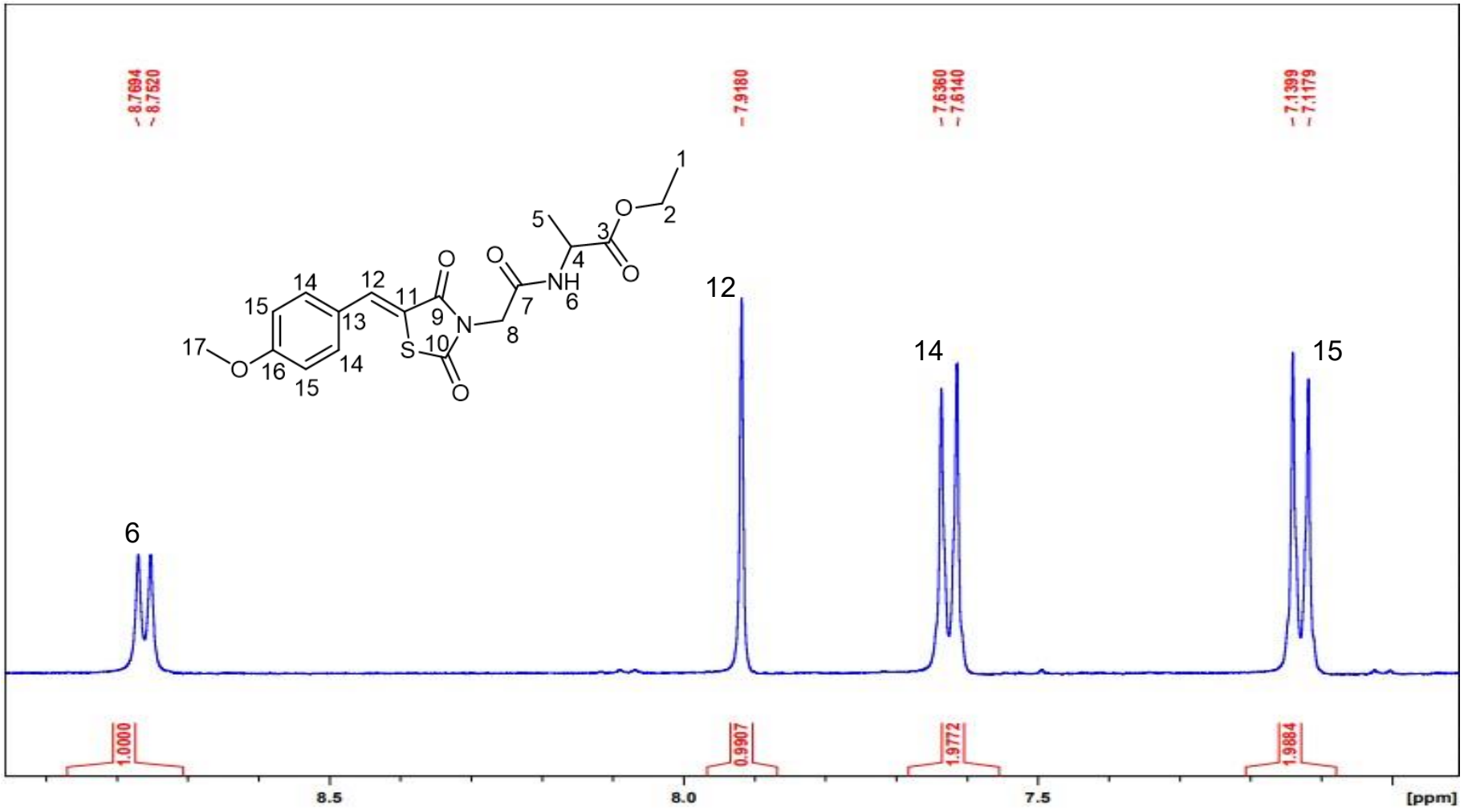

Figure 4.2: A1 ^{1}H NMR spectrum (aromatic region).

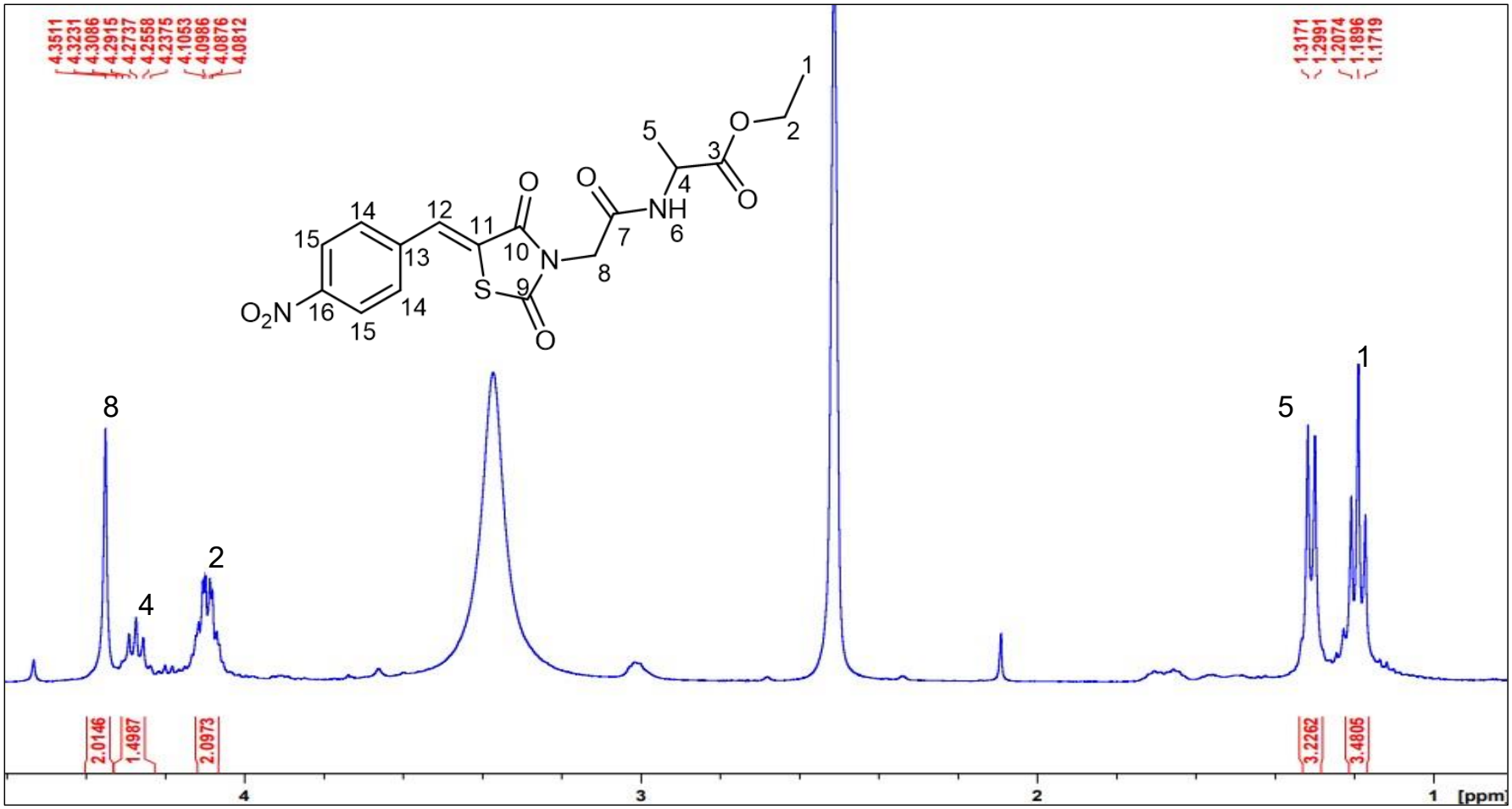

Figure 4.3: A2 ^{1}H NMR spectrum (aliphatic and heteroatomic region).

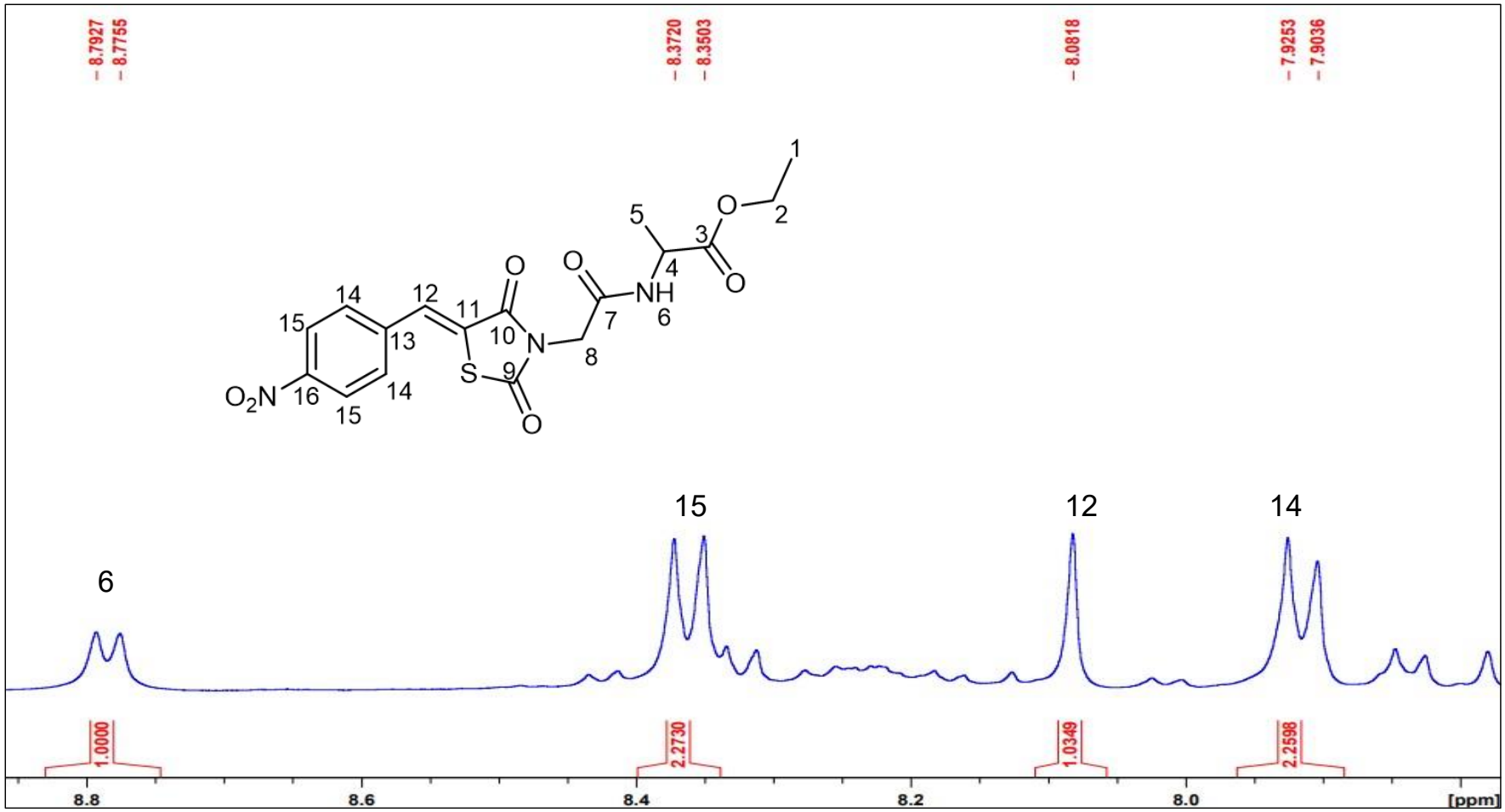

Figure 4.4: A2 ^{1}H NMR spectrum (aromatic region).

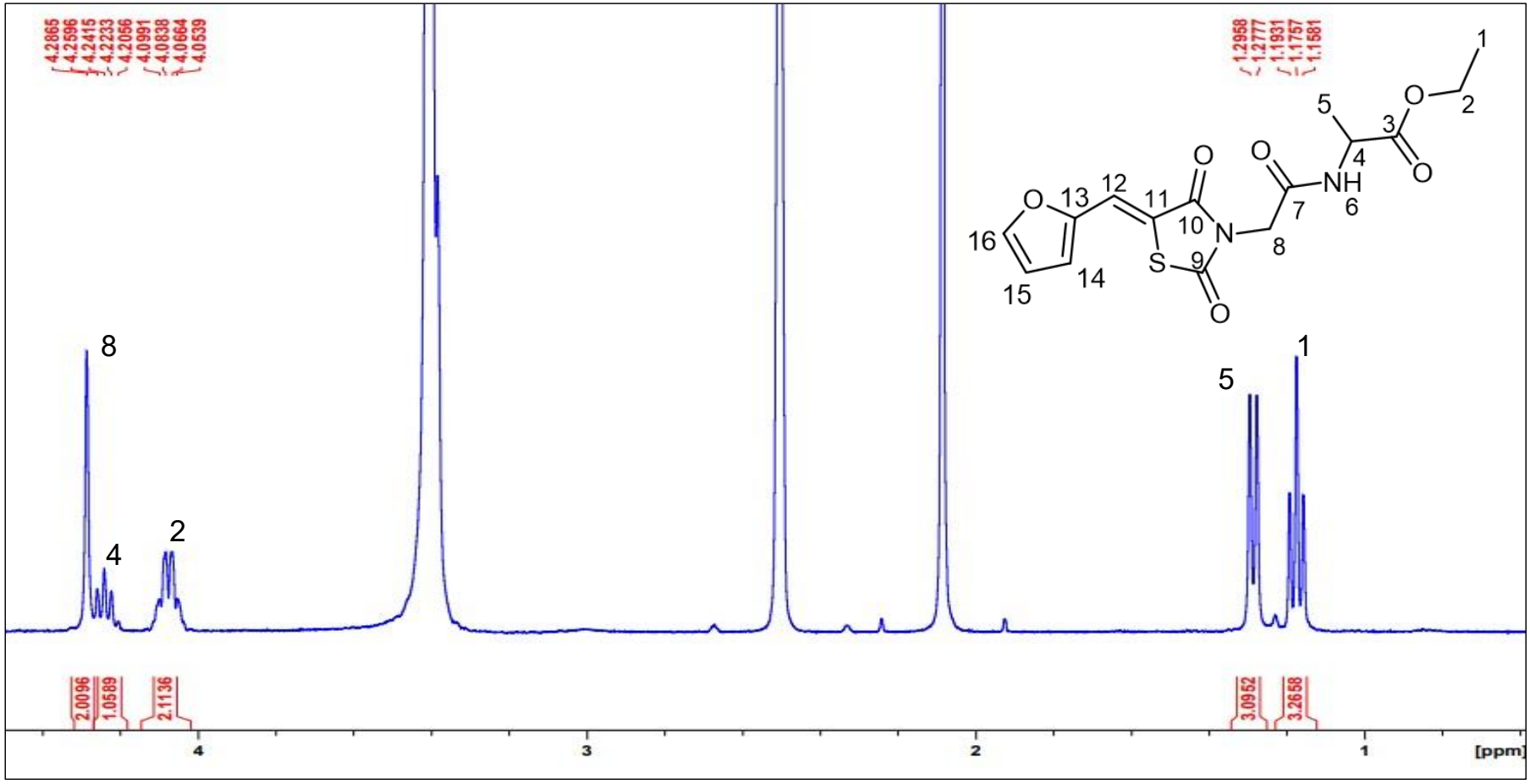

Figure 4.5: A3 ^{1}H NMR spectrum (aliphatic and heteroatomic region).

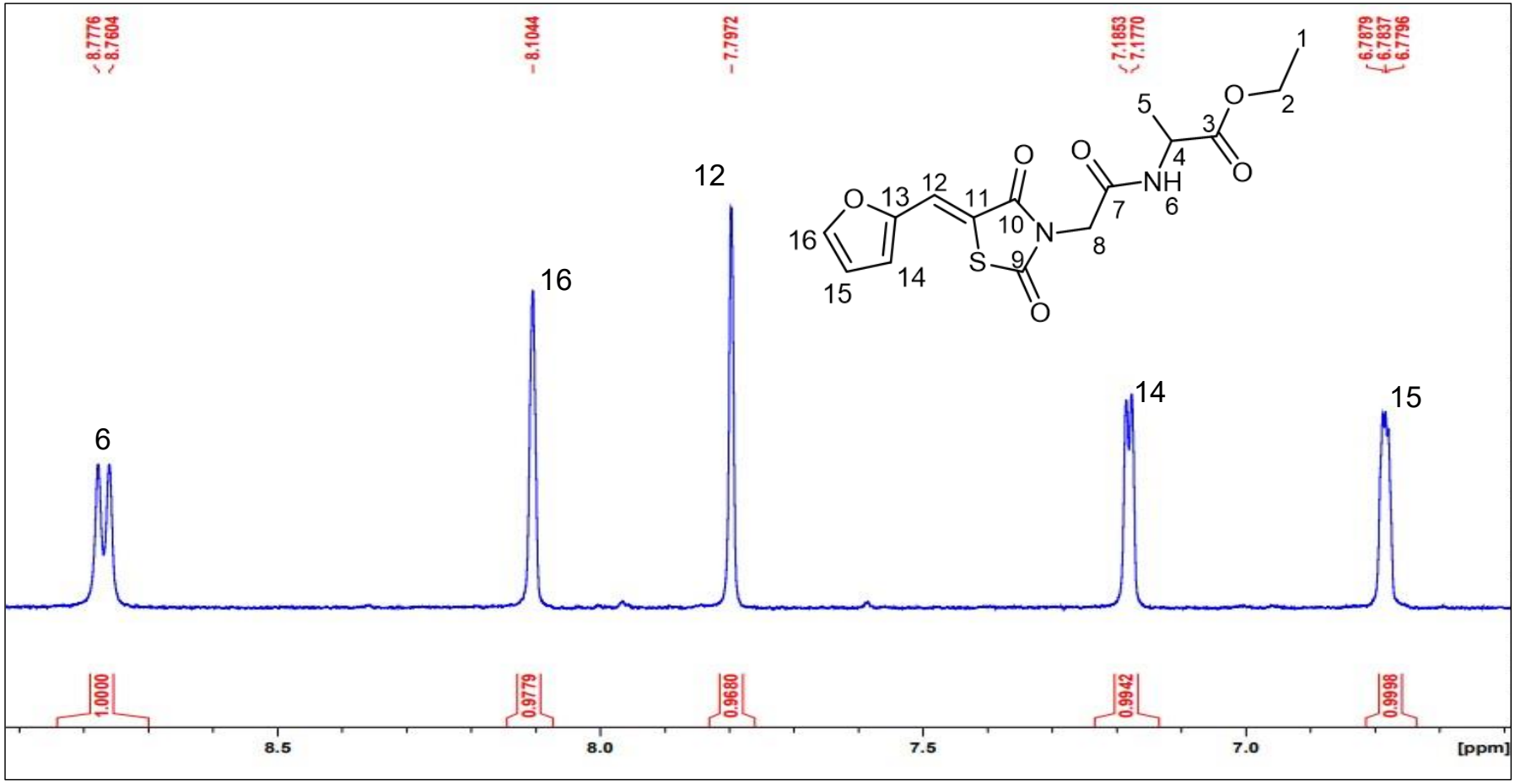

Figure 4.6: A3 ^{1}H NMR spectrum (aromatic region).

Figures 4.7 to 4.9 show the ^{13}C-NMR spectra for the alaninates. The spectra show that all the alaninates have all quaternary carbons (165 ppm to 173 ppm) accounted for: C-3, C-7, C-9, C-10, C-11, C-13, and C-16 (A1 and A2) and all quaternary carbons except for C-16 (A3). Carbons C-8 at 44 ppm and C-11 at 118 ppm (A1 and A3) and 126 ppm (A2), carbons that show the successful attachment of the aliphatic and arylidene chains to the TZD scaffold, are present in all three alaninates.

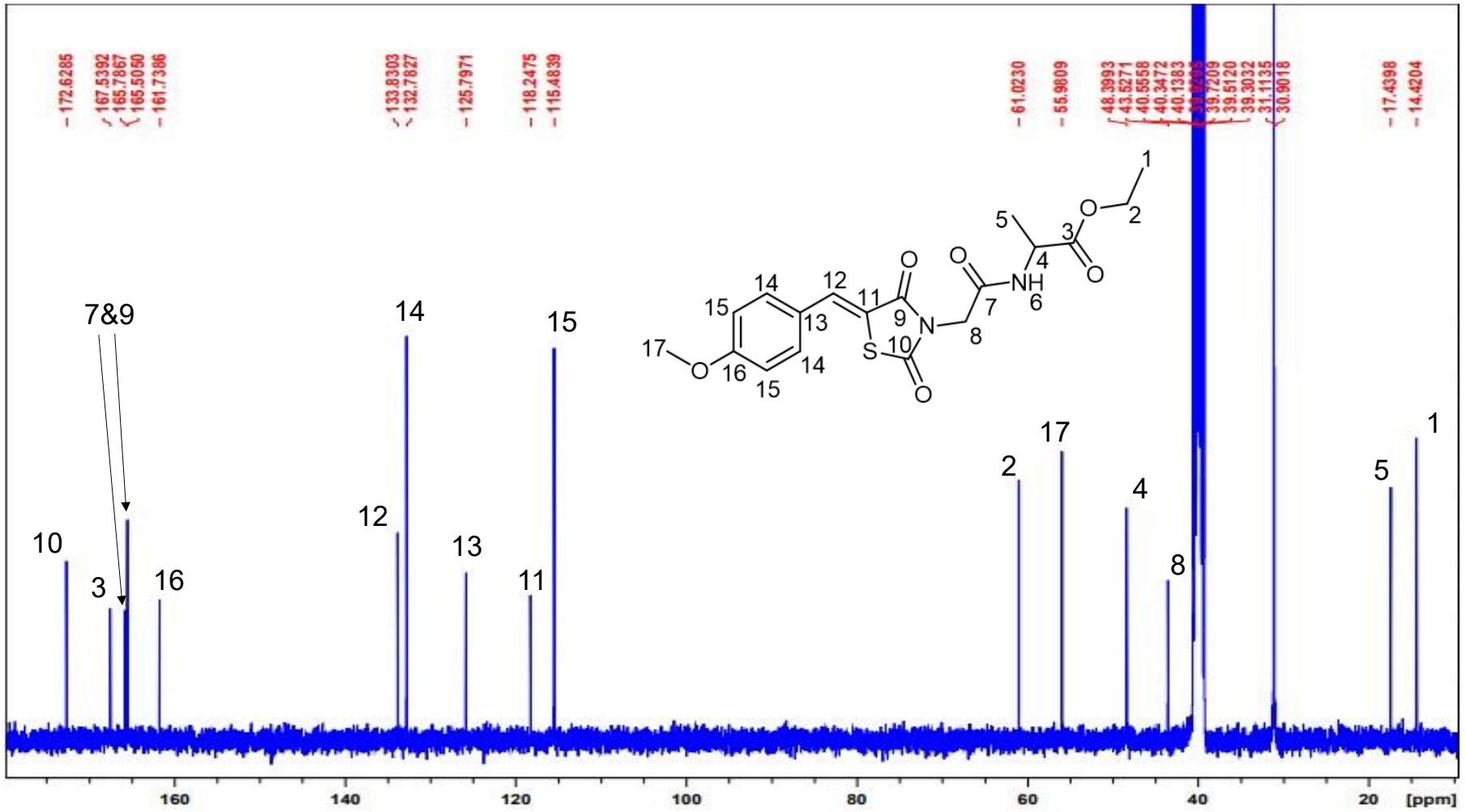

Figure 4.7: A1 ^{13}C NMR spectrum.

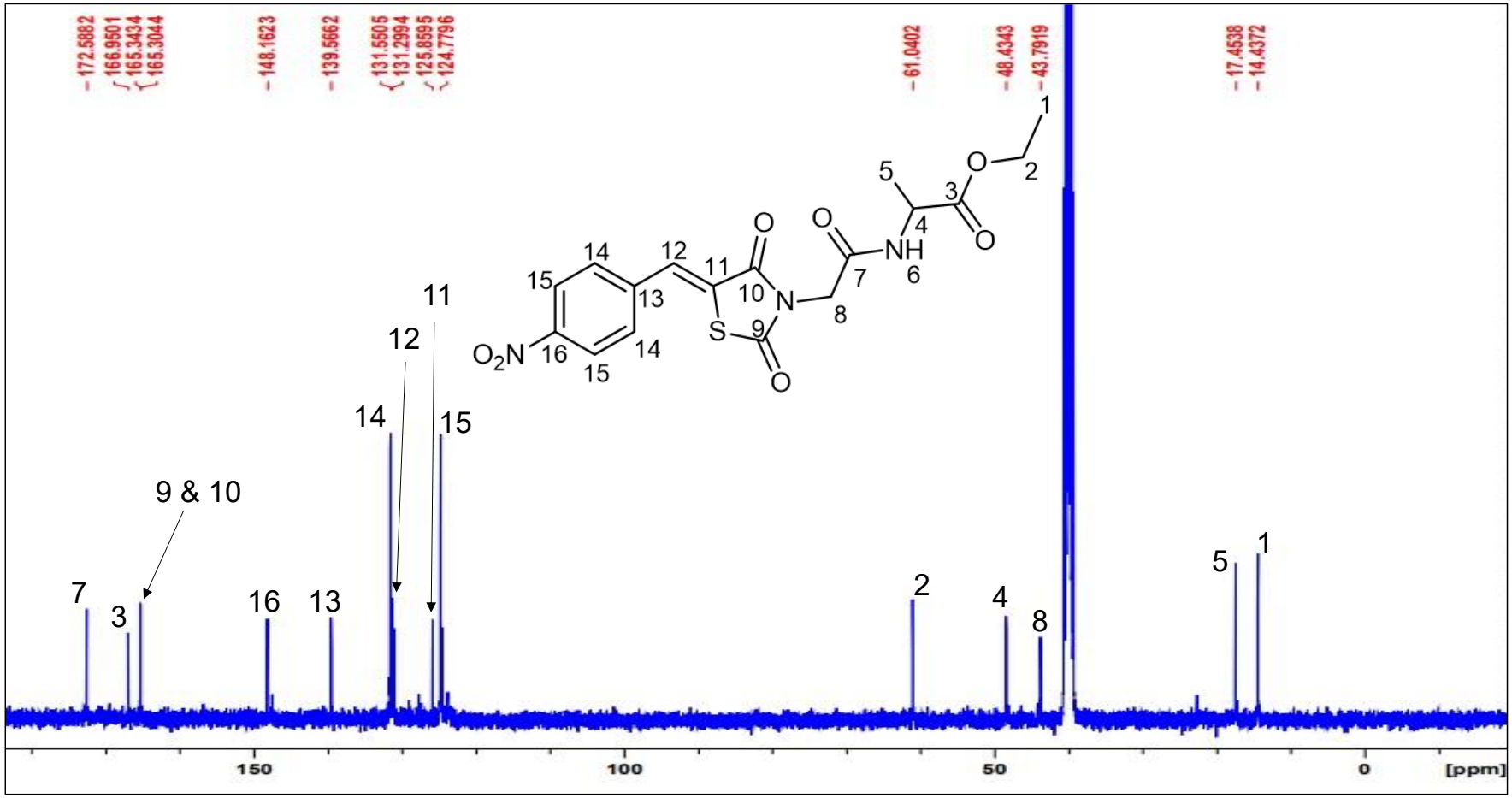

Figure 4.8: A2 ^{13}C NMR spectrum.

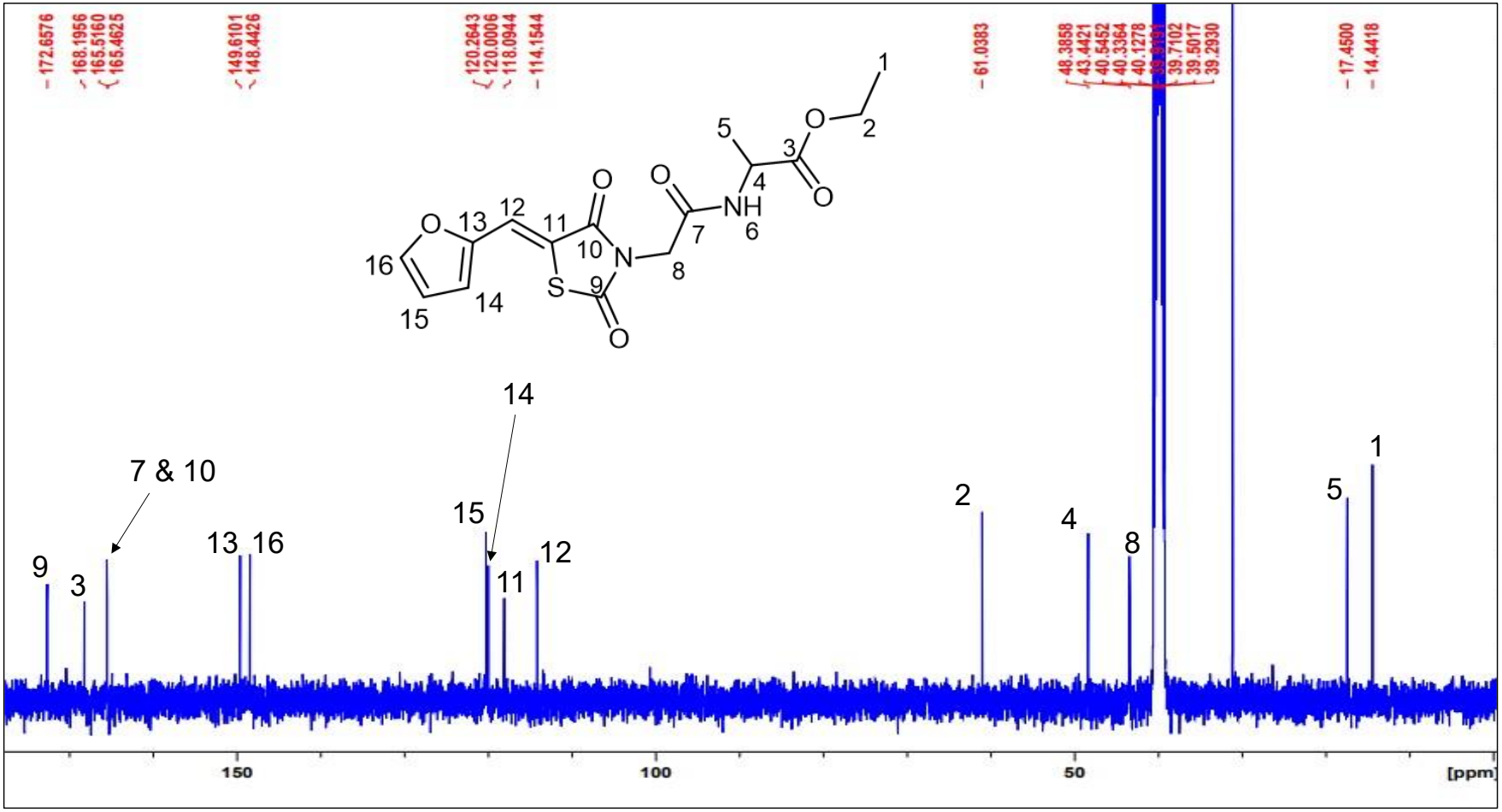

Figure 4.9: A3 ^{13}C NMR spectrum.

Figures 4.10 to 4.13 show the ^{1}H-NMR spectra for the two butanoates. Both compounds have the same aliphatic region: H-1 (triplet) at 1.17 ppm and H-6 (triplet) at 0.88 ppm. In addition, both butanoates show a multiplicity at 1.59 ppm for H-5a H-5b, caused by the chiral carbon at C-4. Whilst both compounds have a similar heteroatomic region (H-2 (quartet), H-4 (multiplet), H-9 (singlet)), only B1 shows a singlet at 3.84 ppm attributed to H-18. Both butanoates show a doublet downfield at 8.70 ppm, ascribed to H-7. As expected, the aromatic region of B1 shows two doublets (H-15 (7.62 ppm), H-16 (7.12 ppm)) and a singlet at 7.93 ppm (H-13). The multiplicities of the aromatic region of B2 are as follows: H-16 dd at 6.75 ppm, H-15 doublet at 7.17 ppm, H-13 singlet at 7.78 ppm and H-17 doublet at 8.07 ppm.

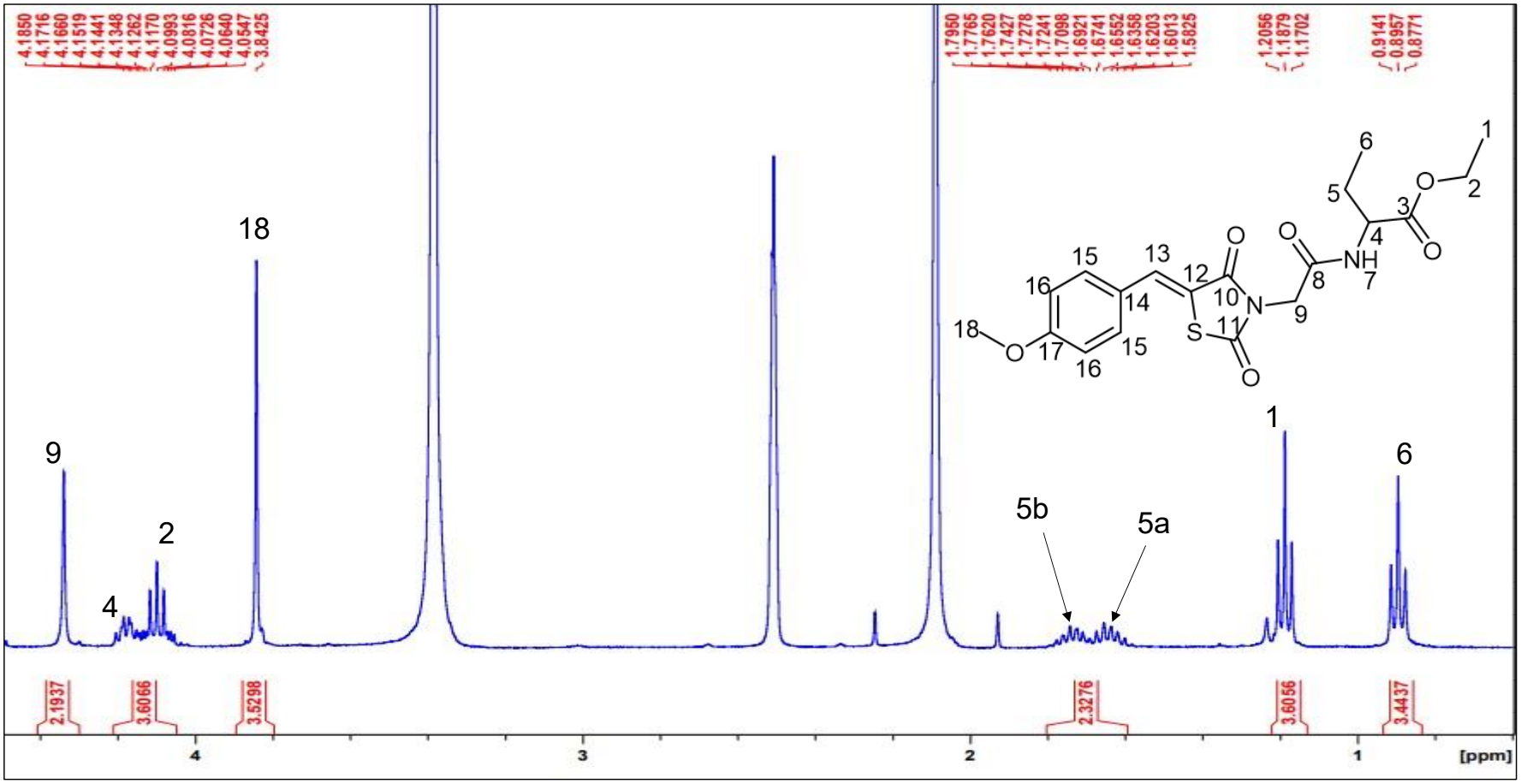

Figure 4.10: B1 ^{1}H NMR spectrum (aliphatic and heteroatomic region).

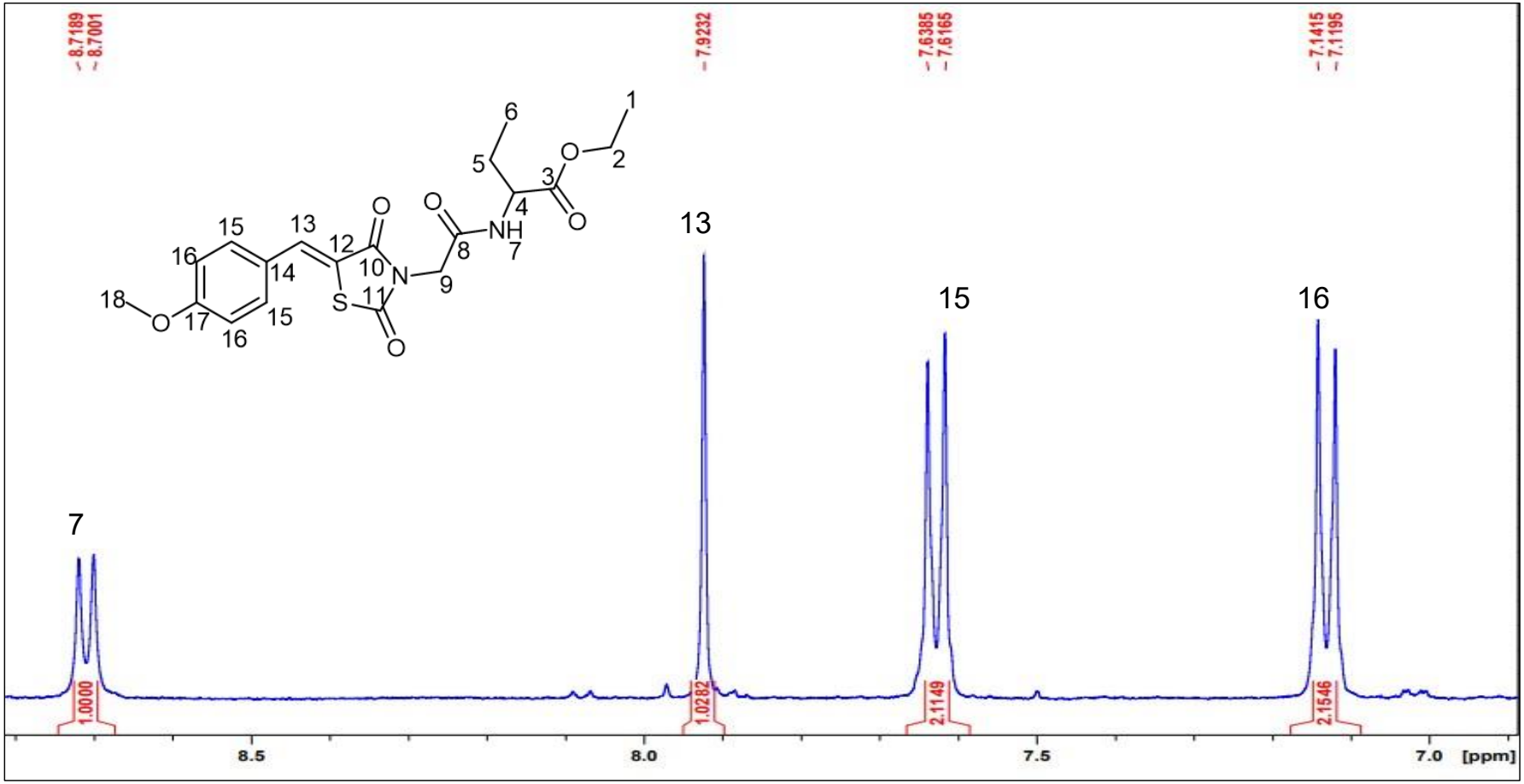

Figure 4.11: B1 ^{1}H NMR spectrum (aromatic region).

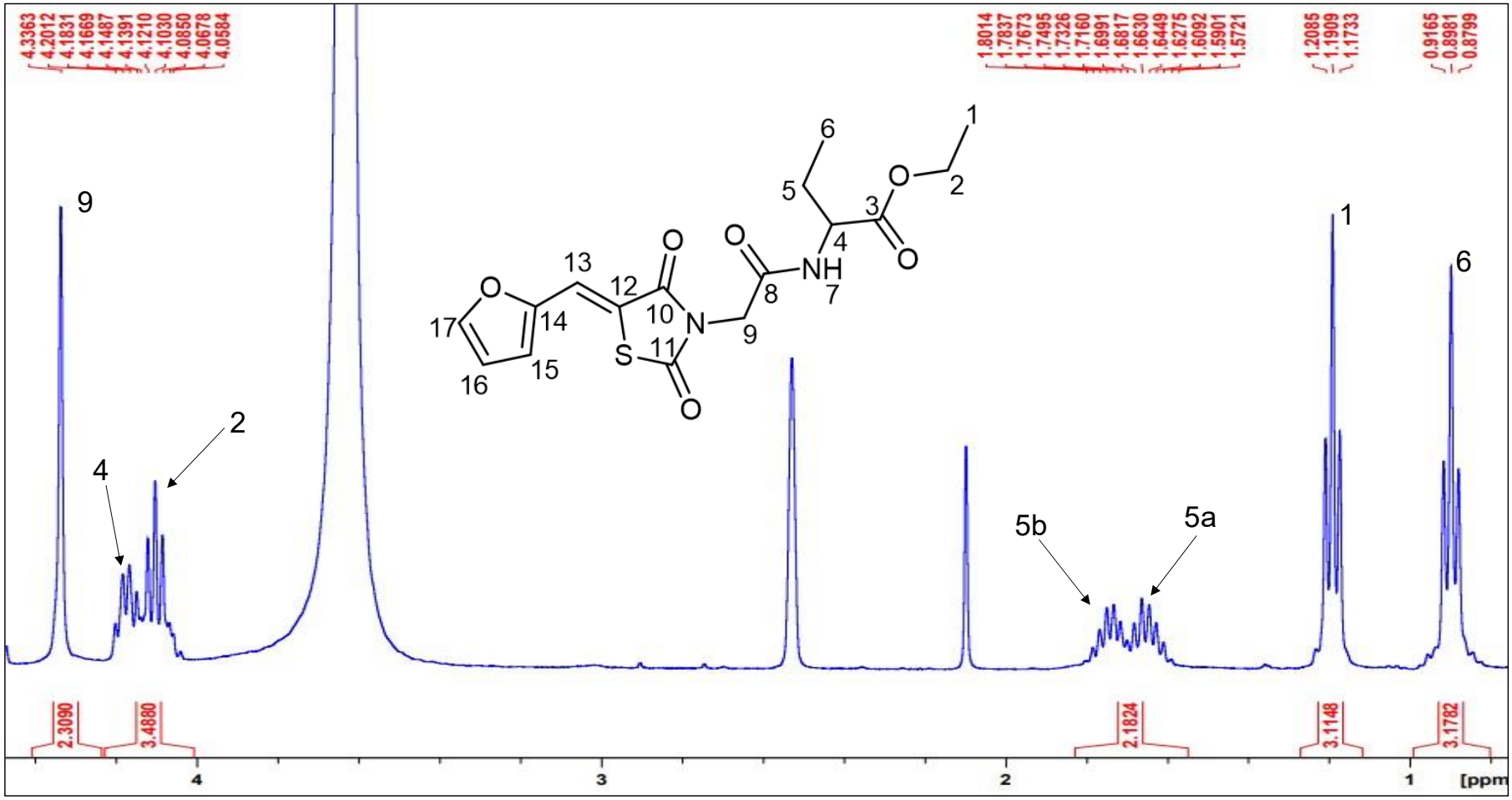

Figure 4.12: B2 ^{1}H NMR spectrum (aliphatic and heteroatomic region).

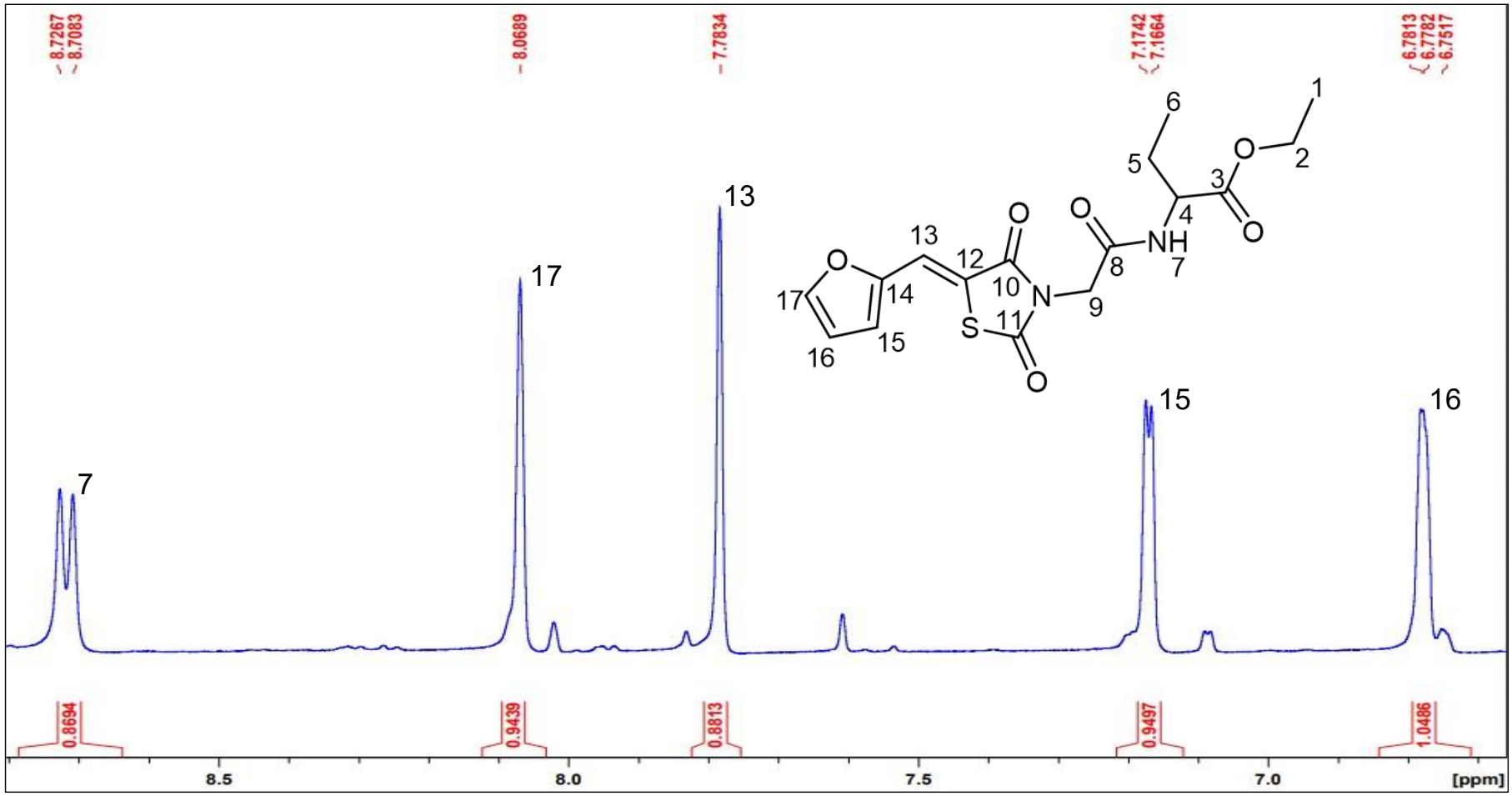

Figure 4.13: B2 ^{1}H NMR spectrum (aromatic region).

Figures 4.14 and 4.15 show the ^{13}C-NMR spectra of B1 and B2. Both spectra show that all the carbons making up the molecules of these compounds are accounted for, including the quaternary carbon C-12 at 118 ppm and the methylene carbon C-9 at 44 ppm, which both indicate successful synthesis of the two butanoates.

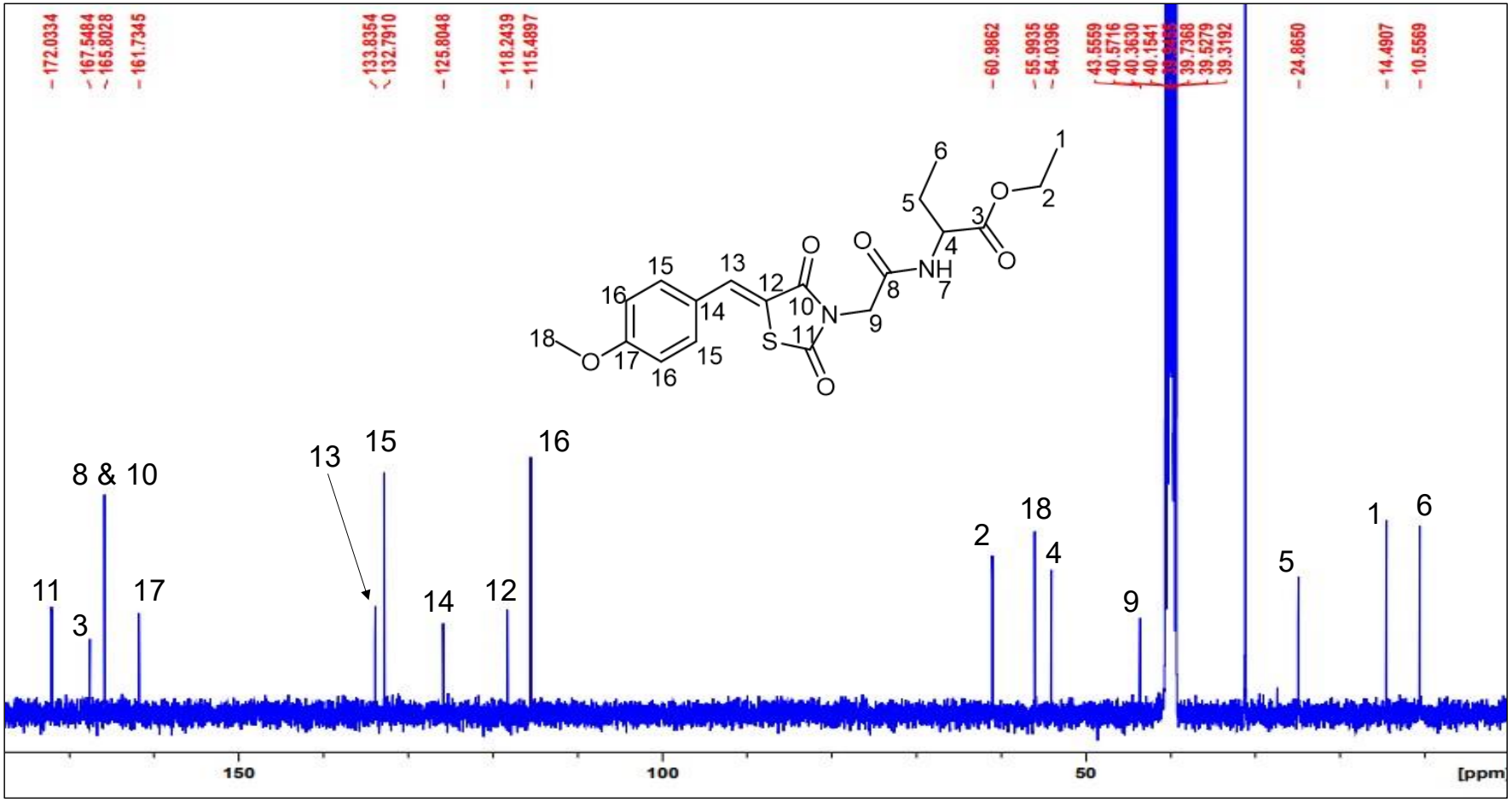

Figure 4.14: B1 ^{13}C NMR spectrum.

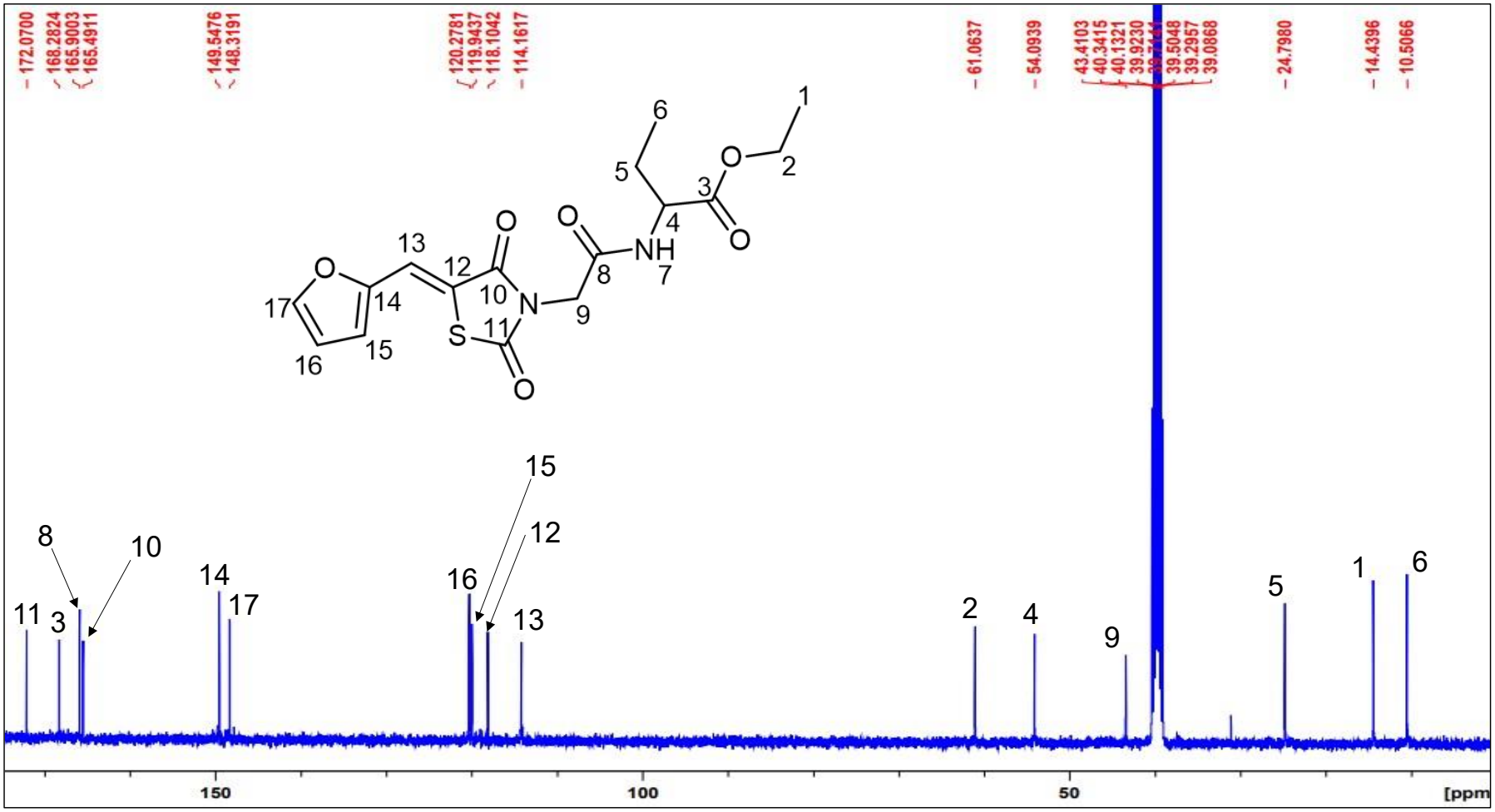

Figure 4.15: B2 ^{13}C NMR spectrum.

Figures 4.16 to 4.21 show the ^{1}H NMR spectra of the glycinates. Once again, the aliphatic regions of all three glycinates are the same: a triplet ascribed to H-1 at 1.11 ppm (G1) and 1.18 ppm (G2 and G3). The heteroatomic region of G1 shows a singlet at 3.77 ppm attributed to the (-OCH_3) protons. All the other peaks in the heteroatomic region are shared by all three glycinates: a doublet (H-4), a dd (H-2) and a singlet (H-7). The aromatic region of G3 is as follows: a singlet at 7.79 ppm (H-11), a doublet at 7.17 ppm (H-13), a dd at 6.77 ppm (H-14) and a doublet at 8.09 ppm (H-15). All glycinates have a downfield triplet attributed to H-5. Both G1 and G2 have the expected two doublets (H-13 and H-14) along with a singlet at H-11 in their aromatic regions.

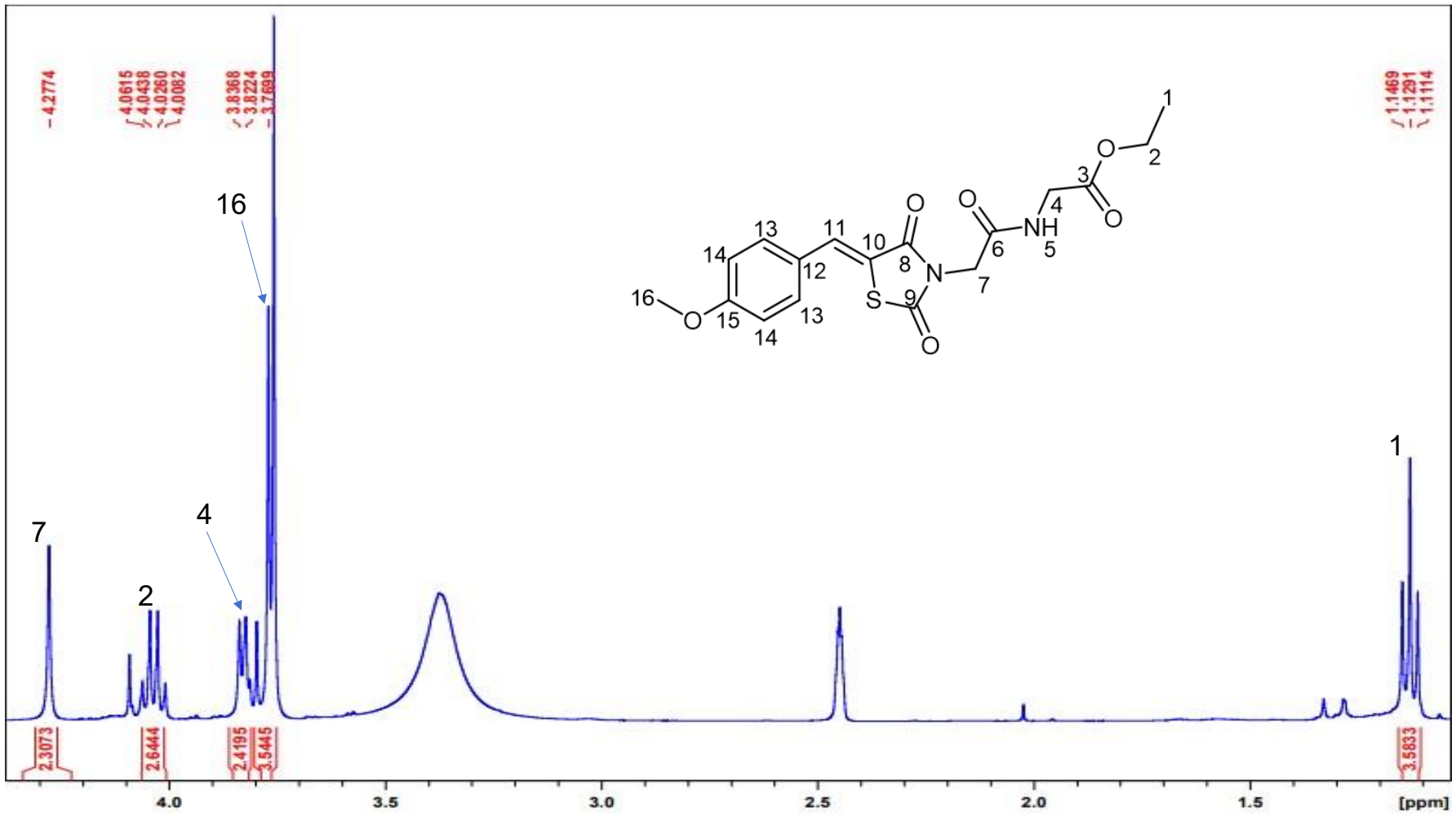

Figure 4.16: G1 ^{1}H NMR spectrum (aliphatic and heteroatomic region).

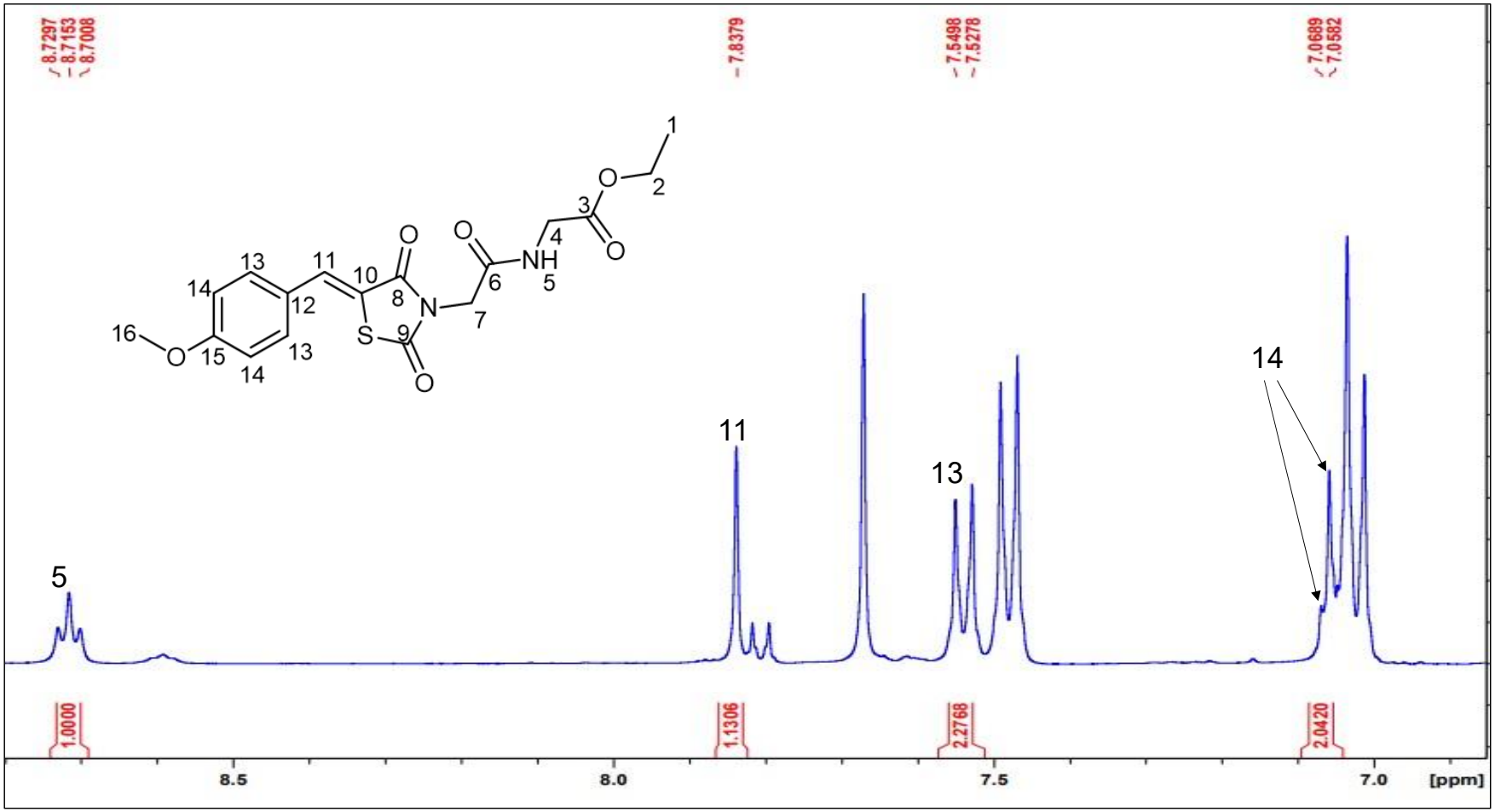

Figure 4.17: G1 ^{1}H NMR spectrum (aromatic region).

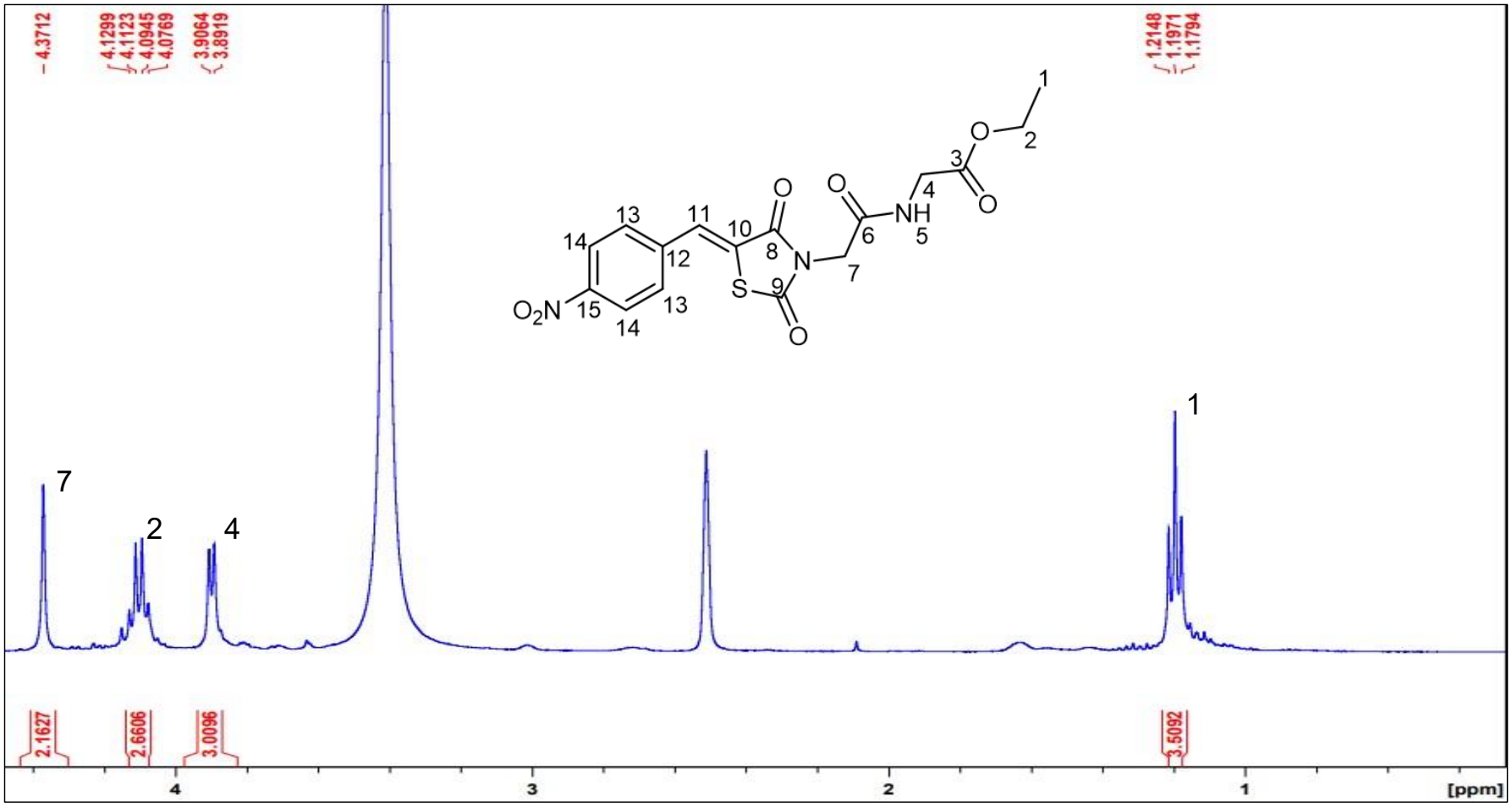

Figure 4.18: G2 ^{1}H NMR spectrum (aliphatic and heteroatomic region).

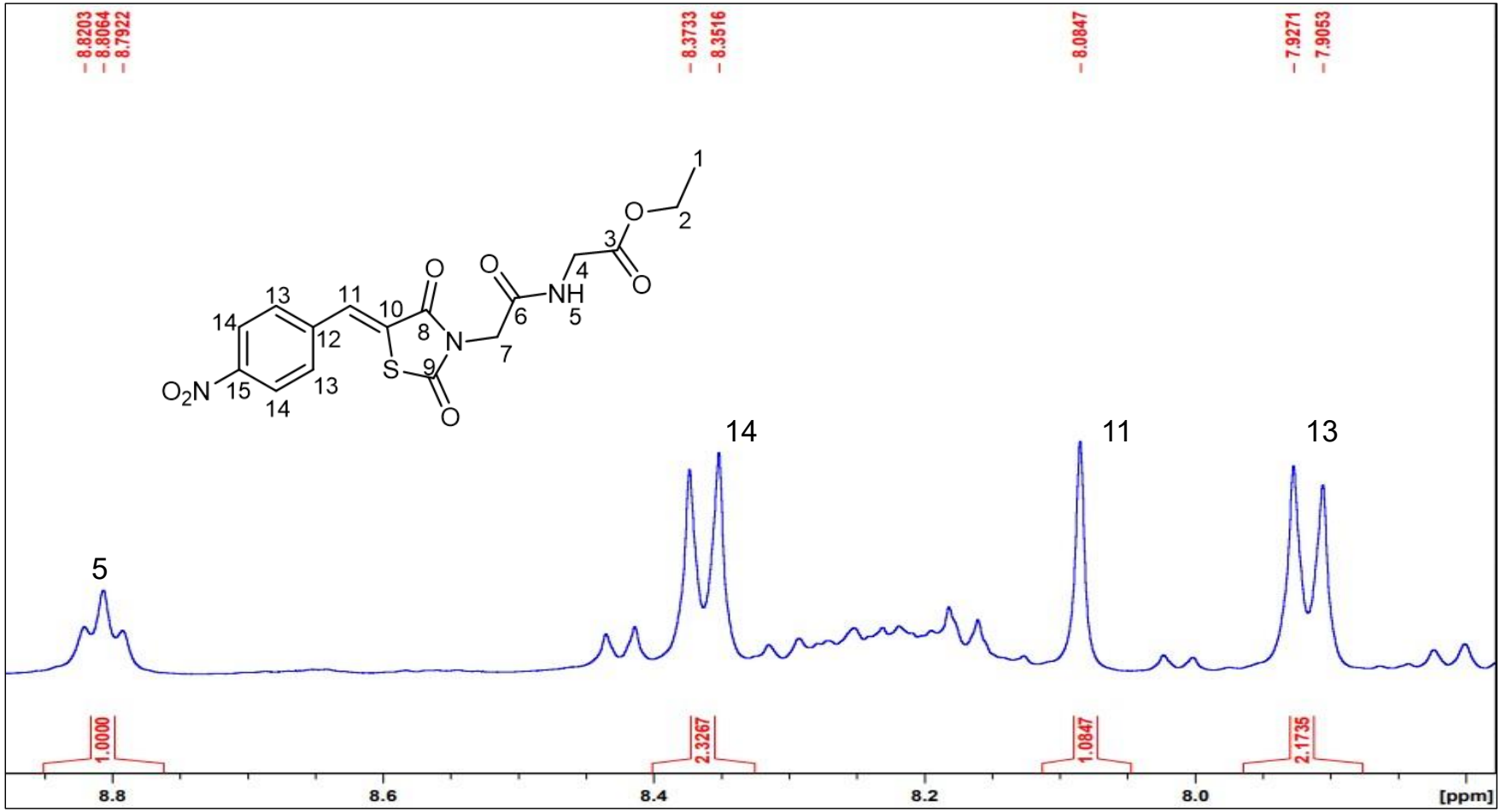

Figure 4.19: G2 ^{1}H NMR spectrum (aromatic region).

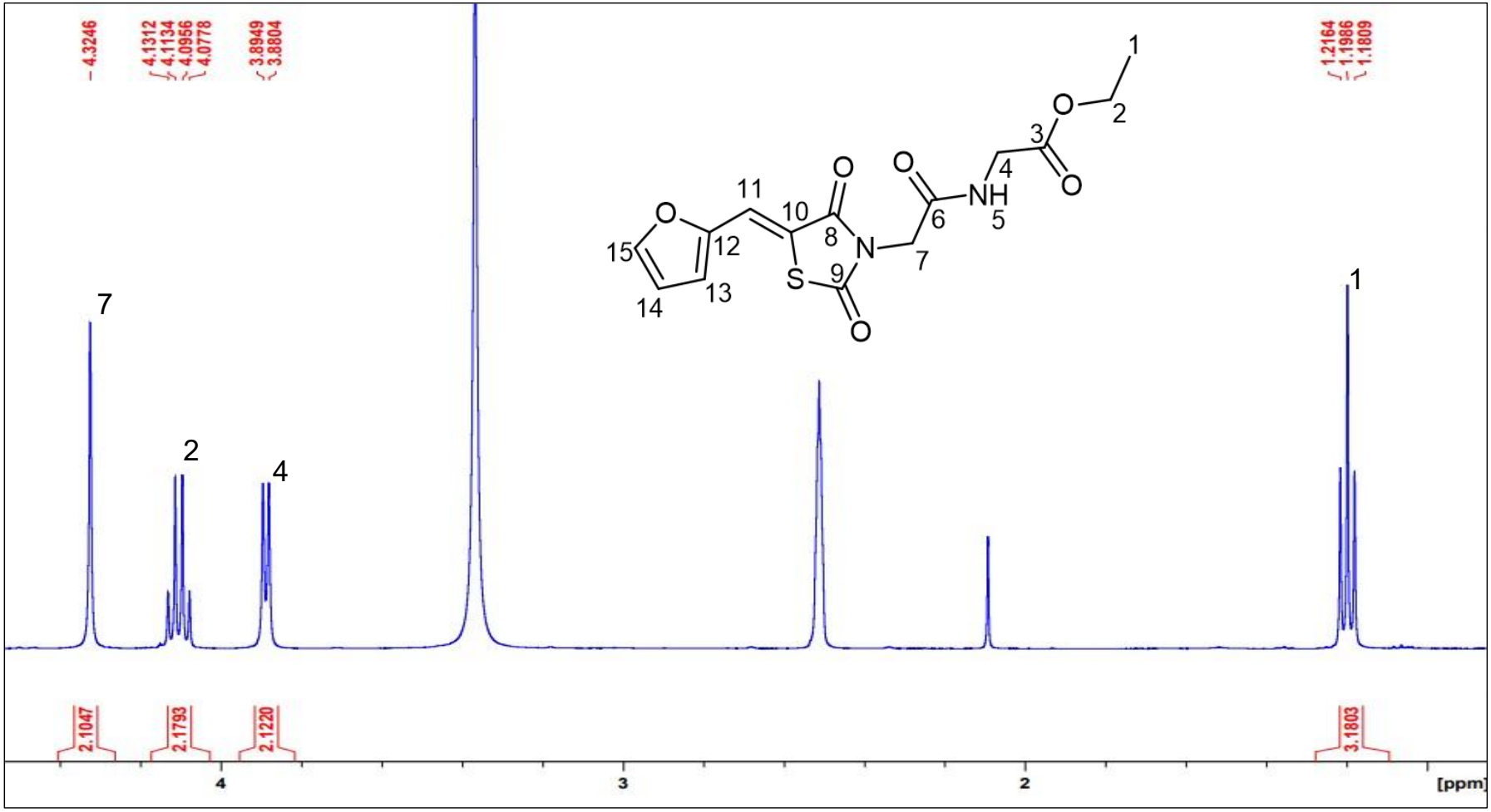

Figure 4.20: G3 ^{1}H NMR spectrum (aliphatic and heteroatomic region).

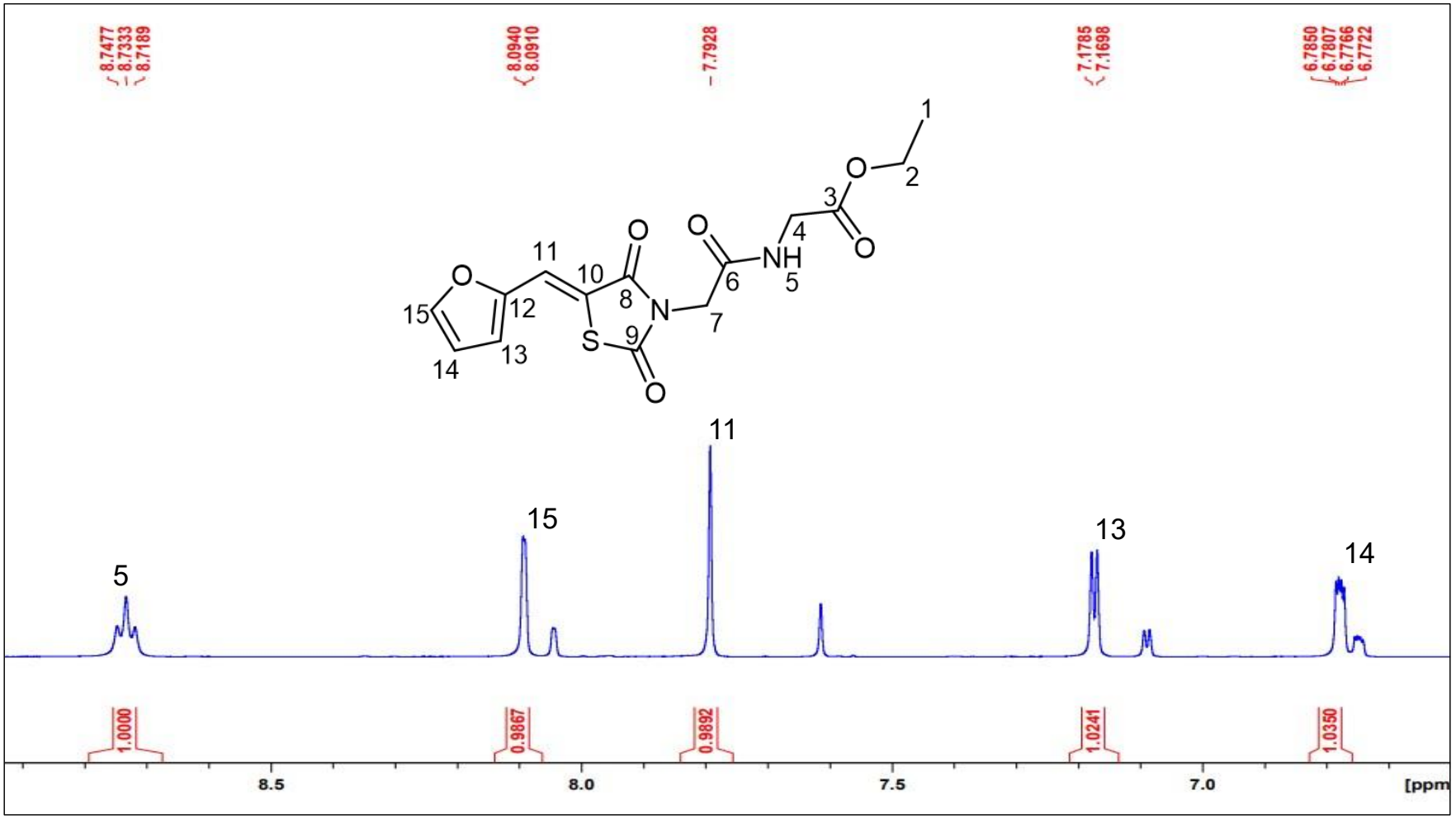

Figure 4.21: G3 ^{1}H NMR spectrum (aromatic region).

Figures 4.22 to 4.24 show the ^{13}C-NMR spectra of the glycinates. All spectra show that all the carbons are accounted for, crucially the quaternary carbons C-9 at 118 ppm (G1), C-10 at 126 ppm and 118 ppm (G2 and G3, respectively) and the methylene carbons C-6 at 44 ppm (G1) and C-7 at 41 ppm (G2 and G3), which indicate successful synthesis of the three glycinates.

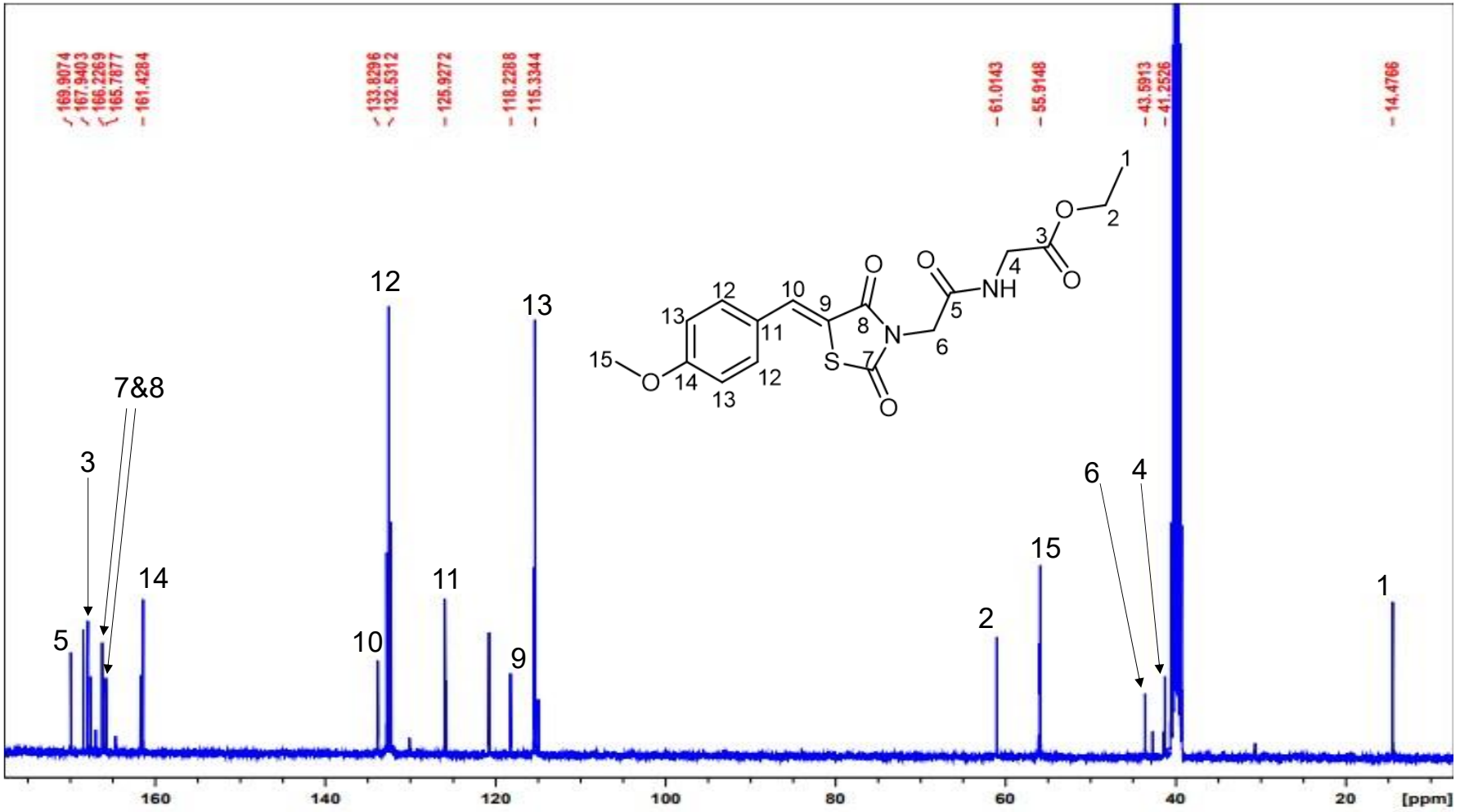

Figure 4.22: G1 ^{13}C NMR spectrum.

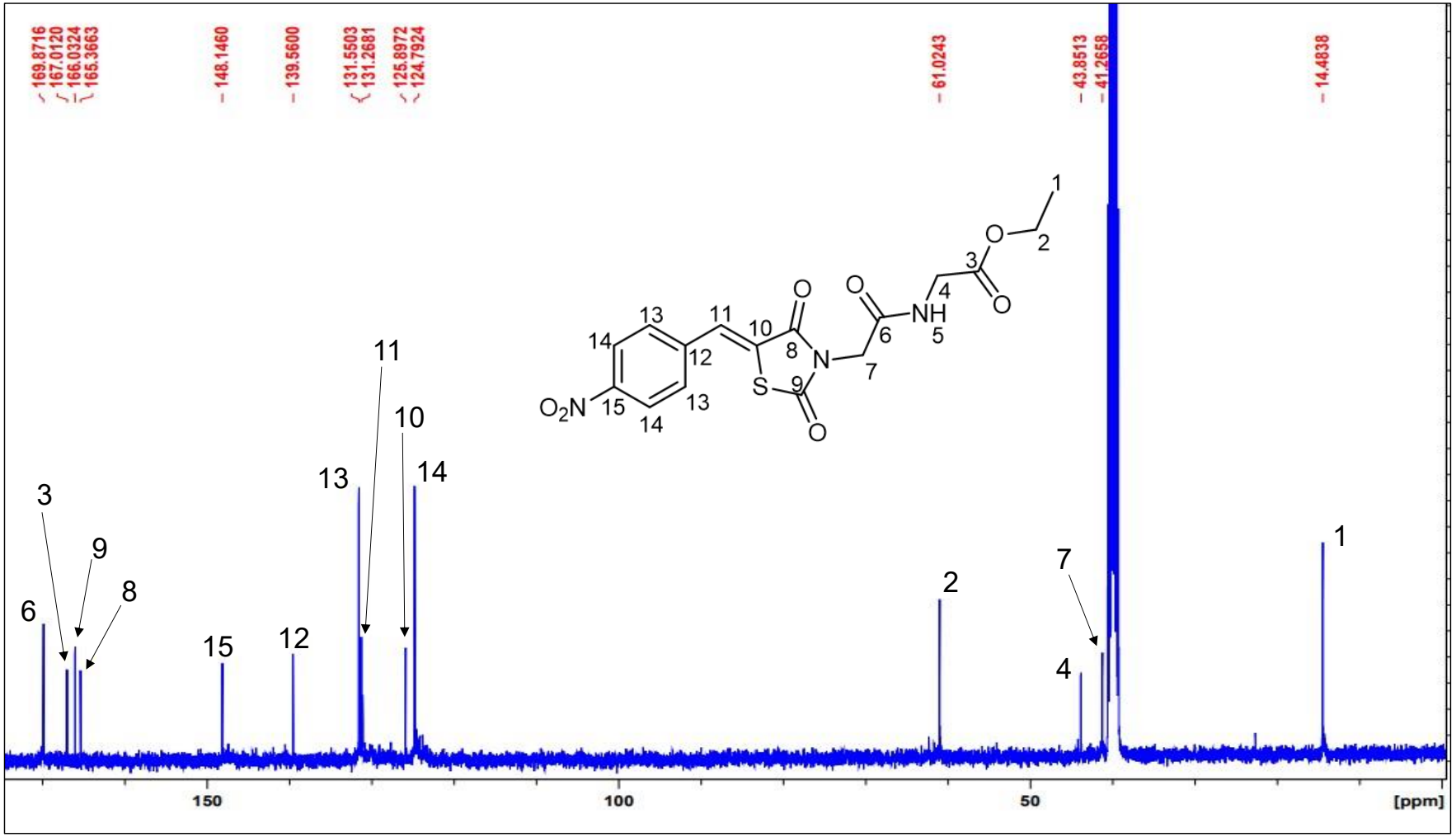

Figure 4.23: G2 ^{13}C NMR spectrum.

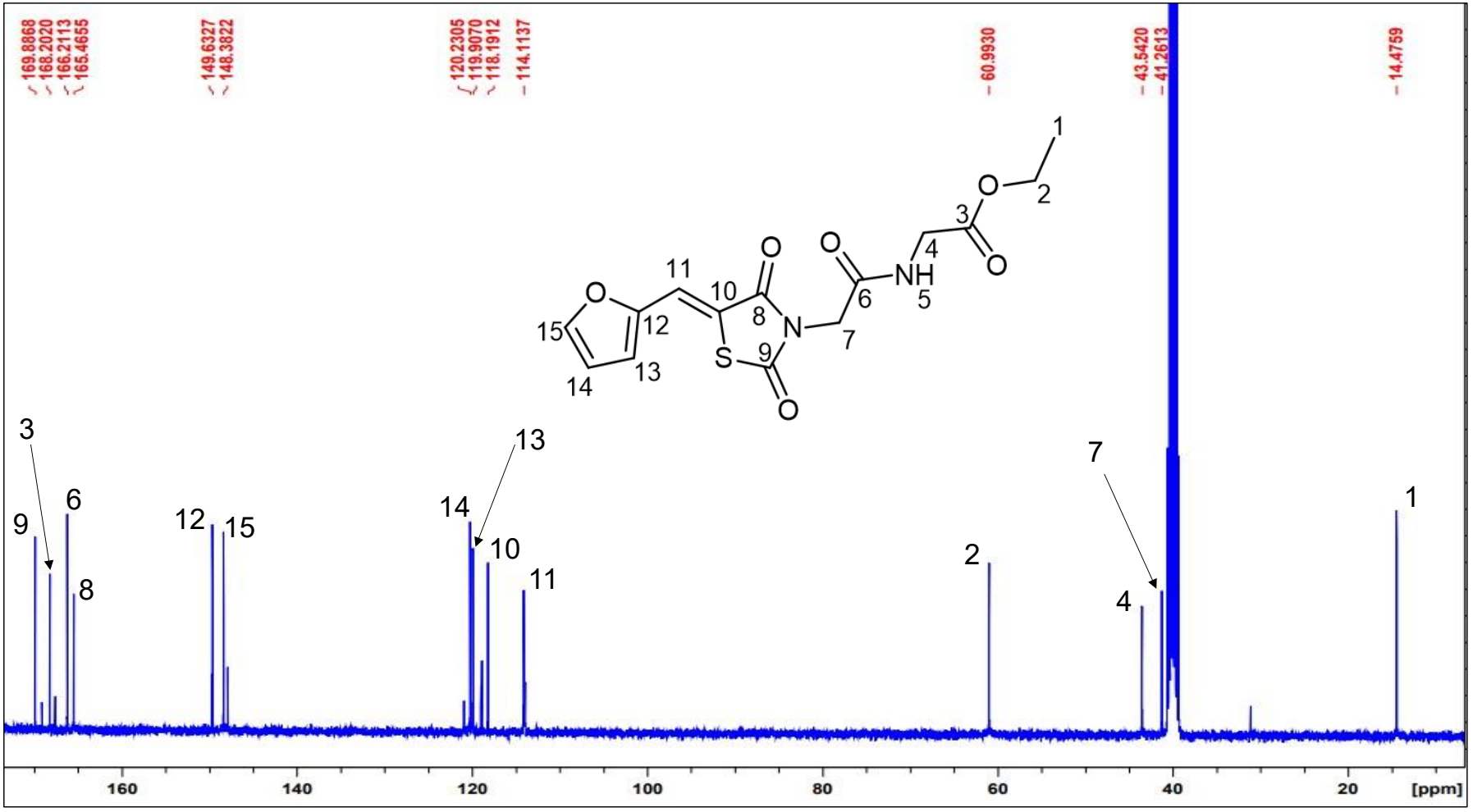

Figure 4.24: G3 ^{13}C NMR spectrum.

4.2 Mild steel

4.2.1 Weight loss analysis

All WL experiments were carried out at four different temperatures: 303.15 K, 313.15 K, 323.15 K and 333.15 K. Figures 4.25 to 4.32 all display the same two trends: under isothermal conditions, an increase in C_{inh} results in a decrease in C_R whilst only increasing the temperature leads to an increase in C_R. The former is due to an increase in θ, protecting the MS surface from highly corrosive Cl^- ions whilst the latter is due to a decrease in θ brought about by desorption of inhibitor molecules from the metal surface [152-154].

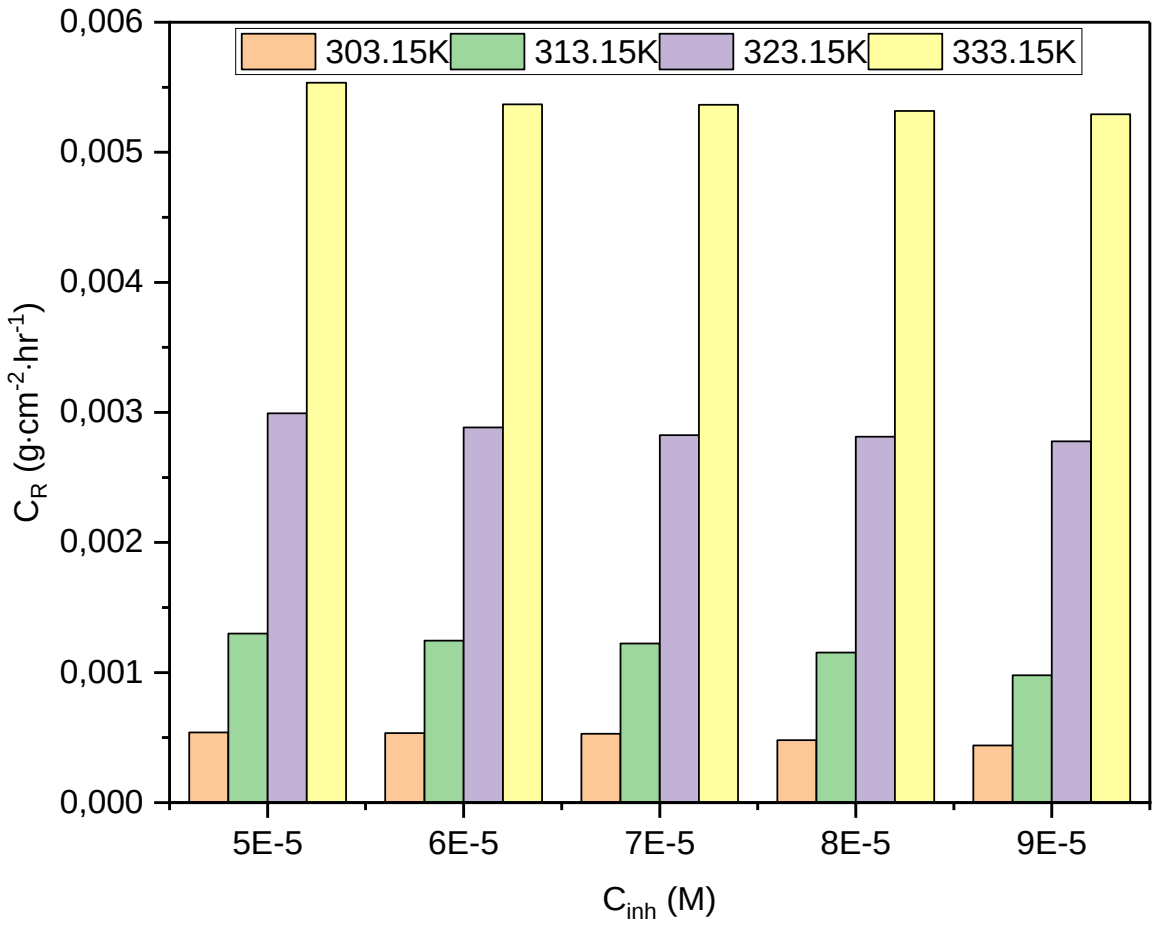

Figure 4.25: Relationship between C_{inh} and C_R for A1 (MS).

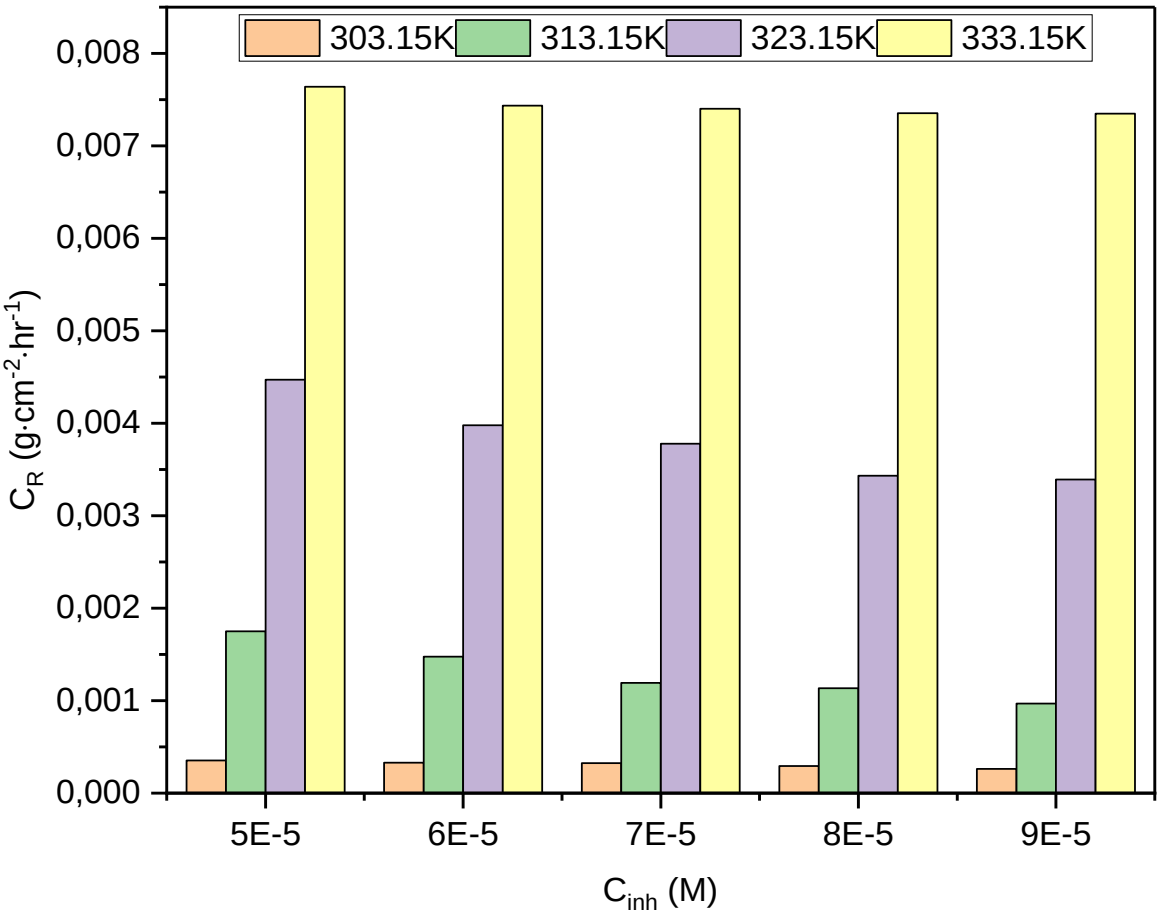

Figure 4.26: Relationship between C_{inh} and C_R for A2 (MS).

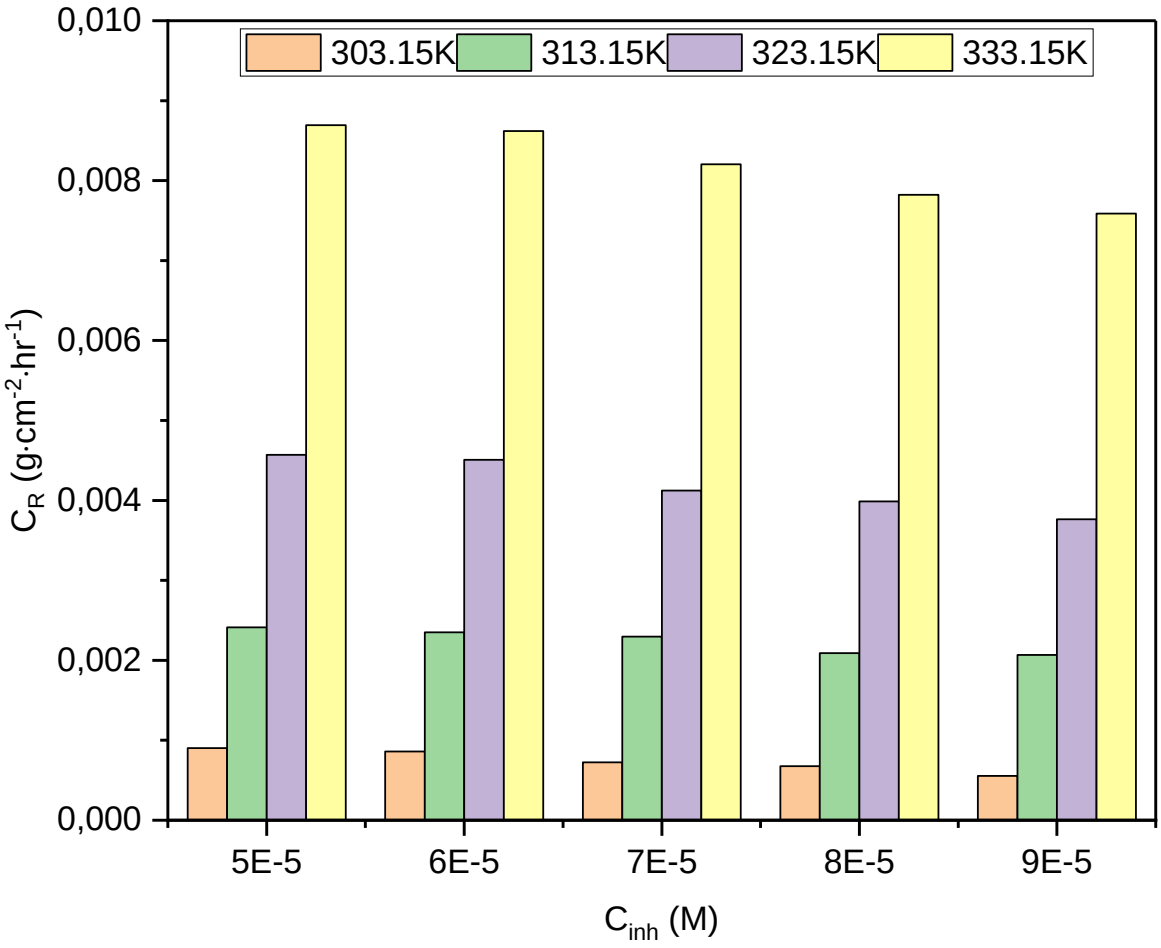

Figure 4.27: Relationship between C_{inh} and C_R for A3 (MS).

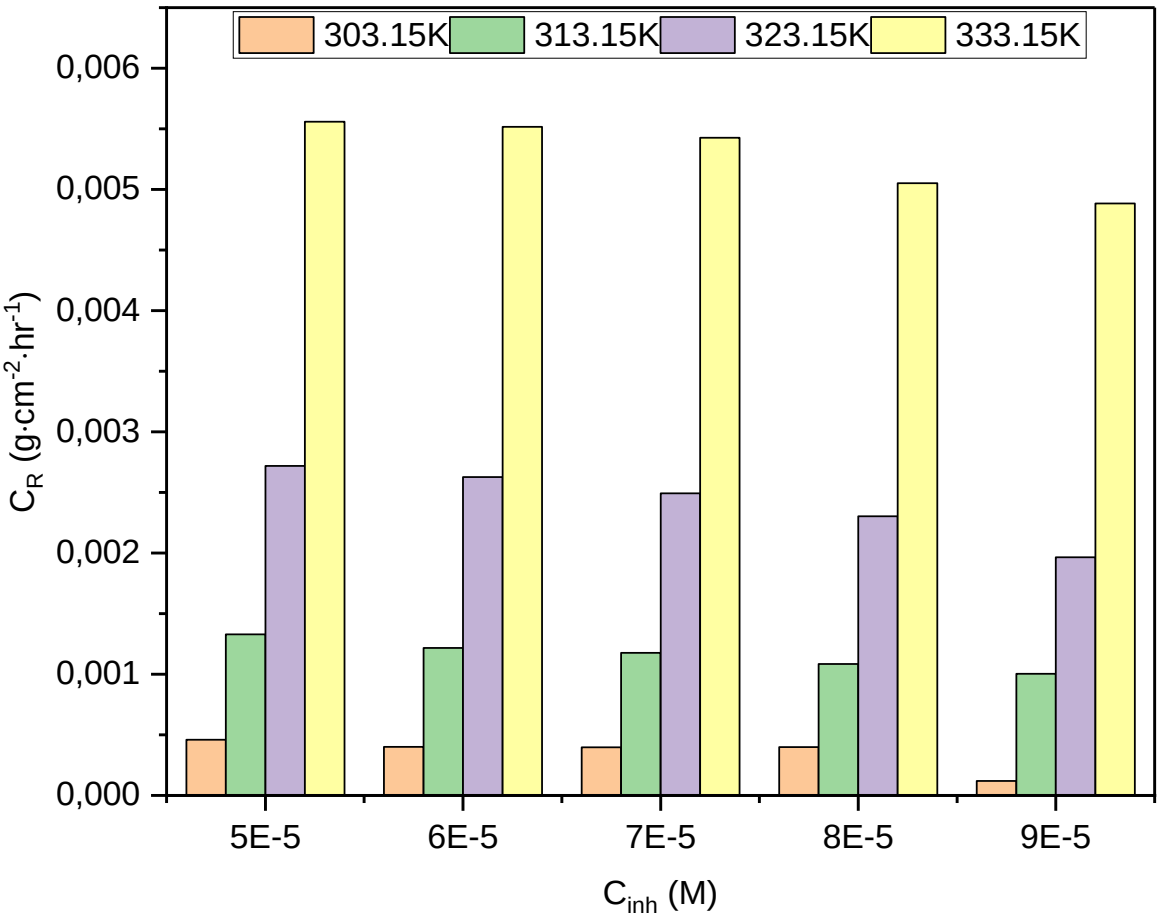

Figure 4.28: Relationship between C_{inh} and C_R for B1 (MS).

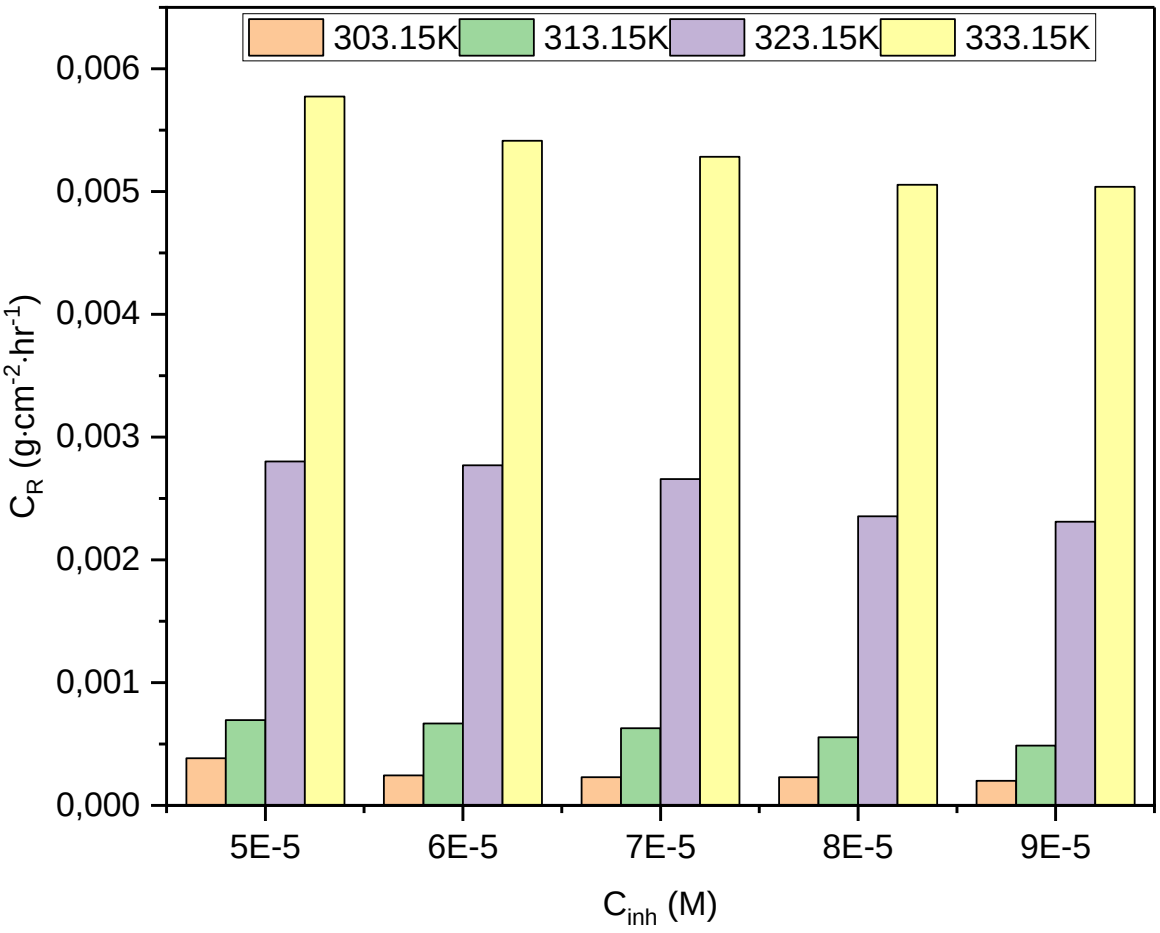

Figure 4.29: Relationship between C_{inh} and C_R for B2 (MS).

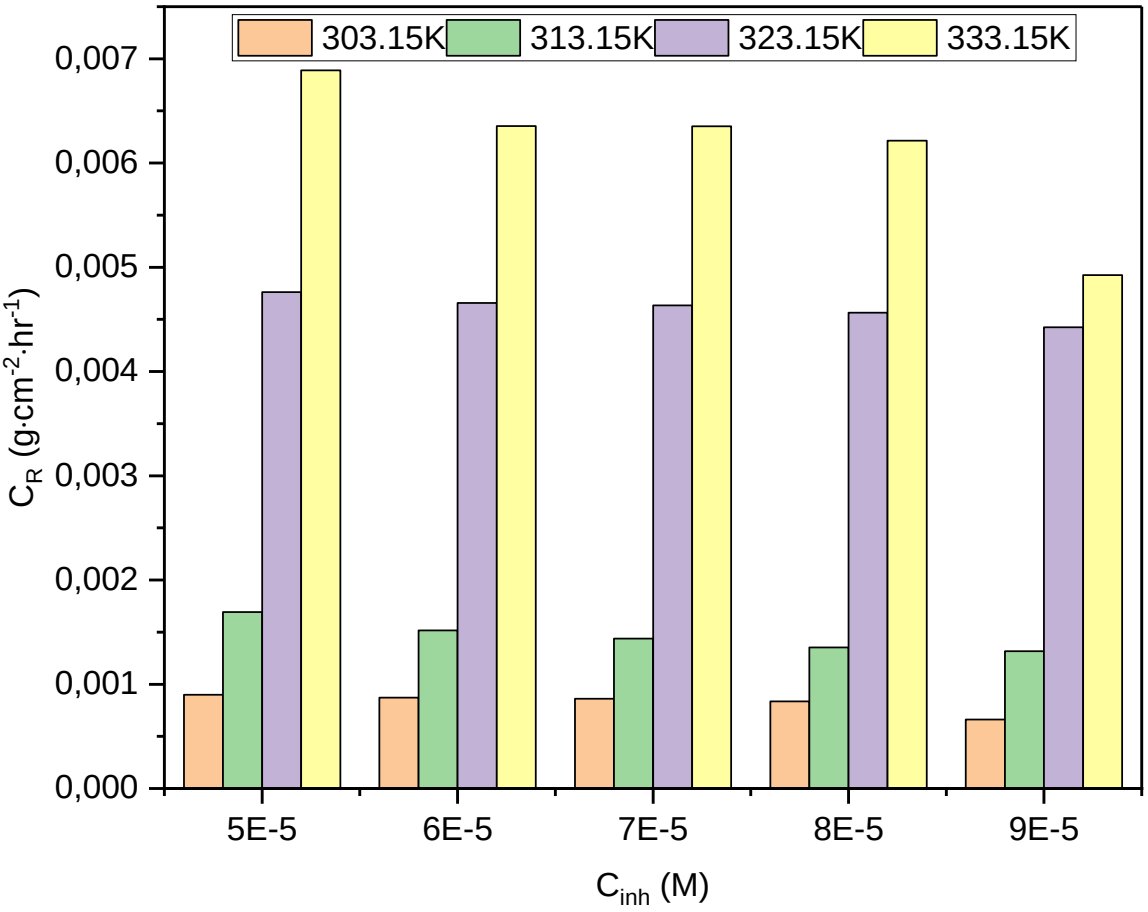

Figure 4.30: Relationship between C_{inh} and C_R for G1 (MS).

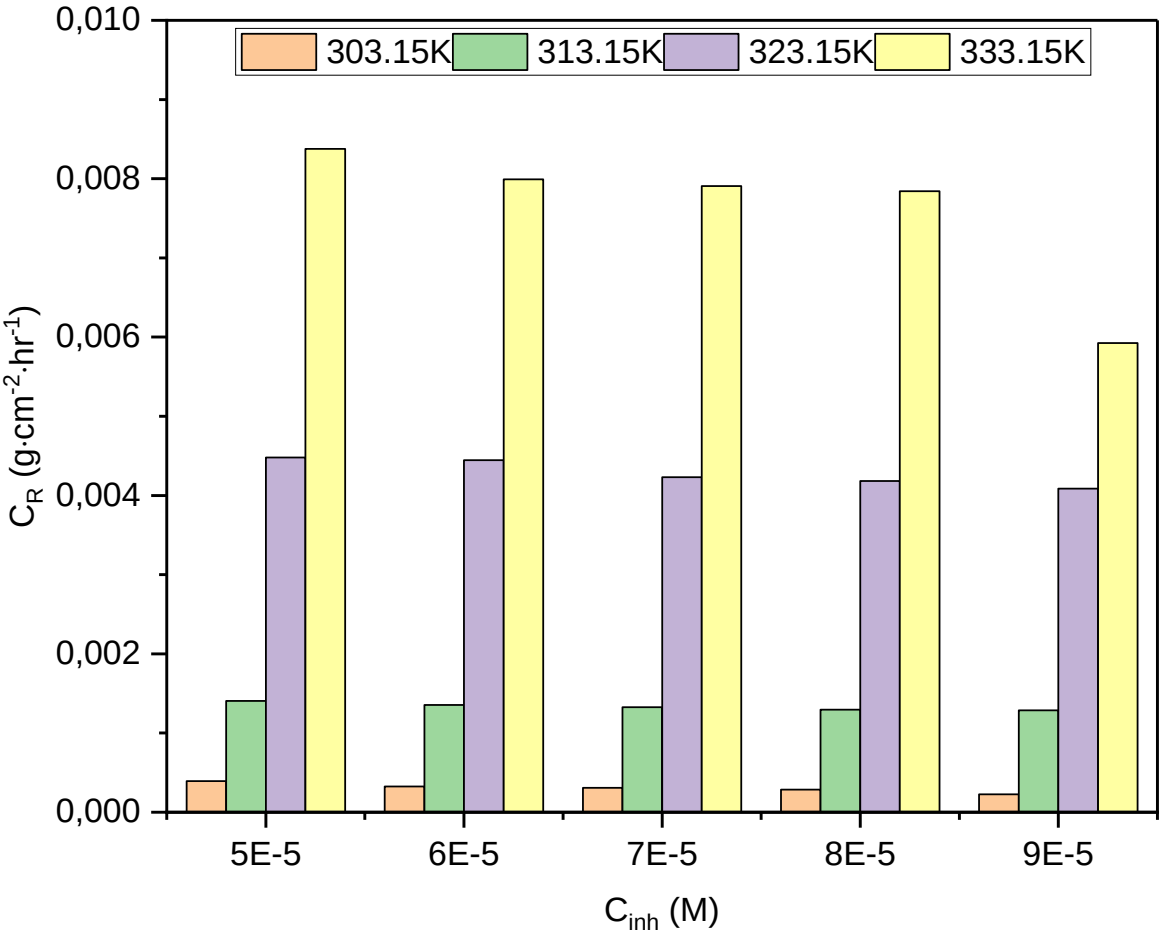

Figure 4.31: Relationship between C_{inh} and C_R for G2 (MS).

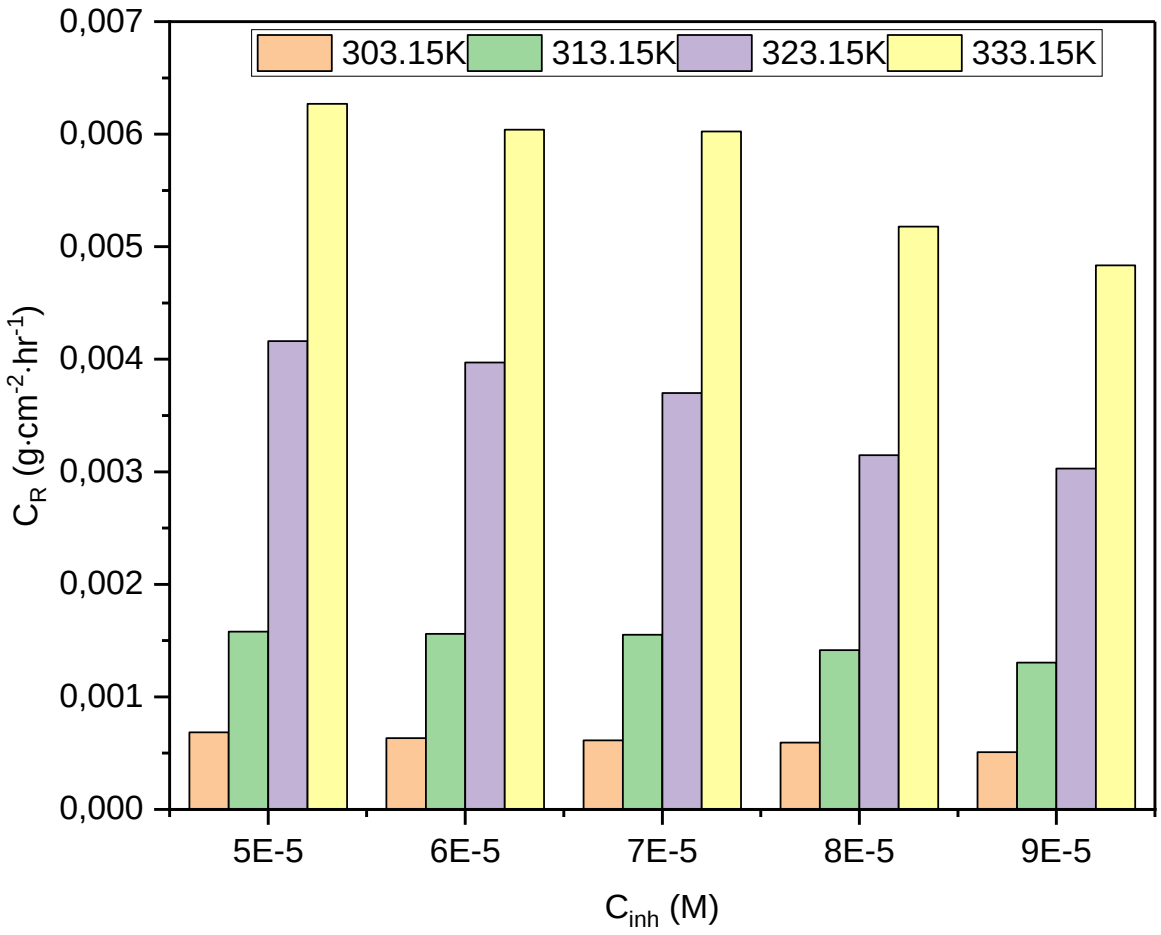

Figure 4.32: Relationship between C_{inh} and C_R for G3 (MS).

Table 4.2 shows the $\%IE_{WL}$ data for the TZDs. As the temperature of the 1 M HCl solution is increased, $\%IE_{WL}$ drops. This is because of a decrease in θ [155]. Some inhibitor molecules desorb from the metal surface due to a weakening of their interactions with the MS surface, resulting in a decrease in both θ and $\%IE_{WL}$ [155]. Table 4.2 also shows that, under isothermal conditions, an increase in C_{inh} results in an increase in $\%IE_{WL}$. This trend is due to an increase in θ [156]. The highest $\%IE_{WL}$ values are all achieved at the lowest temperature, 303.15 K, where temperature related stress on the adsorption film is at a minimum. The three classes of TZD are arranged as follows in order of decreasing maximum $\%IE_{WL}$ achieved: Butanoates>Alaninates>Glycinates. G2 is the only exception as it achieves a maximum $\%IE_{WL}$ of 86.52, higher than the maximum $\%IE_{WL}$ of all three alaninates.

Table 4.2: Effect of temperature and C_{inh} on $\%IE_{WL}$ of TZDs on MS in 1 M HCl.

TZD	Concentration (M)	($\%IE_{WL}$) 303.15 K	($\%IE_{WL}$) 313.15 K	($\%IE_{WL}$) 323.15 K	($\%IE_{WL}$) 333.15 K
A1	5.00E−05	67.81	59.65	54.56	52.18
	6.00E−05	68.15	61.36	56.22	53.63
	7.00E−05	68.41	62.04	57.13	53.64
	8.00E−05	71.39	64.18	57.29	54.06
	9.00E−05	73.77	69.60	57.84	54.28
A2	5.00E−05	78.98	45.72	32.14	34.02
	6.00E−05	80.36	54.17	39.62	35.77
	7.00E−05	80.68	62.96	42.65	36.06
	8.00E−05	82.48	64.79	47.89	36.48
	9.00E−05	84.39	69.93	48.54	36.52
A3	5.00E−05	46.18	25.10	30.65	24.89
	6.00E−05	48.73	27.03	31.57	25.54
	7.00E−05	56.90	28.69	37.43	29.14
	8.00E−05	59.77	35.10	39.49	32.42
	9.00E−05	66.99	35.82	42.89	34.45
B1	5.00E−05	71.52	59.46	59.21	52.94
	6.00E−05	75.24	62.88	60.58	53.29
	7.00E−05	75.41	64.08	62.59	54.06
	8.00E−05	75.30	66.89	65.45	57.23

	9.00E−05	92.57	69.35	70.52	58.64
B2	5.00E−05	75.09	77.88	56.32	52.24
	6.00E−05	84.20	78.72	56.79	55.21
	7.00E−05	85.12	79.97	58.54	56.29
	8.00E−05	85.10	82.29	63.29	58.18
	9.00E−05	87.05	84.46	63.98	58.32
G1	5.00E−05	46.39	47.43	27.73	40.49
	6.00E−05	48.09	52.96	29.30	45.11
	7.00E−05	48.73	55.39	29.68	45.12
	8.00E−05	50.21	57.99	30.73	46.31
	9.00E−05	60.51	59.09	32.86	57.46
G2	5.00E−05	76.54	56.38	32.00	27.65
	6.00E−05	80.57	57.93	32.54	30.97
	7.00E−05	81.63	58.87	35.81	31.69
	8.00E−05	82.91	59.81	36.51	32.26
	9.00E−05	86.52	60.09	38.00	48.82
G3	5.00E−05	59.13	50.97	36.84	45.85
	6.00E−05	62.21	51.58	39.73	47.83
	7.00E−05	63.38	51.85	43.84	47.95
	8.00E−05	64.54	56.05	52.24	55.26
	9.00E−05	69.64	59.54	54.03	58.23

At 303.15 K, A2 achieves the highest $\%IE_{WL}$ compared to A1 and A3. This is most likely due to the presence of two additional O heteroatoms in its molecular structure, allowing A2 to form additional dative covalent bonds with the MS surface (Figure 4.33). The green arrows represent dative covalent bonds whereas the blue arrows represent van der Waals forces.

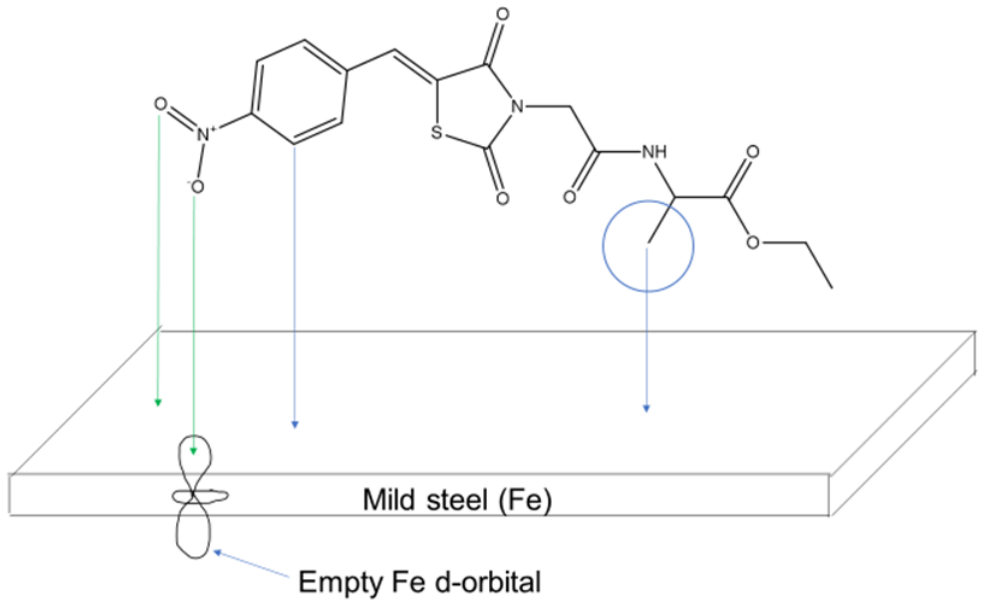

Figure 4.33: Adsorption of A2 onto MS aided by two additional oxygen heteroatoms.

The smaller size of the furan ring in A3 relative to the benzene ring in A1 makes A3 a smaller molecule than A1. The larger benzene ring enables A1 to form a much more extensive adsorption film on the MS surface, hence the higher $\%IE_{WL}$ data displayed by A1. The $\%IE_{WL}$ of the alaninates follows the general trend A2>A1>A3. Larger molecules do not always display high $\%IE_{WL}$ data, however. Zhang *et al.* [157] carried out corrosion studies on two corrosion inhibitors abbreviated IM and CYS. Even though IM had many heteroatoms in its molecular structure, it was very bulky/larger than CYS and this showed in its relatively poor inhibition performance. At a concentration of 10 ppm, CYS had a much lower C_R (0.3991 mm/a) than IM at a concentration of 50 ppm (0.5264 mm/a).

For the most part, B2 achieves much higher $\%IE_{WL}$ data than B1 at all four temperatures. This is most likely because the furan ring shares its electrons much

more readily with the MS surface than the much more energetically stable benzene ring in B1 [158]. The benzene ring in B1 likely adsorbs physically onto the metal surface (physisorption) whereas the furan ring could potentially form dative covalent bonds with the MS surface (Figure 4.34). The $\%IE_{WL}$ of the butanoates follows the general trend B2>B1.

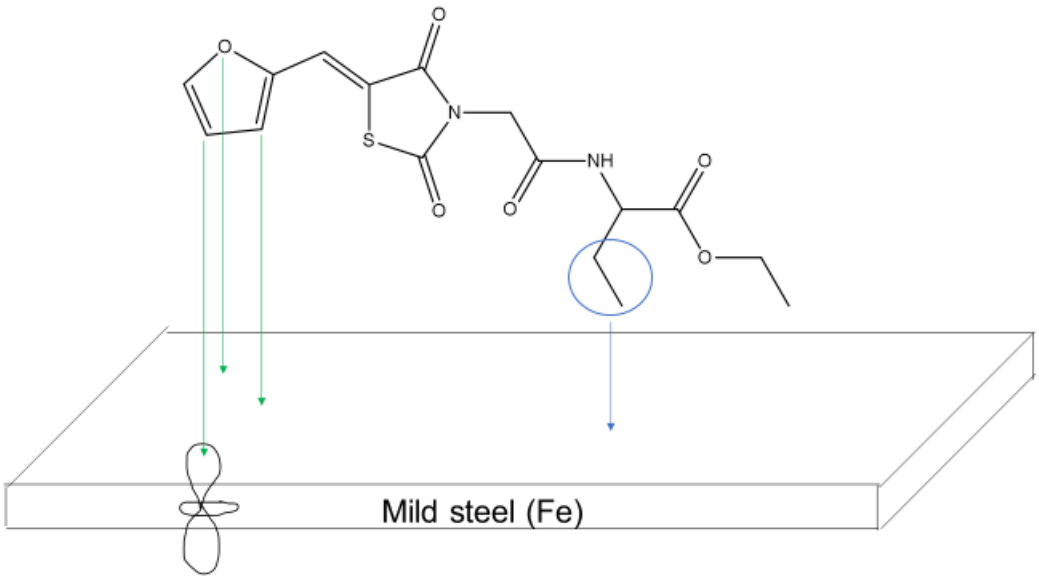

Figure 4.34: Adsorption of B2 onto MS.

At 303.15 K and 313.15 K, G2 has higher $\%IE_{WL}$ data relative to G1 and G3. In addition, G2 has higher $\%IE_{WL}$ data than G1 at 323.15 K. As with A2, the additional O heteroatoms enable G2 to form additional dative covalent bonds with the MS surface (Figure 4.35) hence the higher $\%IE_{WL}$ at the identified temperatures.

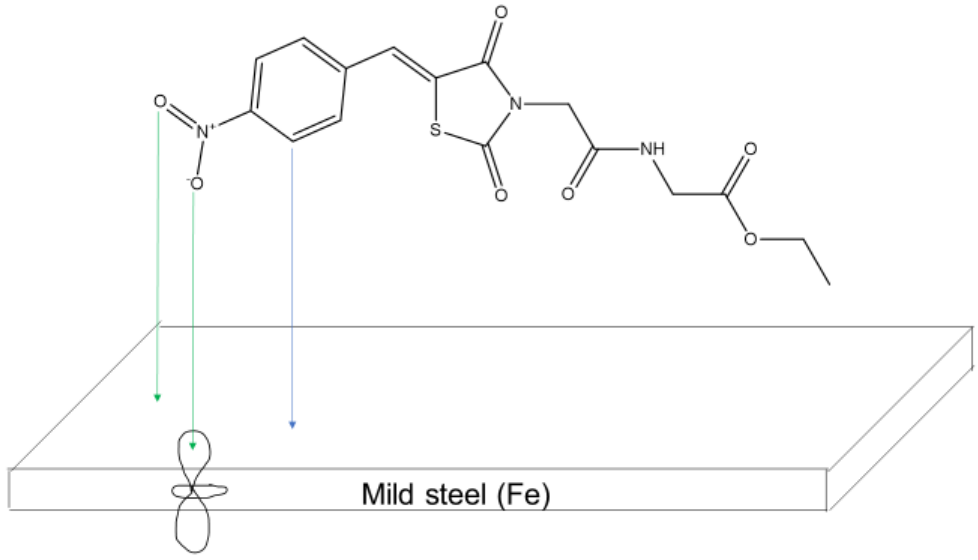

Figure 4.35: Adsorption of G2 onto MS.

However, at 323.15 K and 333.15 K, G3 has a distinct advantage over both G2 and G1. This may be due to the furan ring's ability to potentially form more dative covalent bonds with the metal surface than the (-NO_2) and (-OCH_3) groups in G2 and G1, respectively (Figure 4.36). The O heteroatom, along with the two double bonds in the furan ring, potentially enable G3 to form three additional dative covalent bonds with the MS surface. This third additional bond could give the adsorption film formed by G3 a little more stability at higher temperatures.

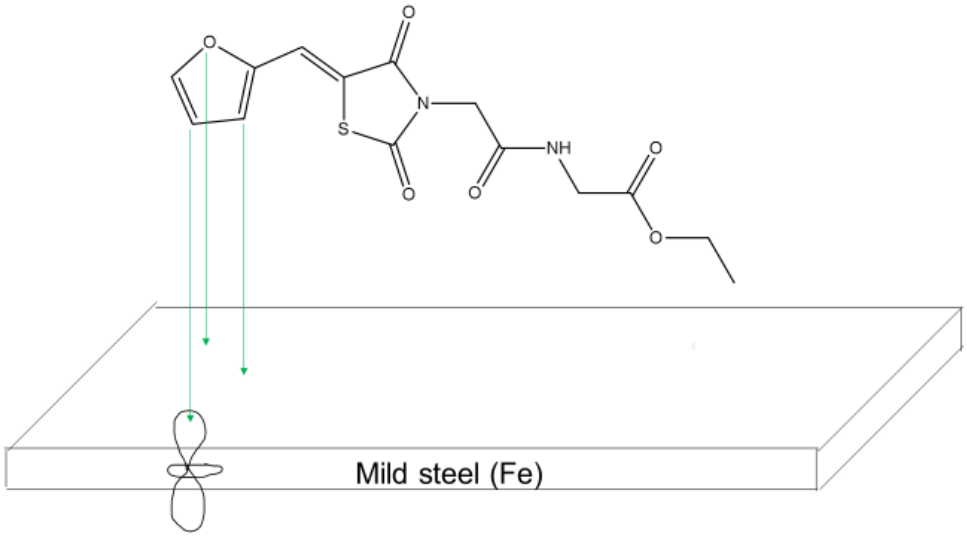

Figure 4.36: Adsorption of G3 onto MS.

4.2.1.1 Adsorption parameters

The LAI is a straight-line plot (Figures 4.37 to 4.44) of C_{inh}/θ vs C_{inh}, with $1/K_{ads}$ as the y-intercept (Equation 21) [159]:

$$\frac{C_{inh}}{\theta} = \frac{1}{K_{ads}} + C_{inh} \qquad (21)$$

All LAI shown have a similar profile: they all intercept the positive y-axis, ensuring the y-intercept is also positive. This in turn means K_{ads} will be positive, which results in a negative $\Delta G°_{ads}$ (see Equation 14), showing spontaneous adsorption onto the MS surface. Equation 14 shows us that a larger K_{ads} results in a more negative $\Delta G°_{ads}$ indicating greater spontaneity of adsorption. However, this is not always the case, perhaps because of the inherent limitations of the LAI.

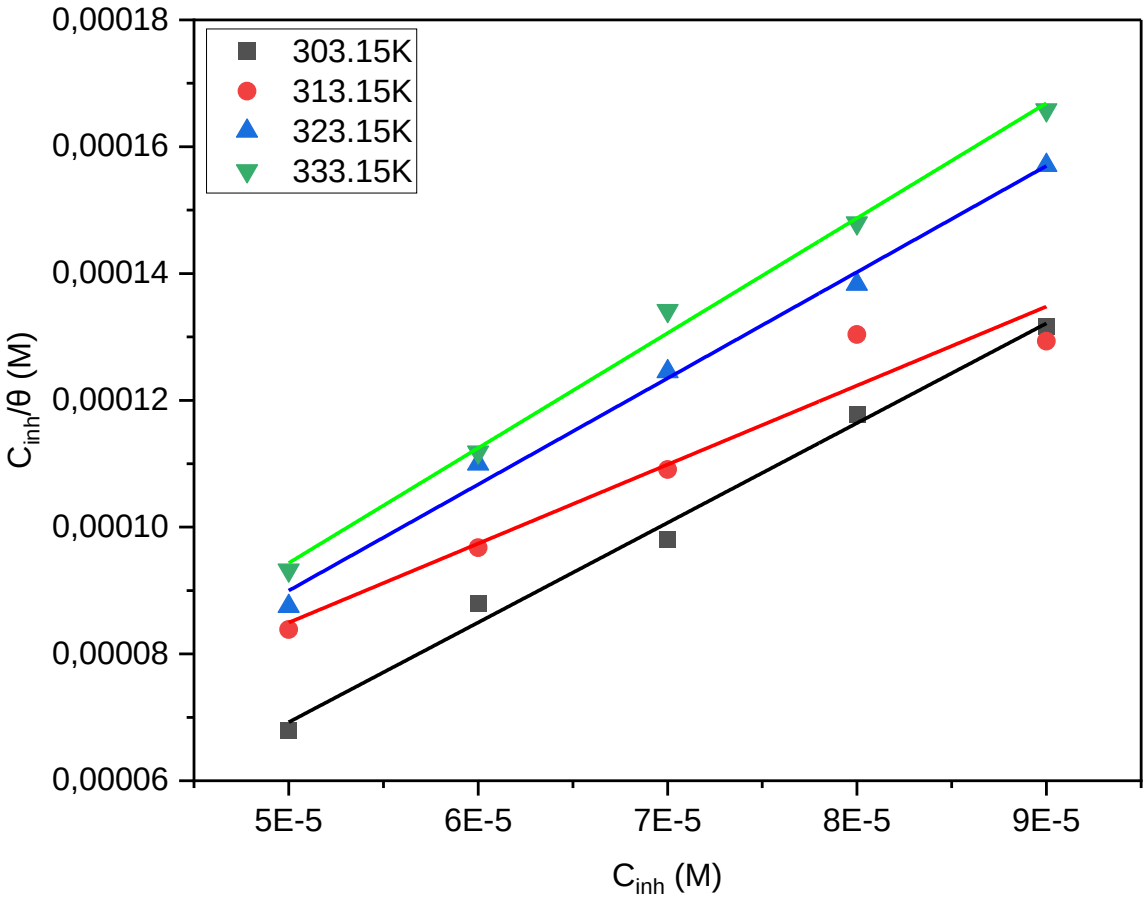

Figure 4.37: A1 Langmuir adsorption isotherms (MS).

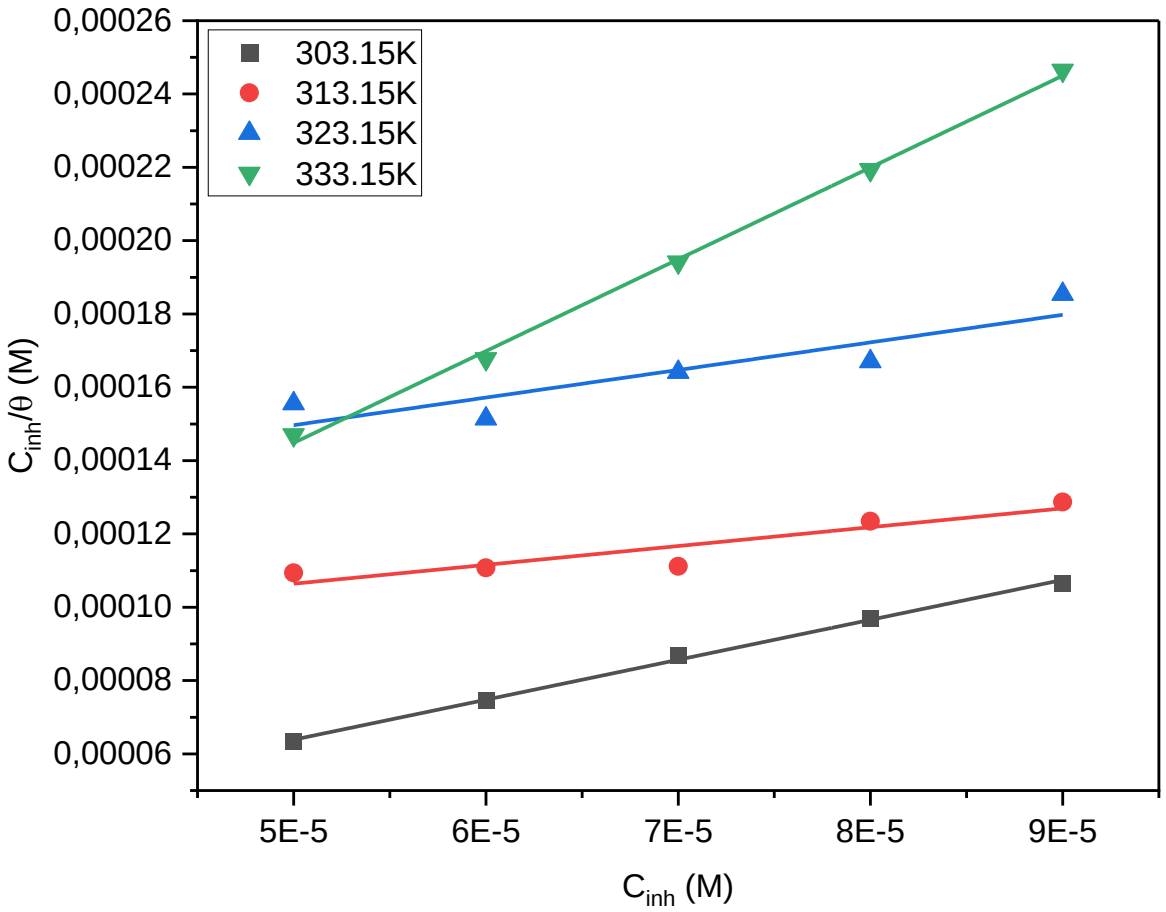

Figure 4.38: A2 Langmuir adsorption isotherms (MS).

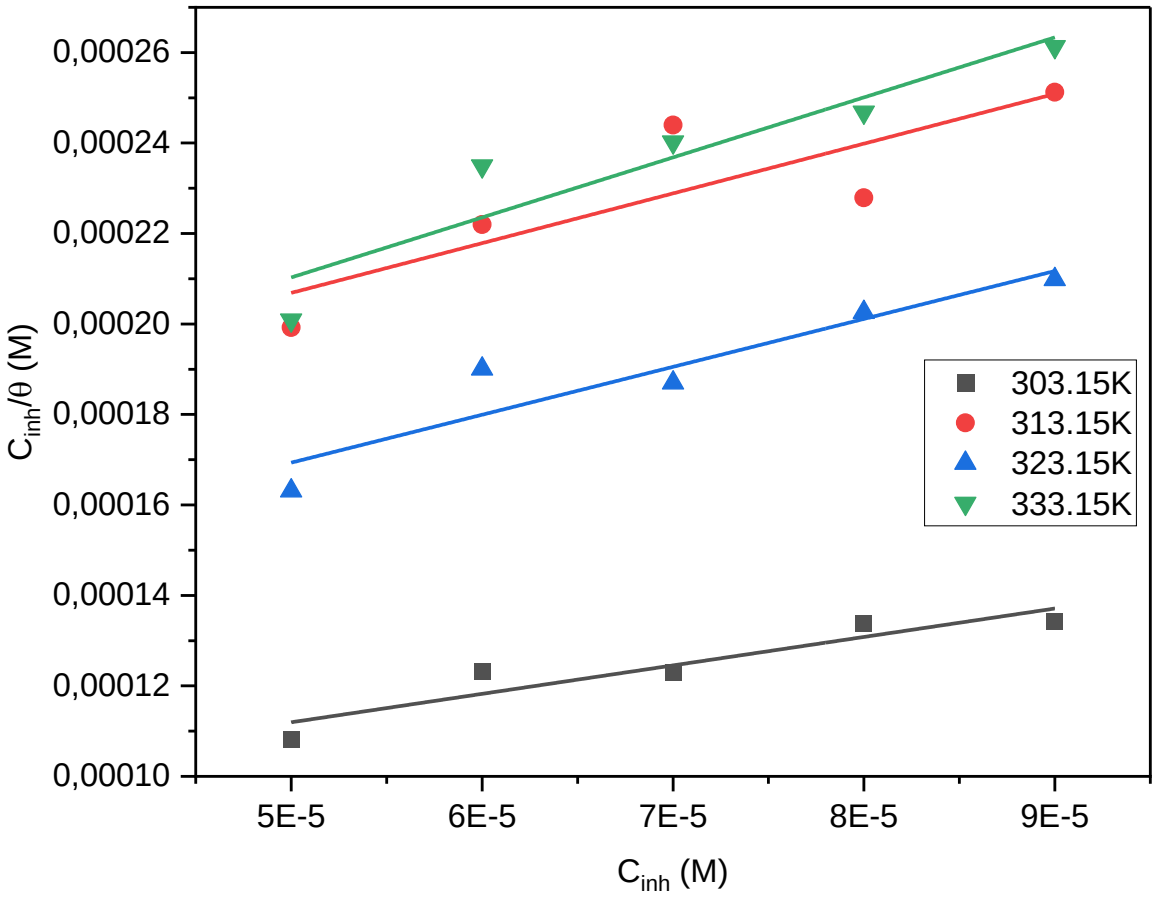

Figure 4.39: A3 Langmuir adsorption isotherms (MS).

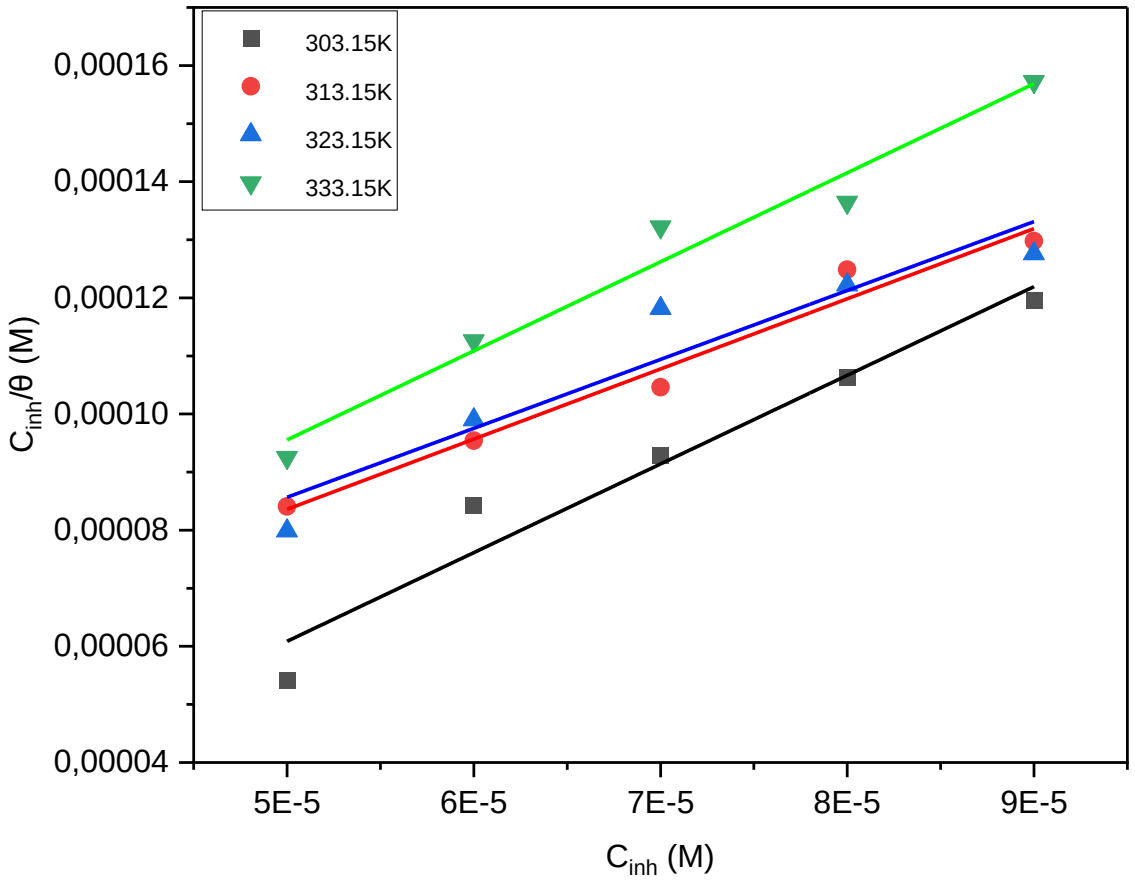

Figure 4.40: B1 Langmuir adsorption isotherms (MS).

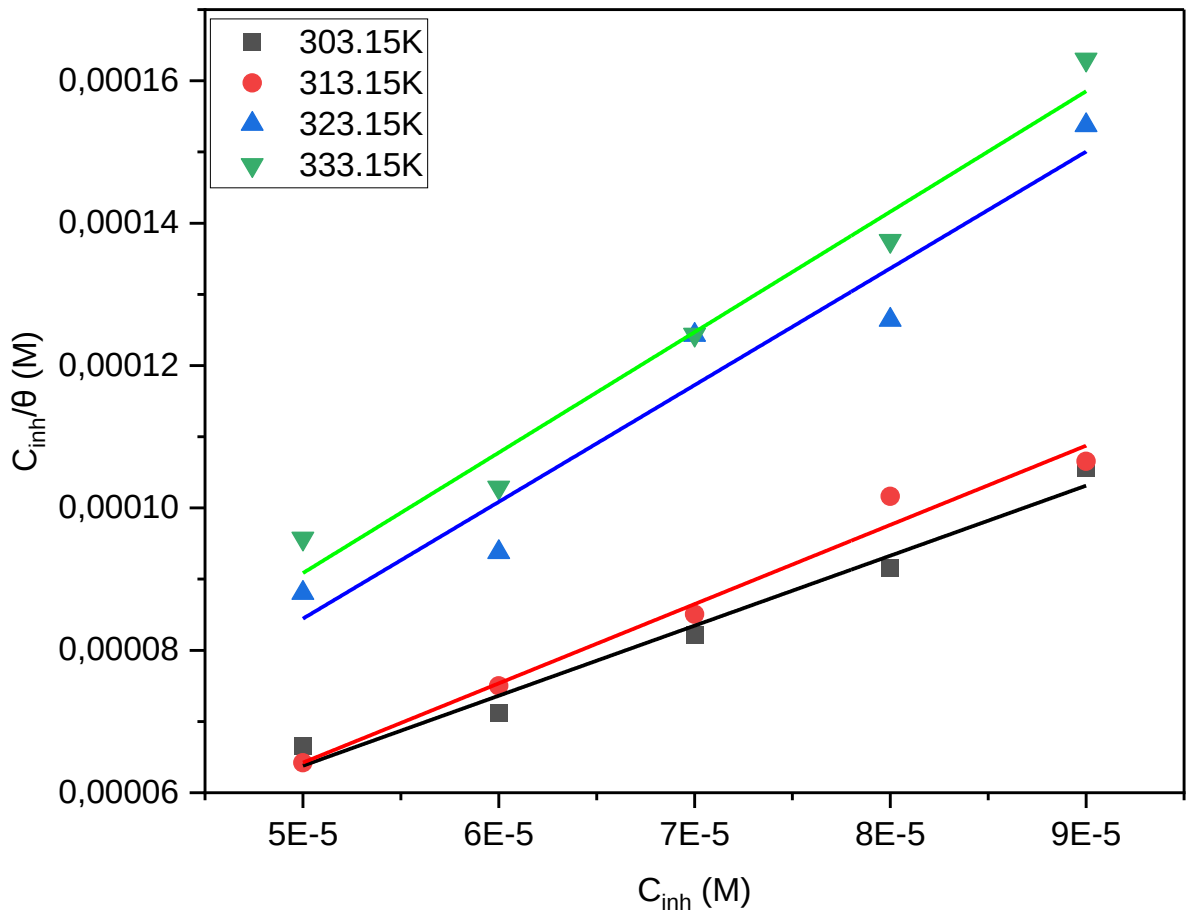

Figure 4.41: B2 Langmuir adsorption isotherms (MS).

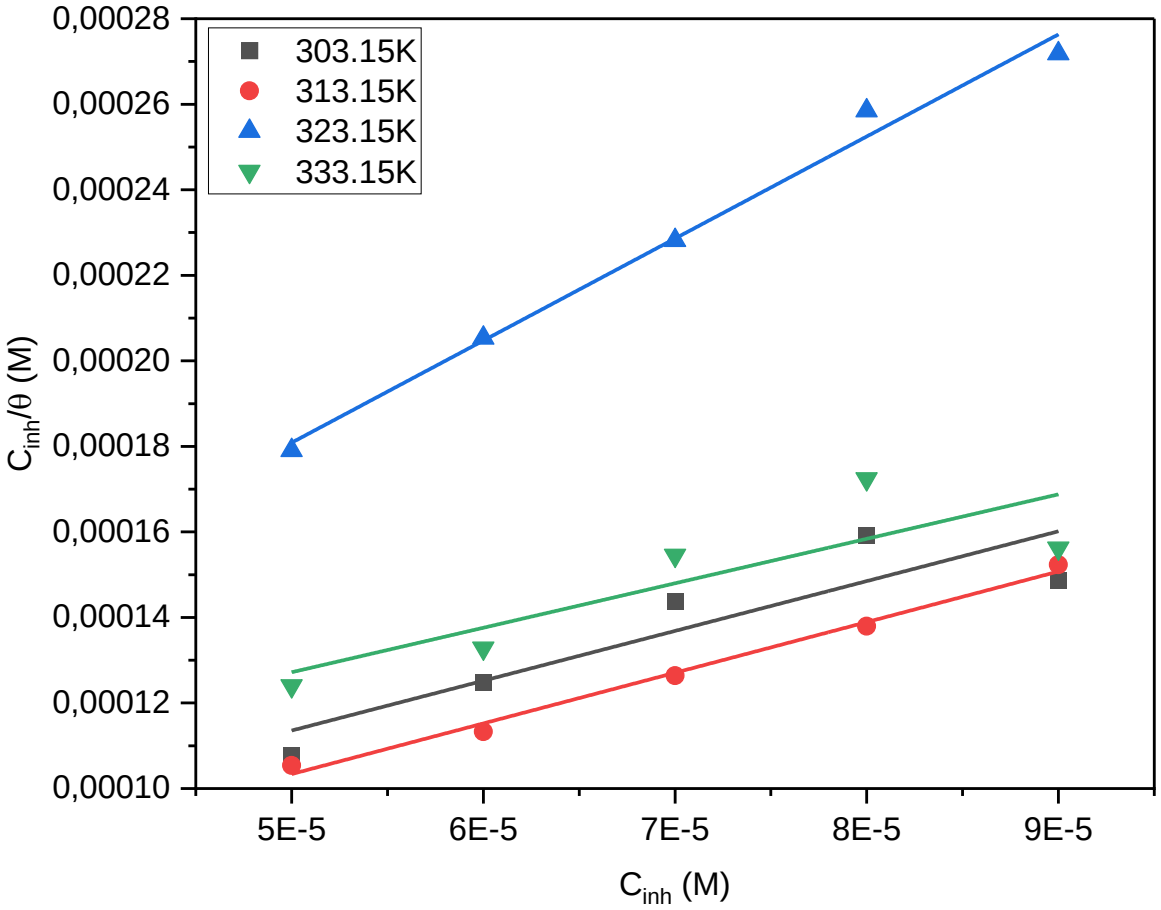

Figure 4.42: G1 Langmuir adsorption isotherms (MS).

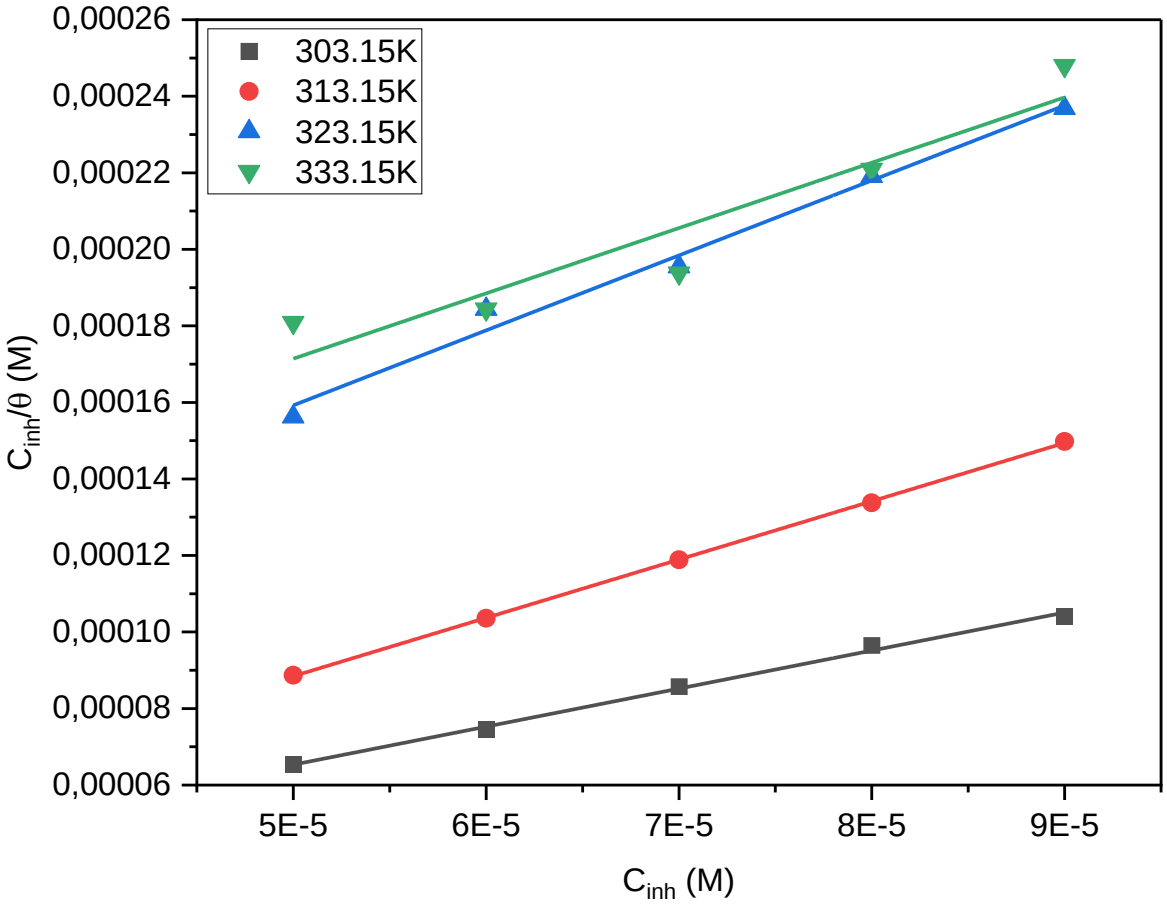

Figure 4.43: G2 Langmuir adsorption isotherms (MS).

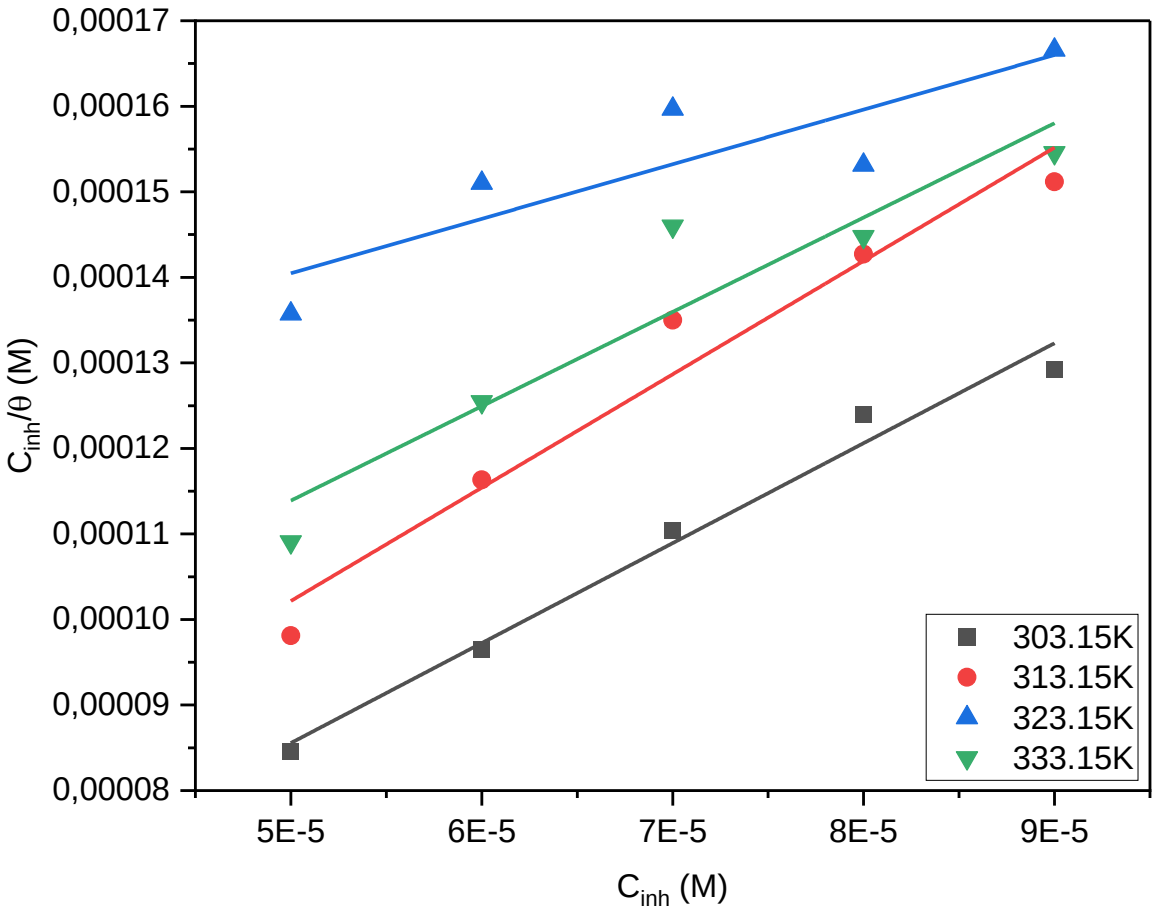

Figure 4.44: G3 Langmuir adsorption isotherms (MS).

Table 4.3 shows a summary of the LAI parameters and adsorption data of the TZDs. Whilst other adsorption isotherms such as the Temkin and Freundlich isotherms were investigated, the LAI provided the best fit for the adsorption data obtained. This can be seen in the r^2 values. All r^2 values are sufficiently close to unity, showing that the LAI fits the adsorption data of all TZDs quite well [160]. All $\Delta G°_{ads}$ data is negative, an indication that all TZDs adsorb spontaneously onto MS [161]. Most of the TZDs adsorb endothermically ($+\Delta H°_{ads}$) except for A1 and the two butanoates. With the exception of A2 and G2, the adsorption process of the TZDs creates quite a great deal of disorder at the metal/solution interface as shown by the positive $\Delta S°_{ads}$ [162].

Table 4.3: TZD adsorption parameters for MS.

TZD	Temperature (K)	r^2	K_{ads} ($L \cdot mol^{-1}$)	$\Delta G°_{ads}$ ($kJ \cdot mol^{-1}$)	$\Delta H°_{ads}$ ($kJ \cdot mol^{-1}$)	$\Delta S°_{ads}$ ($J \cdot mol^{-1} \cdot K^{-1}$)
A1	303.15	0.9920	65685	−38.08	66.93	271.90
	313.15	0.9412	102187	−40.49	66.93	269.84
	323.15	0.9925	668092	−48.27	66.93	295.86
	333.15	0.9952	4462891	−51.92	66.93	275.01
A2	303.15	0.9980	106658	−39.30	−101.78	−206.10
	313.15	0.8530	12388	−34.99	−101.78	−213.28
	323.15	0.8162	8925	−35.23	−101.78	−205.95
	333.15	0.9981	50979	−41.15	−101.78	−182.01
A3	303.15	0.8749	12420	−33.88	−16.06	58.80
	313.15	0.7302	6584	−33.35	−16.06	55.22
	323.15	0.8756	8592	−35.13	−16.06	59.02
	333.15	0.8778	6947	−35.63	−16.06	58.74
B1	303.15	0.9516	33717	−36.40	38.67	178.83
	313.15	0.9735	66812	−39.38	38.67	181.57
	323.15	0.9069	93773	−41.55	38.67	181.63
	333.15	0.9692	131486	−43.77	38.67	181.85
B2	303.15	0.9760	121207	−39.62	72.65	300.86
	313.15	0.9818	429177	−44.22	72.65	298.64
	323.15	0.9377	66684	−40.63	72.65	302.87
	333.15	0.9713	174210	−44.55	72.65	289.17
G1	303.15	0.8056	18075	−34.83	−23.12	38.63
	313.15	0.9918	22638	−36.56	−23.12	42.93
	323.15	0.9895	16247	−36.84	−23.12	42.46
	333.15	0.7155	13299	−37.43	−23.12	42.94

G2	303.15	0.9961	64039	−38.02	−49.06	−36.44
	313.15	0.9998	81544	−39.90	−49.06	−29.26
	323.15	0.9871	16318	−36.85	−49.06	−37.79
	333.15	0.9019	11622	−37.05	−49.06	−36.06
G3	303.15	0.9824	36855	−36.62	−21.58	49.61
	313.15	0.9595	27856	−37.10	−21.58	49.56
	323.15	0.7669	9212	−35.32	−21.58	42.49
	333.15	0.8962	17025	−38.11	−21.58	49.60

The $\Delta H°_{ads}$ of the alaninates shows that only A1 adsorbs onto MS endothermically. The other two alaninates adsorb onto MS exothermically, with A2 adsorbing more exothermically than A3 on the MS surface. This is shown by the more negative $\Delta H°_{ads}$ for A2 (−101.78 $kJ \cdot mol^{-1}$), an indication that more heat energy is released when A2 adsorbs onto MS. More heat energy released means more/stronger interactions formed with the metal surface [163]. Despite the ($-NO_2$) substituent on the benzene ring in A2 being an electron withdrawing group [164], the presence of two O heteroatoms (relative to only one O heteroatom on A3's furan ring) gives A2 the edge over A3, enabling A2 to form additional dative covalent bonds with the MS surface. This is why A2 has more negative $\Delta G°_{ads}$ data than A3, an indication that A2 adsorbs more spontaneously onto MS [165]. A1 has much more negative $\Delta G°_{ads}$ data than both A2 and A3 because the endothermic nature of its adsorption makes it more likely to adsorb onto MS via chemisorption. This is the case because chemisorption is defined as $\Delta G°_{ads} \leq -40$ $kJ \cdot mol^{-1}$ [166]. This may well be because the molecular orientation adopted by A1 during adsorption onto MS enables more multiple bonds and heteroatoms in its molecular structure to participate in the formation of an adsorption film on the MS surface. The $\Delta S°_{ads}$ data for A2 is very large and negative, an indication of the state of order at the metal surface brought about by the formation of an activated complex between A2 and the metal surface [167]. The $\Delta S°_{ads}$ data for A1 and A3 show an increase in disorder due to the displacement of H_2O molecules from the metal surface (Equation 22). However, A1 has larger $\Delta S°_{ads}$ data than A3 most likely because of the larger activated benzene ring displacing more H_2O molecules from the MS surface than the smaller furan ring [168].

$$\mathrm{Inh_{sol}} + \mathrm{nH_2O_{ads}} \rightarrow \mathrm{Inh_{ads}} + \mathrm{nH_2O_{sol}} \qquad (22)$$

where Inh_{sol}, H_2O_{ads}, Inh_{ads} and H_2O_{sol} are the inhibitor molecules in solution, adsorbed water molecules, adsorbed inhibitor molecules and displaced water molecules, respectively.

Some authors use trends in $\Delta S°_{act}$ as a gauge as to whether an activated complex has formed, resulting in the displacement of H_2O molecules from the metal surface. Unlike Nwosu *et al.* [167], Diki *et al.* [169] stated that an increase in $\Delta S°_{act}$ was an indication of the displacement of H_2O molecules from the metal surface. There isn't necessarily a contradiction here because, for the corrosion inhibitor to displace H_2O molecules

from the metal surface, it must first adsorb onto the metal surface, and it can only do that by forming an activated complex with the metal surface. Therefore, both entropy variables can provide the same information.

The $\Delta H°_{ads}$ value for B2 (72.65 kJ·mol^{-1}) is much larger than that of B1 (38.67 kJ·mol^{-1}). This reveals two things:

1. B2 adsorbed more endothermically than B1 onto MS.
2. B2 adsorbed close to the minimum threshold for chemisorption (80 kJ·mol^{-1}) [170].

Despite the presence of a strong ring activating substituent (-OCH_3), the benzene ring remains very stable because of its delocalized pi-electrons [158]. Therefore, the benzene ring in B1 does not give up its electrons easily. This is why the smaller furan ring gives B2 an advantage in adsorbing onto MS at higher temperatures by allowing B2 to form additional dative covalent bonds with the MS surface. This is the reason why B2 has a larger $\Delta H°_{ads}$ than B1. The smaller furan ring also makes B2 smaller and lighter than B1, resulting in B2 adsorbing onto MS much faster and more easily than B1. This is shown by the more negative $\Delta G°_{ads}$ data for B2, an indication that the adsorption of B2 onto MS is more spontaneous than that of B1 [171]. The much larger $\Delta S°_{ads}$ data for B2 shows a much greater state of disorder at the metal surface relative to B1. This is most likely due to the more efficient displacement of H_2O molecules from the metal surface as B2 adsorbs onto MS [172].

The glycinates all adsorb exothermically, with G2 forming more/stronger interactions with the MS surface given it releases more heat energy during adsorption [173] (see Table 4.3). The additional O heteroatoms allow G2 to adsorb more spontaneously onto MS as shown by its much more negative $\Delta G°_{ads}$ data. The negative $\Delta S°_{ads}$ data for G2 is indicative of the state of order at the MS surface, brought about by the formation of an activated complex with MS [174]. However, compared to A2, $\Delta S°_{ads}$ data for G2 shows that the interactions formed between G2 and the MS surface are fewer, most likely due to the absence of an additional methyl group in its molecular structure. Comparing the $\Delta S°_{ads}$ data for G3 and A3 reveals that the methyl group in A3 (blue circle) enables it to displace more H_2O molecules from the MS surface by forming additional van der Waals forces with the metal surface (Figure 4.45).

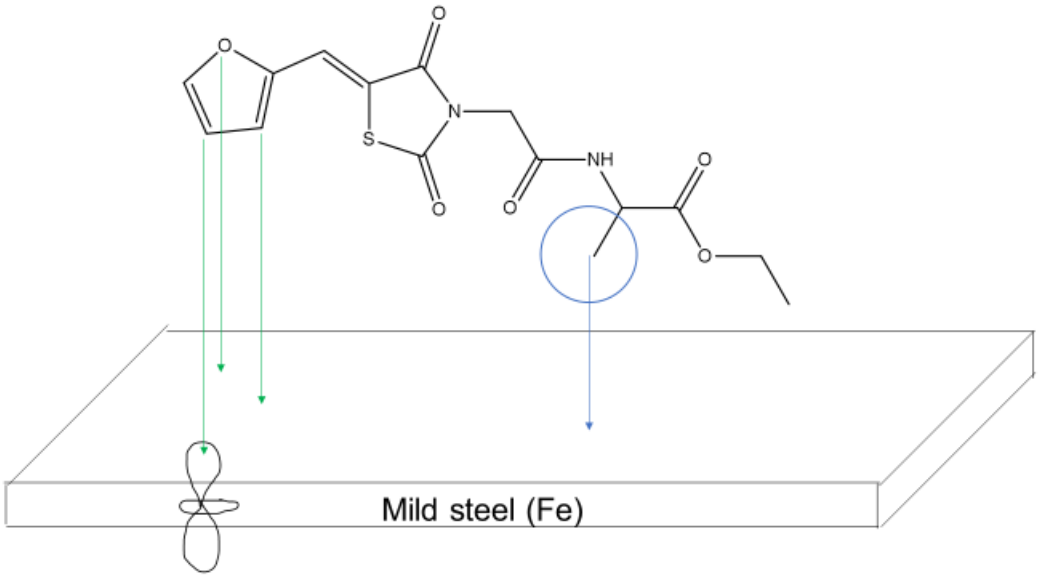

Figure 4.45: Adsorption of A3 onto MS.

4.2.1.2 Activation parameters

Three different activation parameters are discussed in this section: E_a, $\Delta H°_{act}$ and $\Delta S°_{act}$. Activation energy is obtained from the slope of Arrhenius plots (Figures 4.46 to 4.53) which are in turn plotted using the Arrhenius equation (Equation 16). All the Arrhenius plots shown have negative slopes ensuring all E_a values will be positive. In addition, for all Arrhenius plots shown, as C_{inh} is increased, the plots become steeper resulting in a higher E_a. Consequently, the highest E_a values are achieved by the highest C_{inh} (9E−5 M).

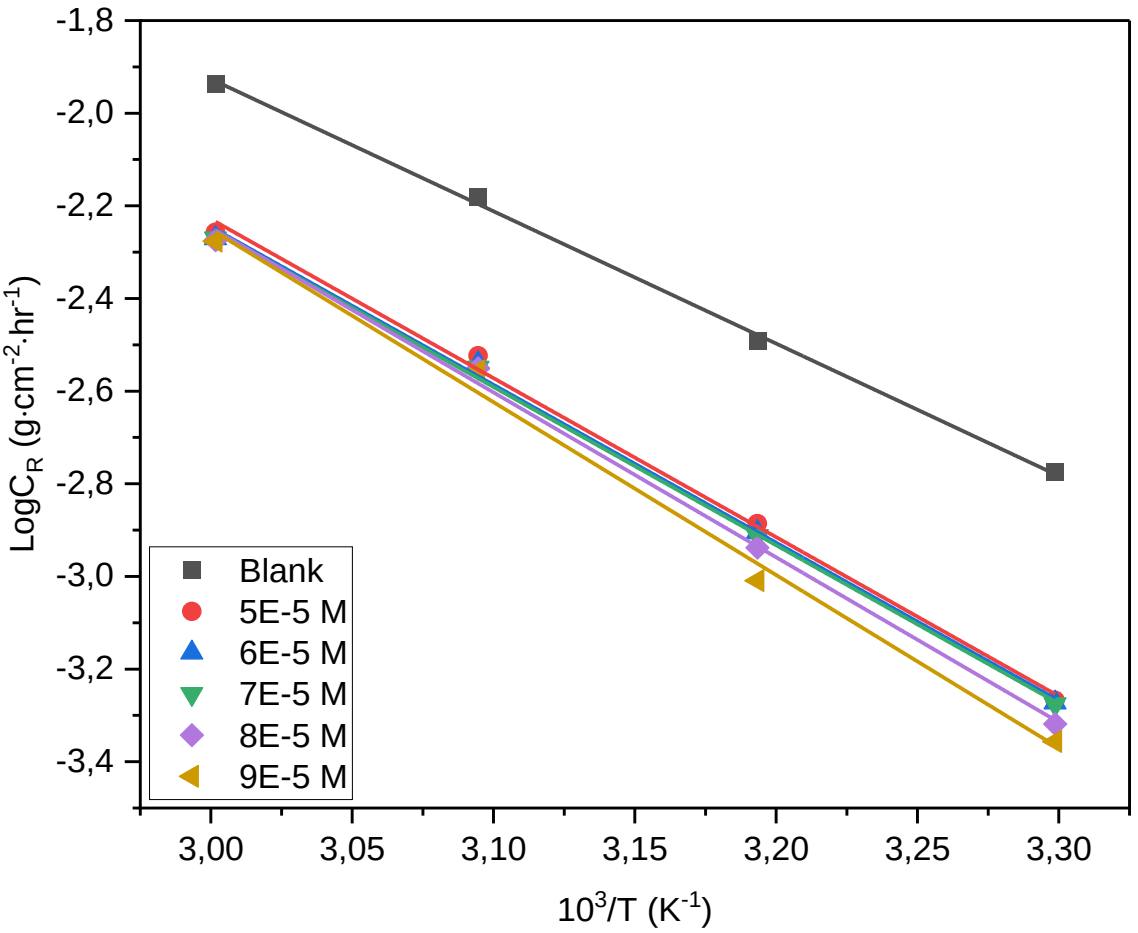

Figure 4.46: A1 Arrhenius plots (MS).

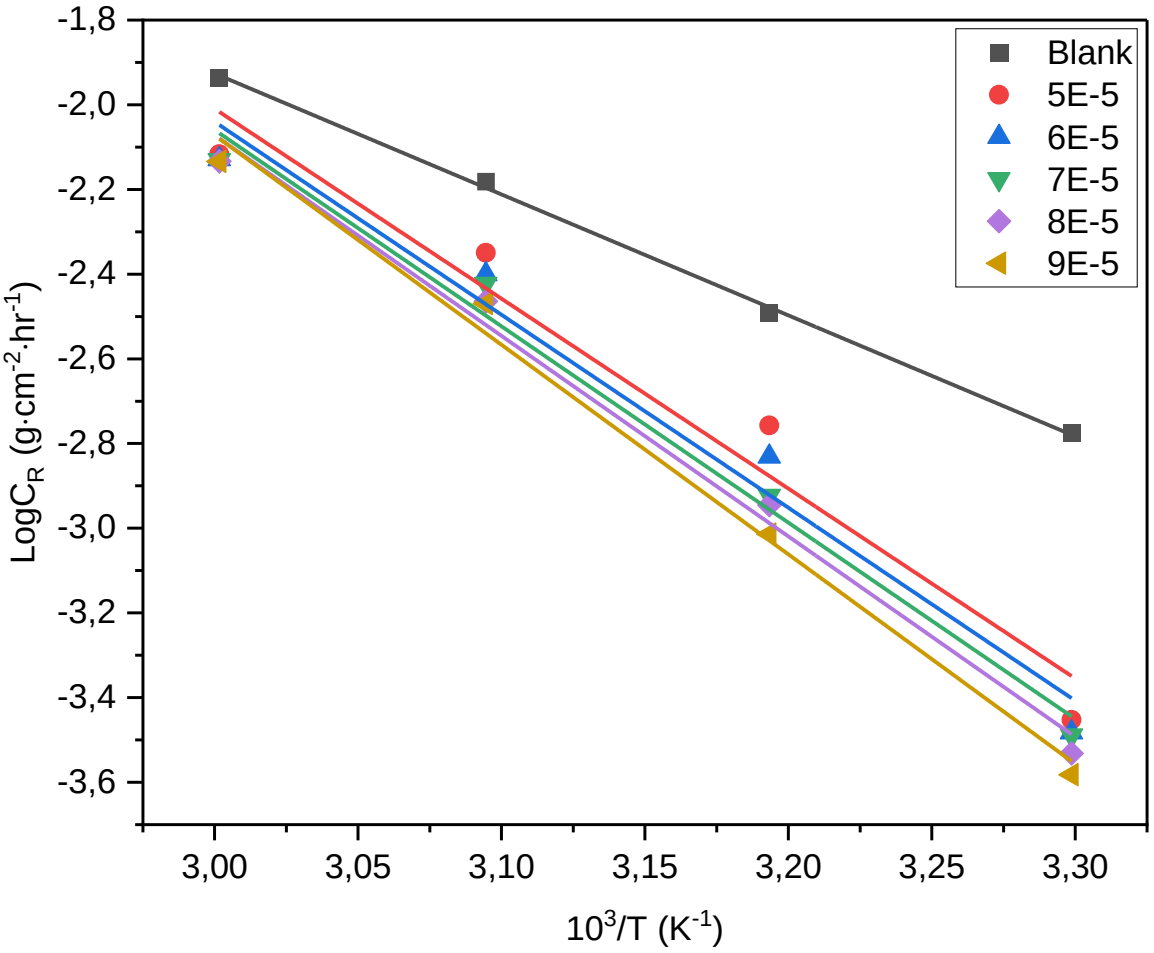

Figure 4.47: A2 Arrhenius plots (MS).

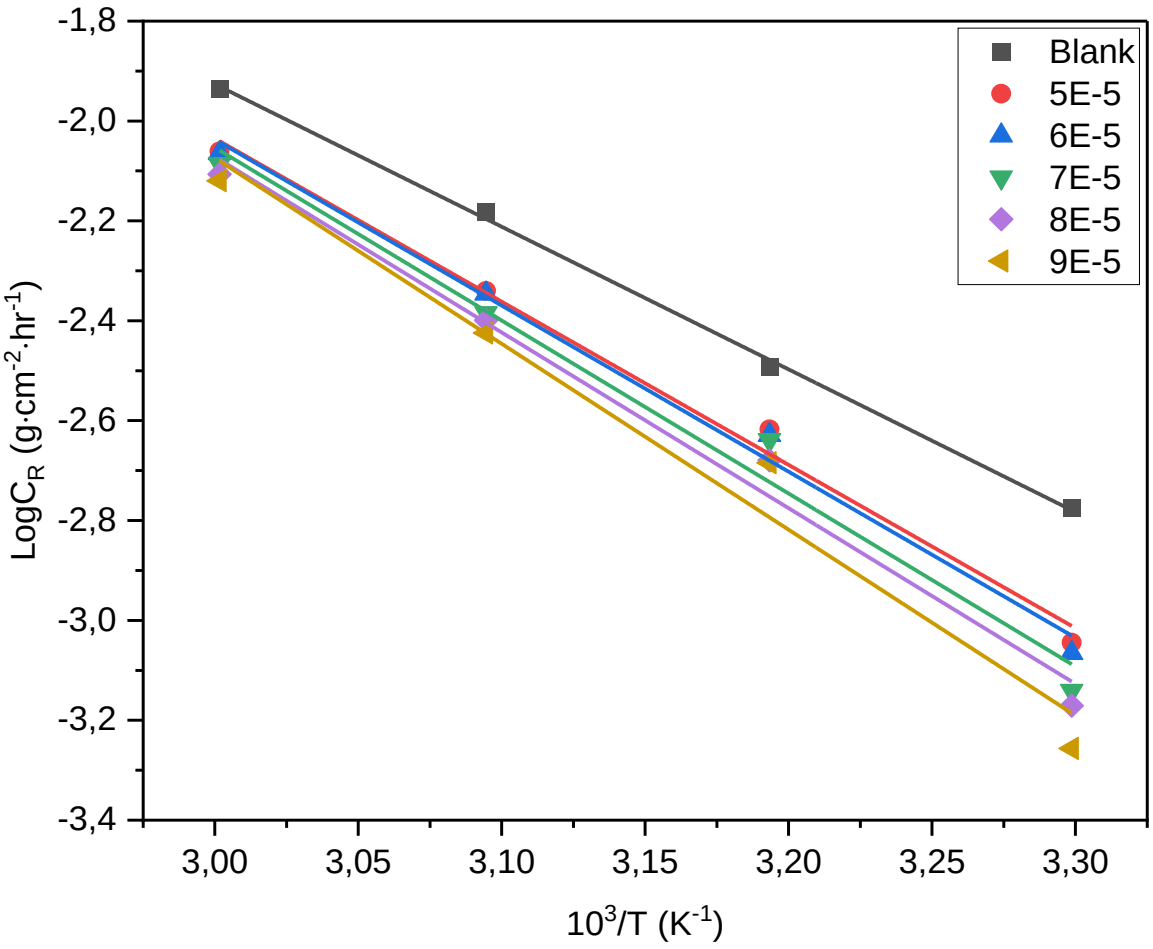

Figure 4.48: A3 Arrhenius plots (MS).

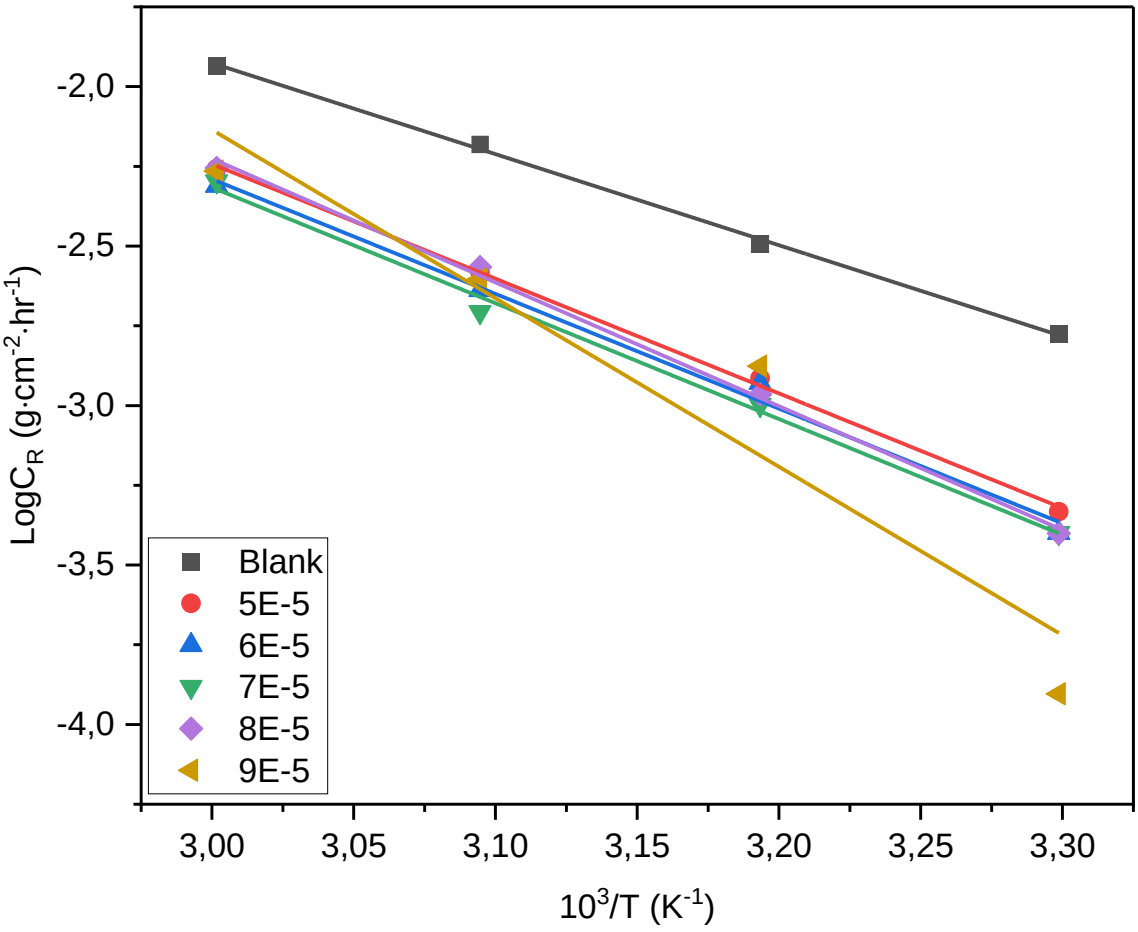

Figure 4.49: B1 Arrhenius plots (MS).

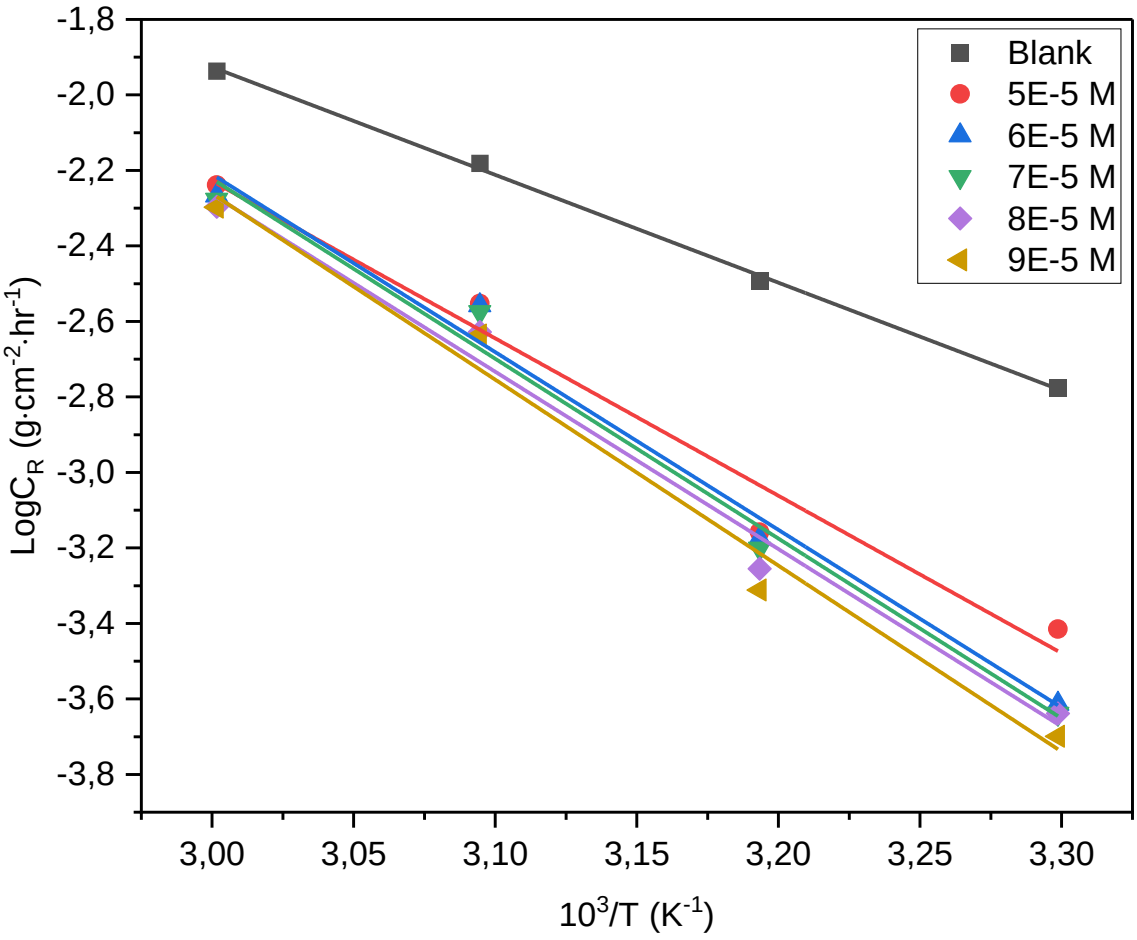

Figure 4.50: B2 Arrhenius plots (MS).

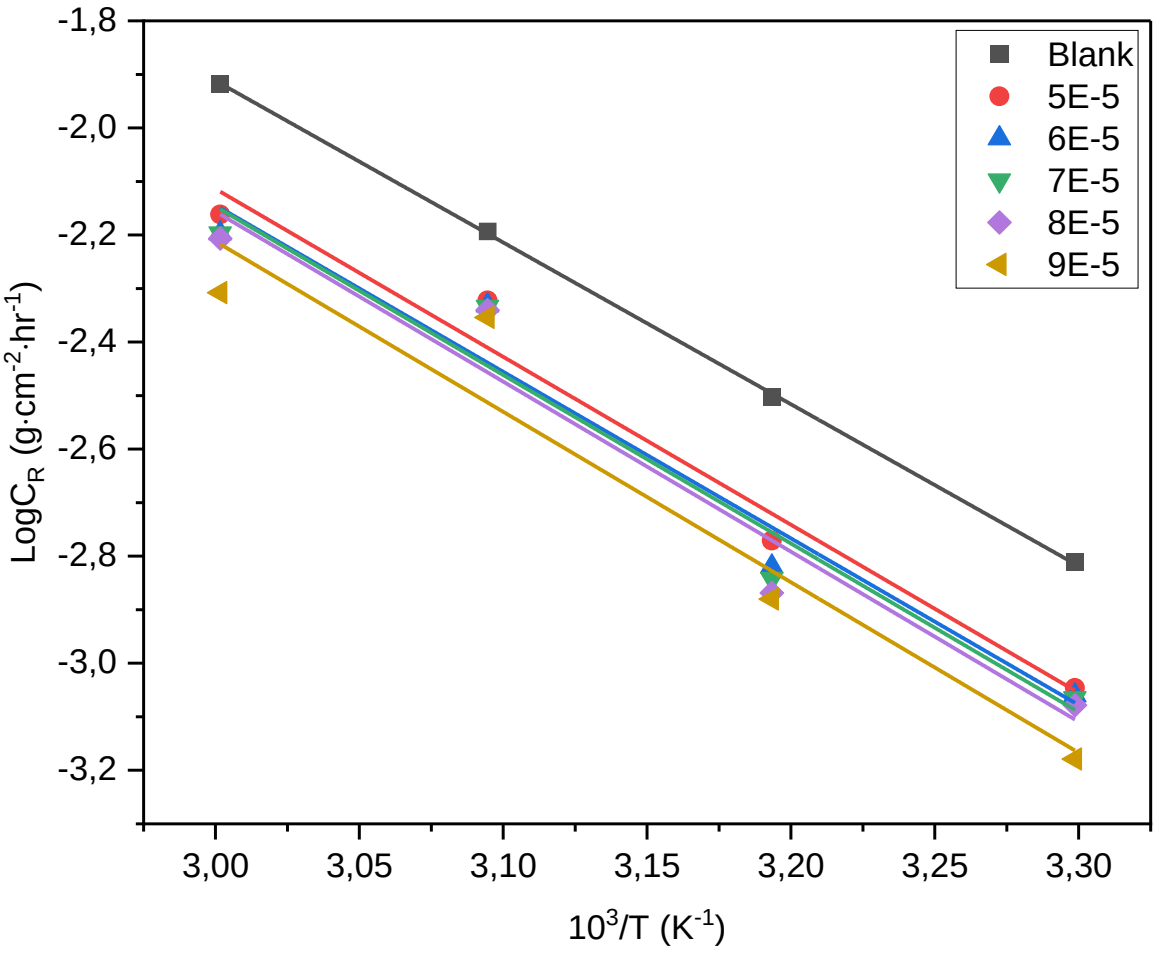

Figure 4.51: G1 Arrhenius plots (MS).

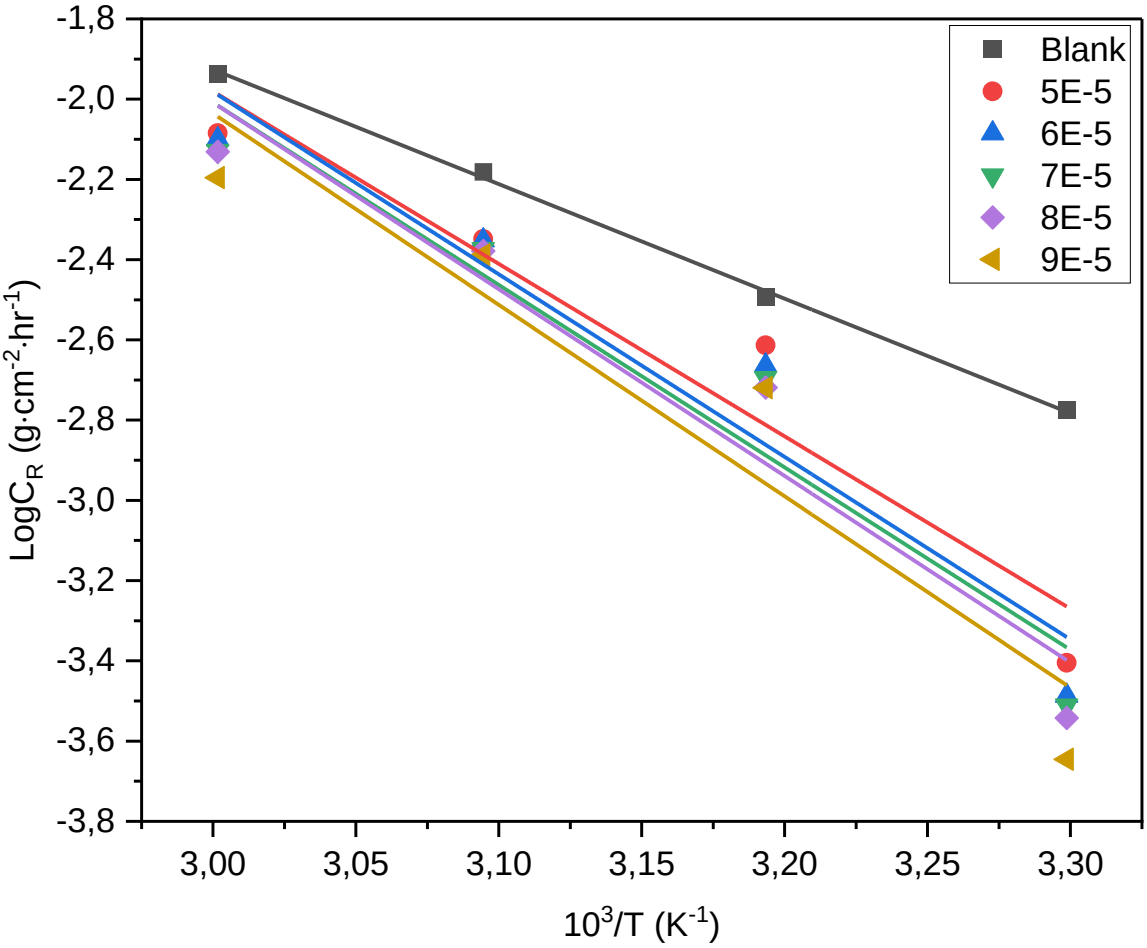

Figure 4.52: G2 Arrhenius plots (MS).

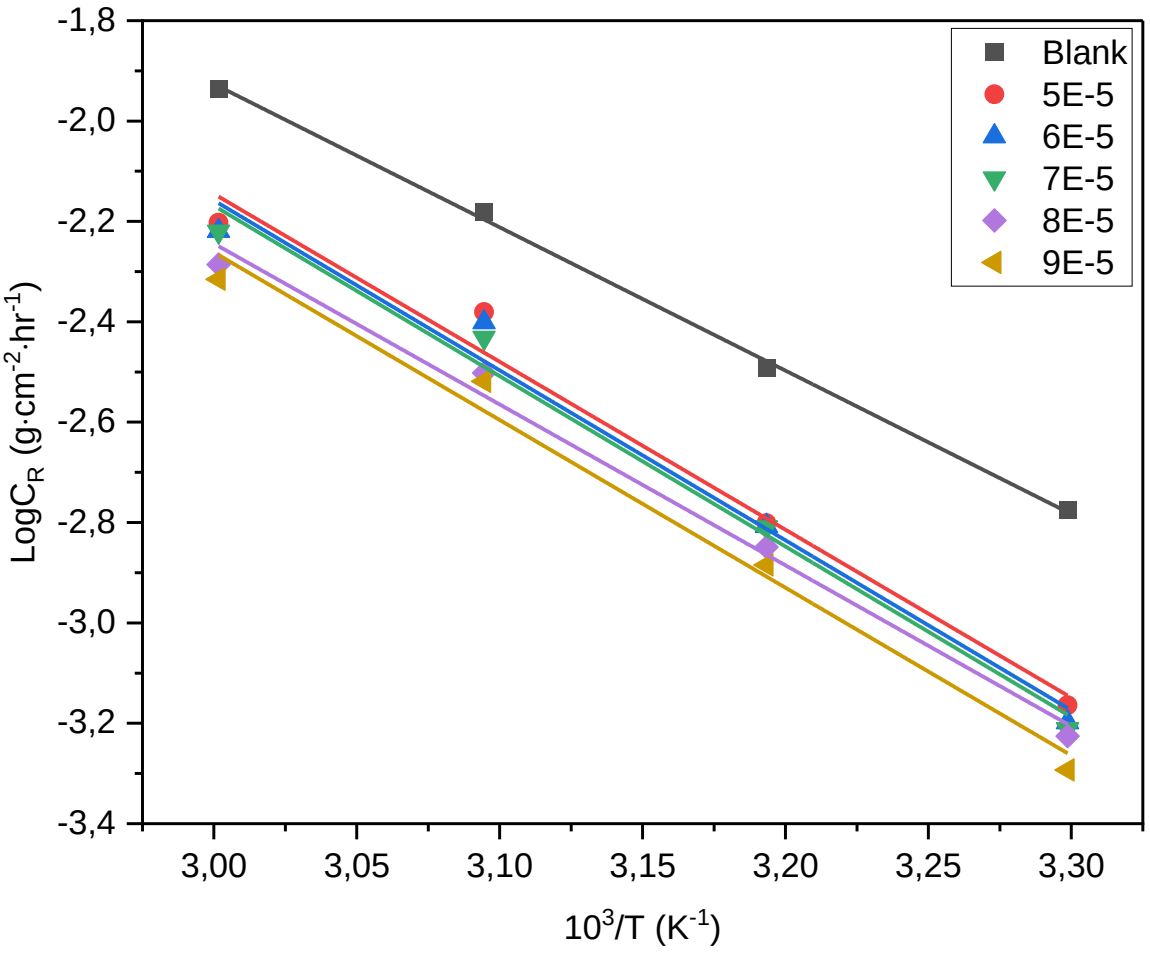

Figure 4.53: G3 Arrhenius plots (MS).

The transition state equation (see Equation 17) is used to obtain $\Delta H°_{act}$ and $\Delta S°_{act}$ using transition state plots (Figures 4.54 to 4.61). Since the transition state equation is an alternative form of the Arrhenius equation [175], it is therefore expected that the transition state plots shown below will have the same profile as the Arrhenius plots shown above. All transition state plots shown have a negative slope, ensuring that all $\Delta H°_{act}$ values will be positive. In addition, as C_{inh} is increased, the slopes of the transition state plots become steeper (more negative), meaning the highest $\Delta H°_{act}$ data is achieved by the highest C_{inh} (9E−5 M). This direct proportionality relationship between $\Delta H°_{act}$ and E_a has been observed elsewhere [176, 177].

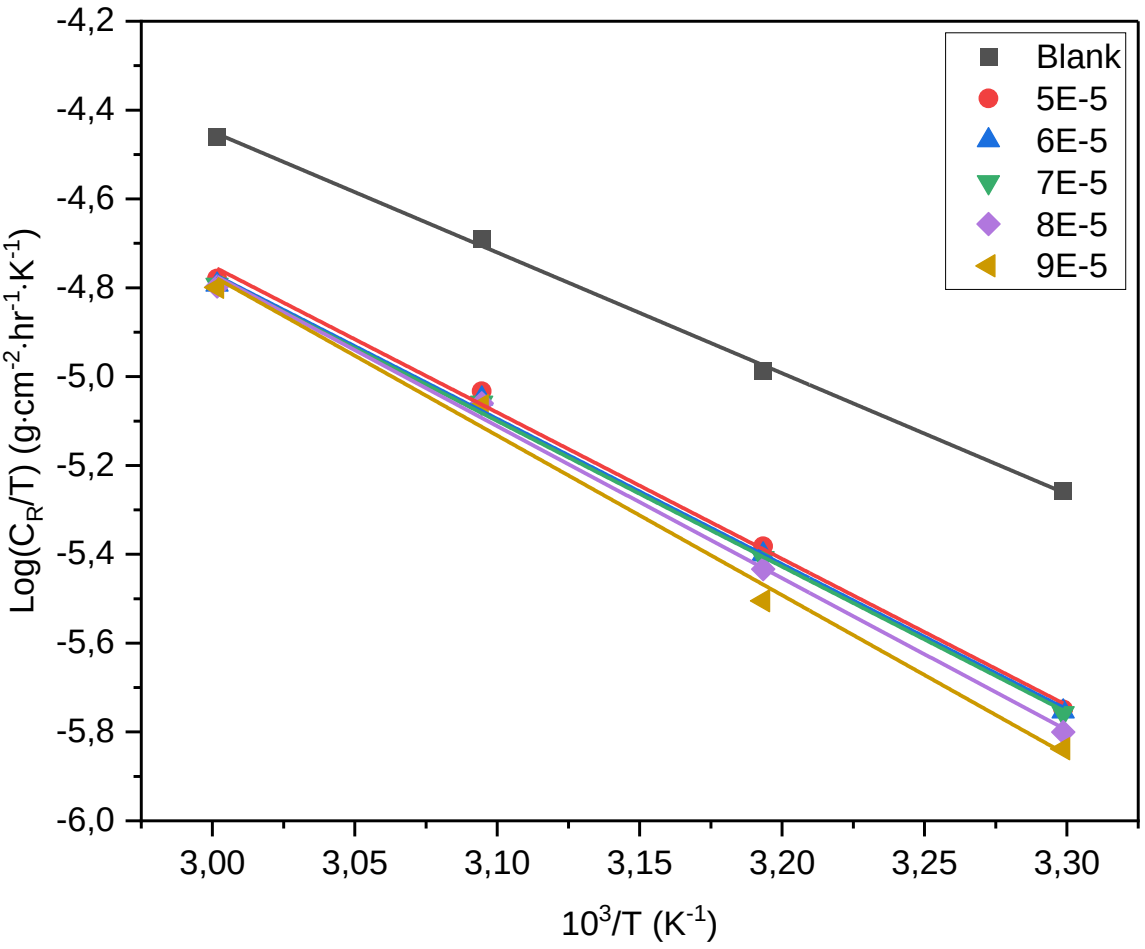

Figure 4.54: A1 Transition state plots (MS).

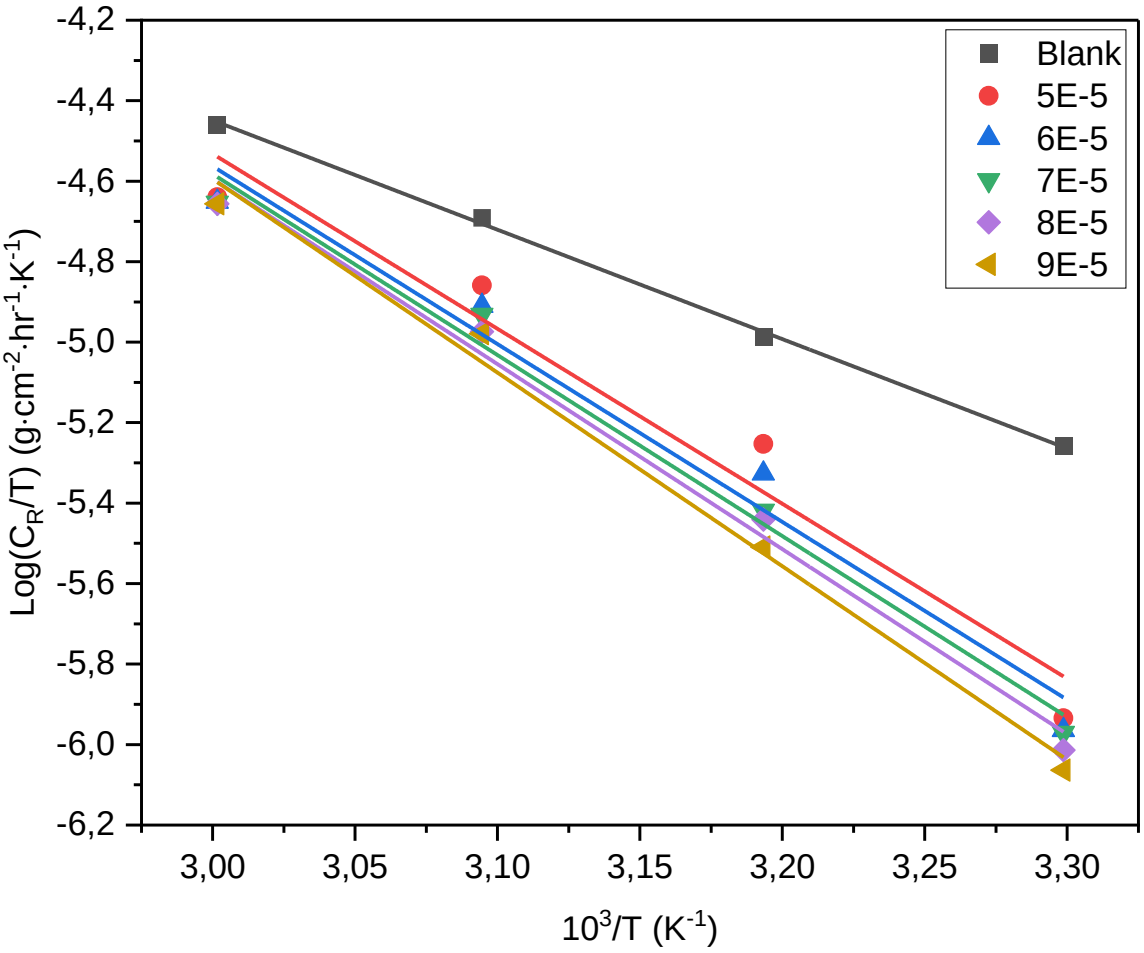

Figure 4.55: A2 Transition state plots (MS).

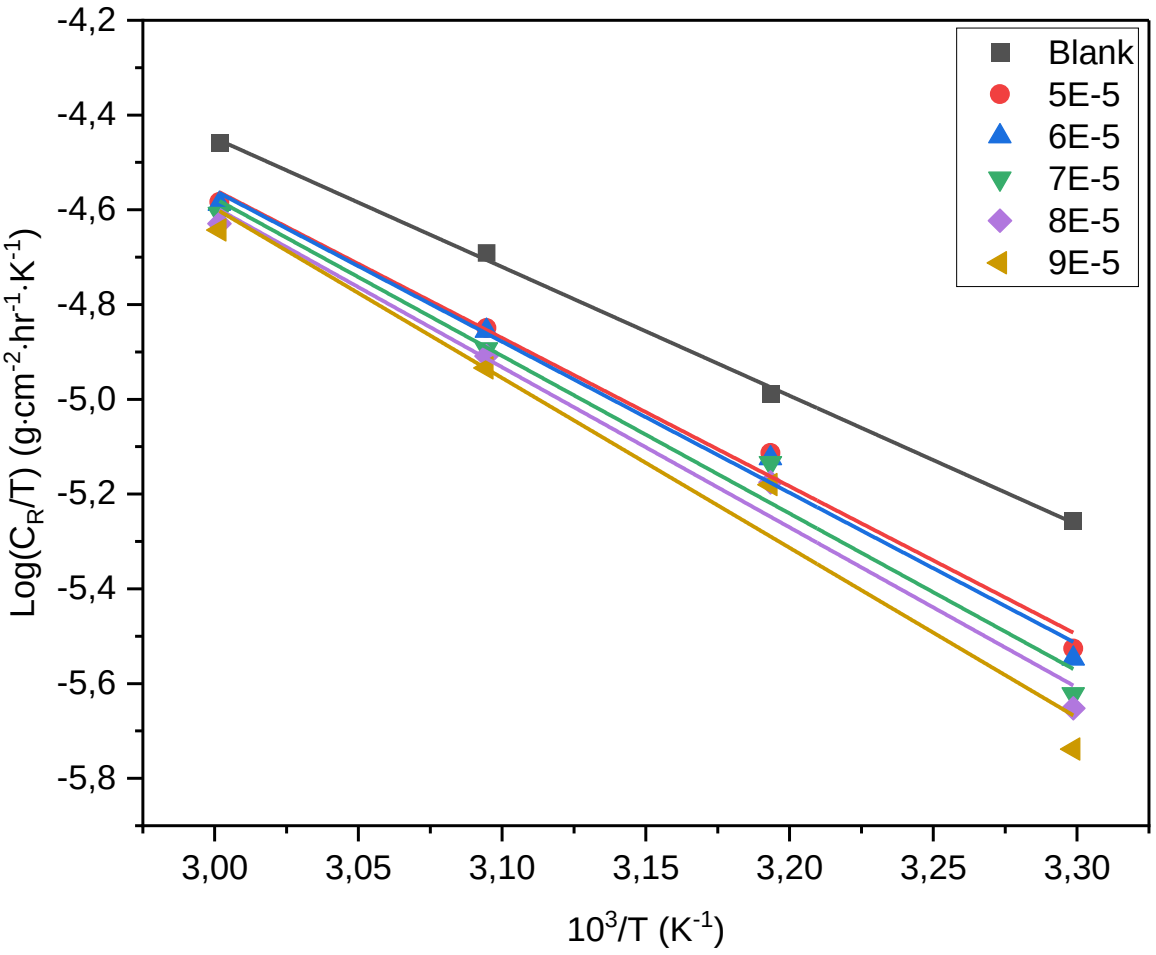

Figure 4.56: A3 Transition state plots (MS).

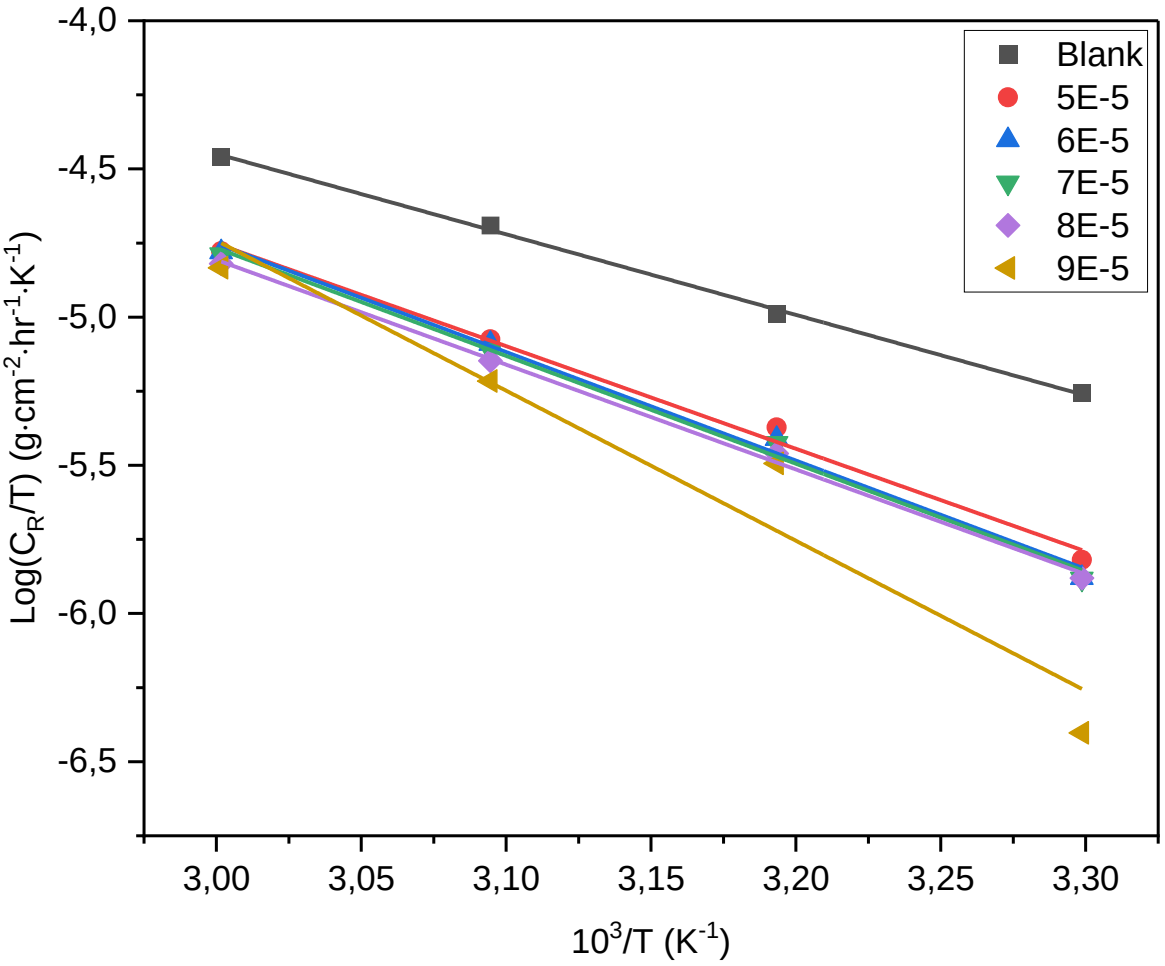

Figure 4.57: B1 Transition state plots (MS).

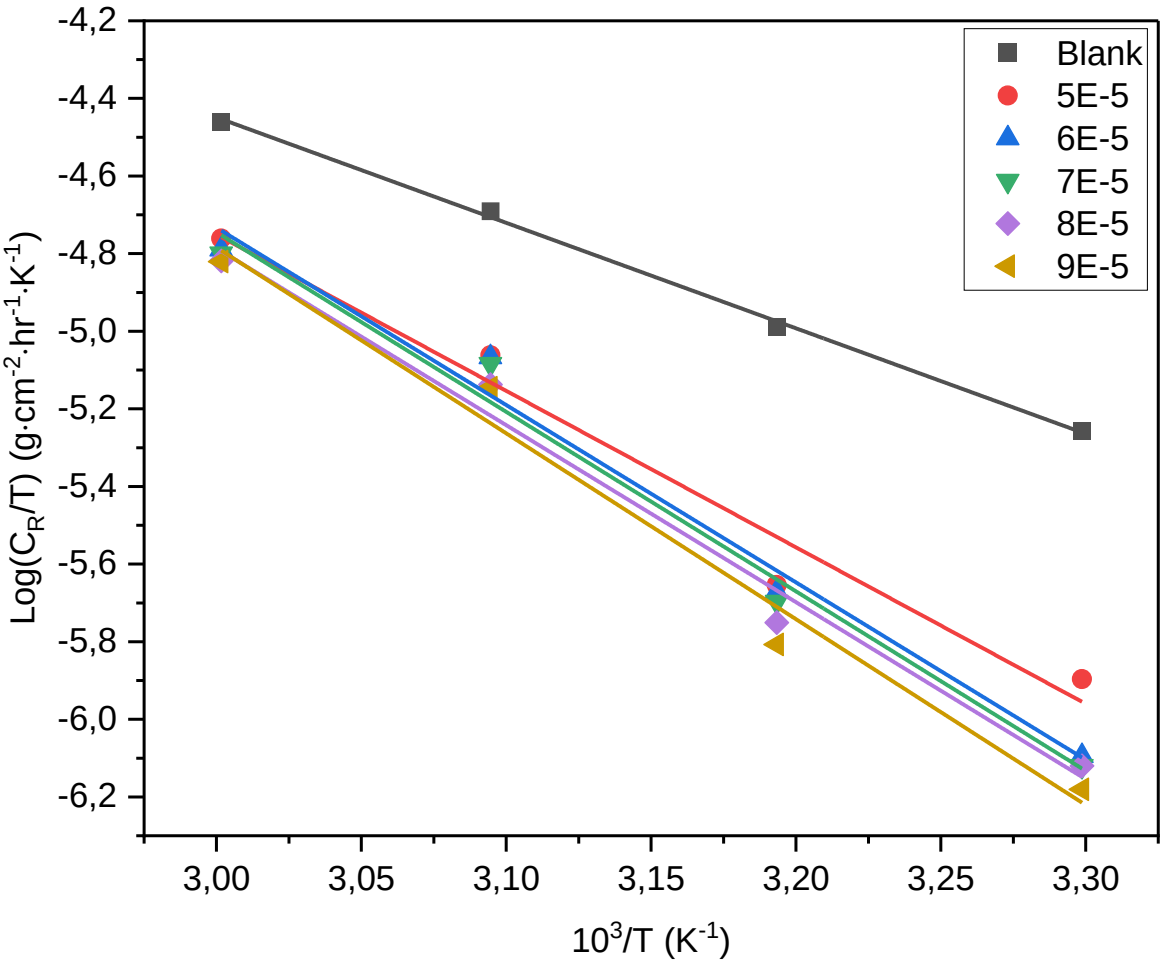

Figure 4.58: B2 Transition state plots (MS).

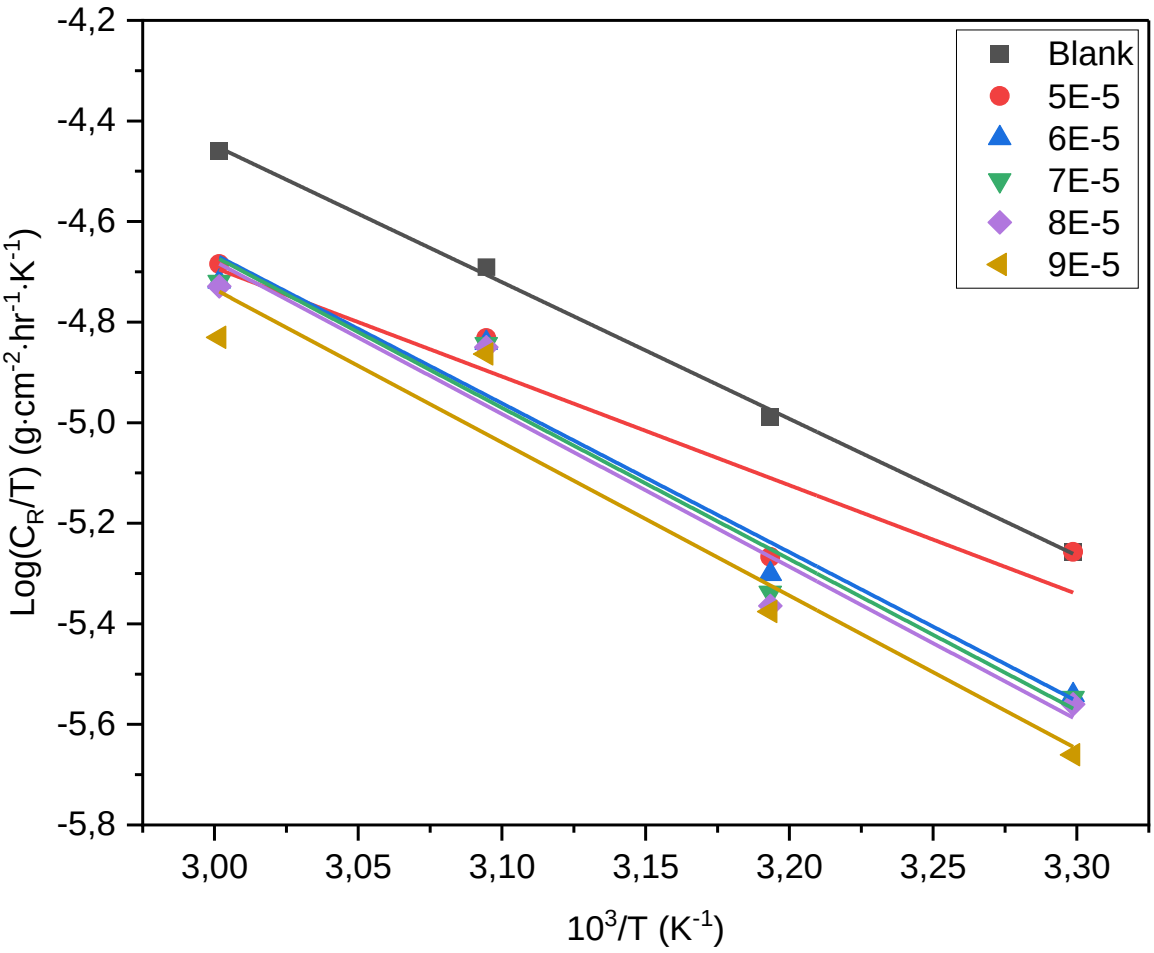

Figure 4.59: G1 Transition state plots (MS).

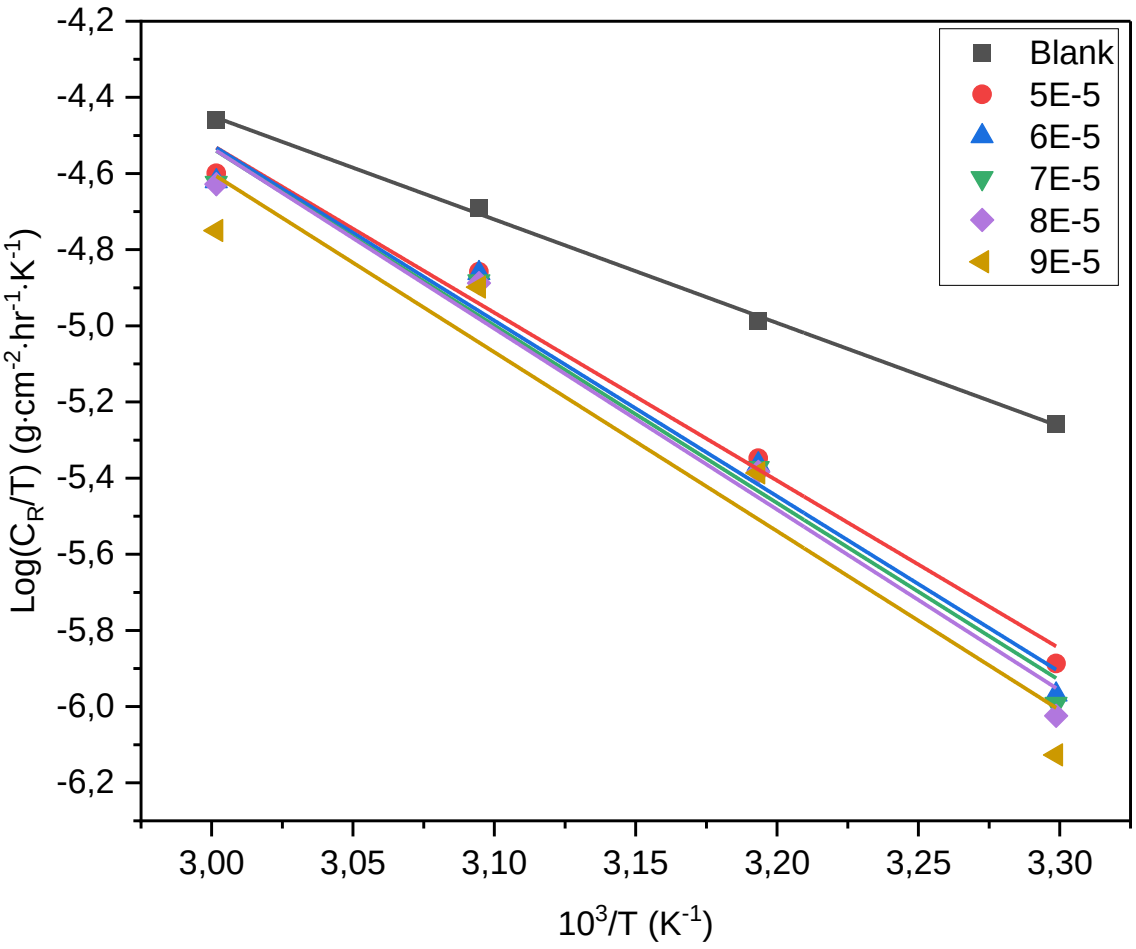

Figure 4.60: G2 Transition state plots (MS).

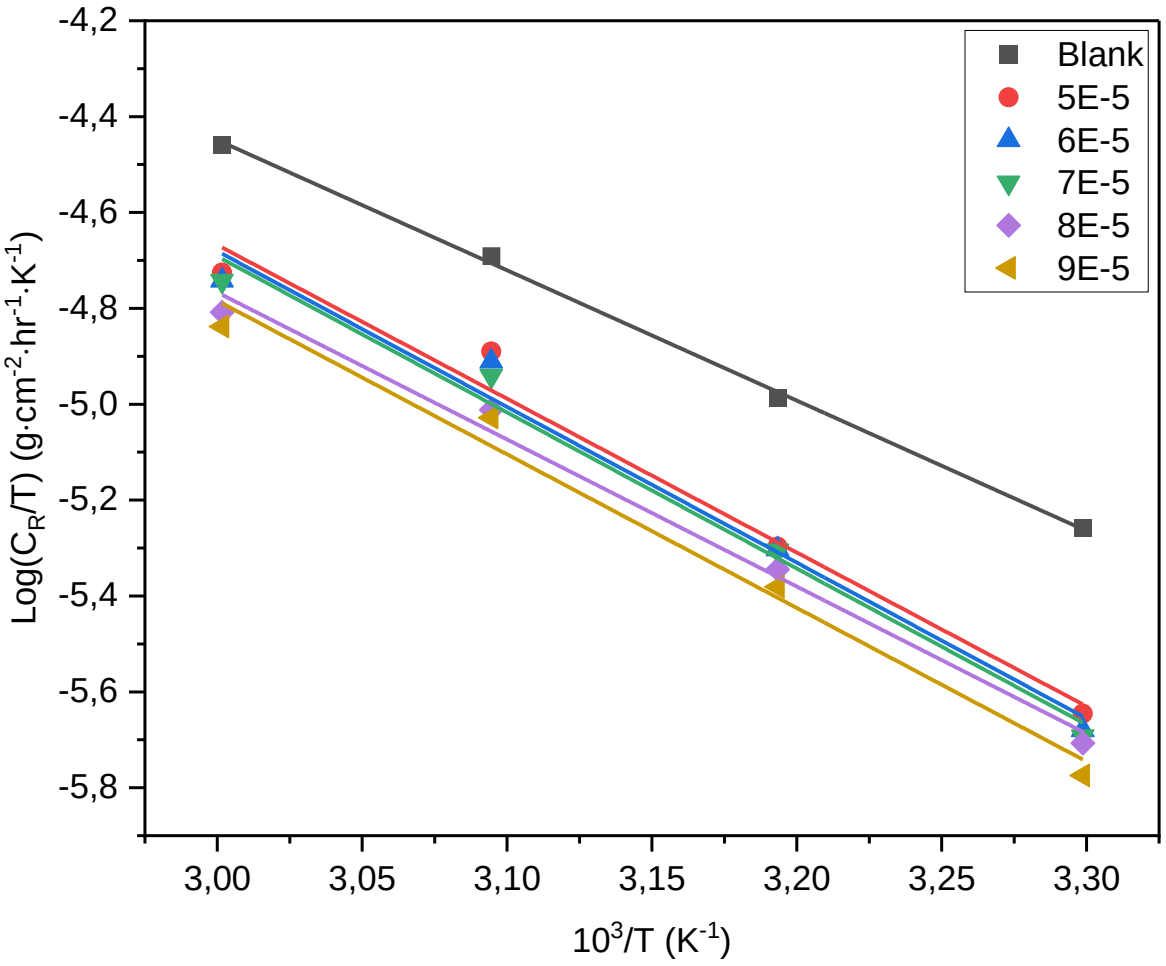

Figure 4.61: G3 Transition state plots (MS).

Table 4.4 shows that as C_{inh} increases, $\Delta S°_{act}$ also increases. This is consistent with the formation of an adsorption film on the metal surface, displacing adsorbed H_2O molecules [178].

Table 4.4 also shows that the inhibited 1 M HCl solutions all have higher E_a than the blank 1 M HCl solution. This is an indication that corrosion of the metal is suppressed in the presence of the TZDs [179]. As C_{inh} is increased, the E_a also increases, indicative of increasing θ and the formation of a protective adsorption film on the metal surface [180].

The E_a data for the alaninates shows that A2 is a stronger inhibitor than A1 and A3 (A2>A3>A1). The extra O heteroatoms in A2's molecular structure allow it to form

additional dative covalent bonds with MS, enhancing its corrosion inhibition effects. Preethi *et al.* [181] suggested that the presence of heteroatoms, specifically O and N, on their Schiff base derivative corrosion inhibitor resulted in dative covalent bonds forming with the MS surface, enhancing corrosion inhibition. The stability of the benzene ring makes A1 a weaker inhibitor than A3. The $\Delta S°_{act}$ data also shows that A2 is much more efficient at displacing H_2O molecules from the MS surface compared to A1 and A3.

Amongst the butanoates, E_a data reveals that B2 is a stronger inhibitor than B1 (B2>B1). Apart from the highest concentration (9E−5 M), all the E_a values for B2 are significantly larger than those of B1. Once again, the stability of the benzene ring most likely prevents B1 from efficiently adsorbing onto MS compared to B2. The benzene ring in B1 also makes B1 bulkier than B2, probably making it an inefficient adsorber. This is why for all concentrations other than 9E−5 M, the $\Delta S°_{act}$ data shows that B2 displaces H_2O molecules from the MS surface more efficiently than B1, enhancing its corrosion inhibition effects. Benzene rings are not always an impediment to effective corrosion inhibition, however. Assad *et al.* [182] noted that organic molecules containing a combination of both heteroatoms and benzene rings (such as the TZDs in this study) make ideal corrosion inhibitor candidates, implying that a benzene ring can sometimes enhance and not impede adsorption onto a metal surface. They go on to further state that aromatic rings are primary adsorption centres [182].

A comparison of the E_a data for the glycinates shows that G2 is a much stronger inhibitor than G1 and G3 (G2>G3>G1). Yet again, the additional O heteroatoms from the ($-NO_2$) group allow G2 to form additional dative covalent bonds with the MS surface, making it a significantly stronger inhibitor than G1 and G3. The $\Delta S°_{act}$ data also reveals the same trend (G2>G3>G1).

A comparison of the E_a data for A2 and G2 reveals that A2 is a stronger inhibitor than G2 (A2>G2). This is most likely due to the presence of a ($-CH_3$) group in the molecular structure of A2, absent in G2, allowing A2 to form additional van der Waals forces with MS. Cao *et al.* [183] noted that of the two corrosion inhibitors whose inhibition effects they investigated, the inhibitor with the longest alkyl chain consistently performed better than the inhibitor with a shorter alkyl chain. The advantage of having a larger alkyl group in the molecular structure of a corrosion inhibitor is also shown in a

comparison of the E_a data for A1, A3, B1 and B2. The following trend was observed, arranged in the order of decreasing effectiveness as a corrosion inhibitor for MS in 1 M HCl: B2>B1>A3>A1. The larger alkyl group in the butanoates allows them to form stronger van der Waals forces with MS, making them stronger corrosion inhibitors than the alaninates.

Table 4.4: TZD activation parameters (MS).

TZD/Blank	Concentration (M)	E_a (kJ·mol^{-1})	$\Delta H°_{act}$ (kJ·mol^{-1})	$\Delta S°_{act}$ (J·mol^{-1}·K^{-1})
Blank	-	54.69	54.68	−118.29
A1	5.00E−05	57.62	62.63	−100.98
	6.00E−05	57.88	62.78	−100.62
	7.00E−05	57.99	63.10	−99.25
	8.00E−05	60.61	65.52	−92.33
	9.00E−05	61.28	68.82	−82.52
A2	5.00E−05	85.88	83.24	−34.62
	6.00E−05	87.25	84.61	−31.10
	7.00E−05	88.78	86.14	−26.90
	8.00E−05	90.68	88.04	−21.44
	9.00E−05	94.76	92.12	−9.19
A3	5.00E−05	62.57	59.93	−105.06
	6.00E−05	63.69	61.05	−101.74
	7.00E−05	66.31	63.67	−94.17
	8.00E−05	67.36	64.72	−91.39
	9.00E−05	71.26	68.62	−79.73
B1	5.00E−05	68.87	68.86	−82.66
	6.00E−05	68.89	68.87	−81.79
	7.00E−05	69.54	69.53	−81.20
	8.00E−05	74.30	74.29	−65.18
	9.00E−05	101.14	101.13	17.05
B2	5.00E−05	79.83	77.19	−56.97
	6.00E−05	90.16	87.52	−27.19
	7.00E−05	91.21	88.57	−25.64
	8.00E−05	89.98	87.34	−22.72

	9.00E−05	94.34	91.70	−14.08
G1	5.00E−05	59.59	41.40	−163.20
	6.00E−05	60.08	56.69	−116.82
	7.00E−05	60.27	57.63	−114.10
	8.00E−05	60.82	58.18	−113.24
	9.00E−05	60.97	58.33	−112.62
G2	5.00E−05	82.30	84.43	−30.93
	6.00E−05	87.14	88.33	−19.23
	7.00E−05	87.06	89.25	−16.62
	8.00E−05	89.10	90.98	−15.61
	9.00E−05	91.36	90.01	−11.43
G3	5.00E−05	64.07	61.43	−112.60
	6.00E−05	64.85	62.21	−105.12
	7.00E−05	65.01	62.37	−102.65
	8.00E−05	61.39	58.75	−100.58
	9.00E−05	63.99	61.35	−100.29

4.2.2 Potentiodynamic polarization

The corrosion of MS is governed by two half-reactions: an oxidation half-reaction and a reduction half-reaction [184]. The oxidation half-reaction, which results in the dissolution of the metal, takes place at the anodic sites on the metal surface [184]. The reduction half-reaction, which results in the formation of H_2 gas in an acidic environment, occurs at the cathodic sites [185]. Therefore, the corrosion of MS is a reduction/oxidation (redox) reaction.

To further understand this redox reaction, MS coupons were subjected to PDP analysis at 303.15 K. Using an SP-150 Biologic instrument (Seyssinet-Pariset, France), the potential at the WE was varied anodically (positive going potential), producing a current response. A plot of both WE potential and logarithm of corrosion current ($\log_{icorr}$) data yielded Tafel plots (Figures 4.62 to 4.69).

All the Tafel plots shown consist of two types of curves: the cathodic curves (on the left) and the anodic curves (on the right). The two curves intersect at E_{corr}, where both half reactions occur at the same rate (no net current is generated) [186]. As C_{inh} is

increased, all Tafel plots show a downward shift due to a reduction in log_{icorr}, with the lowest log_{icorr} consistently achieved by an C_{inh} of 9E−5 M. This reduction in log_{icorr} as C_{inh} is increased is consistent with the formation of an adsorption film on the metal surface, protecting it from corrosion [187].

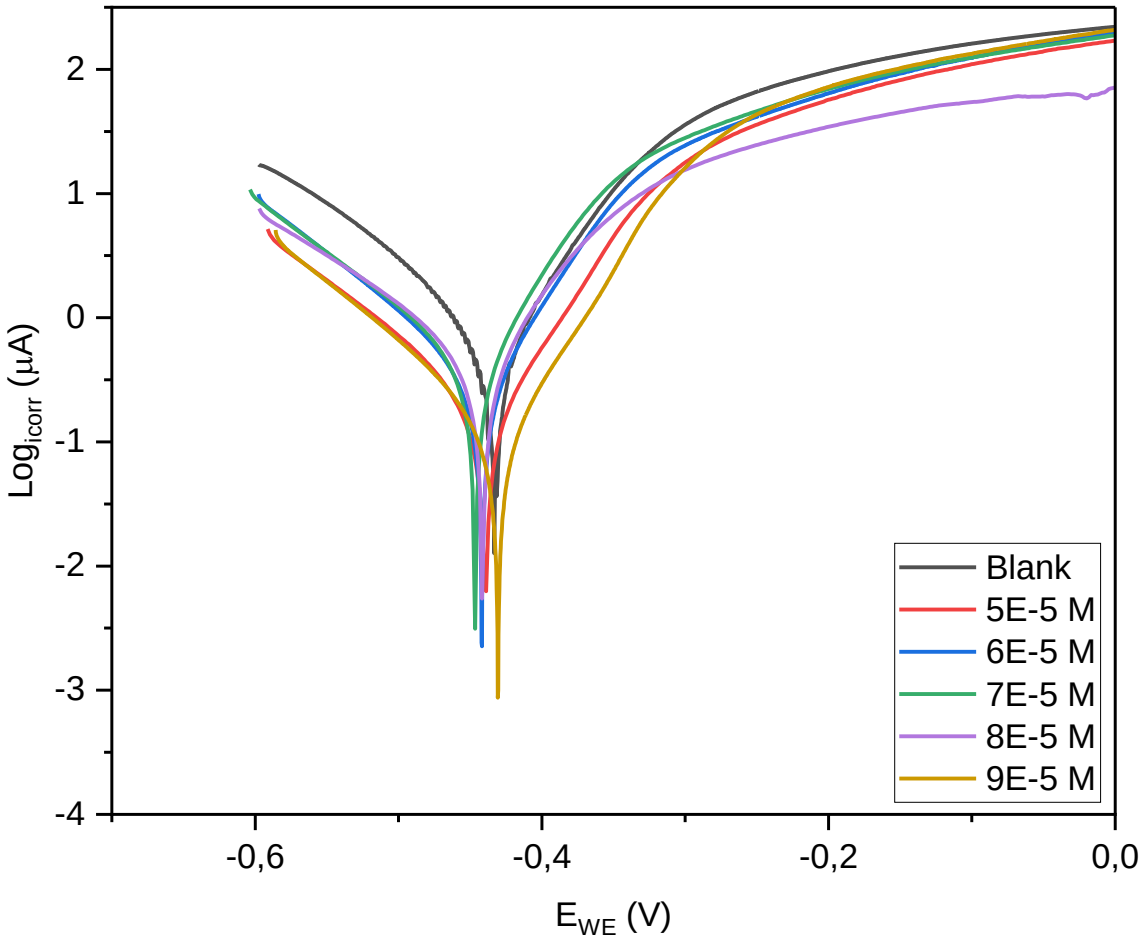

Figure 4.62: Expanded Tafel plot for A1 (MS).

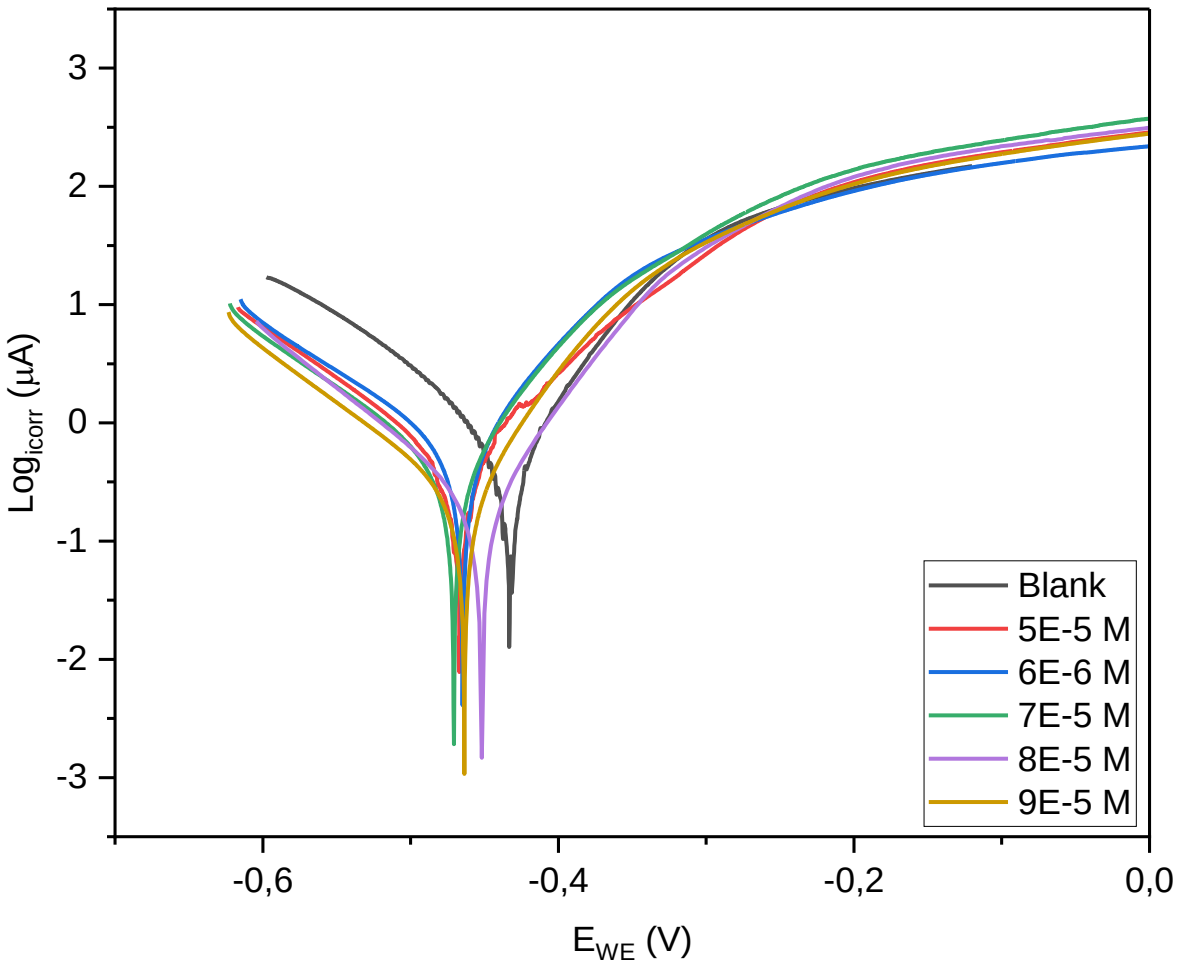

Figure 4.63: Expanded Tafel plot for A2 (MS).

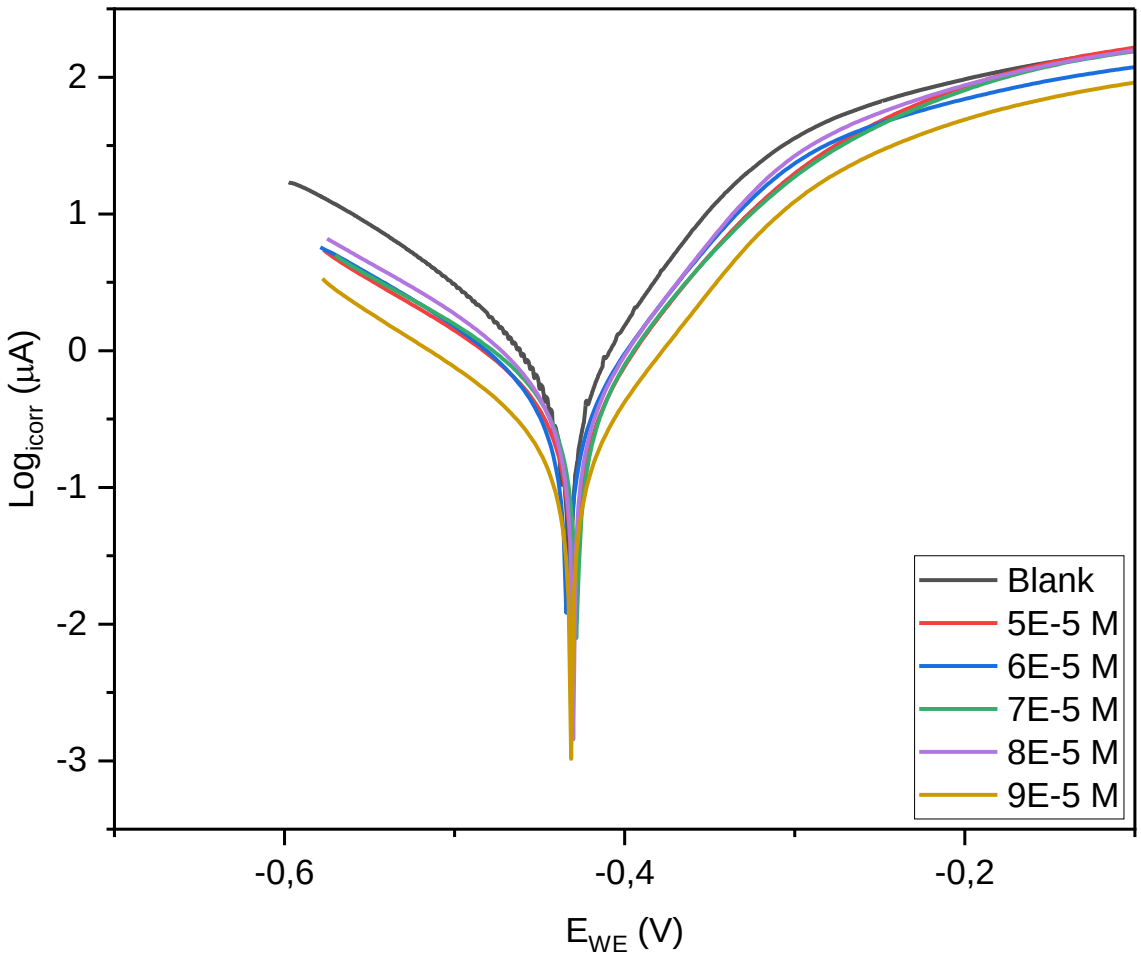

Figure 4.64: Expanded Tafel plot for A3 (MS).

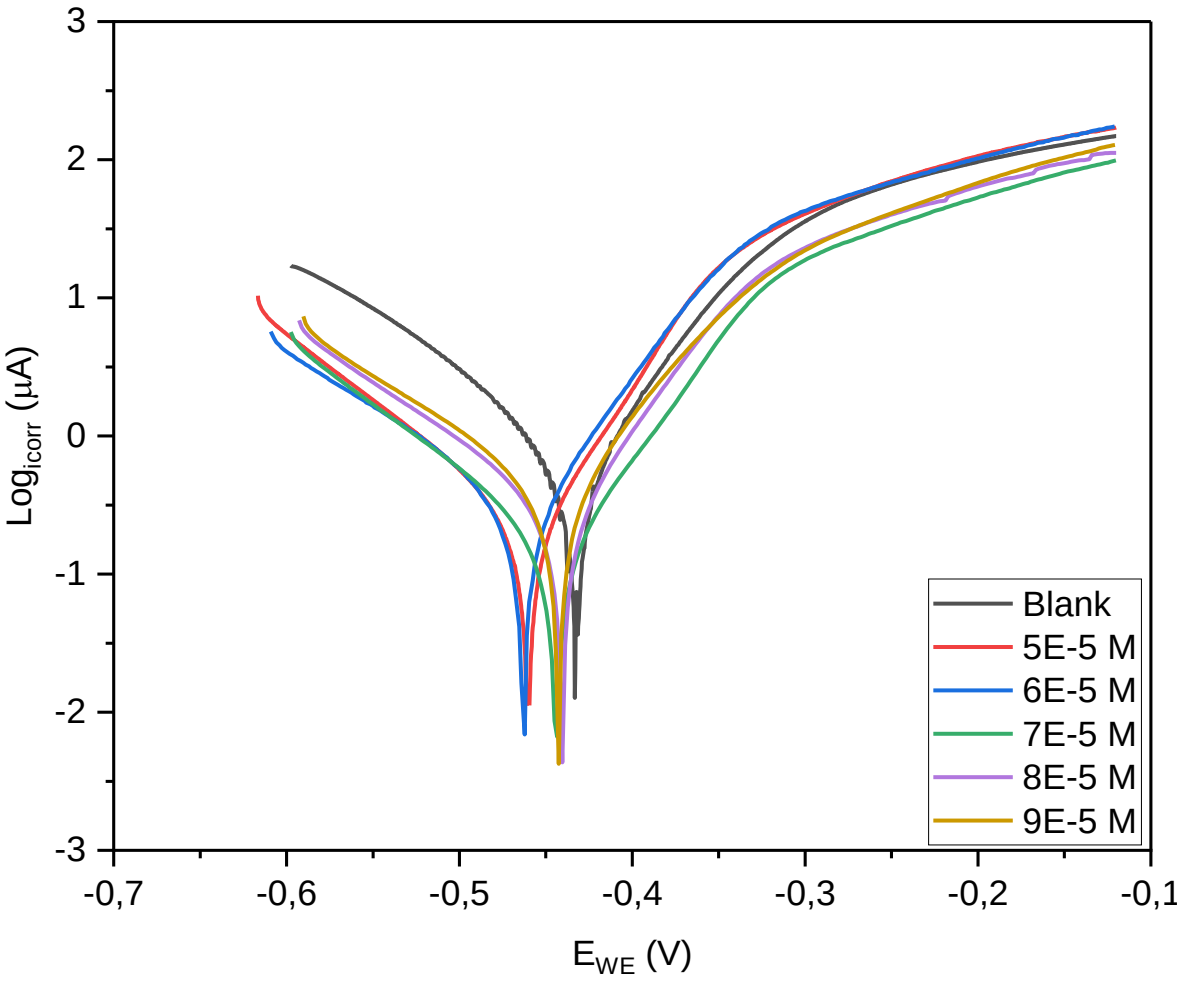

Figure 4.65: Expanded Tafel plot for B1 (MS).

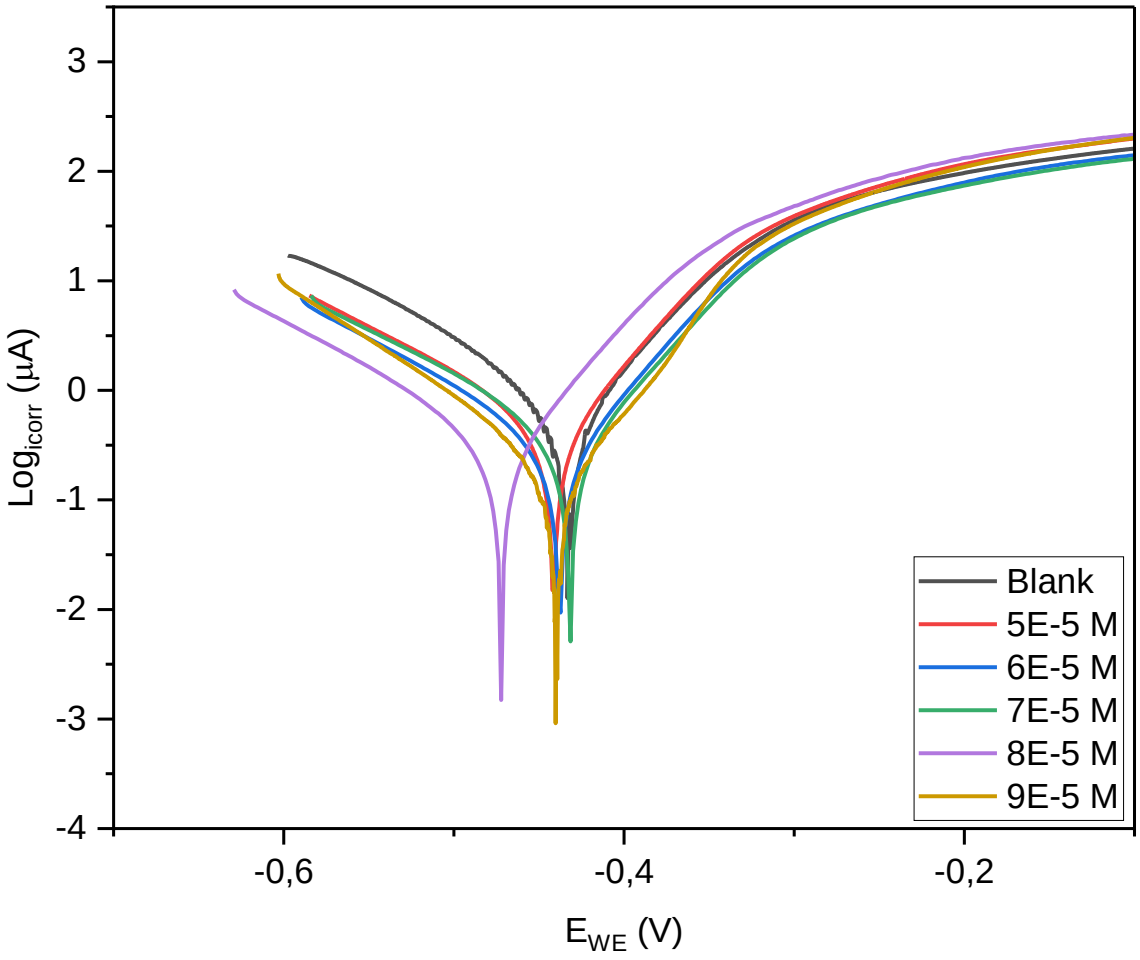

Figure 4.66: Expanded Tafel plot for B2 (MS).

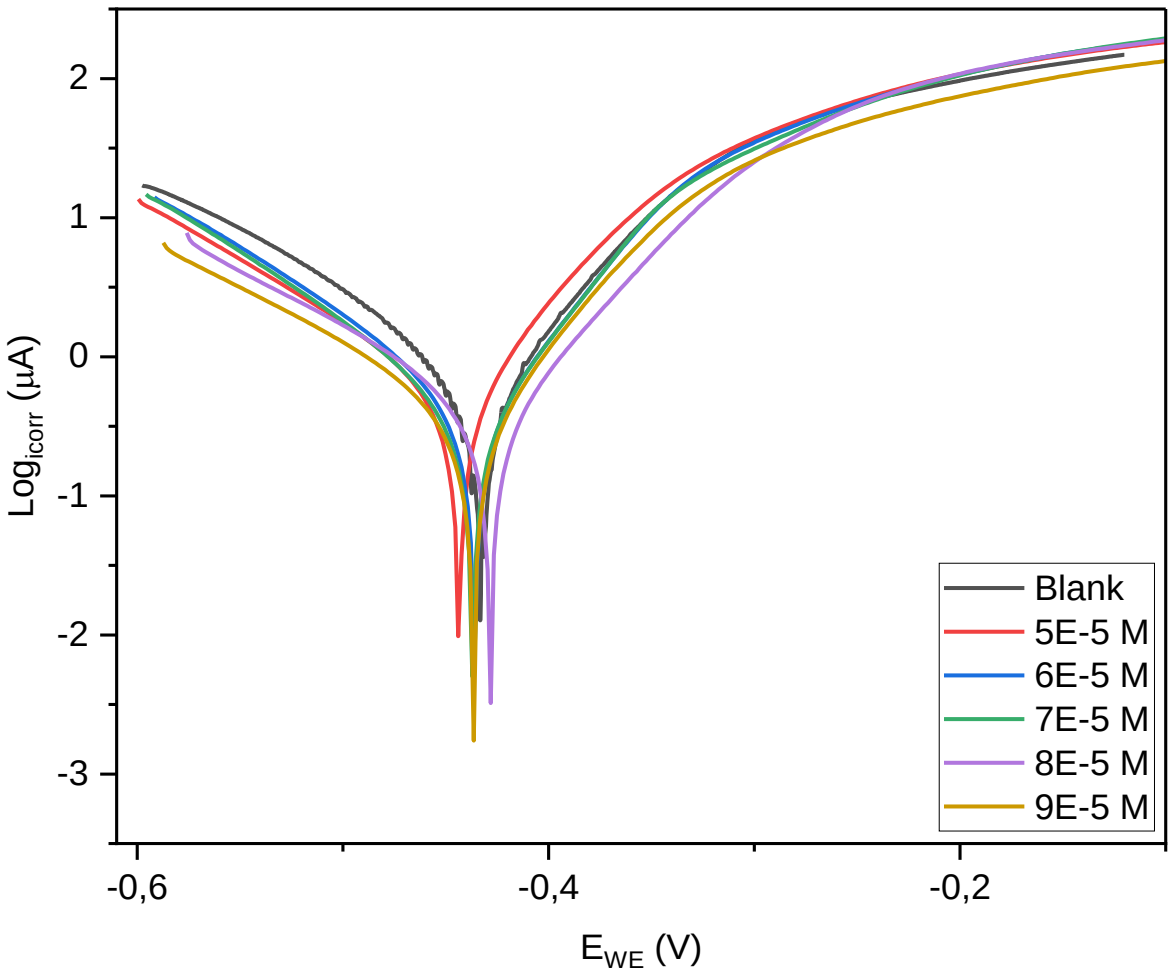

Figure 4.67: Expanded Tafel plot for G1 (MS).

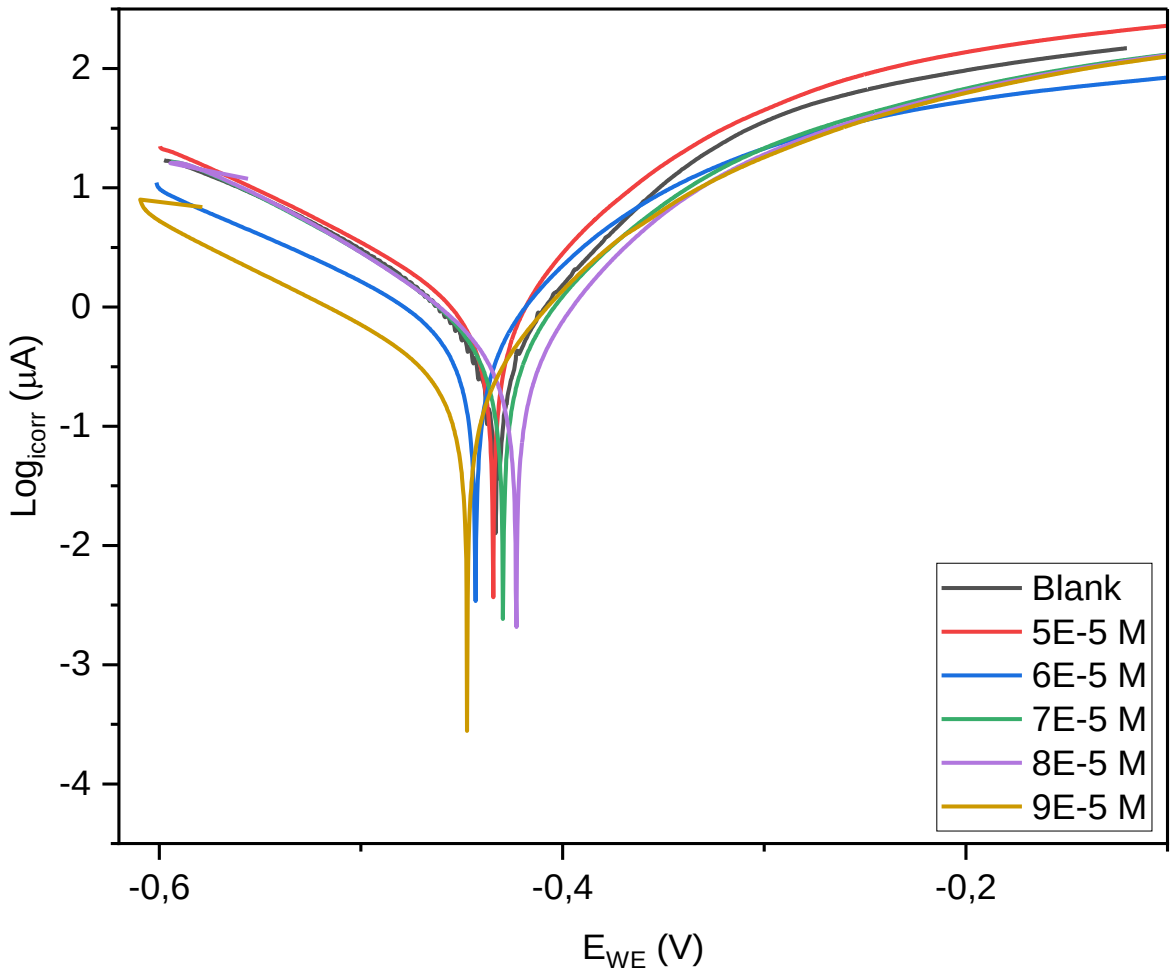

Figure 4.68: Expanded Tafel plot for G2 (MS).

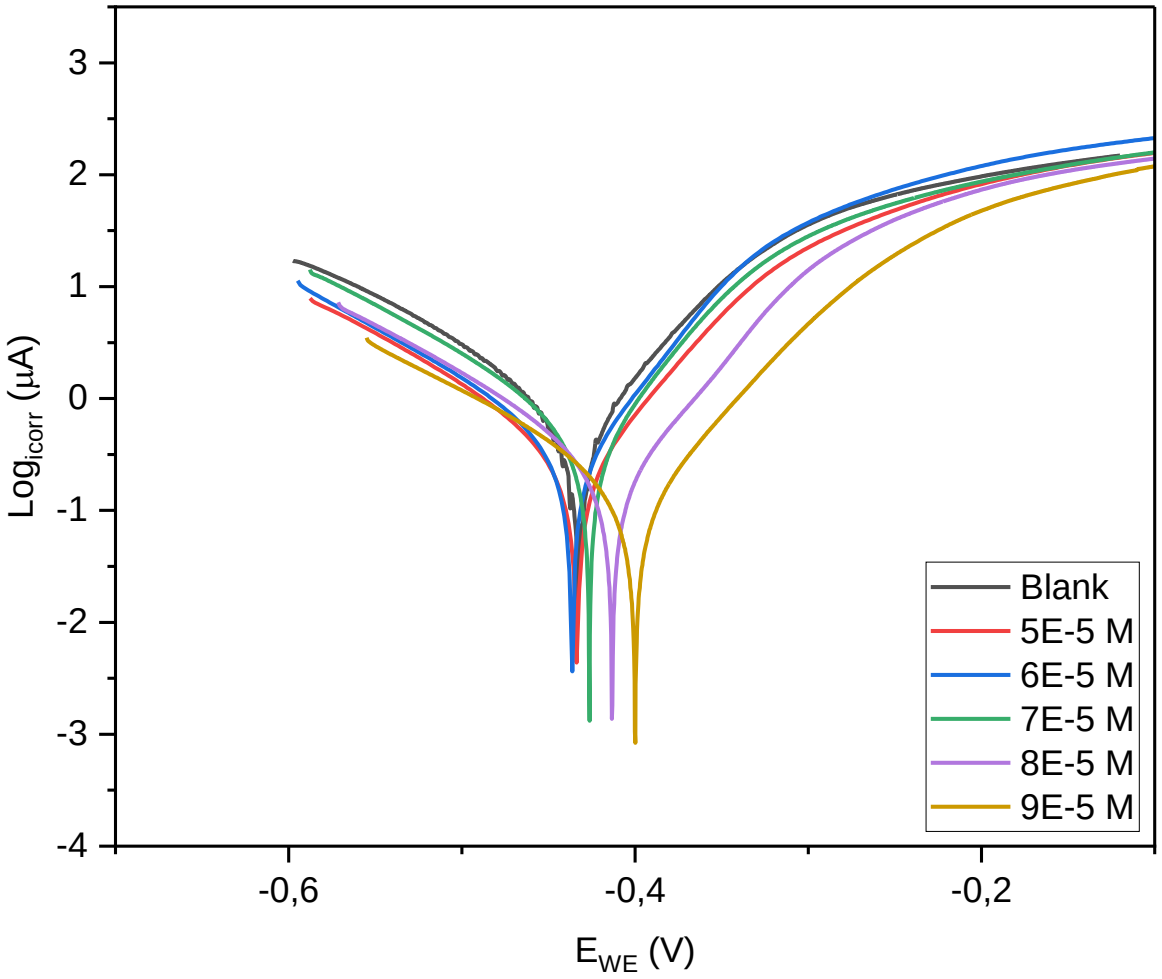

Figure 4.69: Expanded Tafel plot for G3 (MS).

The PDP parameters shown in Table 4.5 were obtained using the Tafel analysis mode in Biologic EC-Lab software. Linear regression was carried out on both the anodic and cathodic arms of the Tafel plot, enabling the calculation of E_{corr}, i_{corr}, β_a and β_c constants. The C_R was calculated after inputting the surface area of the metal, its density, and its equivalent molar weight (see Equation 20).

As C_{inh} is increased, i_{corr} and R_p decrease and increase respectively, resulting in an increase in $\%IE_{PDP}$ [188]. This is consistent with the formation of an adsorption film on the metal surface [189, 190]. The $\%IE_{PDP}$ for A2 is consistently larger than that of G2. This is because A2 has an additional methyl group (circled in blue), allowing it to form additional van der Waals interactions with the MS surface (blue arrow) (Figure 4.70).

Verma *et al.* [191] stated that generally, an increase in the alkyl/hydrocarbon chain favours corrosion inhibition. This further confirms the advantage that the additional methyl group gives A2 relative to G2 in corrosion inhibition activity. Alkyl groups, especially when they are very long, do not always play a positive role in corrosion inhibition. Wang *et al.* [192] noted that alkyl groups negatively affect the protection of a metal surface from a corrosive environment by causing steric hinderance with neighbouring alkyl groups, reducing the compactness of the adsorption film. Whilst the methyl group in A2 is not big, it is likely that A2 molecules nonetheless experience slightly more steric hinderance than G2 molecules. However, in this case, the additional alkyl group has not hindered but enhanced A2's inhibition performance through the formation of additional van der Waals forces with the MS surface.

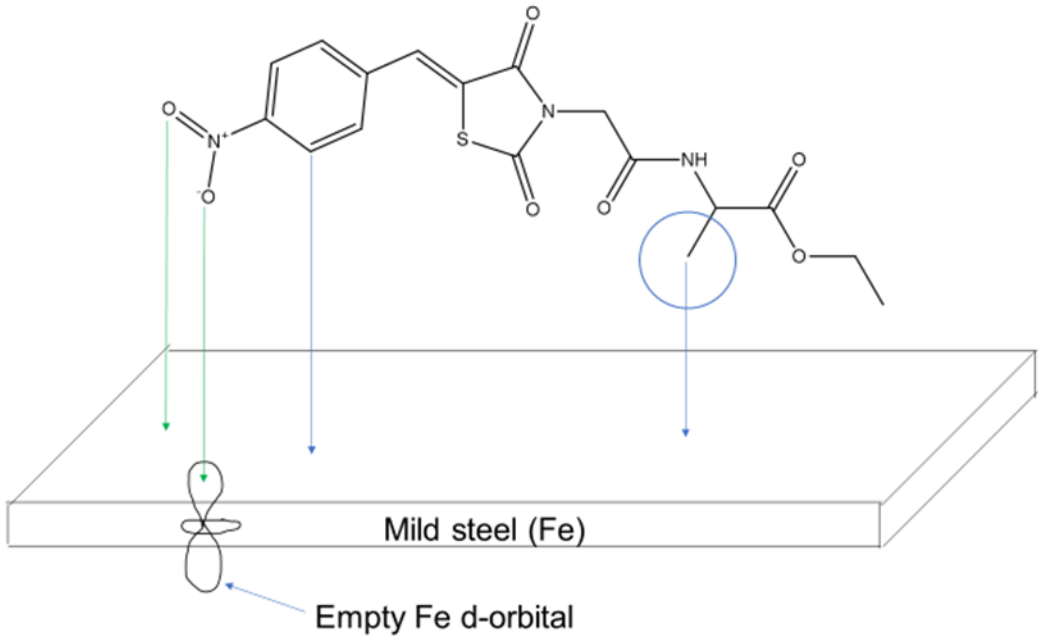

Figure 4.70: Adsorption of A2 onto MS.

Compared to G1 and G3, G2 achieves much higher %IE_{PDP} data. This is most likely due to the presence of two additional O heteroatoms in its molecular structure, enabling G2 to form additional dative covalent bonds with the MS surface (green arrows) (Figure 4.71). Liu *et al.* [193] highlighted the ability of heteroatoms, including O heteroatoms, to form dative covalent bonds with a metal surface, enhancing the inhibition effect of the corrosion inhibitor.

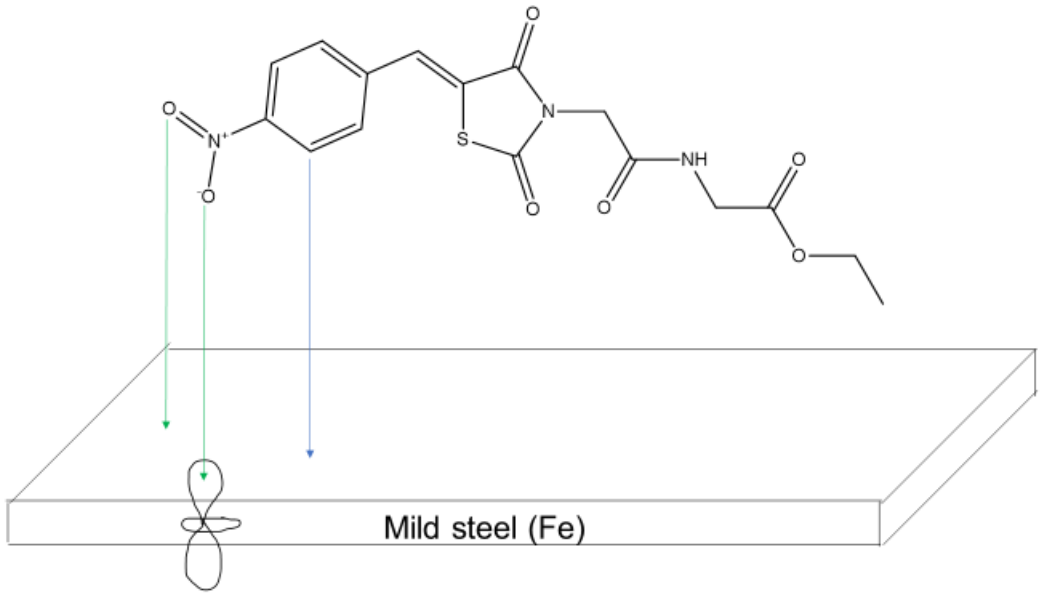

Figure 4.71: Adsorption of G2 onto MS.

Amongst the butanoates, B1 has higher %IE_{PDP} data than B2. Even though the stability of the aromatic ring makes it an unlikely participant in the formation of an adsorption film on the metal surface in terms of dative covalent bonds, it does make the B1 molecule larger in size. This allows B1 to form a much more extensive adsorption film on the MS surface, supported by additional van der Waals interactions between the benzene ring and the metal surface (blue arrow) (Figure 4.72).

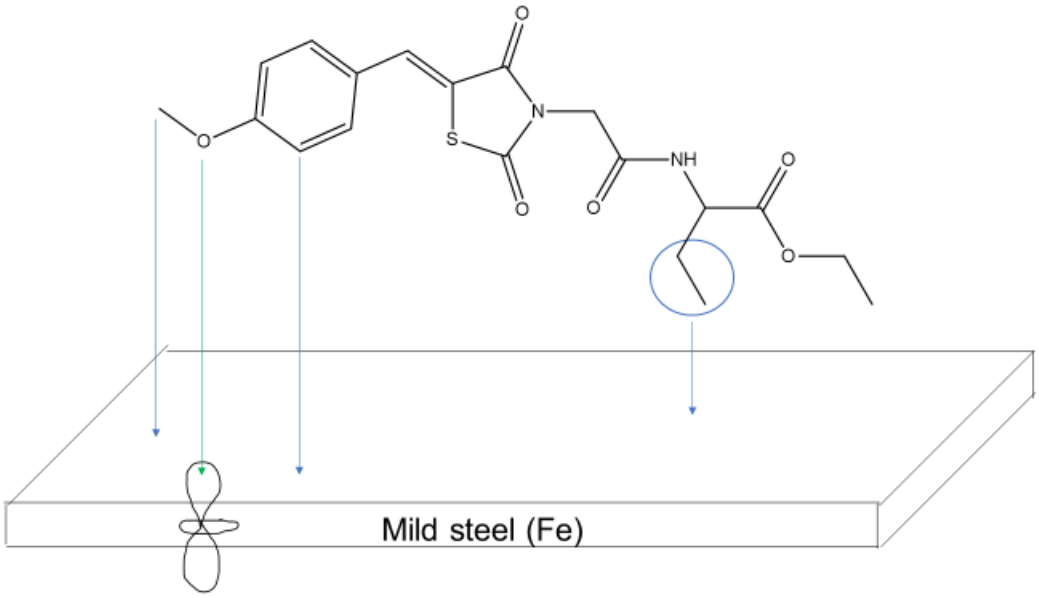

Figure 4.72: Adsorption of B1 onto MS.

The difference between E_{corr} for the uninhibited and inhibited solutions is <85mV. This is an indication that all the TZDs are mixed action inhibitors, inhibiting corrosion at both the anodic and cathodic sites on the metal surface [194]. Most of the E_{corr} values for the inhibited 1 M HCl solutions are shifted to more negative potentials relative to that of the blank 1 M HCl solution. Umasankareswari *et al.* [195] noted that, on addition of a corrosion inhibitor abbreviated CHL to a corrosive medium, the E_{corr} of MS shifted from −831mV to −818mV, a more positive potential, indicating that CHL inhibits corrosion predominantly at the anodic sites on the MS surface. The E_{corr} values shown in Table 4.4 show a negative shift from the blank 1 M HCl solution, therefore indicating a predominance of cathodic protection.

The C_R for all TZDs is less than that of the blank 1 M HCl solution (Table 4.5). In addition, as C_{inh} is increased, C_R decreases. This is consistent with the formation of an adsorption film on the MS surface [196].

Table 4.5: TZD PDP parameters (MS).

TZD/Blank	Concentration (M)	C_R (mpy)	E_{corr} (mV)	R_p (Ω)	β_a (mV·dec^{-1})	β_c (mV·dec^{-1})	i_{corr} (µA)	%IE_{PDP}
Blank	-	380	−426	180	70	127	866	-
A1	5.00E−05	206	−437	283	61	104	450	48
	6.00E−05	183	−439	392	68	111	400	54
	7.00E−05	160	−443	425	68	115	351	59
	8.00E−05	99	−441	668	71	134	218	75
	9.00E−05	62	−429	781	58	115	135	84
A2	5.00E−05	216	−465	408	64	101	473	56
	6.00E−05	151	−466	489	73	115	331	63
	7.00E−05	98	−467	641	83	116	215	72
	8.00E−05	78	−449	767	76	124	171	77
	9.00E−05	63	−463	934	59	108	137	81
A3	5.00E−05	150	−430	344	50	73	328	48
	6.00E−05	89	−432	435	67	128	194	59
	7.00E−05	69	−427	447	74	56	167	60
	8.00E−05	76	−429	835	67	116	152	78
	9.00E−05	49	−431	977	62	132	106	82
B1	5.00E−05	155	−455	379	53	94	339	61
	6.00E−05	135	−456	415	60	126	295	66
	7.00E−05	123	−439	437	59	104	270	69
	8.00E−05	88	−435	449	58	120	191	78
	9.00E−05	67	−438	690	63	123	146	83
B2	5.00E−05	224	−434	273	75	126	490	43
	6.00E−05	202	−433	369	75	127	442	49
	7.00E−05	199	−432	390	78	119	435	50
	8.00E−05	183	−446	438	60	122	400	54

	9.00E−05	158	−435	471	57	124	346	60
G1	5.00E−05	117	−449	251	45	61	295	28
	6.00E−05	112	−435	275	58	99	265	34
	7.00E−05	103	−437	293	53	78	193	38
	8.00E−05	101	−430	308	53	90	179	41
	9.00E−05	88	−434	385	52	90	174	53
G2	5.00E−05	284	−432	267	58	117	622	32
	6.00E−05	226	−439	420	76	119	495	57
	7.00E−05	178	−429	588	86	123	390	69
	8.00E−05	98	−423	593	74	136	216	70
	9.00E−05	89	−442	839	68	128	195	79
G3	5.00E−05	175	−430	316	52	76	384	43
	6.00E−05	123	−433	329	58	87	270	45
	7.00E−05	80	−420	366	63	113	175	51
	8.00E−05	66	−410	573	51	112	144	69
	9.00E−05	48	−398	732	56	111	104	75

4.2.3 Electrochemical impedance spectroscopy

Electrochemical impedance spectroscopy is a quick and accurate technique that can be used to better understand the corrosion process occurring at a metal surface. Using OriginPro graphing and analysis software, a plot of impedance data points produced the Nyquist plots shown below (Figures 4.73 to 4.80).

All the Nyquist plots shown are imperfect in shape and their presence is an indication that the corrosion of MS in 1 M HCl is a charge transfer driven process [197]. For all Nyquist plots shown, an increase in C_{inh} results in an increase in the diameter of the semi-circles, an indication that an adsorption film has been formed on the metal surface, protecting the metal from corrosion [198]. Consequently, for all Nyquist plots shown, the highest concentration (9E−5 M) consistently achieves the highest $R_{ct.}$ Therefore, of the five concentrations studied, 9E−5 M provides optimum protection for MS in 1 M HCl.

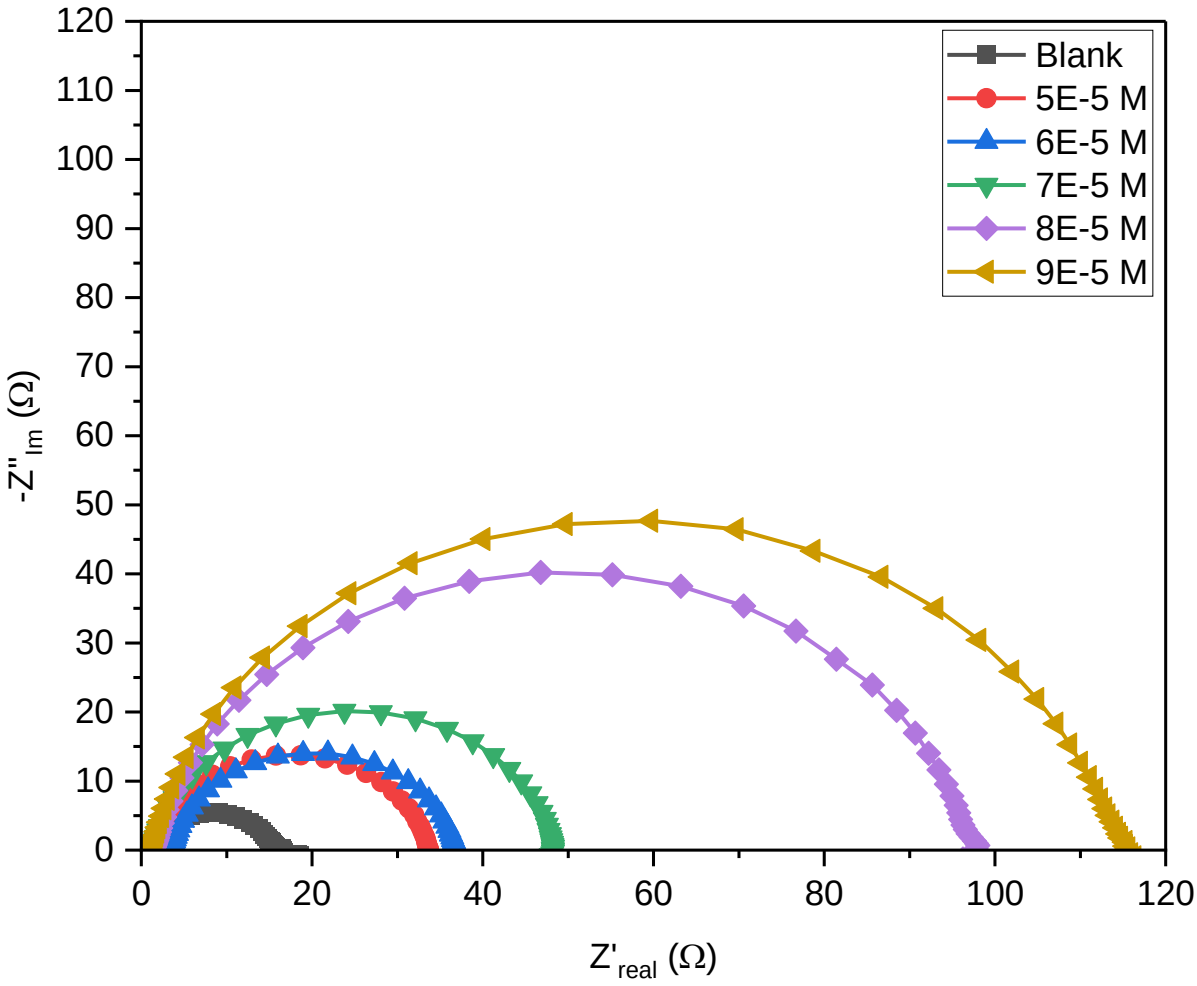

Figure 4.73: Nyquist plots for A1 (MS).

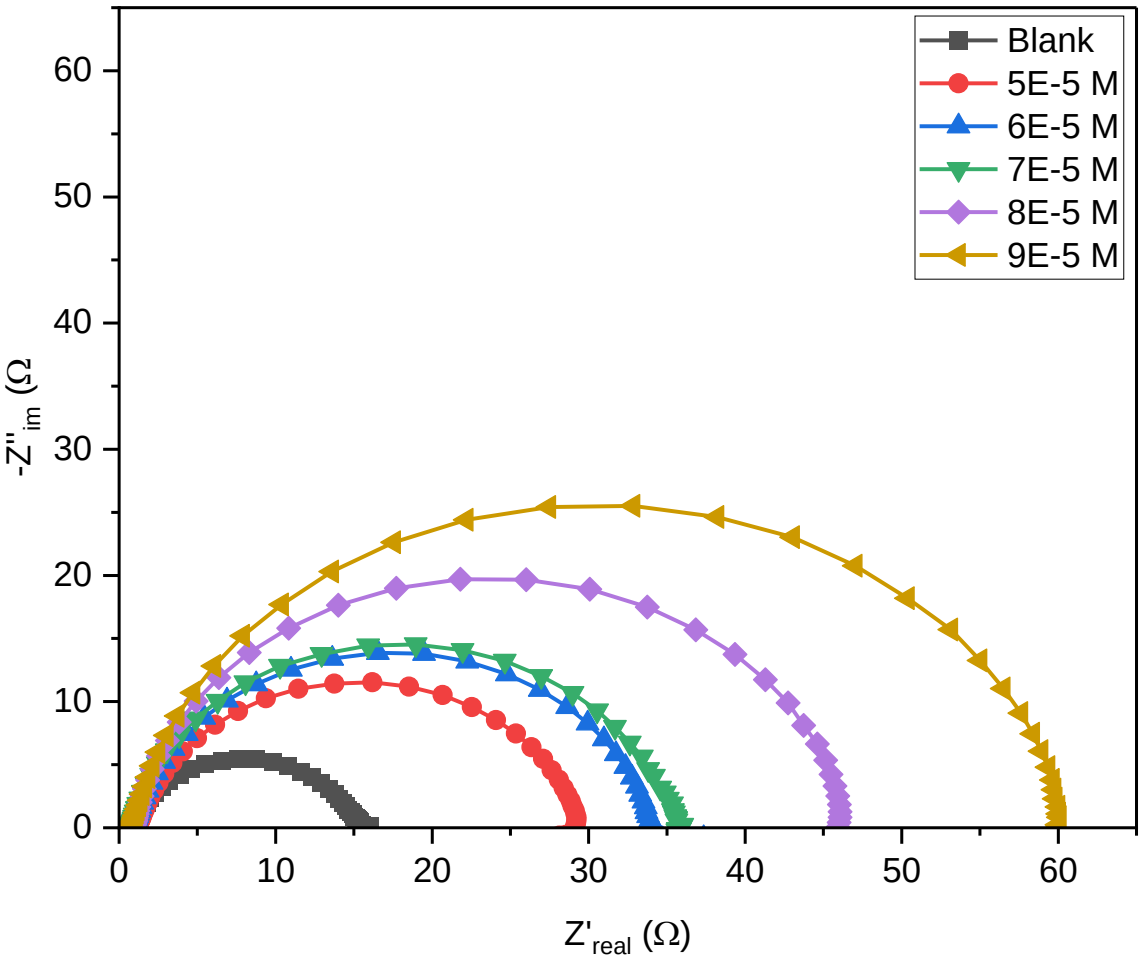

Figure 4.74: Nyquist plots for A2 (MS).

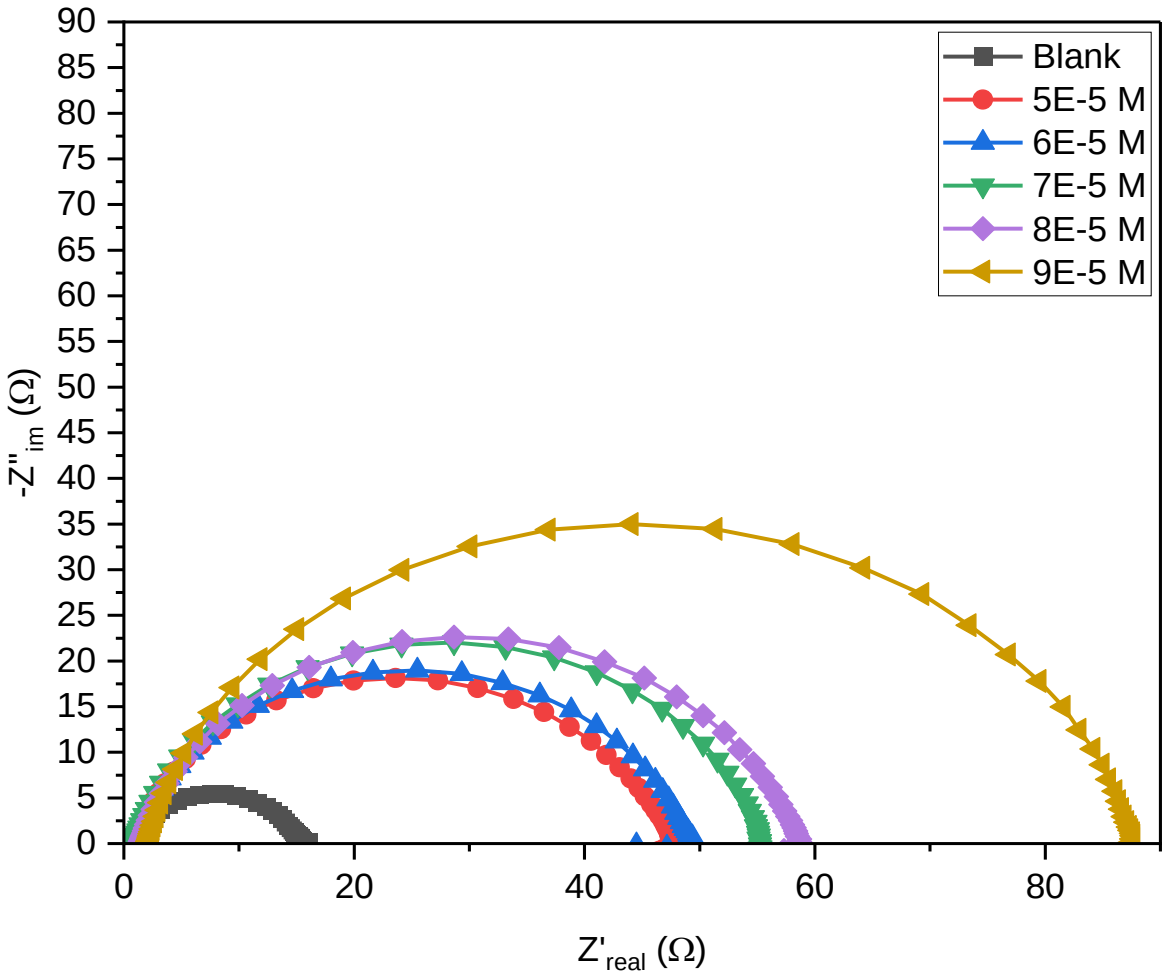

Figure 4.75: Nyquist plots for A3 (MS).

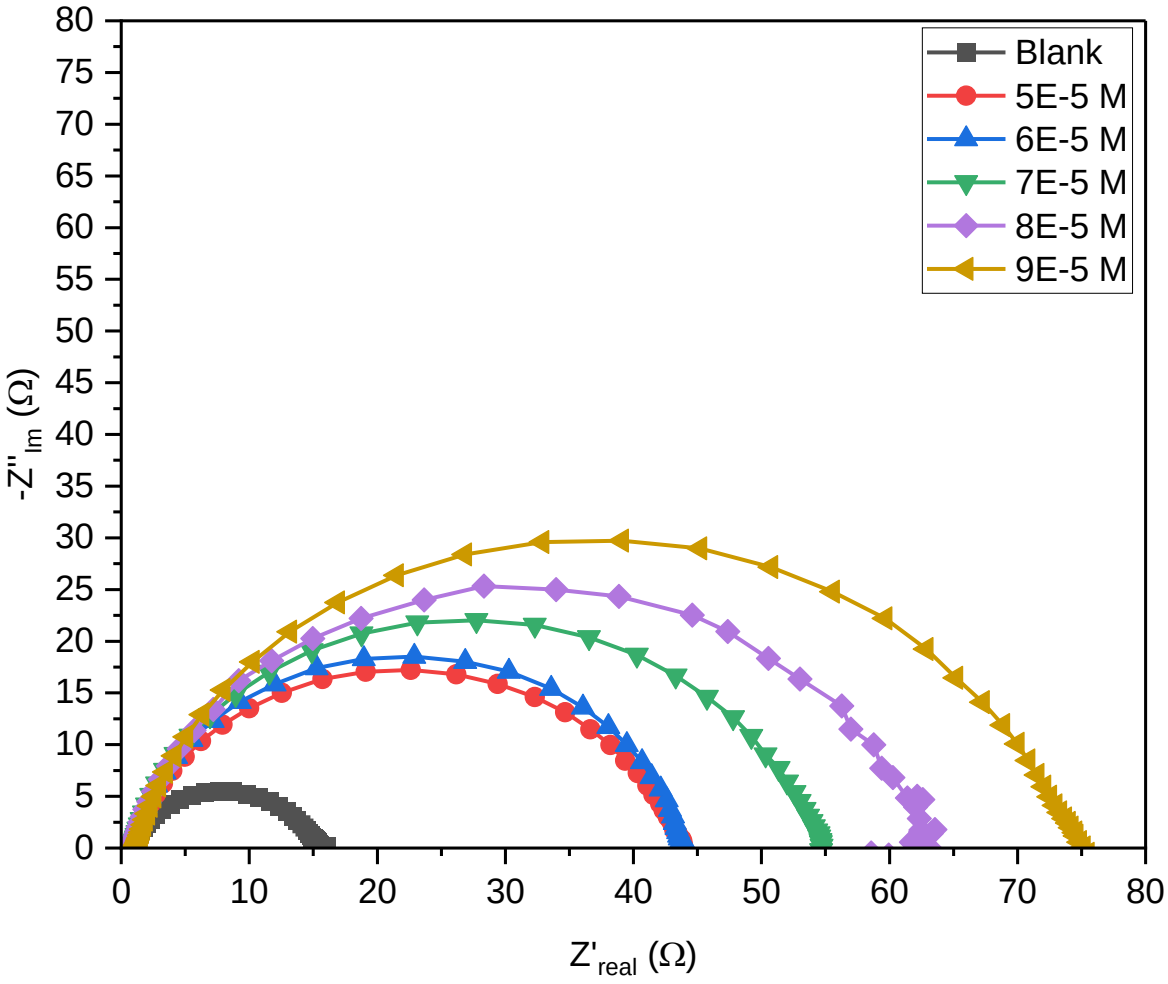

Figure 4.76: Nyquist plots for B1 (MS).

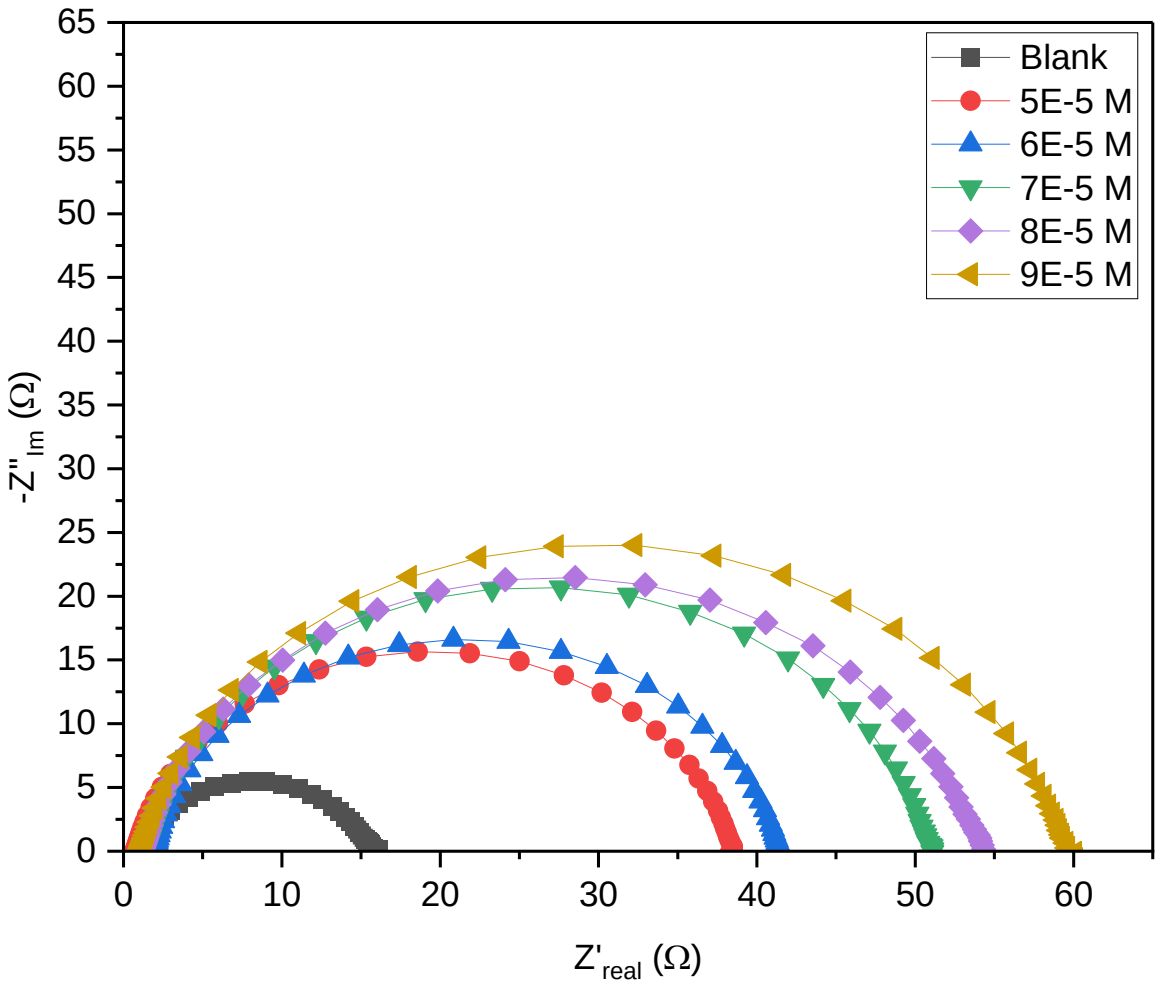

Figure 4.77: Nyquist plots for B2 (MS).

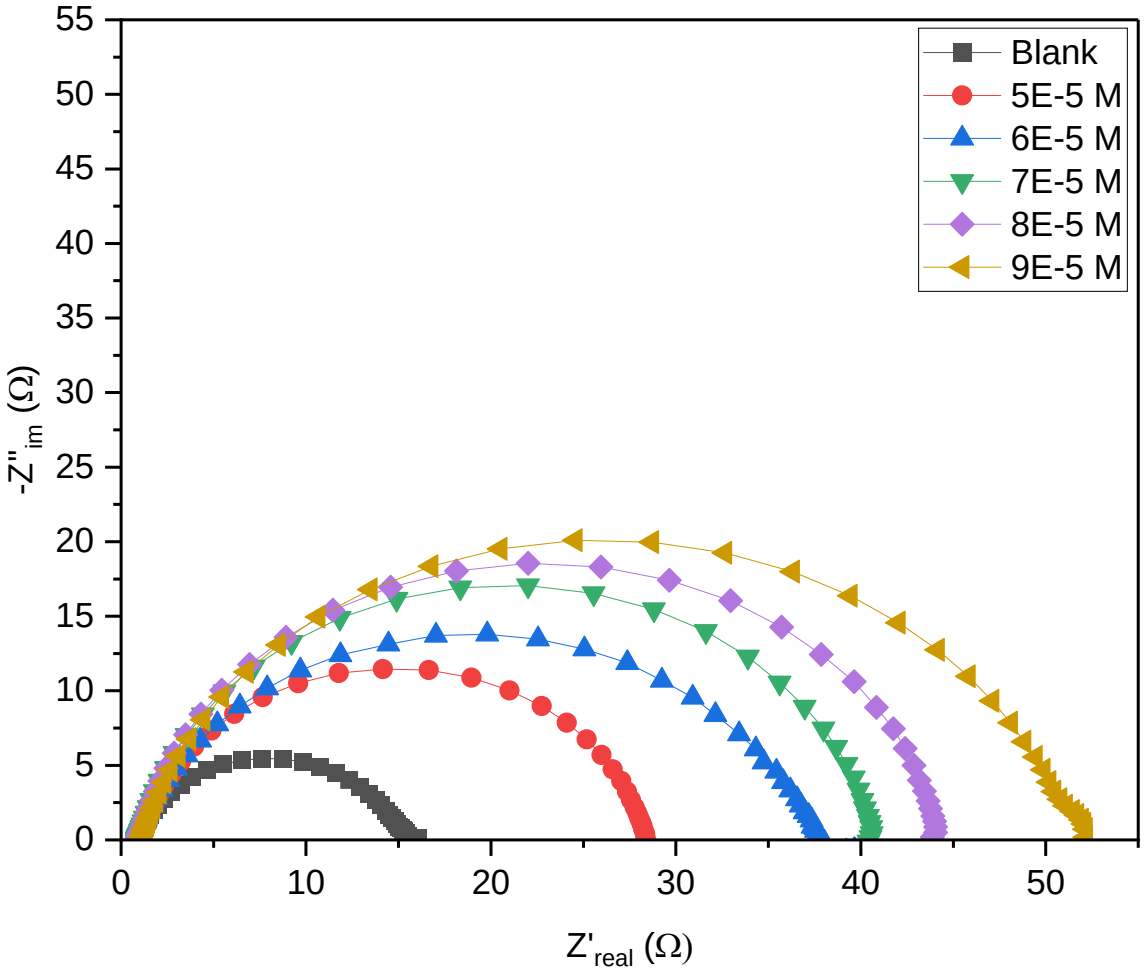

Figure 4.78: Nyquist plots for G1 (MS).

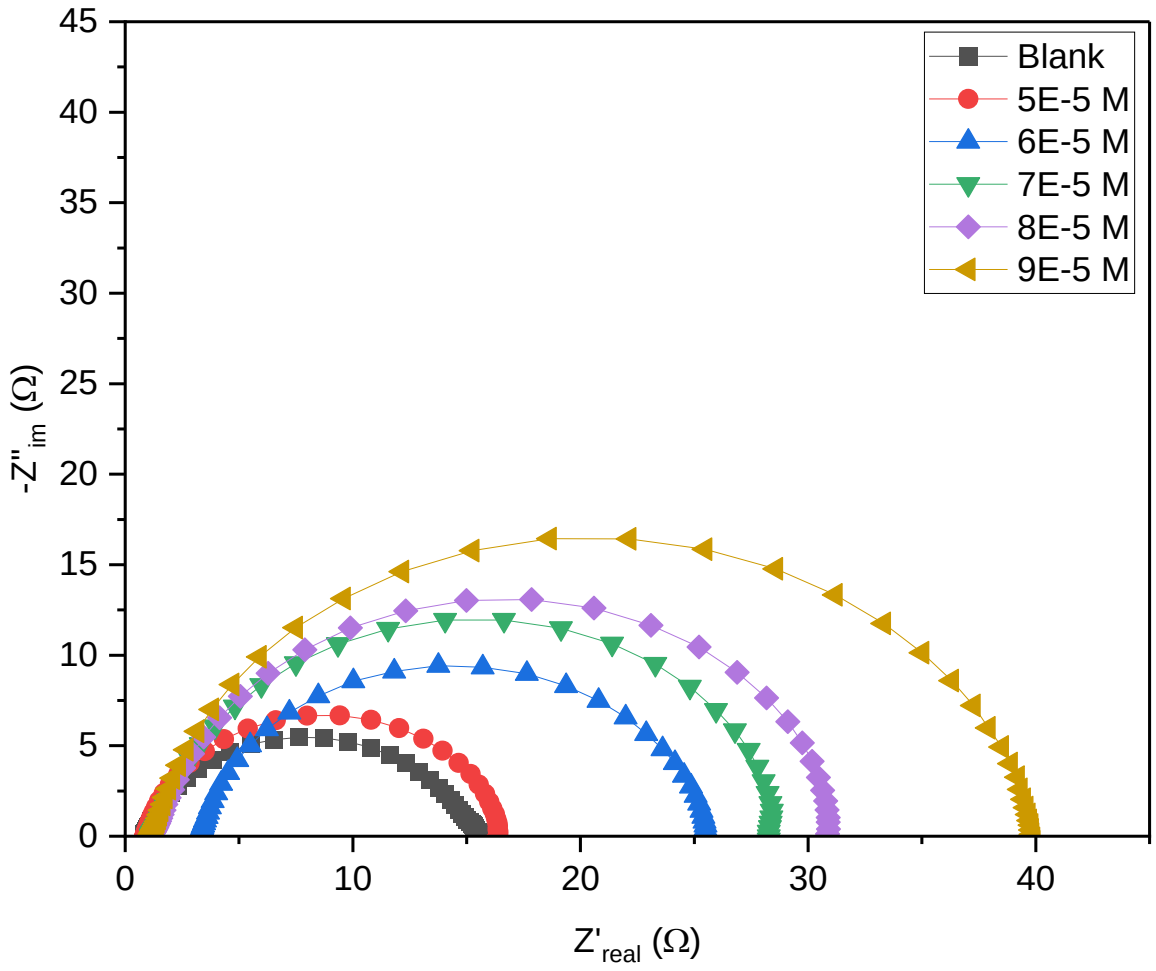

Figure 4.79: Nyquist plots for G2 (MS).

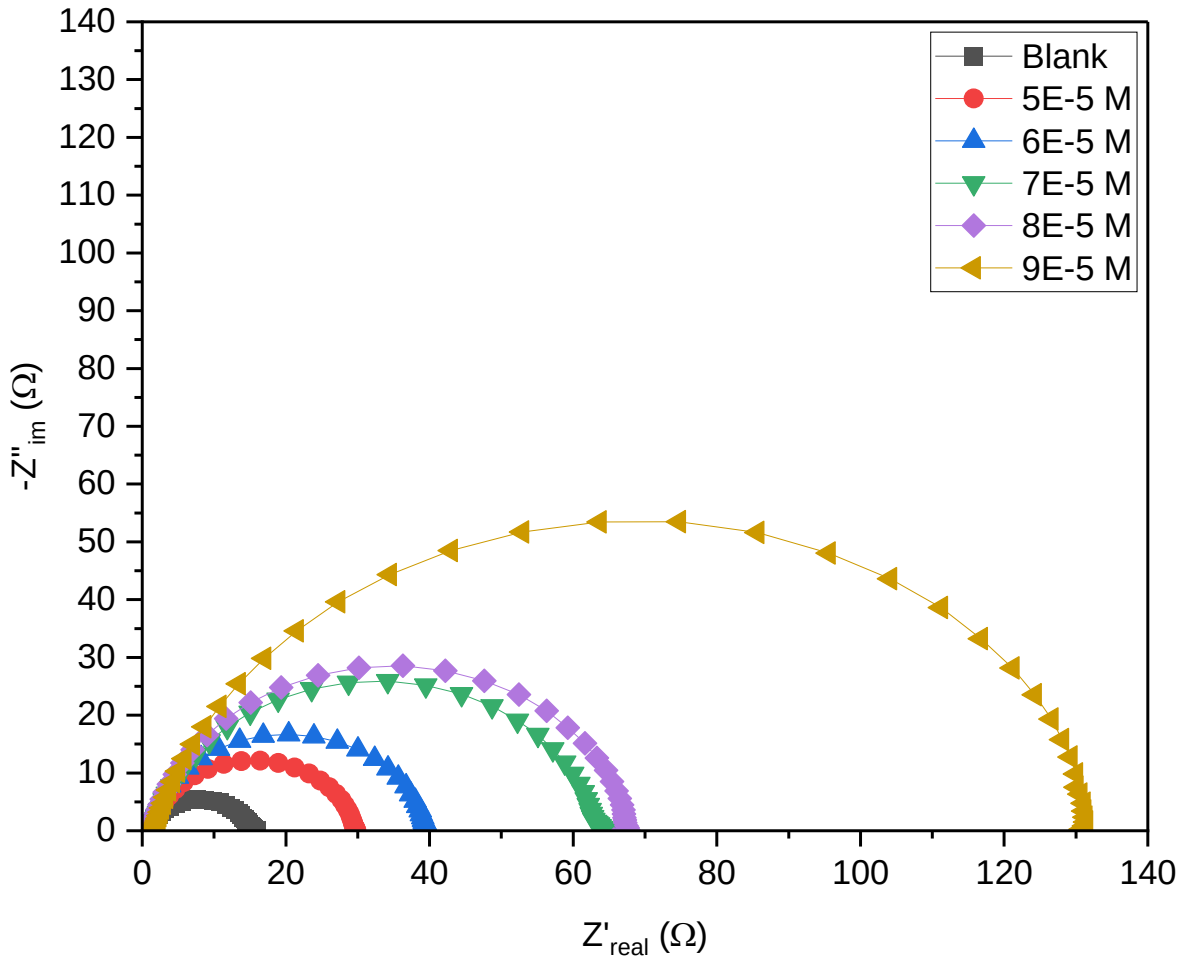

Figure 4.80: Nyquist plots for G3 (MS).

Using ZSimDemo 3.30d software, a modified Randels circuit (Figure 4.81) was fitted to the impedance data obtained, enabling the calculation of EIS parameters (Table 4.6). The Randels circuit in Figure 4.81 consists of three circuit components: R1 (R_s), R2 (R_{ct}) and Q2 (Constant phase element (CPE)) [199]. The low chi-squared (X^2) values indicate that a modified Randels circuit was a very good fit for the impedance data obtained [200]. Although Lemine *et al.* [200] have a much stricter standard for what a X^2 value should be to show good fit ($<10^{-6}$), Gangan *et al.* [201] have a much more lenient standard, stating a X^2 value around 10^{-3} shows a good fit.

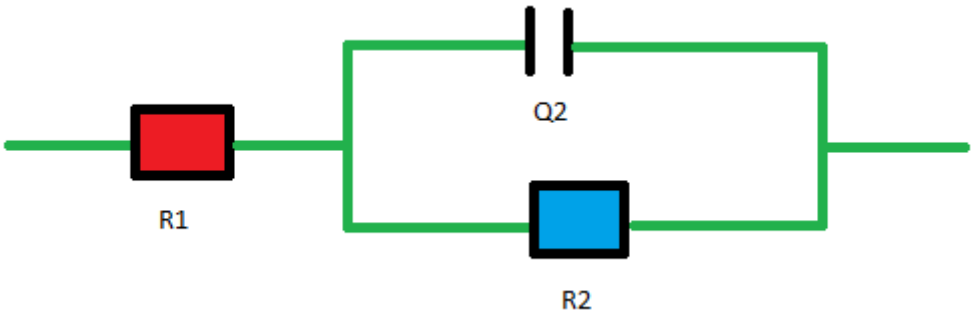

Figure 4.81: Modified Randels circuit.

As C_{inh} is increased, R_{ct} increases too (Table 4.6). This is indicative of the formation of an adsorption film on the metal surface, protecting it from corrosion [202]. The CPE takes into consideration the WE surface heterogeneity/roughness, which causes the WE to deviate from ideal capacitor behaviour [203]. Therefore, to correct for this deviation, the CPE constant (Y_0) is used to obtain a C_{dl} that considers the WE surface roughness (Equation 23). As C_{inh} is increased, C_{dl} decreases (Table 4.6). This is due to the displacement of H_2O molecules on the WE surface as TZD molecules adsorb onto it [204].

$$C_{dl} = \left(\frac{(Y_0 R_{ct})^{\frac{1}{n}}}{R_{ct}} \right) \qquad (23)$$

where n is the phase shift [205].

The phase shift is a parameter associated with WE surface roughness: the closer n is to 1, the smoother the WE surface is and therefore the greater its capacitive behaviour [206]. Therefore, the high n values shown are indicative of the pseudo-capacitive behaviour of the MS WE.

Table 4.6: TZD EIS parameters (MS).

TZD/Blank	Concentration (M)	R_{ct} (Ω)	R_s (Ω)	X^2	n	C_{dl} (µF)	%IE
Blank	-	15.27	0.73	0.0008478	0.7951	225.14	-
A1	5.00E−05	32.38	1.18	0.0008916	0.88	158.83	52.84
	6.00E−05	33.50	1.26	0.000829	0.8908	128.23	54.42
	7.00E−05	46.77	1.30	0.001104	0.8677	104.15	67.35
	8.00E−05	96.14	1.40	0.0003723	0.8826	101.15	84.12
	9.00E−05	114.54	3.47	0.001083	0.8785	93.85	86.66
A2	5.00E−05	27.75	0.8189	0.001957	0.8925	97.78	44.97
	6.00E−05	34.22	0.7393	0.001315	0.8816	95.21	55.38
	7.00E−05	34.71	0.8671	0.00827	0.8627	91.65	56.01
	8.00E−05	45.53	1.178	0.001446	0.8605	87.32	66.46
	9.00E−05	58.95	0.9251	0.001118	0.9054	87.03	74.10
A3	5.00E−05	46.13	2.146	0.0001898	0.8829	146.92	66.90
	6.00E−05	48.23	1.402	0.0004716	0.8576	133.44	68.34
	7.00E−05	54.42	0.9844	0.0007182	0.8581	102.71	71.94
	8.00E−05	56.71	0.8469	0.0008539	0.8566	100.42	73.07
	9.00E−05	85.39	0.9708	0.0006044	0.844	85.62	82.12
	5.00E−05	42.82	0.856	0.007498	0.9035	129.44	64.34
	6.00E−05	43.41	0.865	0.01525	0.8817	104.13	64.82

B1	7.00E−05	53.22	0.897	0.0009147	0.8649	101.81	71.31
	8.00E−05	61.03	0.932	0.0006241	0.8861	96.00	74.98
	9.00E−05	73.69	1.156	0.001487	0.8594	84.33	79.29
B2	5.00E−05	37.28	1.361	0.0008737	0.8712	136.32	59.04
	6.00E−05	38.80	1.191	0.0005247	0.867	130.30	60.64
	7.00E−05	49.66	1.084	0.0007696	0.8747	112.47	69.25
	8.00E−05	52.91	20.32	0.000008797	0.8848	100.83	71.14
	9.00E−05	58.43	0.7312	0.001249	0.8841	96.15	73.87
G1	5.00E−05	27.04	1.124	0.0007091	0.8602	218.17	43.53
	6.00E−05	37.07	0.8656	0.002148	0.8255	211.86	58.81
	7.00E−05	39.17	1.067	0.001574	0.8815	137.02	61.02
	8.00E−05	42.72	0.8712	0.003238	0.8762	117.69	64.26
	9.00E−05	50.54	0.8862	0.002675	0.8846	98.93	69.79
G2	5.00E−05	22.24	1.167	0.00261	0.8754	130.07	31.34
	6.00E−05	31.82	0.9871	0.00179	0.8902	108.06	52.01
	7.00E−05	33.97	0.9721	0.001156	0.8896	96.17	55.05
	8.00E−05	38.97	3.285	0.0003819	0.8935	86.27	60.82
	9.00E−05	40.06	1.104	0.001531	0.8955	78.30	61.88
G3	5.00E−05	28.56	3.595	0.2917	0.968	149.52	46.53
	6.00E−05	38.96	1.705	0.0003579	0.8578	144.96	60.81
	7.00E−05	59.72	1.187	0.0007877	0.8878	128.36	74.43

	8.00E−05	66.32	0.773	0.001059	0.8983	123.49	76.98
	9.00E−05	131.6	1.115	0.001415	0.8791	114.79	88.40

4.2.4 Adsorption film analysis

Padhi and Behera [207] described FTIR as a simple, quick, non-destructive, and affordable technique for determining the chemical composition of a sample. The ability for FTIR to analyse solids [208] makes it a useful technique for corrosion studies. For a molecule to absorb infrared radiation, it must have a net dipole moment and as such only a sample that possesses such molecules can be characterized using FTIR [209]. The FTIR spectra show that all the TZDs successfully formed adsorption films on the MS surface (Figures 4.82 to 4.89).

All the TZDs have an aliphatic secondary amine (-N-H) (green squares/green arrows) in their structures [210, 211]. In addition, all the TZDs have carbonyl functional groups (-C=O) (blue squares/blue arrows) in their structures: two in the 2,4-thiazolidinedione scaffold and two more in the aliphatic chain attached to the N heteroatom on the 2,4-thiazolidinedione moiety. Both (-N-H) and (-C=O) peaks are absent in the adsorption film spectra, an indication that they take part in the formation of an adsorption film on the MS surface [212].

All TZDs have (-C-H) alkyl/aromatic peaks (yellow squares/yellow arrows) in their spectra [213, 214]. These peaks differ in intensity, however. The two butanoates (Figures 4.85 and 4.86) have the most intense (-C-H) alkyl stretches as they have two ethyl groups in their structures. In addition, B1 (Figure 4.85) has an additional (-C-H) aromatic stretch due to the ($-OCH_3$) group attached to the benzene ring. Therefore, B1 has a much more intense (-C-H) alkyl/aromatic peak relative to B2. The glycinates have the least intense (-C-H) alkyl/aromatic peaks because they only have one alkyl group in their aliphatic chains. These alkyl/aromatic peaks also disappear in the adsorption film spectra, an indication that the (-C-H) groups play a role in the formation of an adsorption film, undoubtedly through physisorption [215, 216]. The TZDs containing a ($-NO_2$) group (A2 (Figure 4.83) and G2 (Figure 4.88)) show two distinct peaks related to the ($-NO_2$) functional group, indicated by the purple arrows: asymmetric stretch (1500-1650 cm^{-1}) and a symmetric stretch (1260-1400 cm^{-1}) [217].

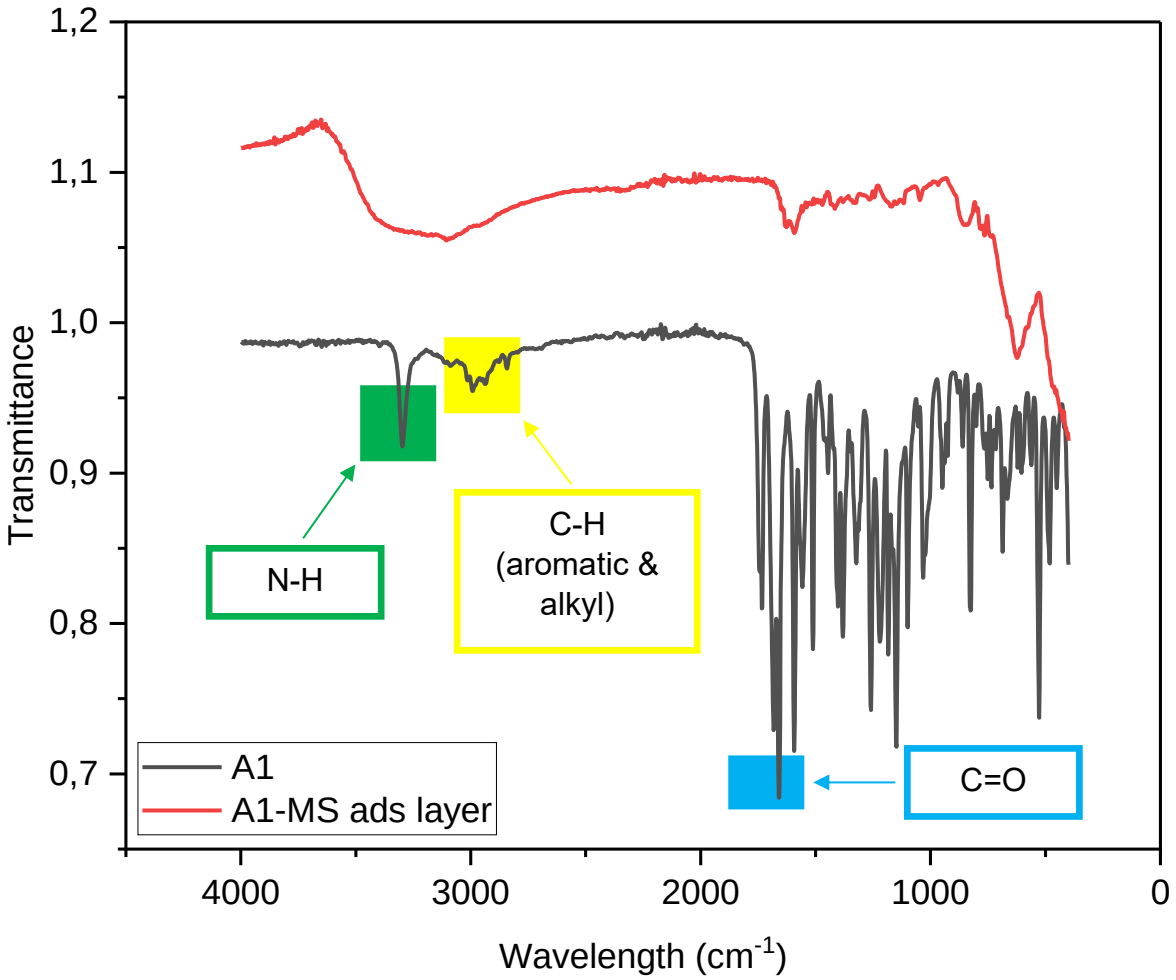

Figure 4.82: A1 FTIR plots (MS).

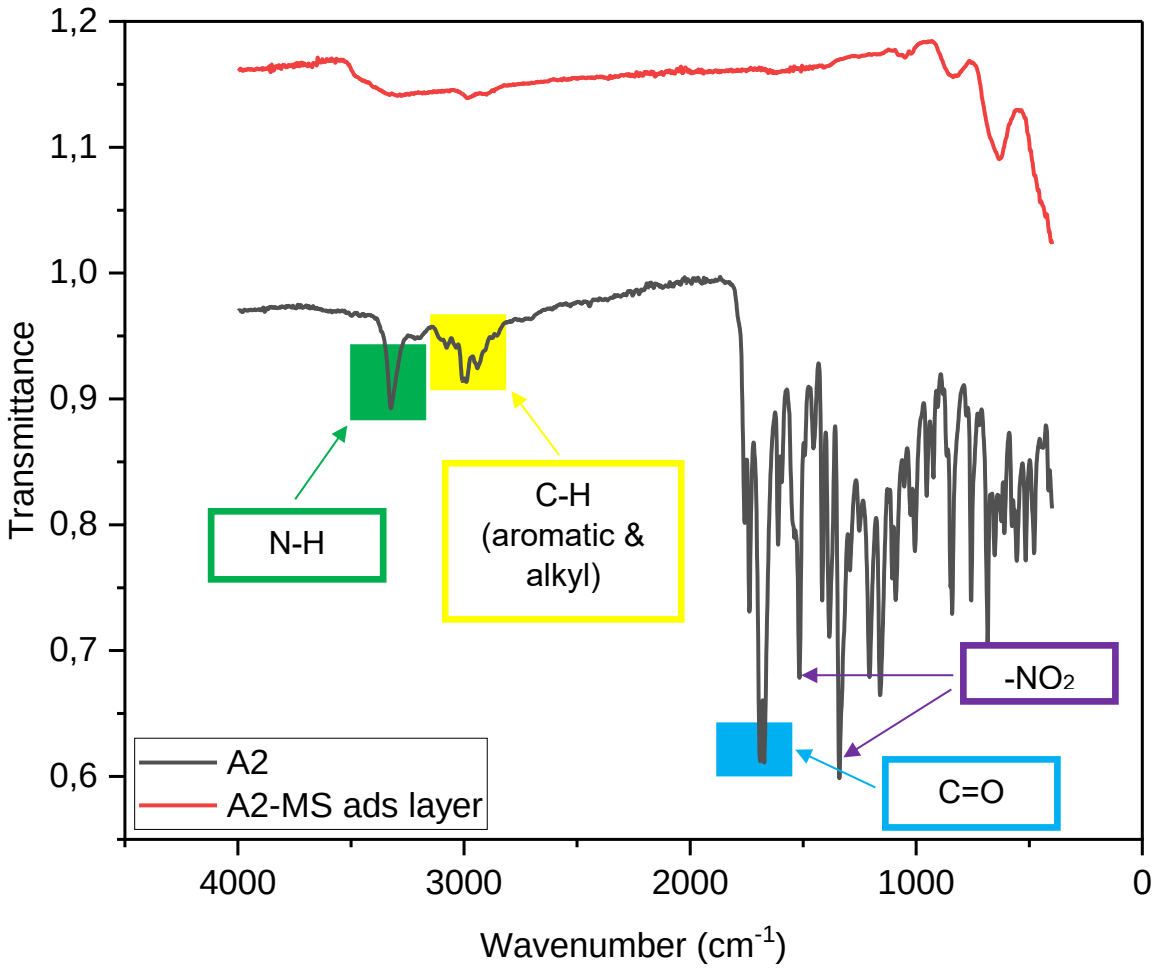

Figure 4.83: A2 FTIR plots (MS).

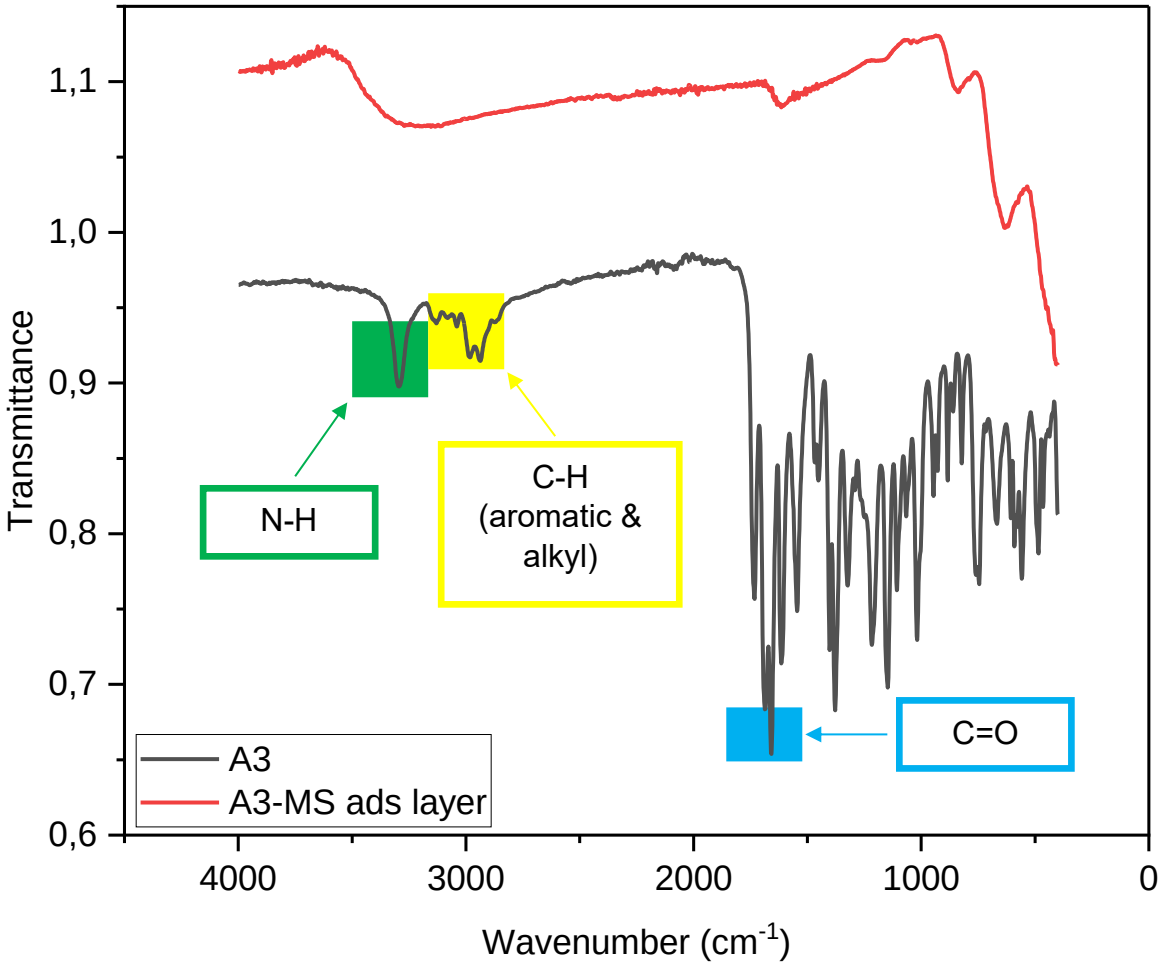

Figure 4.84: A3 FTIR plots (MS).

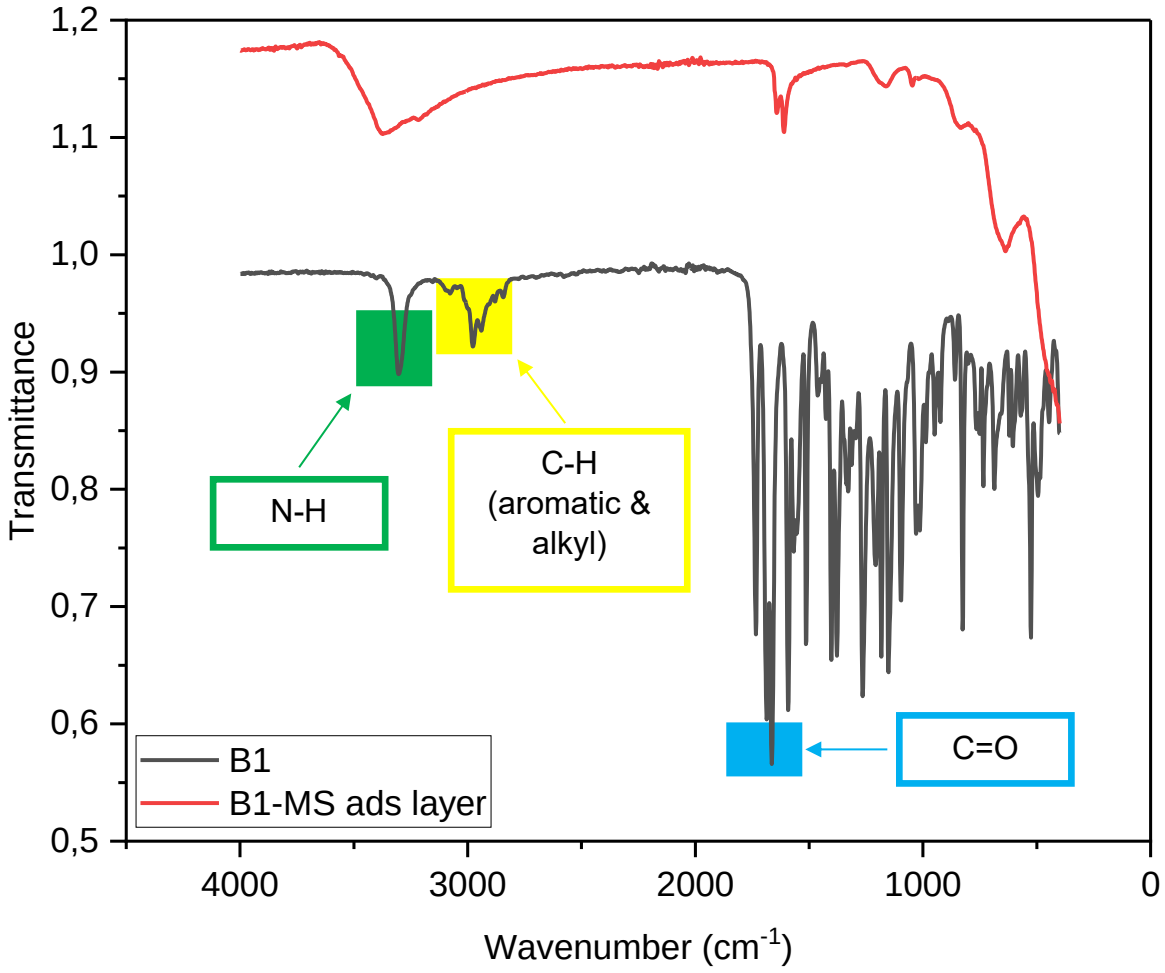

Figure 4.85: B1 FTIR plots (MS).

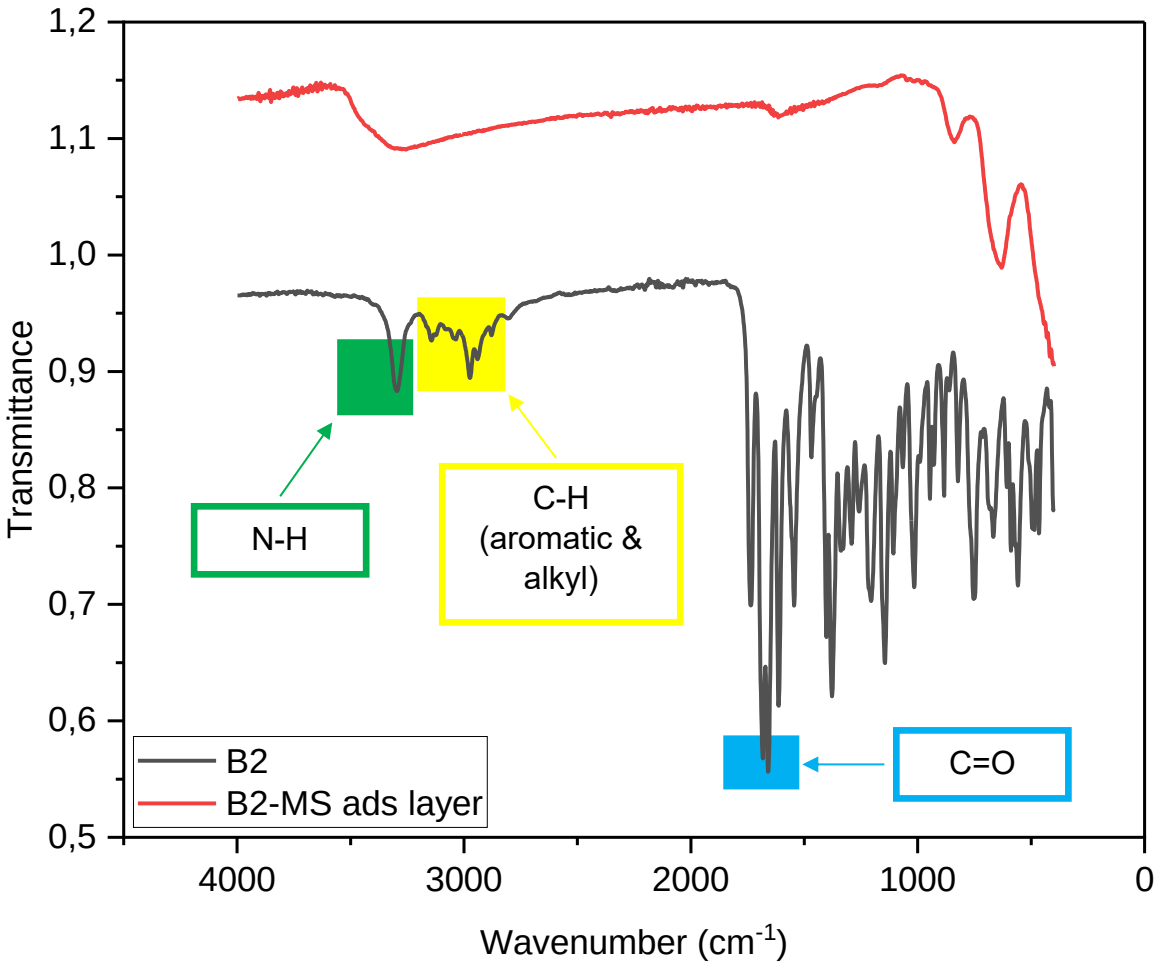

Figure 4.86: B2 FTIR plots (MS).

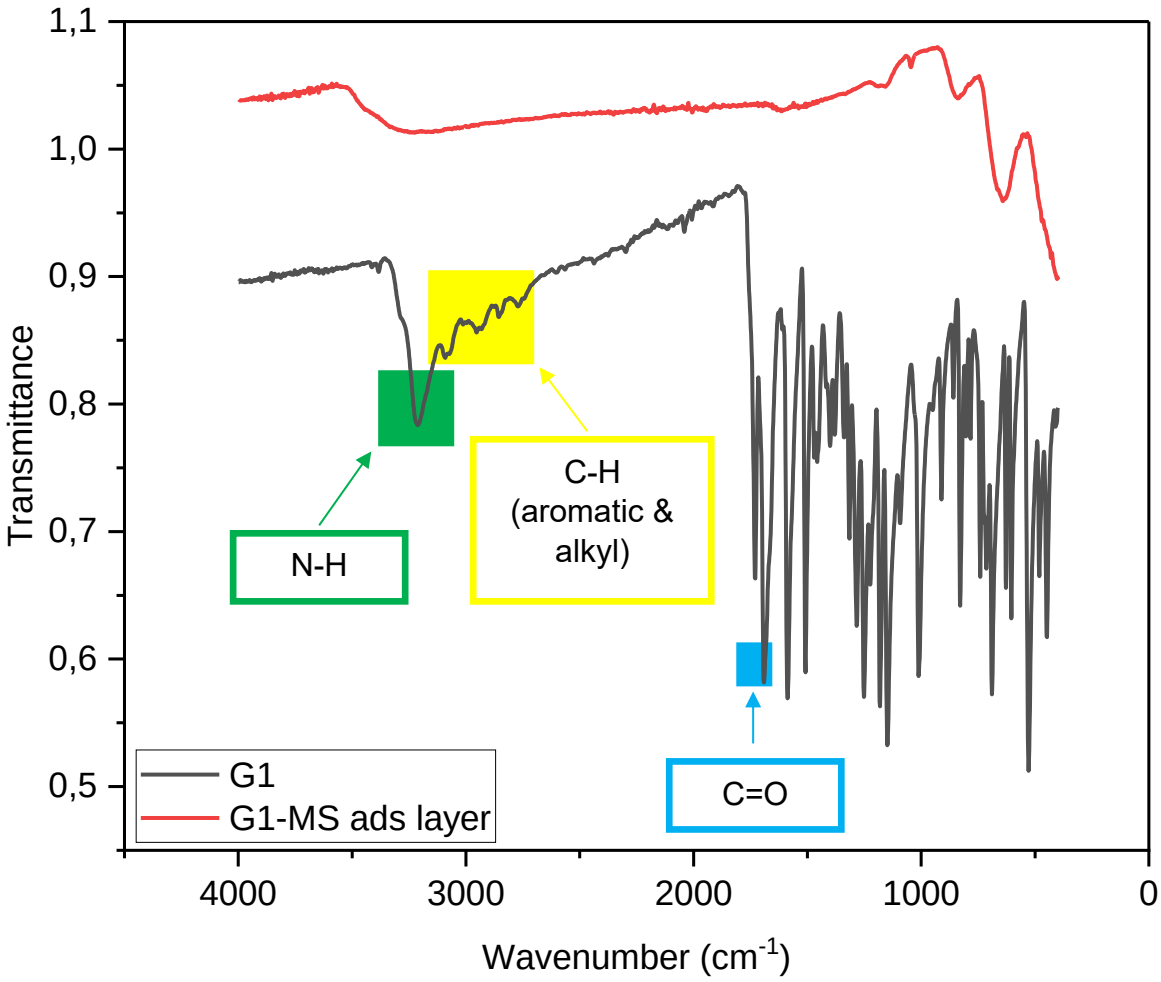

Figure 4.87: G1 FTIR plots (MS).

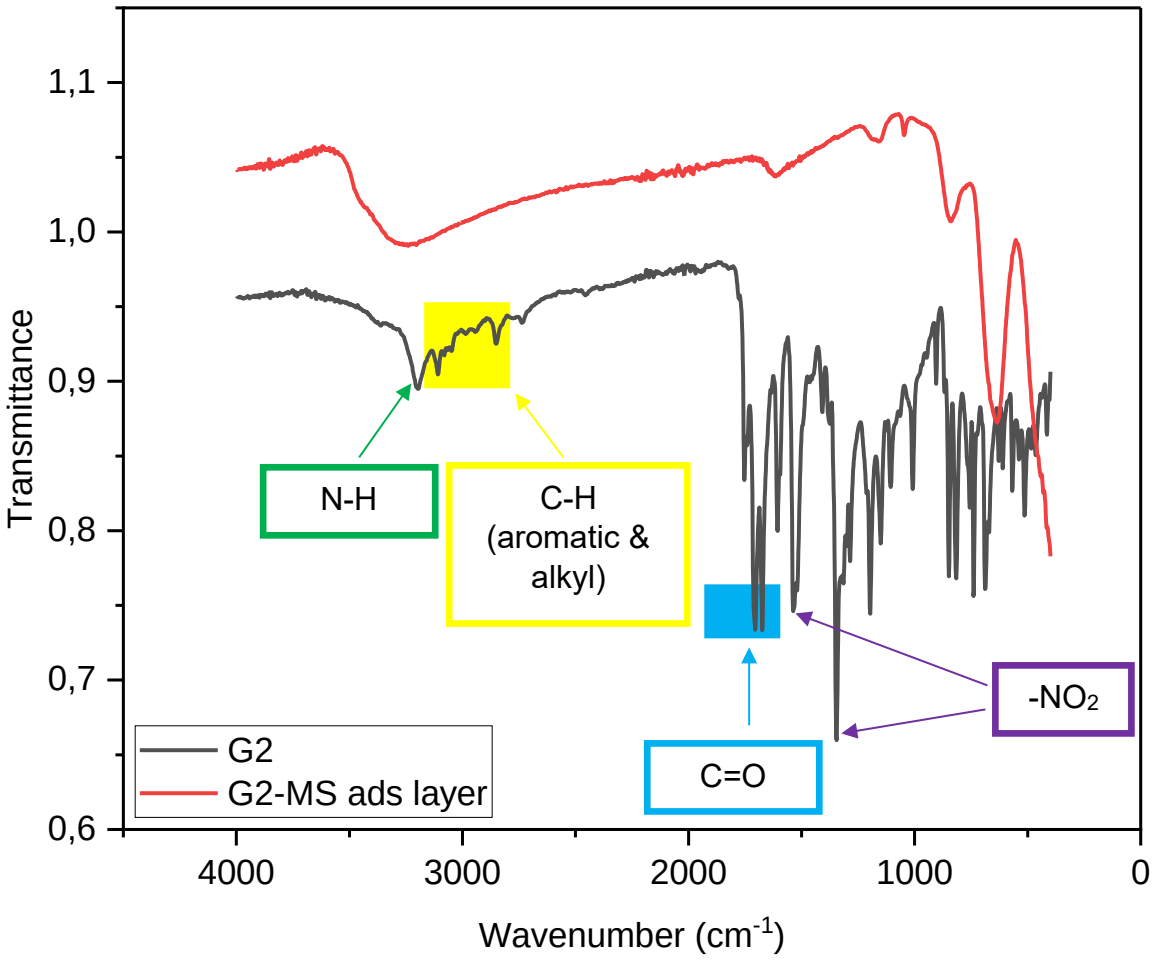

Figure 4.88: G2 FTIR plots (MS).

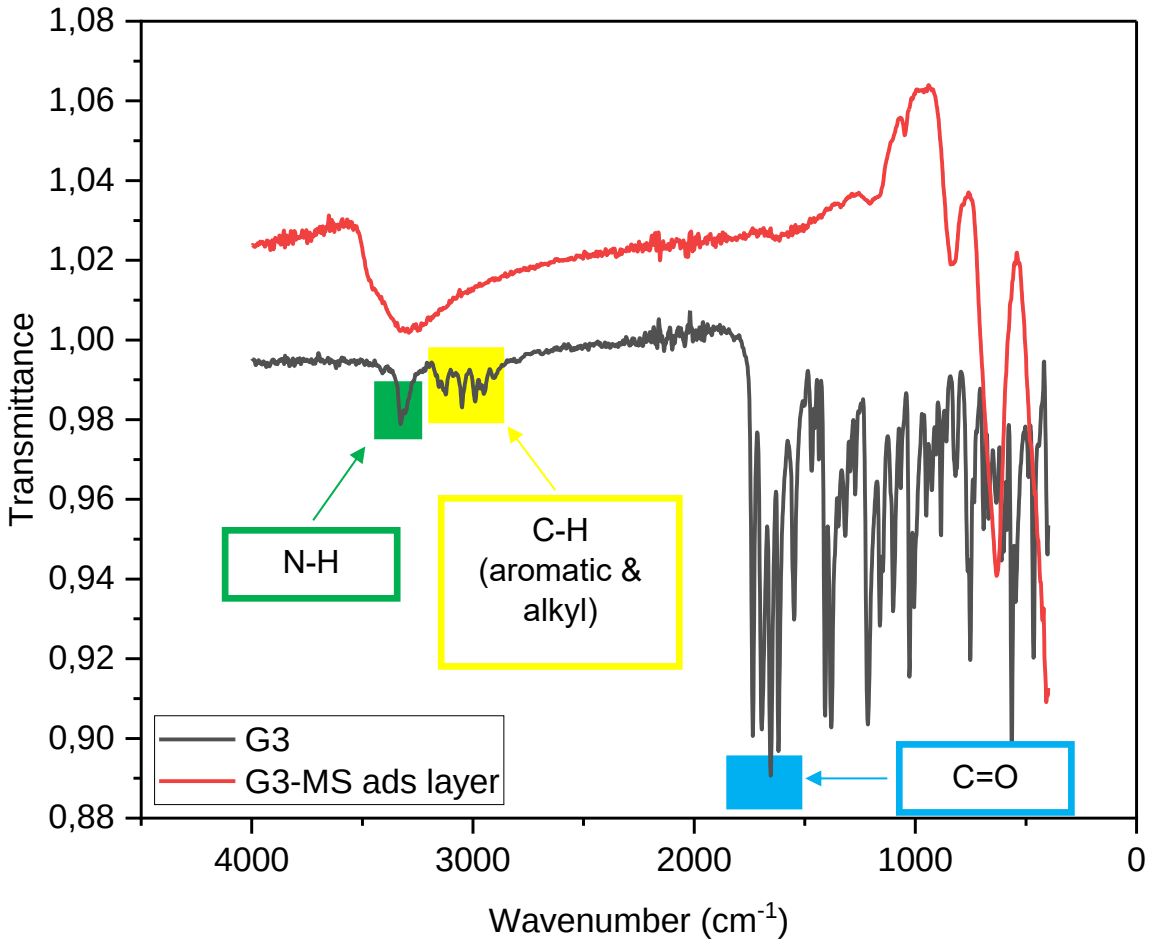

Figure 4.89: G3 FTIR plots (MS).

4.3 Zinc

4.3.1 Weight loss studies

As with MS, all WL experiments were carried out at four different temperatures: 303.15 K, 313.15 K, 323.15 K and 333.15 K. Under isothermal conditions, all Figures (Figures 4.90 to 4.97) show the same trend: an increase in C_{inh} results in a decrease in C_R. This is due to an increase in θ [218]. In addition, all Figures show that as the temperature is increased at constant C_{inh}, the C_R increases. This is due to desorption of molecules from the zinc surface, reducing θ and therefore exposing the metal surface to the corrosive environment [219].

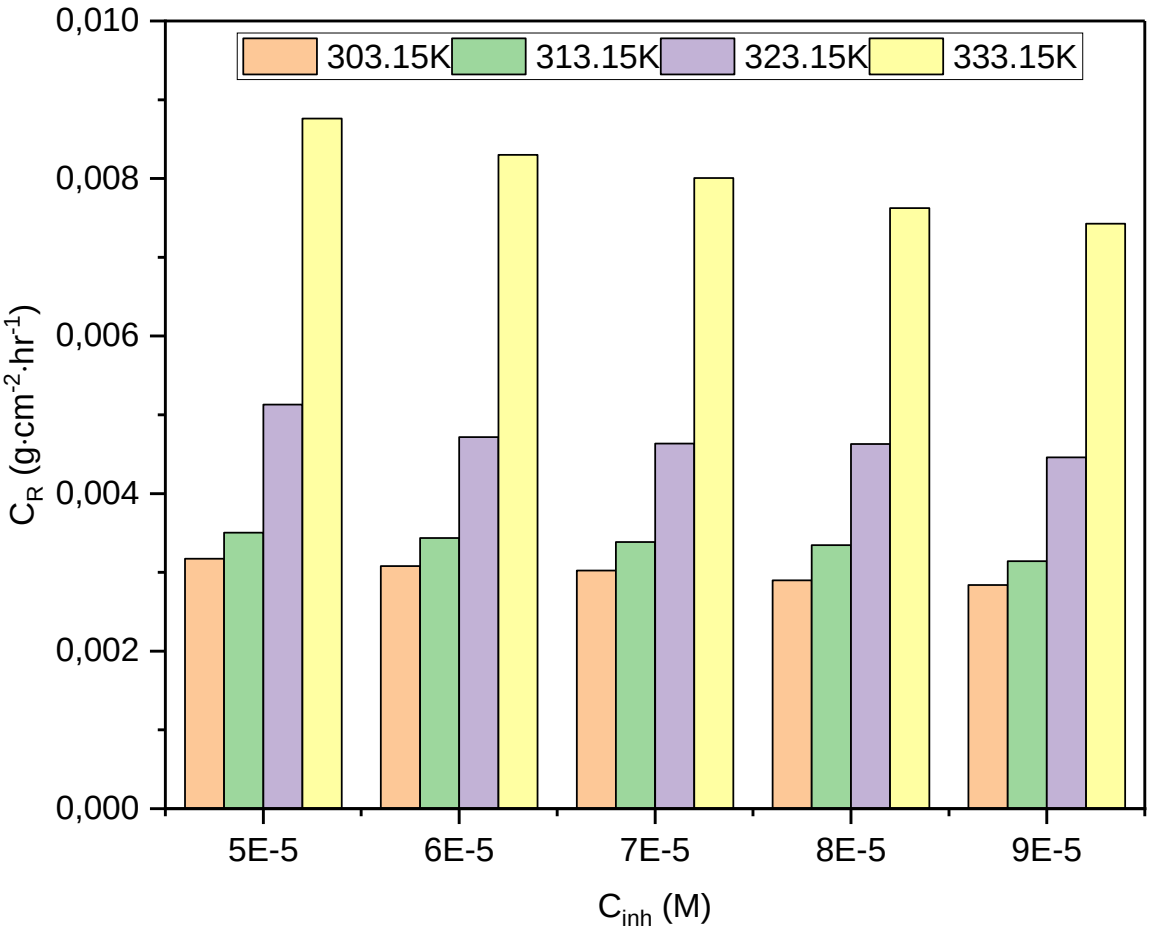

Figure 4.90: Relationship between C_{inh} and C_R for A1 (zinc).

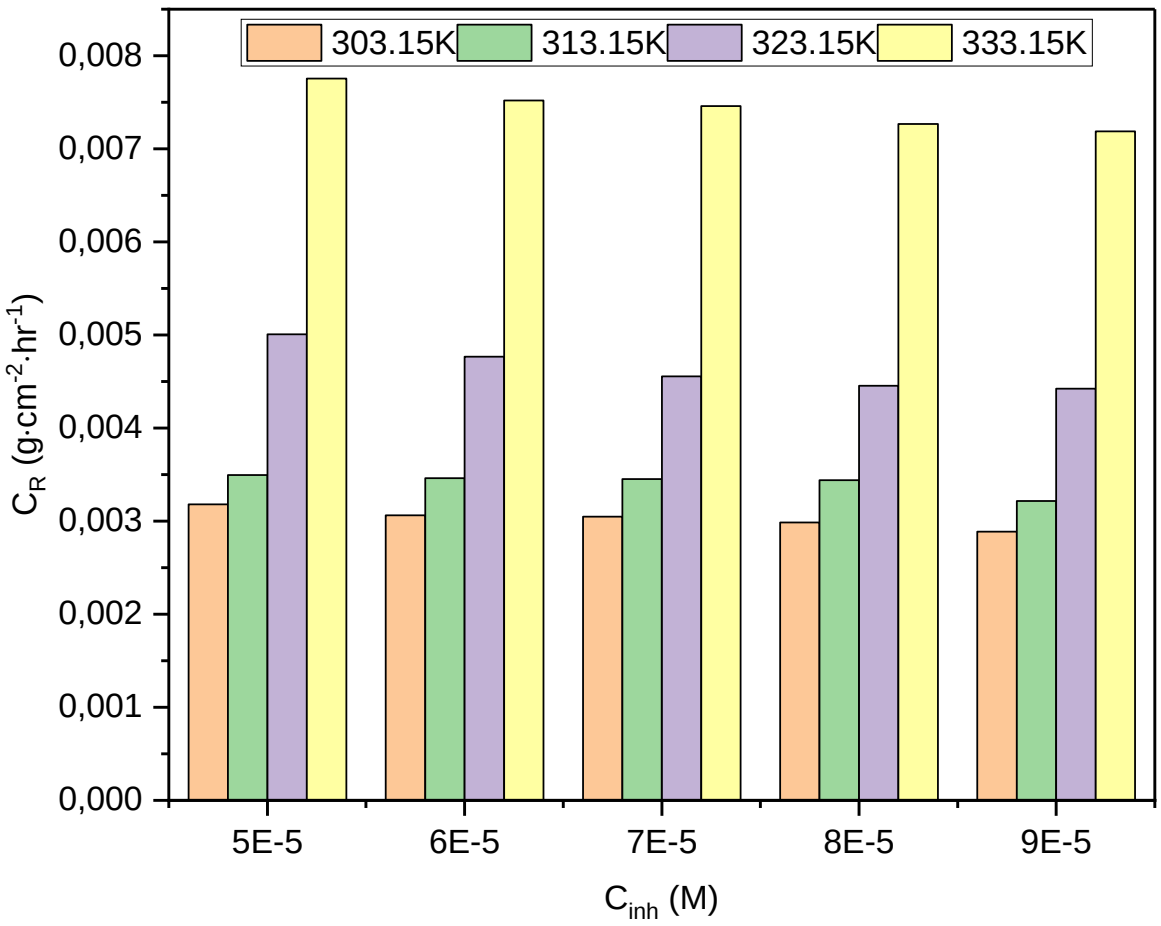

Figure 4.91: Relationship between C_{inh} and C_R for A2 (zinc).

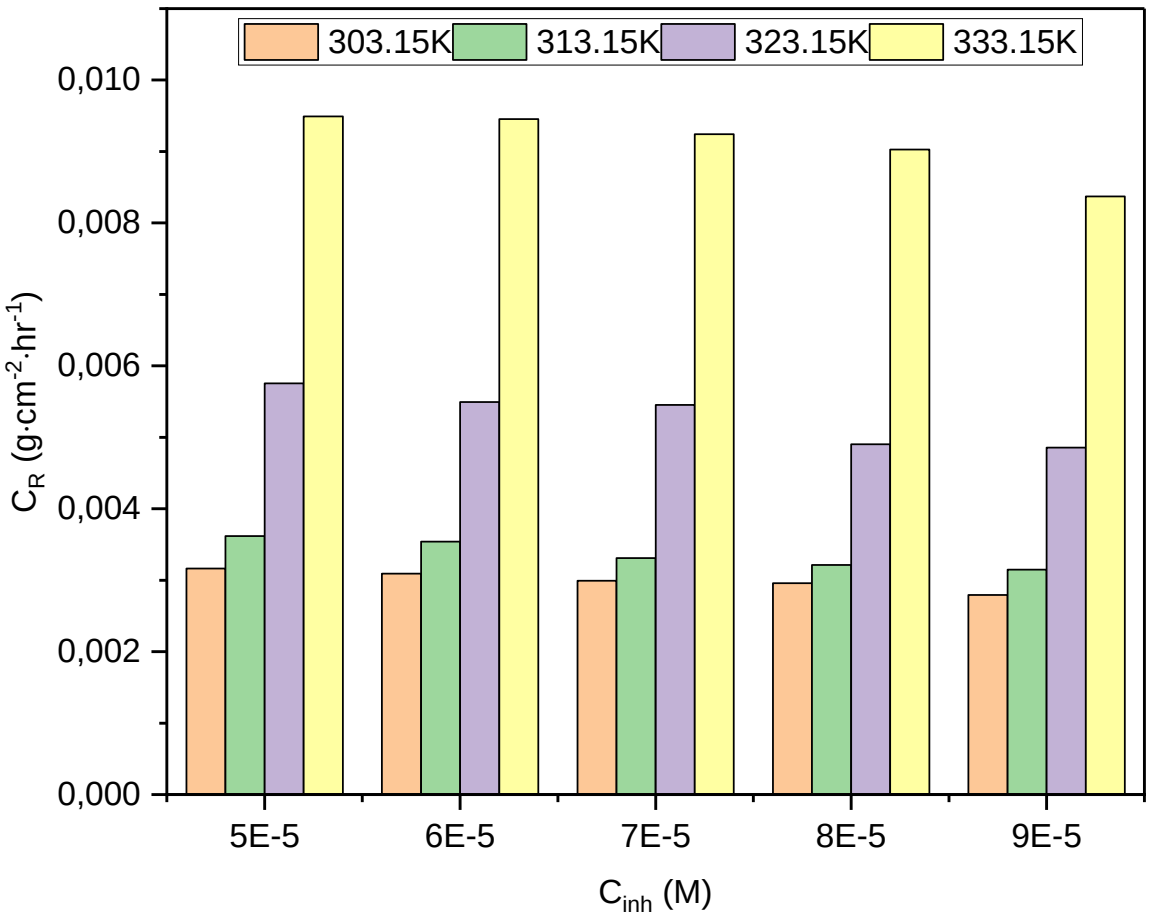

Figure 4.92: Relationship between C_{inh} and C_R for A3 (zinc).

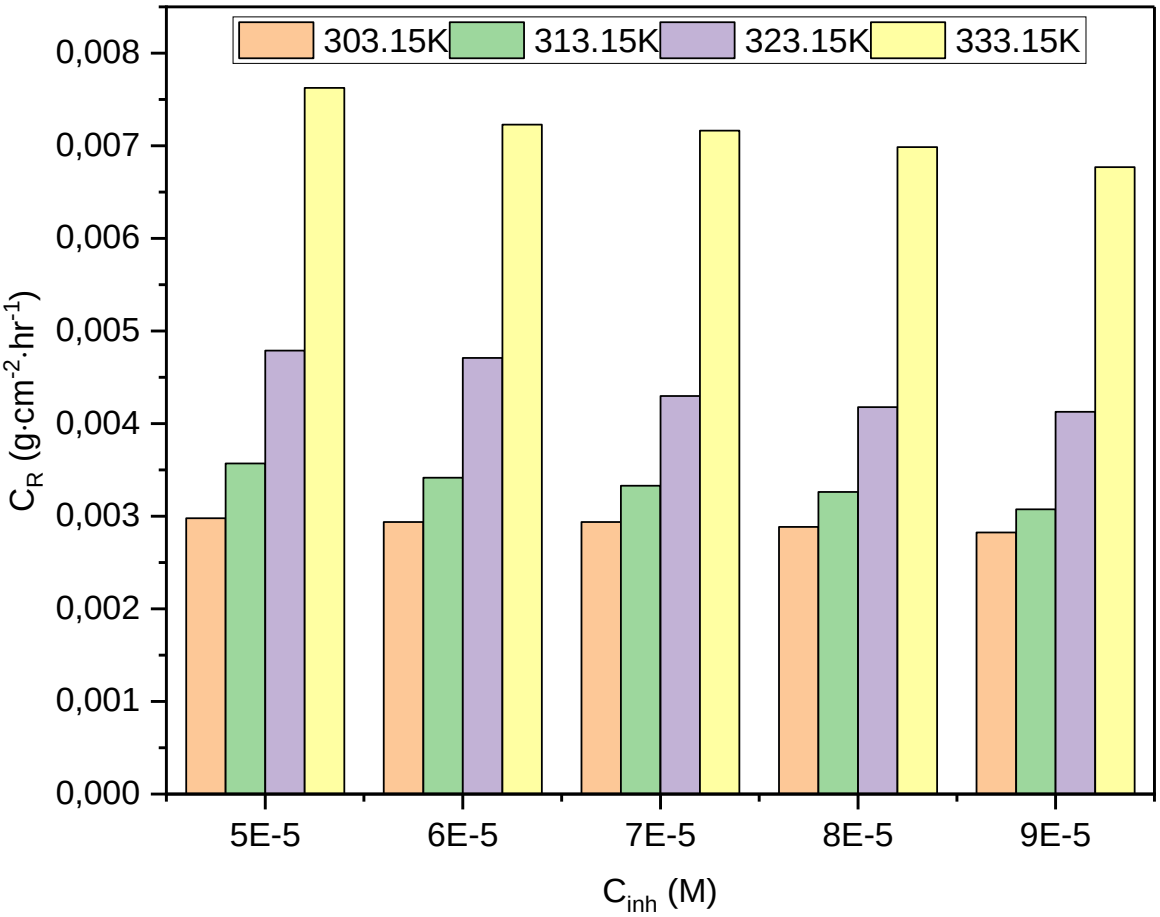

Figure 4.93: Relationship between C_{inh} and C_R for B1 (zinc).

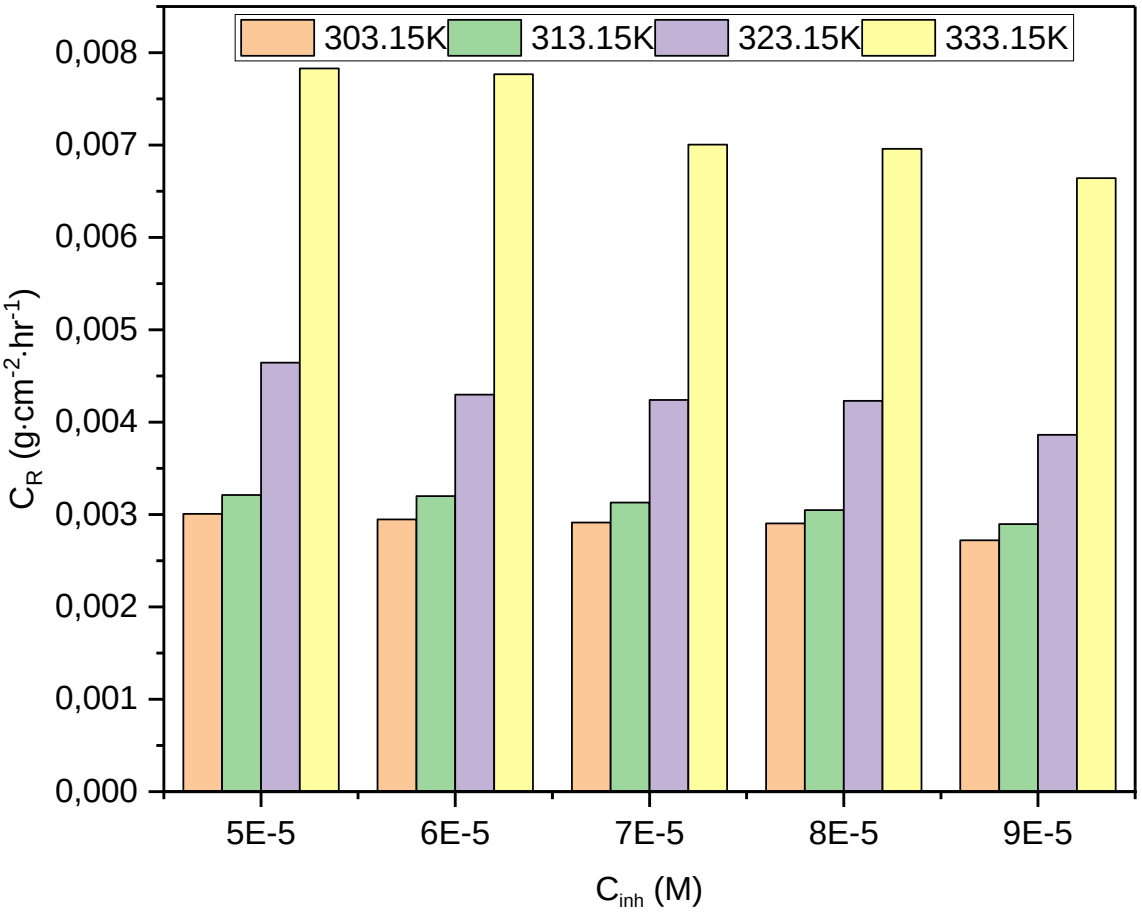

Figure 4.94: Relationship between C_{inh} and C_R for B2 (zinc).

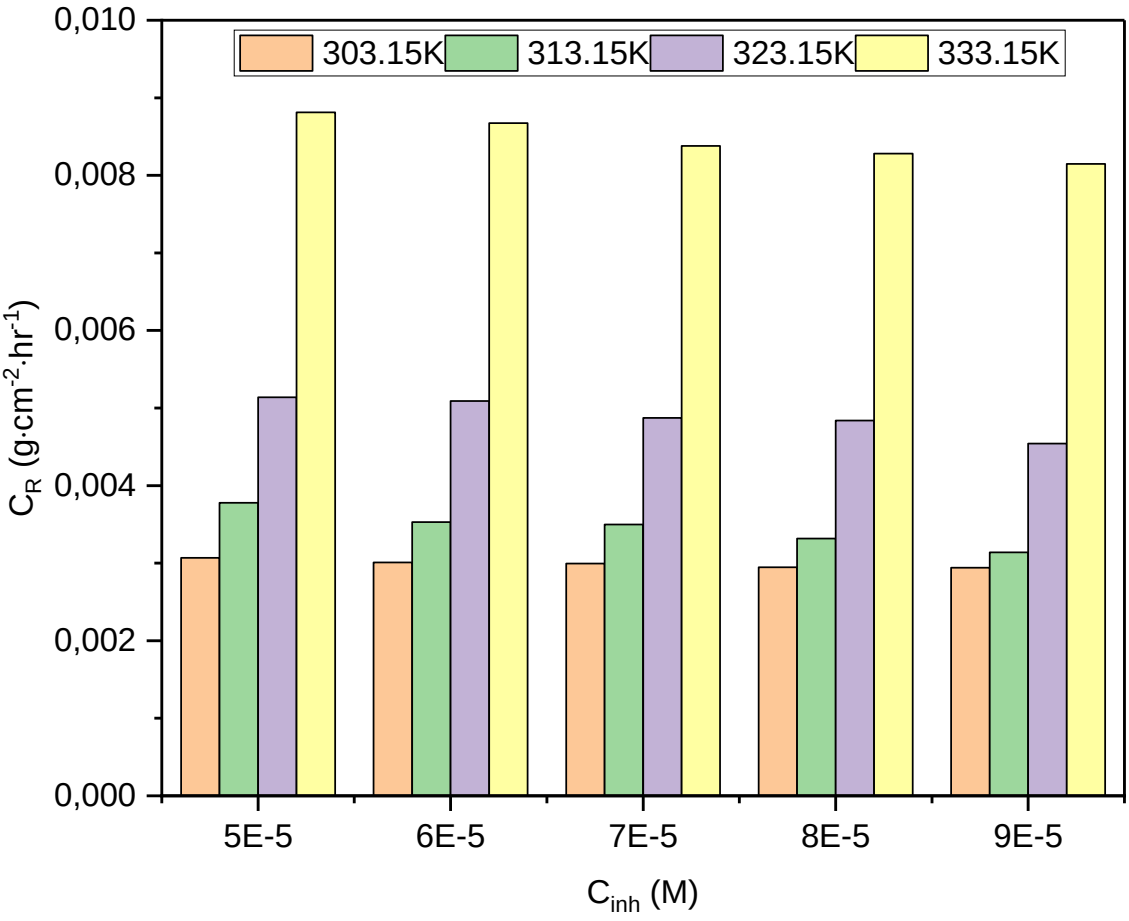

Figure 4.95: Relationship between C_{inh} and C_R for G1 (zinc).

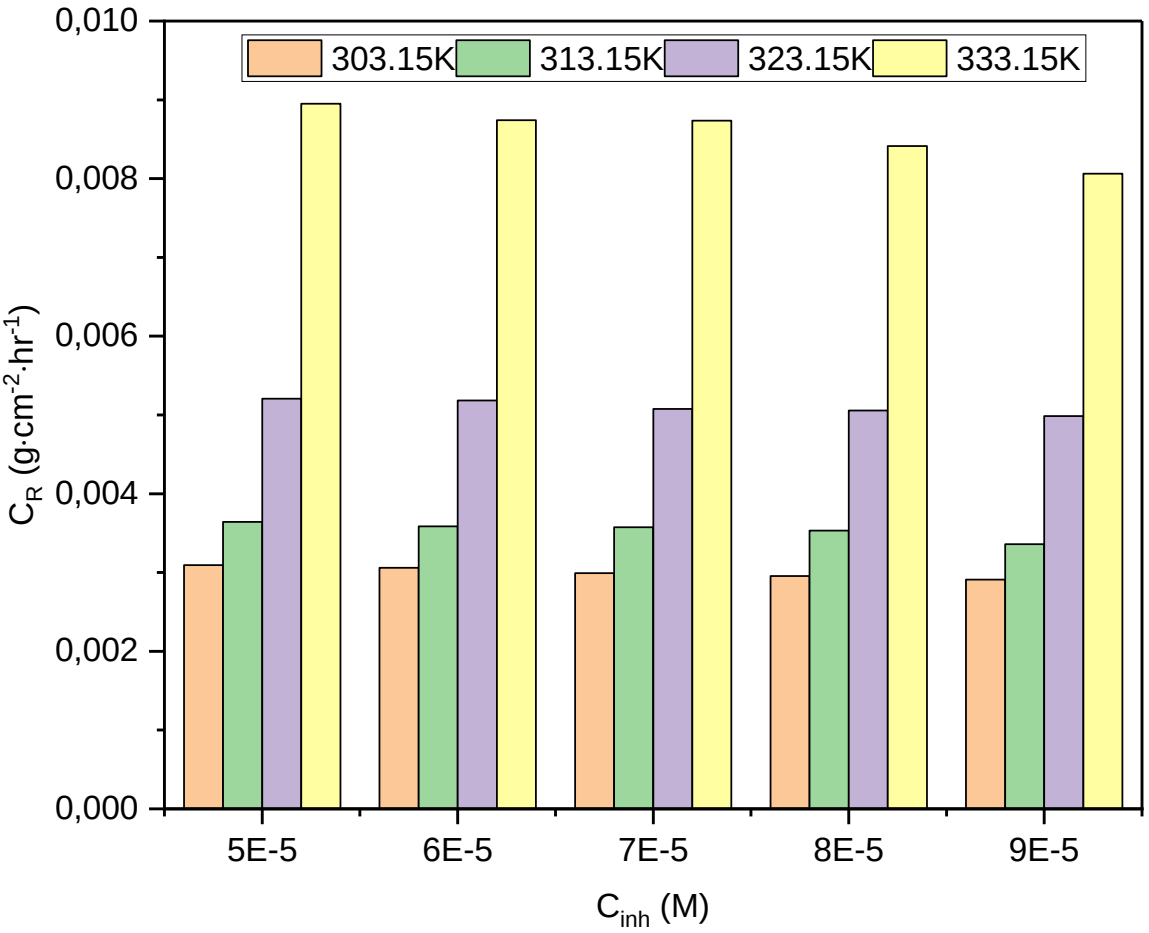

Figure 4.96: Relationship between C_{inh} and C_R for G2 (zinc).

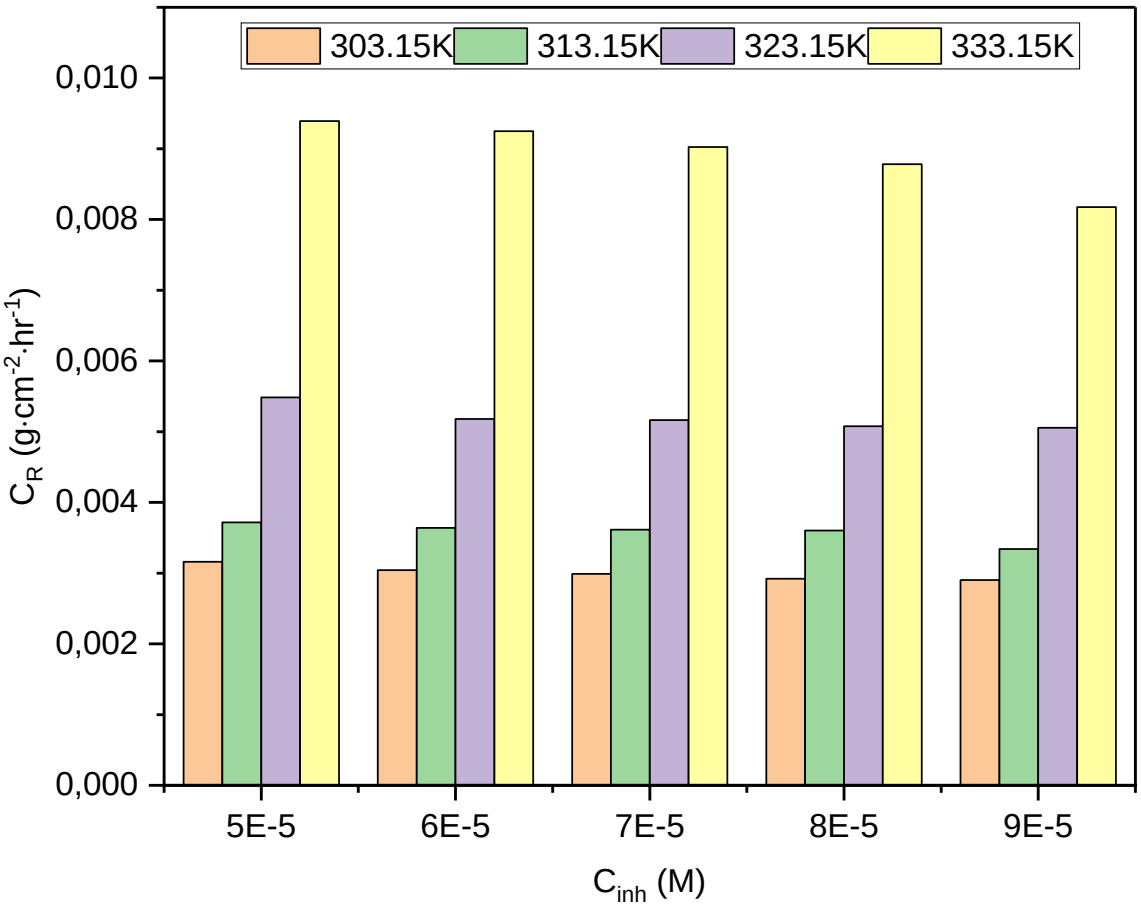

Figure 4.97: Relationship between C_{inh} and C_R for G3 (zinc).

As the temperature is increased, the $\%IE_{WL}$ also increases (Table 4.7). Nahle *et al.* [220] stated that a decrease in $\%IE_{WL}$ with an increase in temperature signifies physisorption. Therefore, the opposite must also be true, that is, an increase in $\%IE_{WL}$ with an increase in temperature signifies chemisorption. Table 4.7 also shows that, at constant temperature, an increase in C_{inh} results in an increase in $\%IE_{WL}$. This trend has been observed elsewhere and is due to an increase in θ [221].

The $\%IE_{WL}$ data shows the following trend in the corrosion inhibition strength of the TZDs: Butanoates>Alaninates>Glycinates. However, even after 5 hours of immersion in 1 M HCl, the additional alkyl groups in the molecular structures of the alaninates and butanoates seemingly hinder their adsorption onto zinc, not giving them any distinct advantage over glycinates. This is shown by the fact that the $\%IE_{WL}$ data for

the alaninates and butanoates is not that much larger than that of the glycinates. Deng *et al.* [222] noted that, at higher concentrations, the corrosion inhibitors with larger alkyl groups performed significantly worse at adsorbing onto galvanized steel as shown by their much lower %IE. The $\%IE_{WL}$ data in Table 4.7 agrees with the findings of Deng *et al.* [222] because alaninates and butanoates only have a small advantage over glycinates even at the highest concentration (9E−5 M).

The formation of a ZnO passive film on the metal surface can complicate the adsorption of TZDs onto the metal surface as it forms a physical barrier between the metal surface and any chemical species in the electrolyte. This may be the reason why small $\%IE_{WL}$ data was achieved for the adsorption of the TZDs onto zinc relative to MS.

Table 4.7: The effect of temperature and C_{inh} on $\%IE_{WL}$ (zinc).

TZD	Concentration (M)	($\%IE_{WL}$) 303.15 K	($\%IE_{WL}$) 313.15 K	($\%IE_{WL}$) 323.15 K	($\%IE_{WL}$) 333.15 K
A1	5.00E−05	22.89	37.14	37.43	39.16
	6.00E−05	25.14	38.39	42.47	42.36
	7.00E−05	26.53	39.28	43.47	44.40
	8.00E−05	29.60	40.02	43.52	47.05
	9.00E−05	31.03	43.66	45.60	48.44
A2	5.00E−05	22.72	37.30	38.91	46.15
	6.00E−05	25.57	37.91	41.86	47.79
	7.00E−05	25.92	38.10	44.43	48.21
	8.00E−05	27.43	38.29	45.67	49.54
	9.00E−05	29.86	42.32	46.06	50.09
A3	5.00E−05	23.11	35.13	29.81	34.09
	6.00E−05	24.84	36.51	33.00	34.35
	7.00E−05	27.26	40.66	33.48	35.84
	8.00E−05	28.08	42.38	40.19	37.31
	9.00E−05	32.15	43.53	40.78	41.88
B1	5.00E−05	27.61	35.96	41.58	47.06
	6.00E−05	28.60	38.74	42.56	49.81
	7.00E−05	28.65	40.27	47.56	50.25

	8.00E−05	29.90	41.52	49.03	51.50
	9.00E−05	31.37	44.84	49.64	53.00
B2	5.00E−05	26.96	42.38	43.34	45.64
	6.00E−05	28.39	42.64	47.58	46.07
	7.00E−05	29.21	43.88	48.27	51.37
	8.00E−05	29.47	45.32	48.38	51.68
	9.00E−05	33.88	48.04	52.88	53.89
G1	5.00E−05	25.44	32.26	37.30	38.82
	6.00E−05	26.91	36.70	37.89	39.78
	7.00E−05	27.22	37.24	40.56	41.81
	8.00E−05	28.43	40.53	40.97	42.51
	9.00E−05	28.52	43.72	44.60	43.43
G2	5.00E−05	24.79	34.69	36.50	37.85
	6.00E−05	25.66	35.68	36.76	39.31
	7.00E−05	27.30	35.87	38.06	39.35
	8.00E−05	28.21	36.63	38.32	41.59
	9.00E−05	29.29	39.73	39.17	44.02
G3	5.00E−05	23.19	33.34	33.09	34.80
	6.00E−05	26.05	34.72	36.80	35.77
	7.00E−05	27.35	35.16	37.02	37.33
	8.00E−05	29.04	35.42	38.06	39.03
	9.00E−05	29.51	40.08	38.34	43.23

4.3.1.1 Adsorption parameters

Figures 4.98 to 4.105 show the LAI for the adsorption of the TZDs onto zinc. All the isotherms shown are like those for MS in terms of having positive slopes. However, they differ from the LAI for MS in the sense that the zinc LAI for the lowest temperature, 303.15 K, are consistently the topmost isotherms. This means the isotherm at 303.15 K has the largest y-intercept value, translating to the lowest K_{ads} value. This is not always the case however, perhaps an indication of the limitations of the LAI in modelling real world phenomena [223].

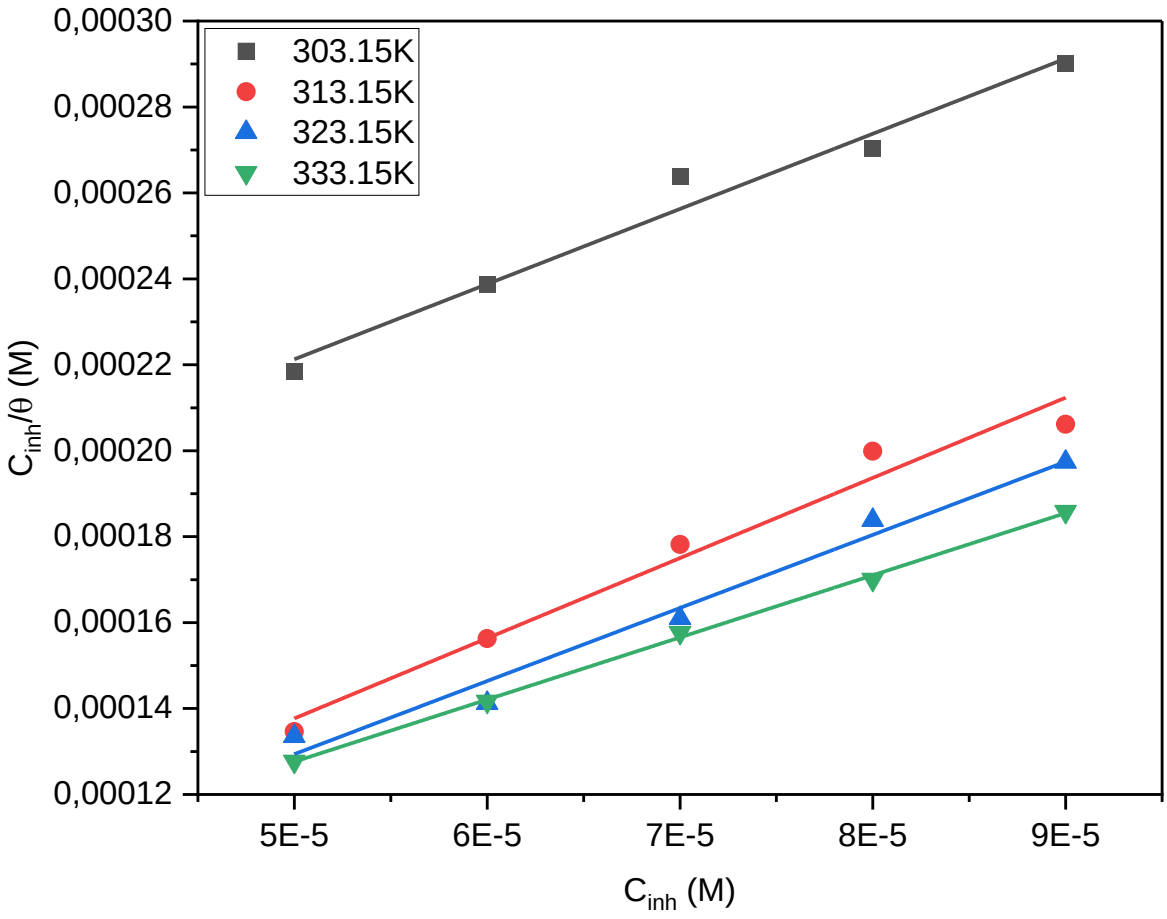

Figure 4.98: A1 Langmuir adsorption isotherms (zinc).

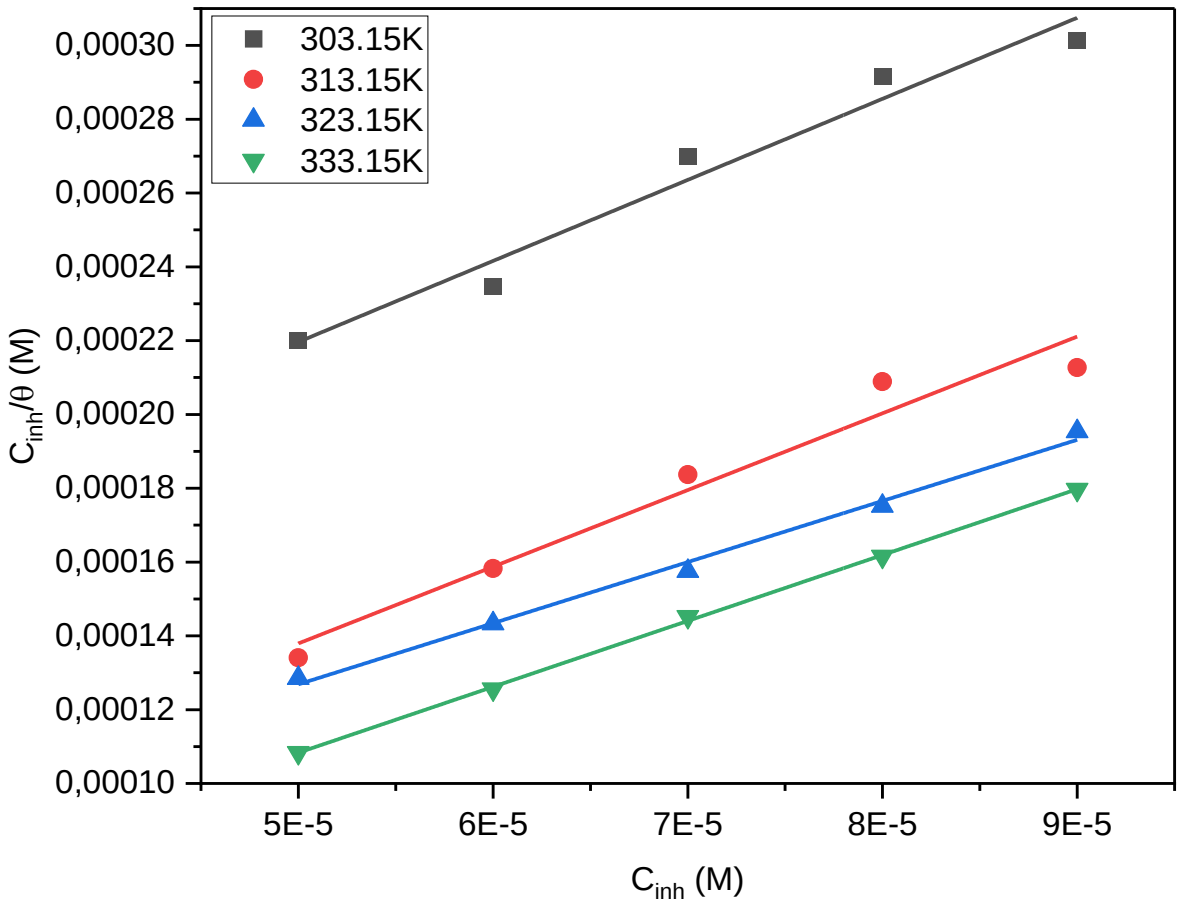

Figure 4.99: A2 Langmuir adsorption isotherms (zinc).

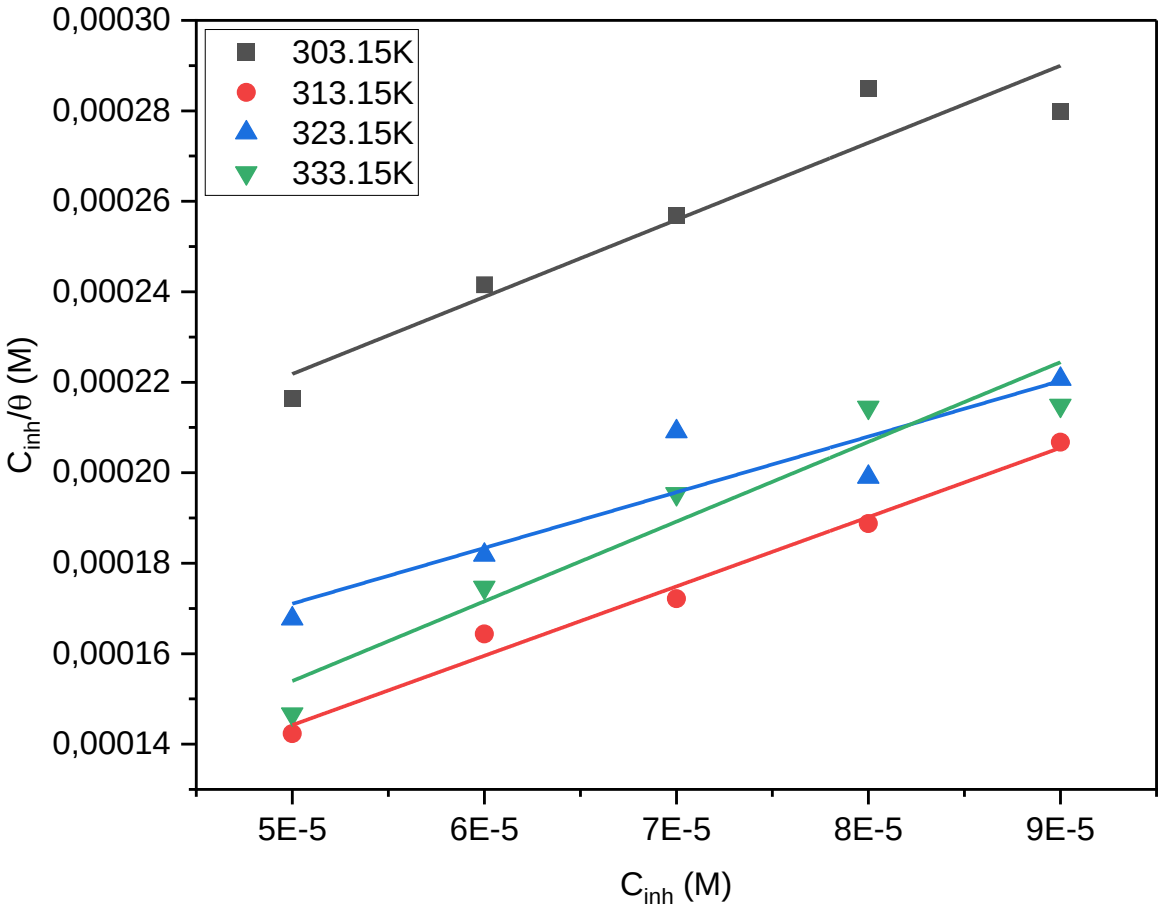

Figure 4.100: A3 Langmuir adsorption isotherm (zinc).

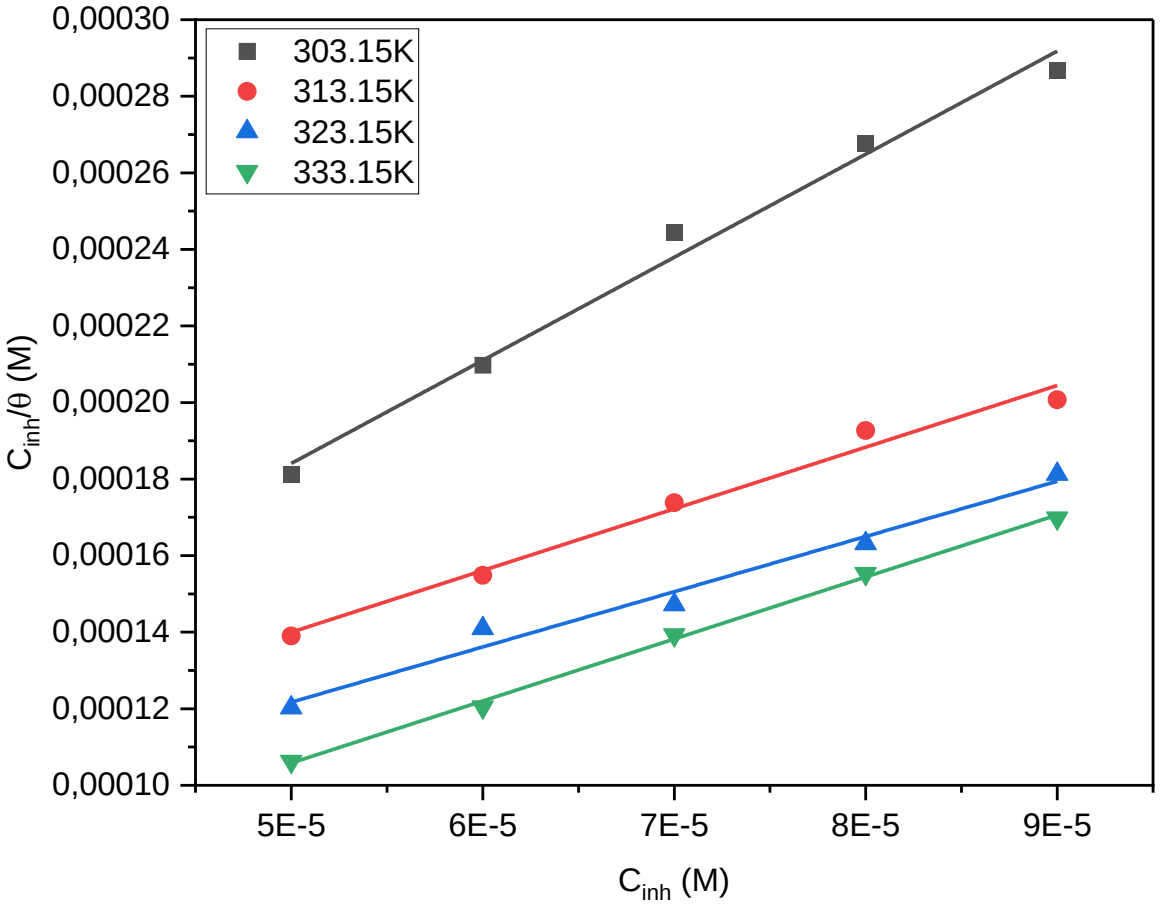

Figure 4.101: B1 Langmuir adsorption isotherms (zinc).

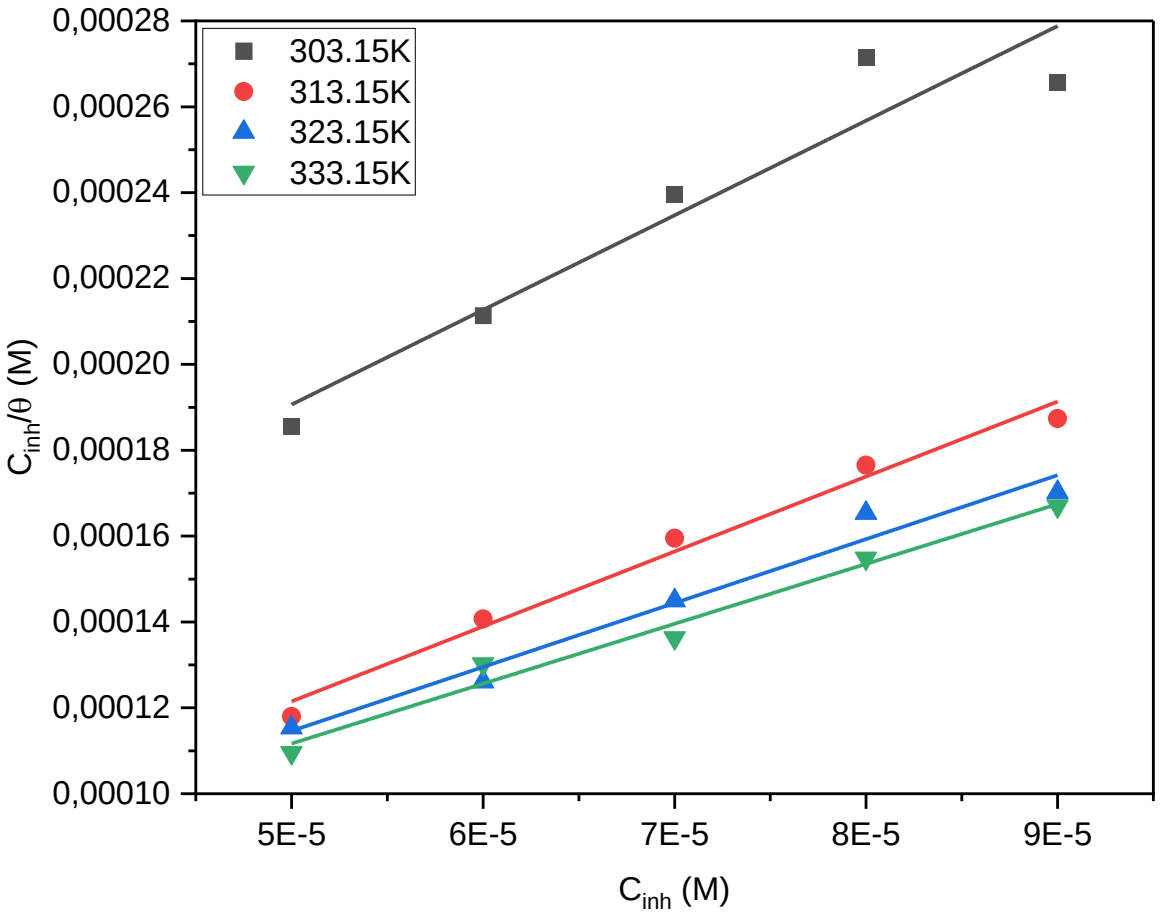

Figure 4.102: B2 Langmuir adsorption isotherms (zinc).

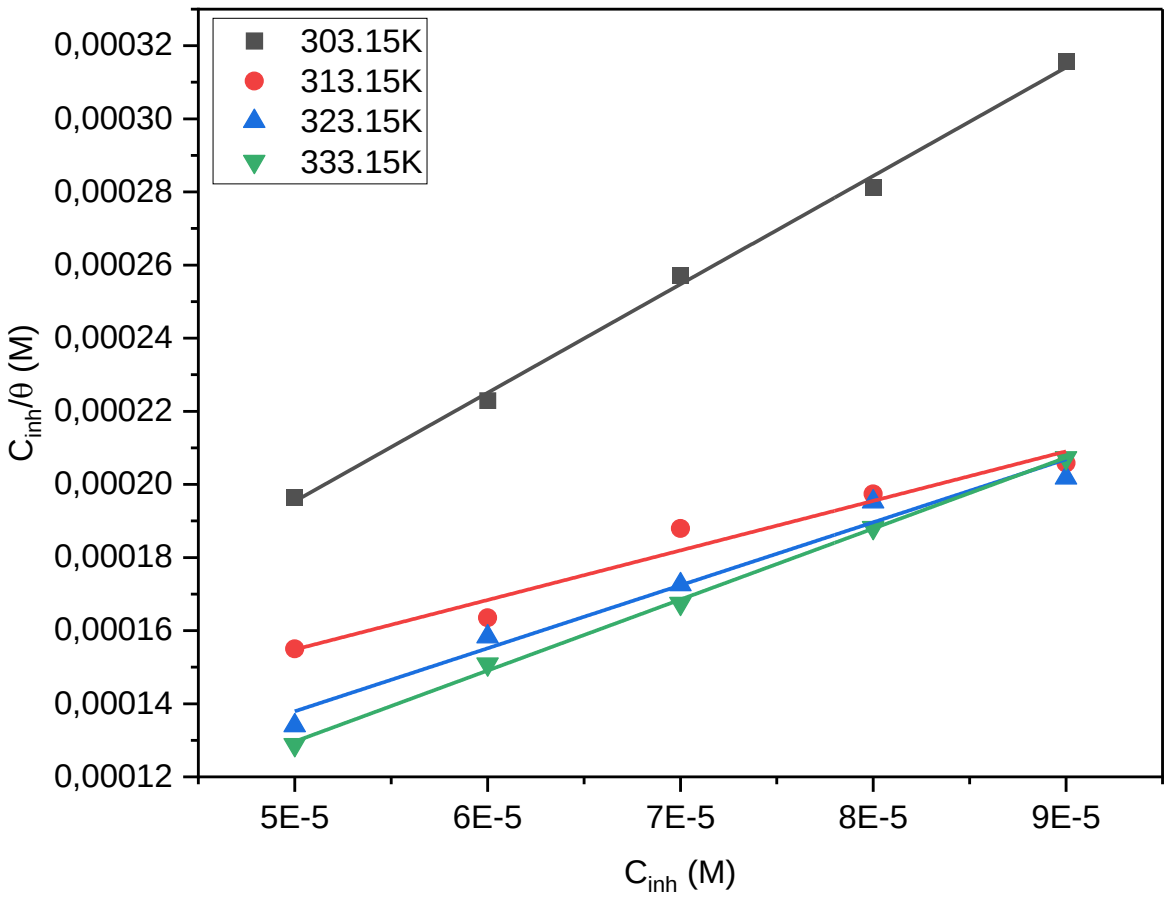

Figure 4.103: G1 Langmuir adsorption isotherms (zinc).

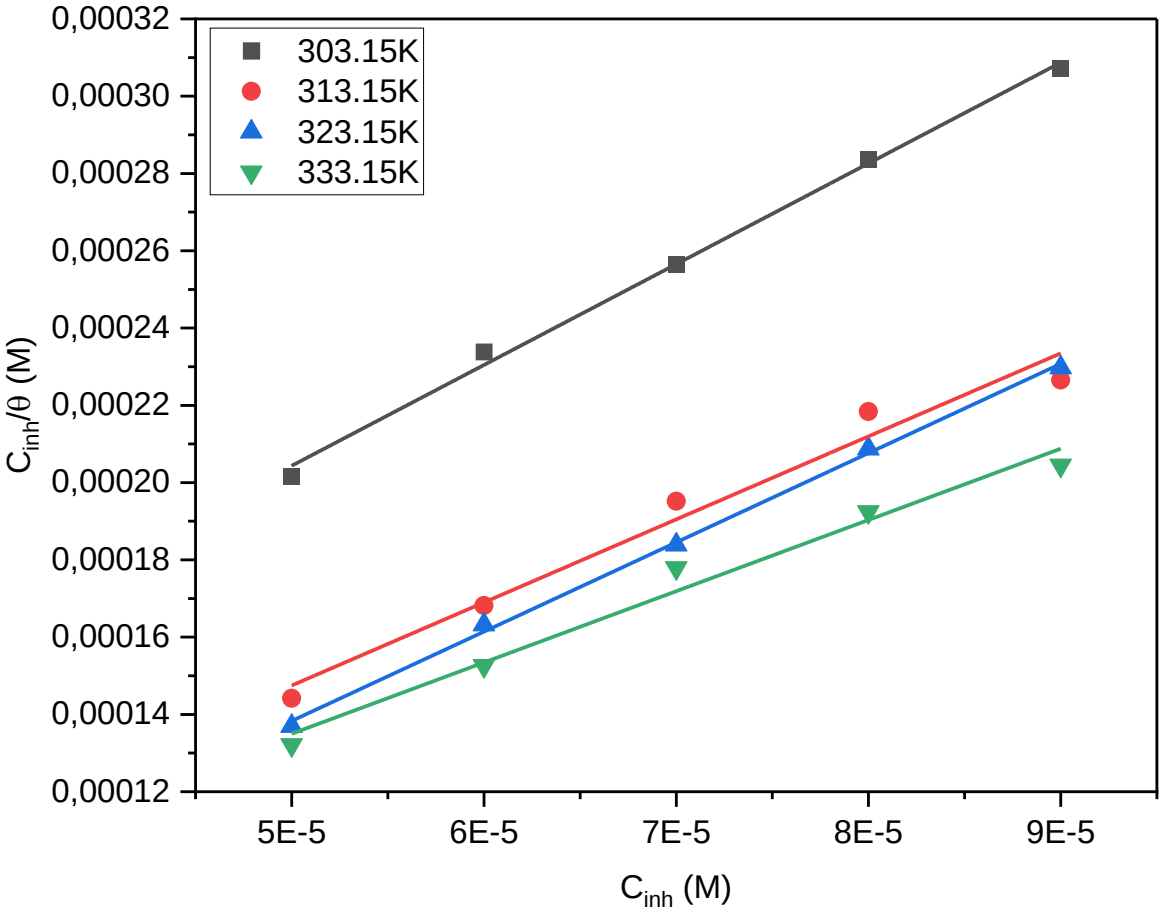

Figure 4.104: G2 Langmuir adsorption isotherms (zinc).

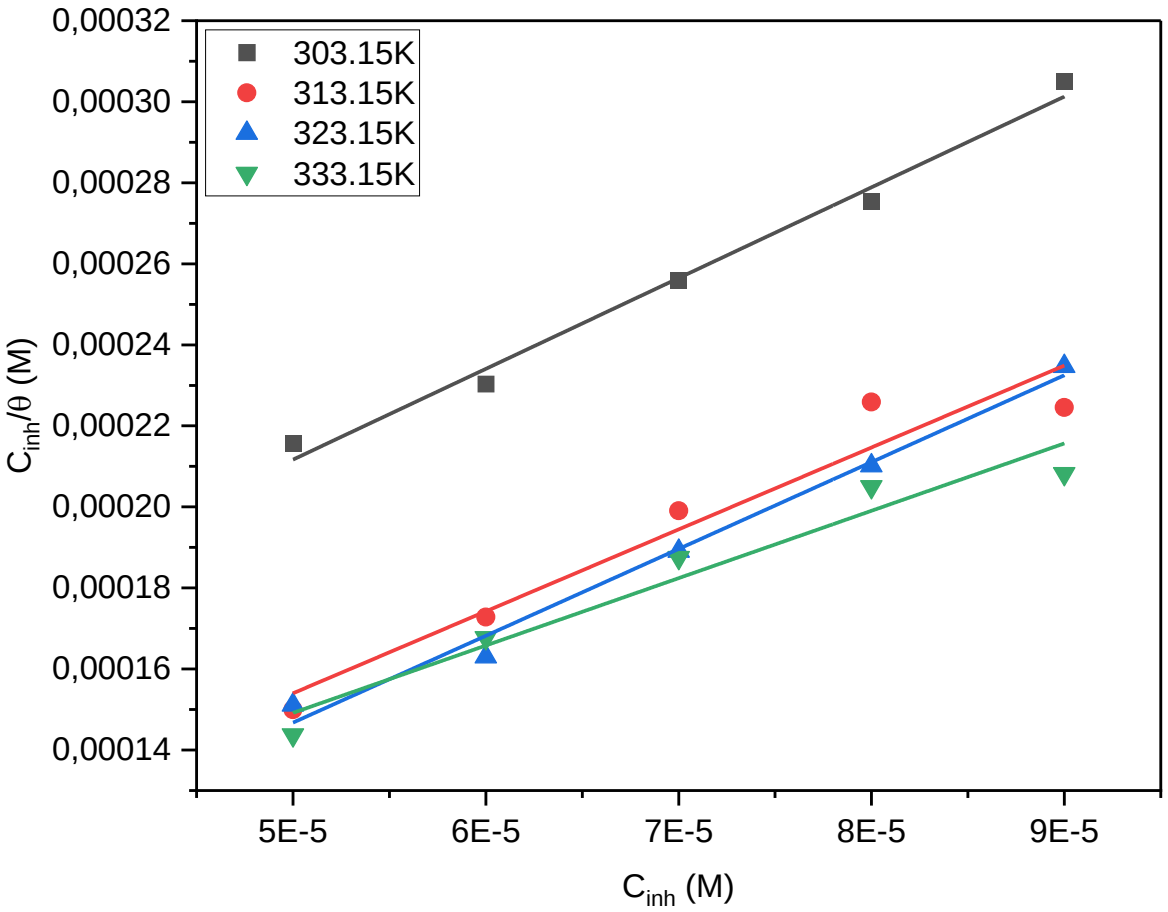

Figure 4.105: G3 Langmuir adsorption isotherms (zinc).

Given the high r^2 values attained (Table 4.8), the LAI was found to be the best at modelling the adsorption of the TZDs onto zinc. The LAI r^2 values for zinc are consistently much closer to unity compared to those of MS. The LAI makes several assumptions one of which is that there is no interaction between adjacent adsorbed molecules [224]. However, Ballantine Jr *et al.* [225] noted that the LAI can be inaccurate when modelling real world phenomena. This is most likely the case in this research. Although the best isotherm to describe the adsorption of the TZDs onto both MS and zinc in this study, the much larger deviations from unity for MS r^2 values (see Table 4.3) relative to those of zinc show that there most likely are interactions between adjacent adsorbed molecules on MS. After all, it is well established that when large organic molecules come close together, there will be steric interactions between them [226]. The LAI r^2 values for zinc may be much higher because much fewer TZD

molecules adsorb onto the zinc surface, reducing crowding on the zinc metal surface and therefore inhibitor molecule interactions. This explanation is substantiated by the low $\%IE_{WL}$ data obtained for zinc (see Table 4.7).

The negative $\Delta G°_{ads}$ data shows that the adsorption of the TZDs onto zinc is not only spontaneous but, becomes more spontaneous as the temperature is increased [227]. In addition, the adsorption of the TZDs onto zinc transitions from a mixed type of adsorption to increasingly chemisorption [227]. These trends in $\Delta G°_{ads}$ explain the increase in $\%IE_{WL}$ as the temperature of the aggressive environment is increased (see Table 4.7).

The positive $\Delta H°_{ads}$ data shows that all TZDs adsorb onto zinc endothermically. This means an increase in temperature would favour adsorption of the TZDs onto zinc. This is confirmed by the increasing $\%IE_{WL}$ data as temperature is increased (see Table 4.7). The magnitude of the $\Delta S°_{ads}$ also shows the large extent of disorder brought about at the metal surface by the displacement of adsorbed H_2O molecules (Equation 22) as the TZDs adsorb onto zinc [228].

Amongst the alaninates and glycinates, A2 and G2 respectively have the largest $\Delta S°_{ads}$ data. This is most likely because the ($-NO_2$) group facilitates the formation of additional dative covalent bonds with the zinc surface [229], strong interactions that displace more H_2O molecules adsorbed on the zinc surface. Of the two butanoates, B1 displaces more adsorbed H_2O molecules probably by virtue of its larger molecular size, a phenomenon also noted by Arellanes-Lozada *et al.* [230] when they noted that large polymers promote favourable corrosion inhibition by displacing adsorbed H_2O molecules from a metal surface.

Table 4.8: TZD adsorption parameters (zinc).

TZD	Temperature (K)	r^2	K_{ads} ($L \cdot mol^{-1}$)	$\Delta G°_{ads}$ ($kJ \cdot mol^{-1}$)	$\Delta H°_{ads}$ ($kJ \cdot mol^{-1}$)	$\Delta S°_{ads}$ ($J \cdot mol^{-1} \cdot K^{-1}$)
A1	303.15	0.9746	7473	−32.60	45.48	257.55
	313.15	0.9730	22545	−36.55	45.48	261.94
	323.15	0.9793	22570	−37.72	45.48	257.46
	333.15	0.9988	18088	−38.28	45.48	251.39
A2	303.15	0.9670	9108	−33.10	47.11	264.60
	313.15	0.9605	29435	−37.25	47.11	269.39
	323.15	0.9943	22716	−37.74	47.11	262.58
	333.15	0.9994	52545	−41.23	47.11	265.17
A3	303.15	0.9118	7319	−32.55	27.21	197.14
	313.15	0.9842	14794	−35.46	27.21	200.12
	323.15	0.8473	9135	−35.29	27.21	193.42
	333.15	0.9256	15188	−37.79	27.21	195.12
B1	303.15	0.9887	20238	−35.11	37.63	239.94
	313.15	0.9856	16831	−35.79	37.63	234.45
	323.15	0.9794	20171	−37.42	37.63	232.23
	333.15	0.9980	40301	−40.50	37.63	234.49
B2	303.15	0.9165	12434	−33.89	27.49	202.47
	313.15	0.9845	29227	−37.23	27.49	206.68
	323.15	0.9715	24898	−37.99	27.49	202.63
	333.15	0.9806	23855	−39.04	27.49	199.72
G1	303.15	0.9974	21252	−35.24	42.66	256.96
	313.15	0.9612	11488	−34.80	42.66	247.35
	323.15	0.9729	19328	−37.31	42.66	247.46
	333.15	0.9987	30714	−39.74	42.66	247.35

G2	303.15	0.9968	13528	−34.10	47.94	270.63
	313.15	0.9741	24982	−36.82	47.94	270.68
	323.15	0.9986	43899	−39.51	47.94	270.63
	333.15	0.9804	23374	−38.99	47.94	260.93
G3	303.15	0.9893	10031	−33.34	45.13	258.85
	313.15	0.9376	18901	−36.09	45.13	259.36
	323.15	0.9889	25261	−38.03	45.13	257.31
	333.15	0.9482	15143	−37.78	45.13	248.87

4.3.1.2 Activation parameters

Figures 4.106 to 4.113 show Arrhenius plots for five different TZD concentrations. The E_a for each C_{inh} was calculated from the slope of the corresponding plot. All Figures have negative slopes ensuring that all E_a calculated are positive (see Equation 16). All Arrhenius plots are parallel to one other, with the lowest C_{inh} (5E−5 M) making up the topmost Arrhenius plot whilst the highest C_{inh} (9E−5 M) has its plot consistently being the lowest. In most of the Figures shown, there is a noticeable decrease in the slope of the Arrhenius plots as C_{inh} is increased, signifying an inverse proportionality relationship between E_a and C_{inh}.

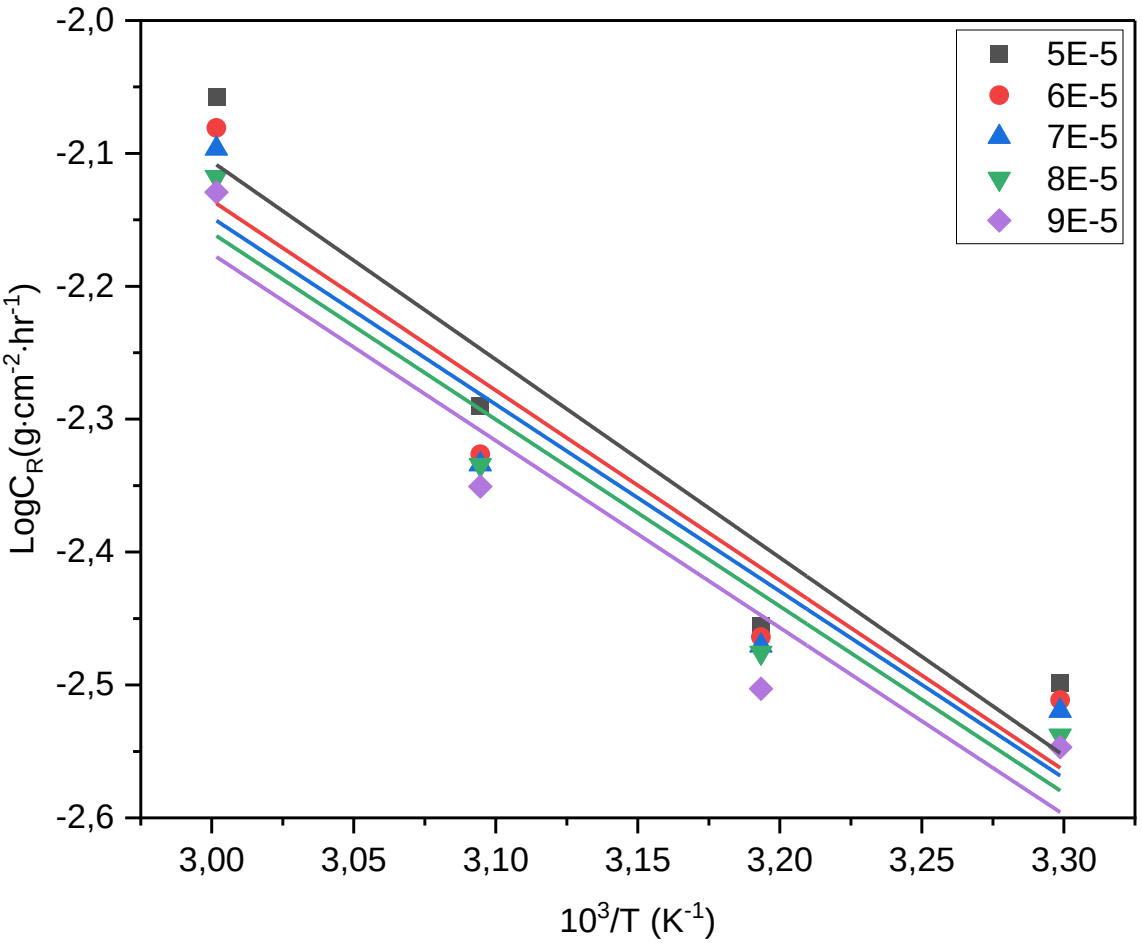

Figure 4.106: A1 Arrhenius plots (zinc).

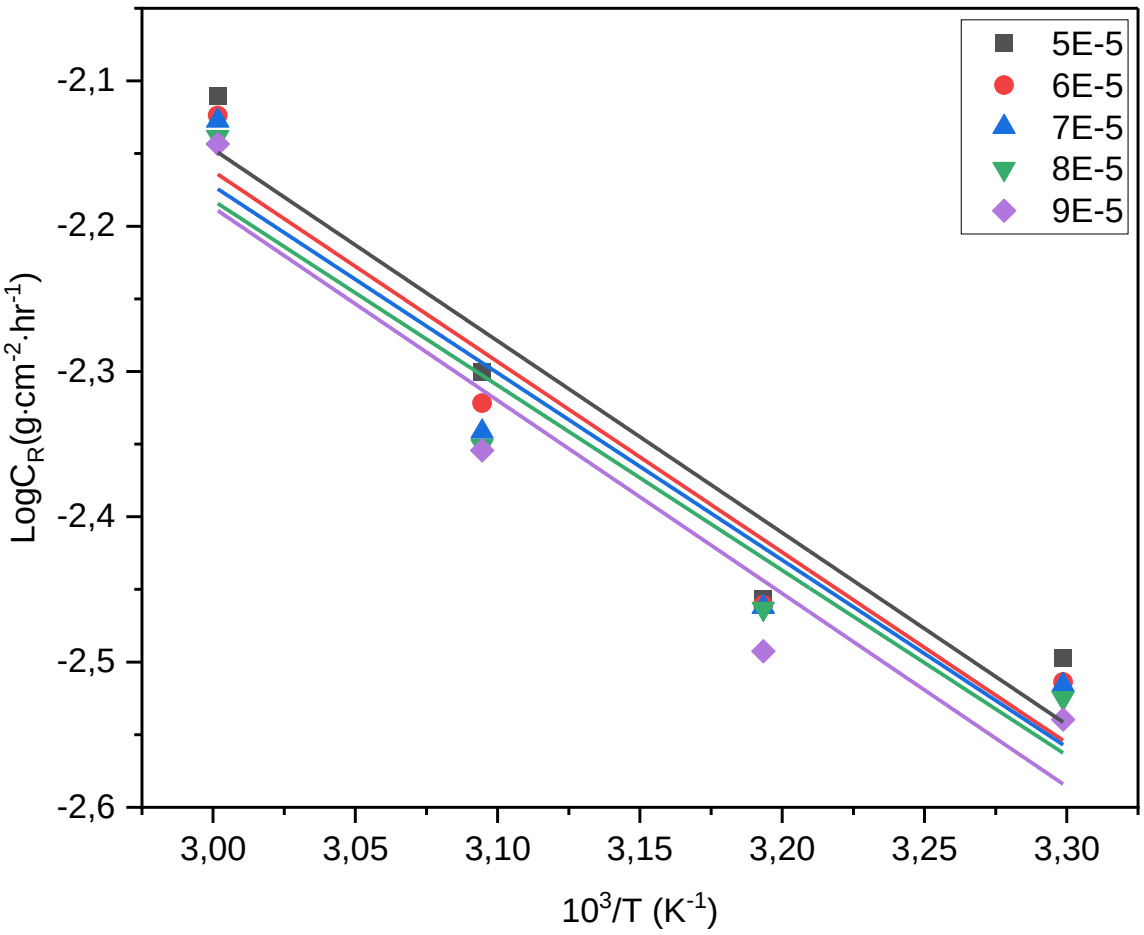

Figure 4.107: A2 Arrhenius plots (zinc).

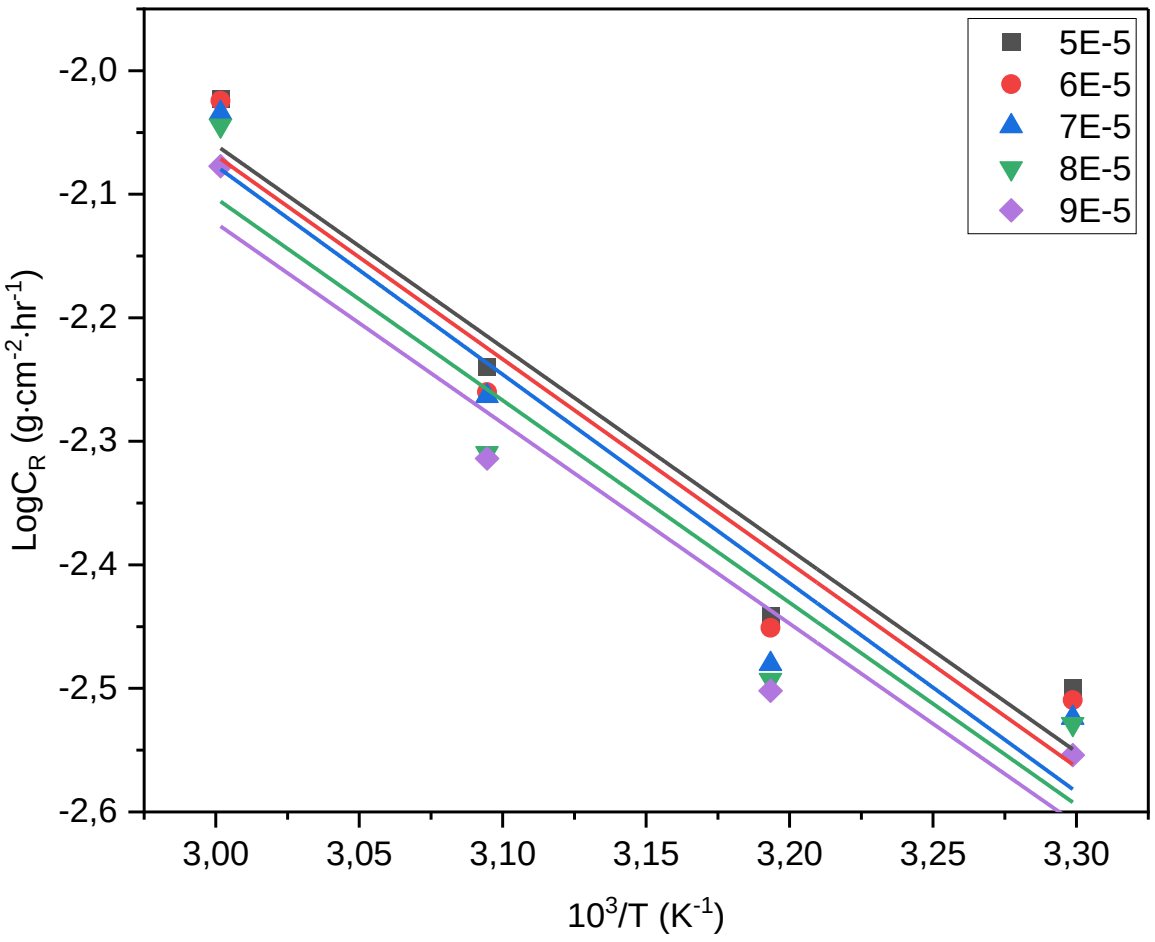

Figure 4.108: A3 Arrhenius plots (zinc).

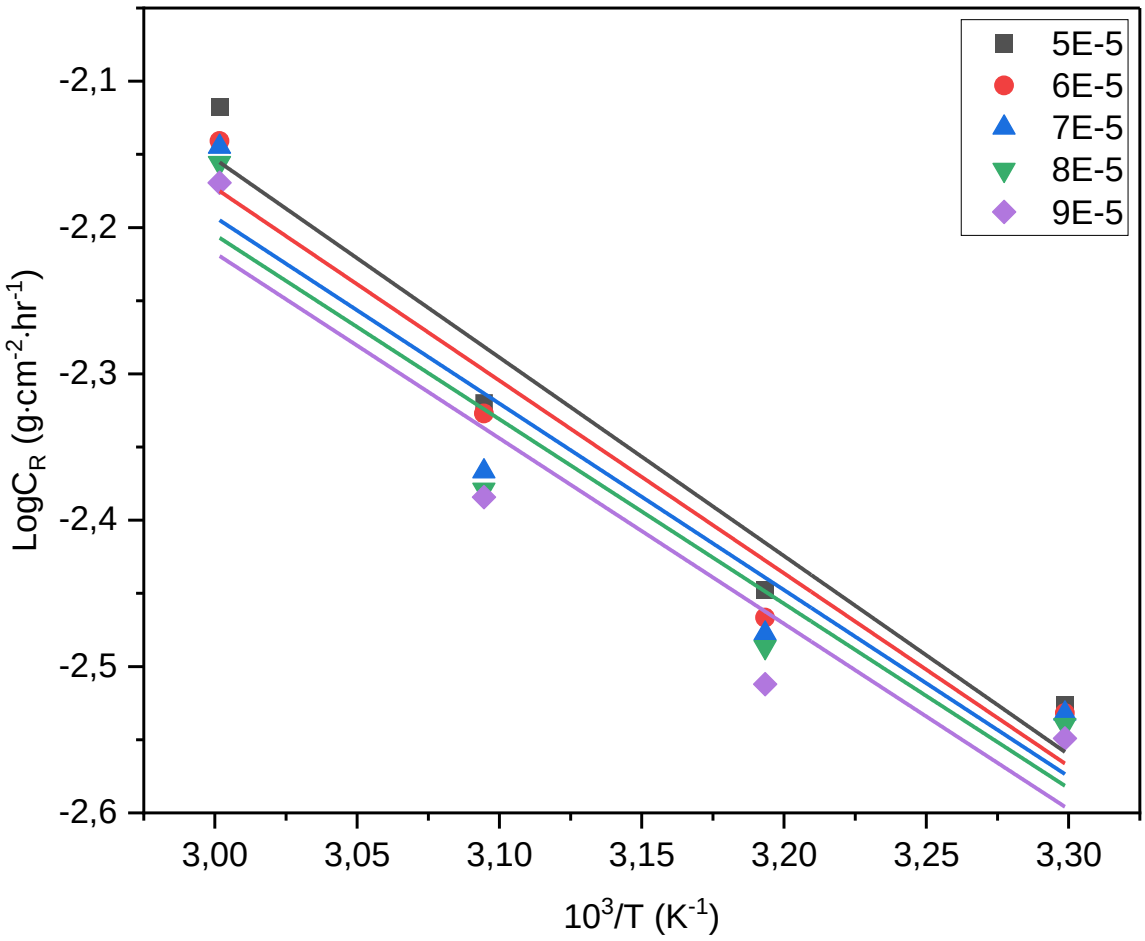

Figure 4.109: B1 Arrhenius plots (zinc).

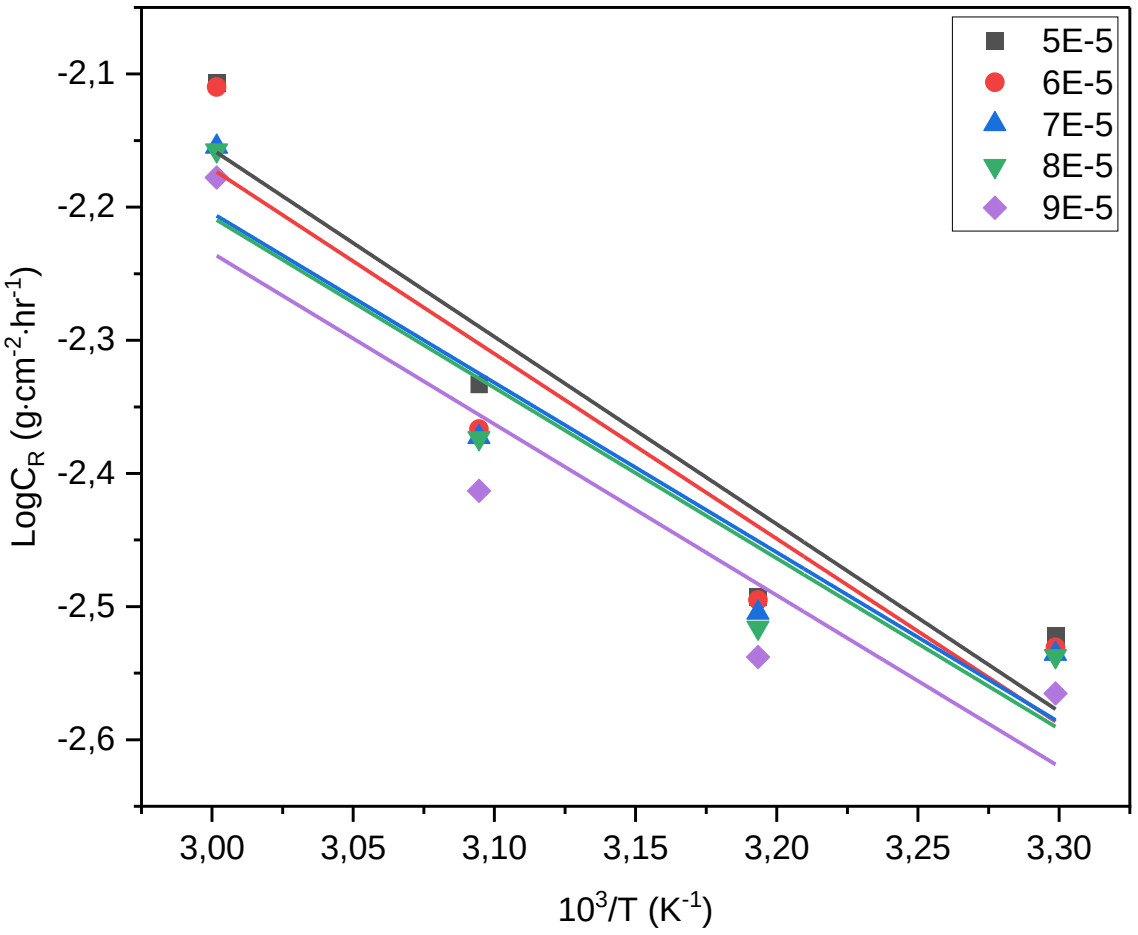

Figure 4.110: B2 Arrhenius plots (zinc).

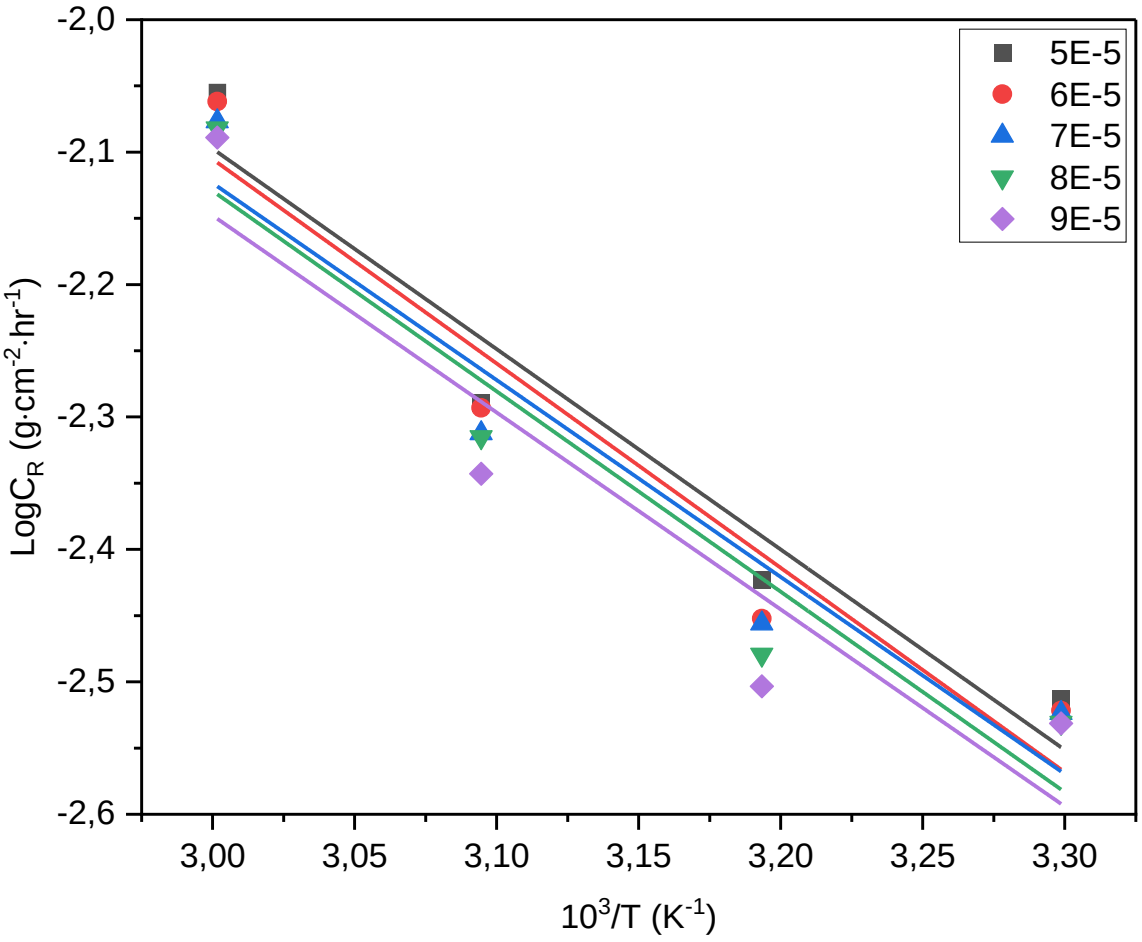

Figure 4.111: G1 Arrhenius plots (zinc).

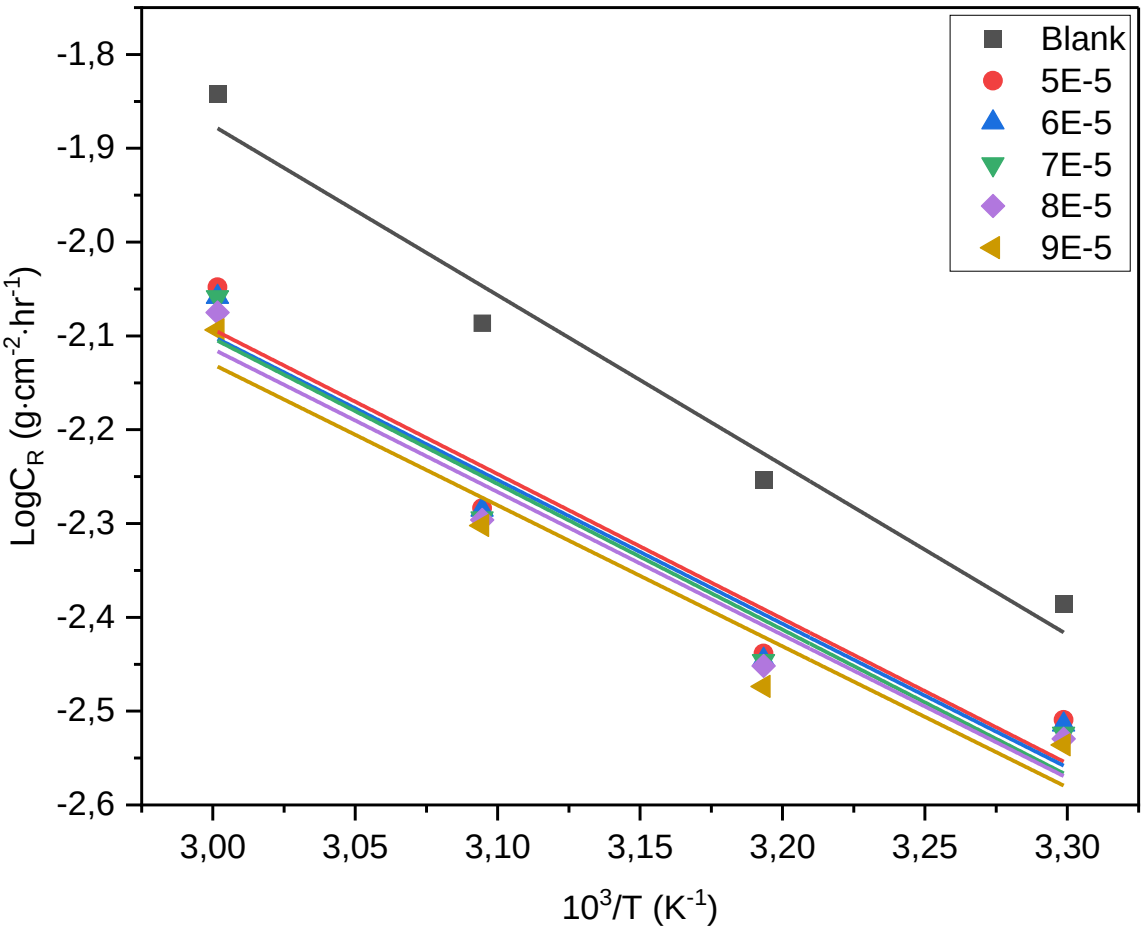

Figure 4.112: G2 Arrhenius plots (zinc).

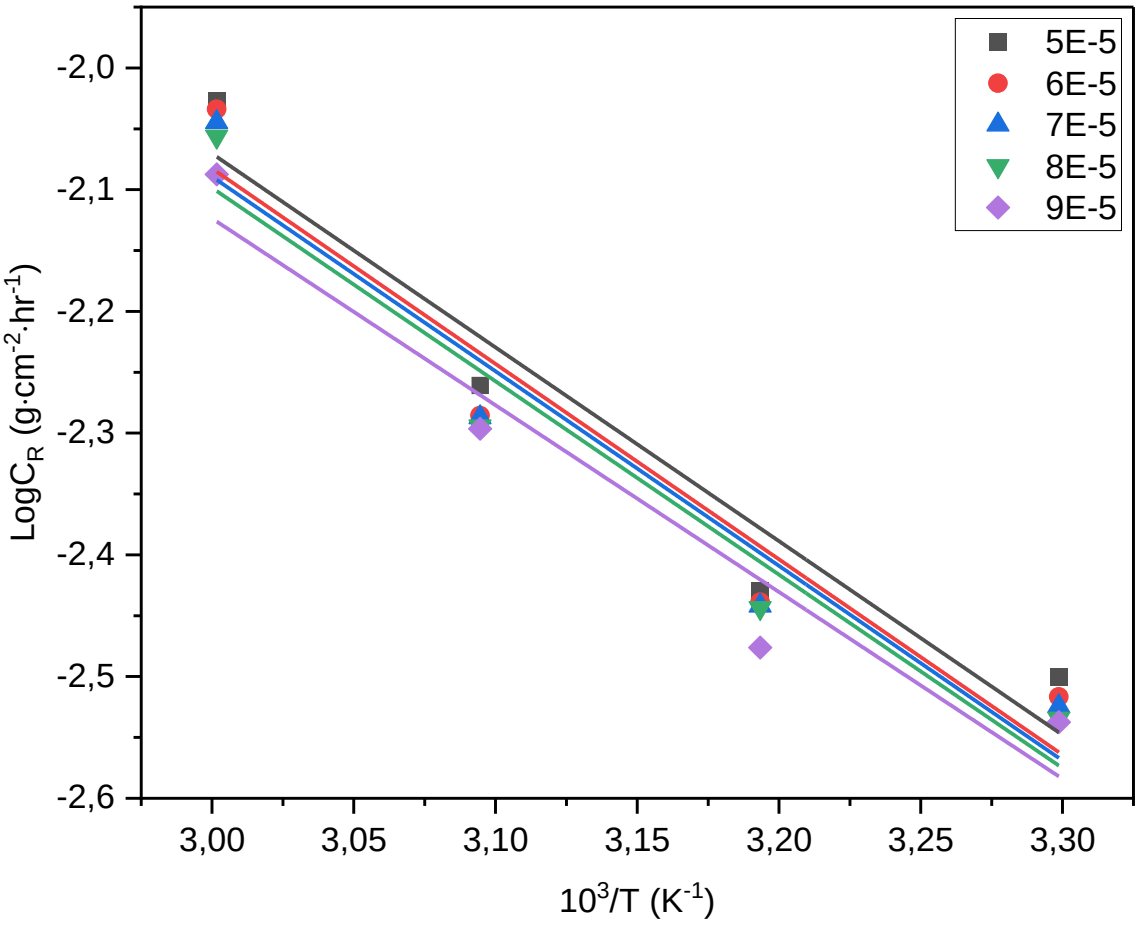

Figure 4.113: G3 Arrhenius plots (zinc).

Figures 4.114 to 4.121 show transition state plots for five different TZD concentrations. These plots were used to calculate $\Delta H°_{act}$ and $\Delta S°_{act}$ from the slopes and intercepts of the plots respectively (see Equation 17). Since the transition state equation is very similar to the Arrhenius equation [231], the plots show a very similar profile to the Arrhenius plots shown above. The slopes of all transition state plots shown are negative, ensuring that all $\Delta H°_{act}$ data is positive. As C_{inh} is increased, the magnitudes of the slopes of the transition state plots decrease, indicating an inverse proportionality relationship between C_{inh} and $\Delta H°_{act.}$ However, C_{inh} is directly proportional to $\Delta S°_{act}$ since the y-axis is negative, ensuring that a decrease in the magnitude of the y-intercept of the transition state plot with increasing C_{inh} results in an increase in $\Delta S°_{act.}$

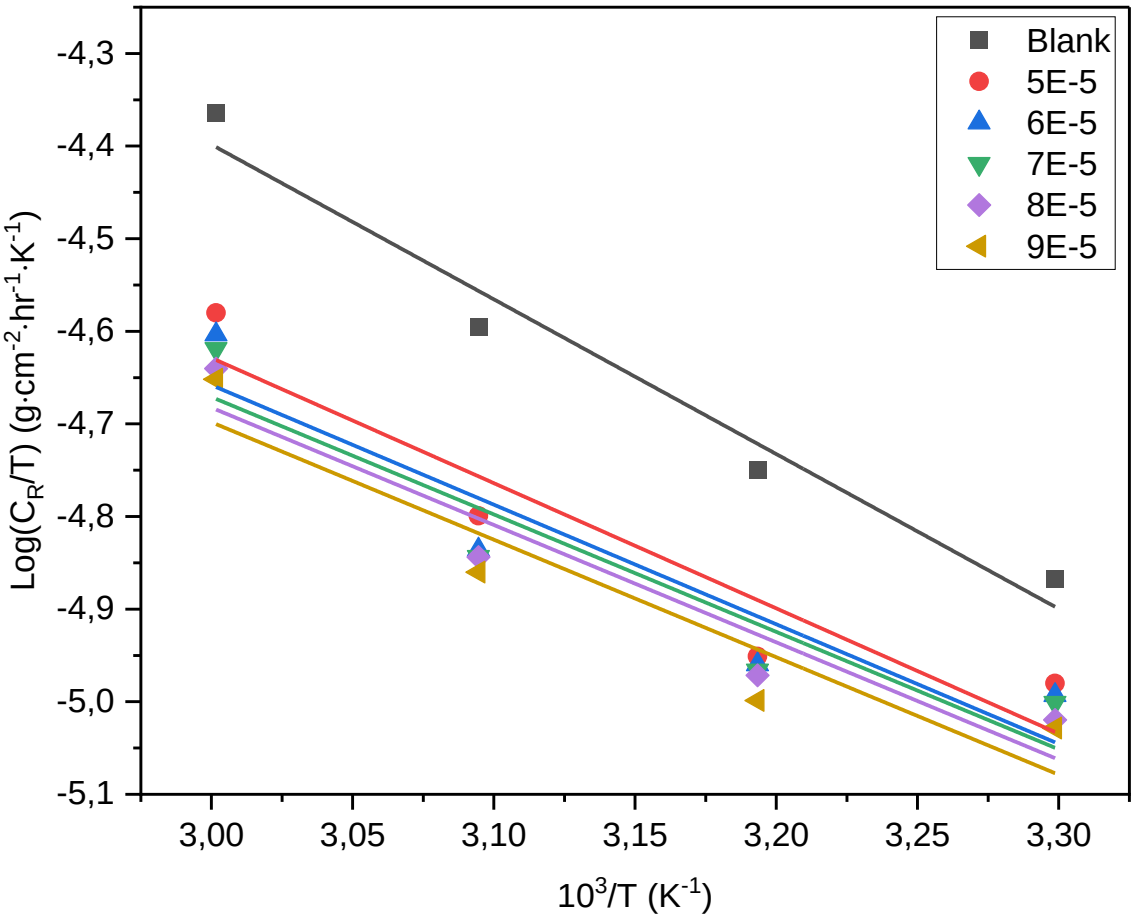

Figure 4.114: A1 Transition state plots (zinc).

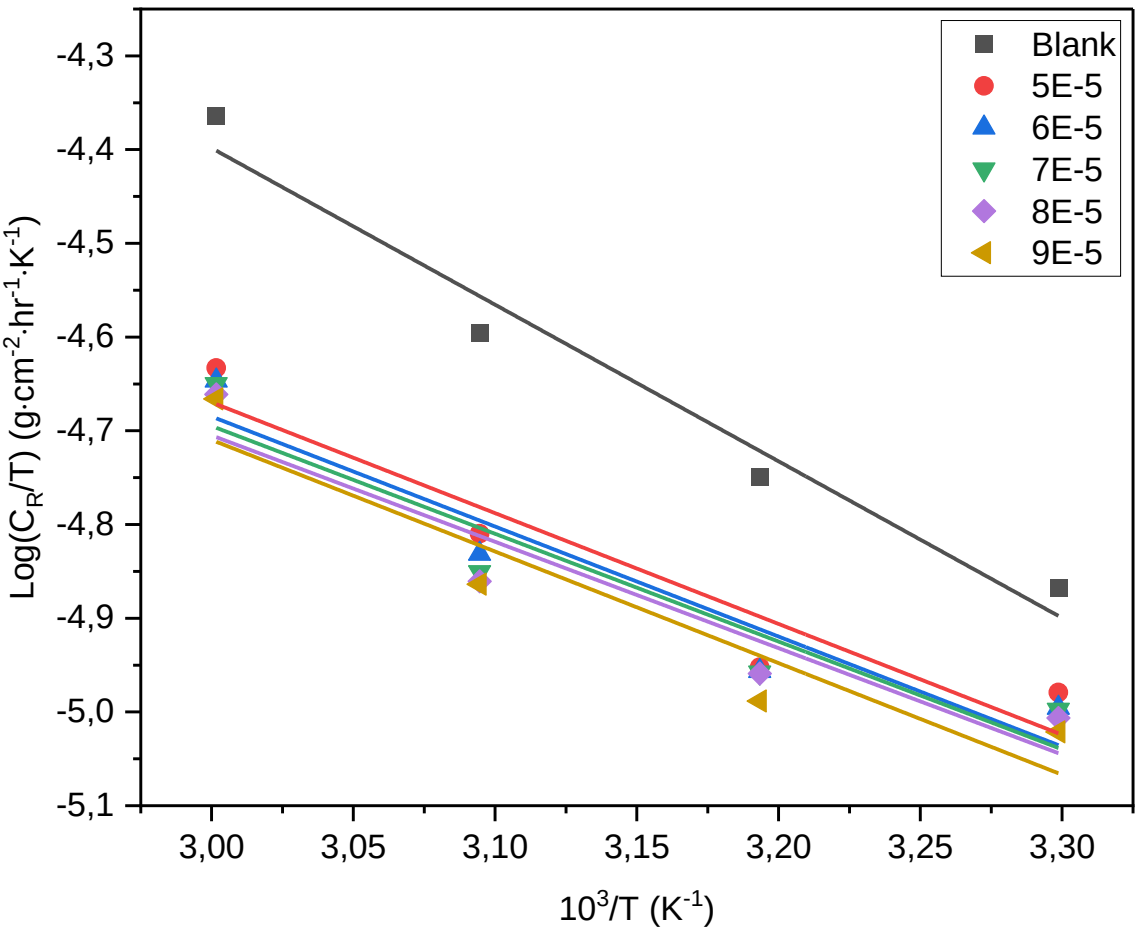

Figure 4.115: A2 Transition state plots (zinc).

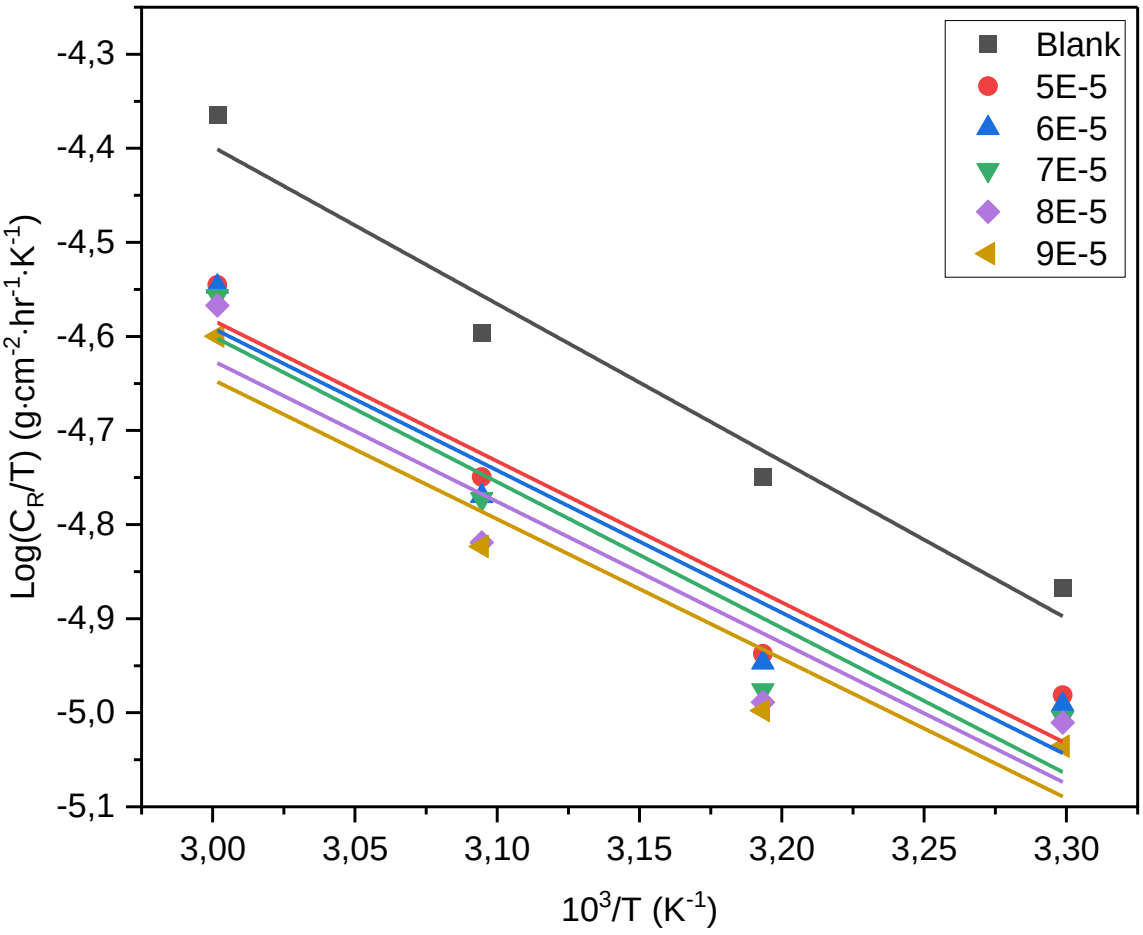

Figure 4.116: A3 Transition state plots (zinc).

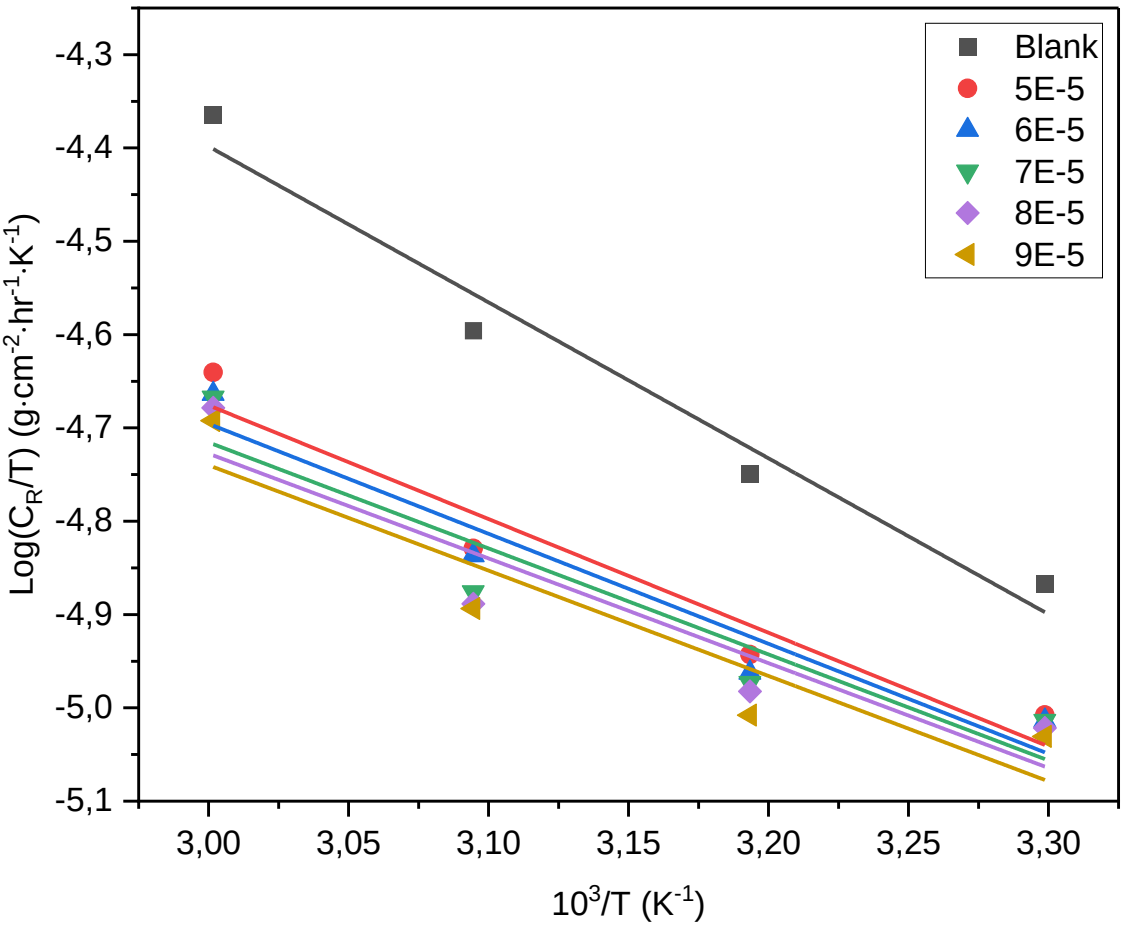

Figure 4.117: B1 Transition state plots (zinc).

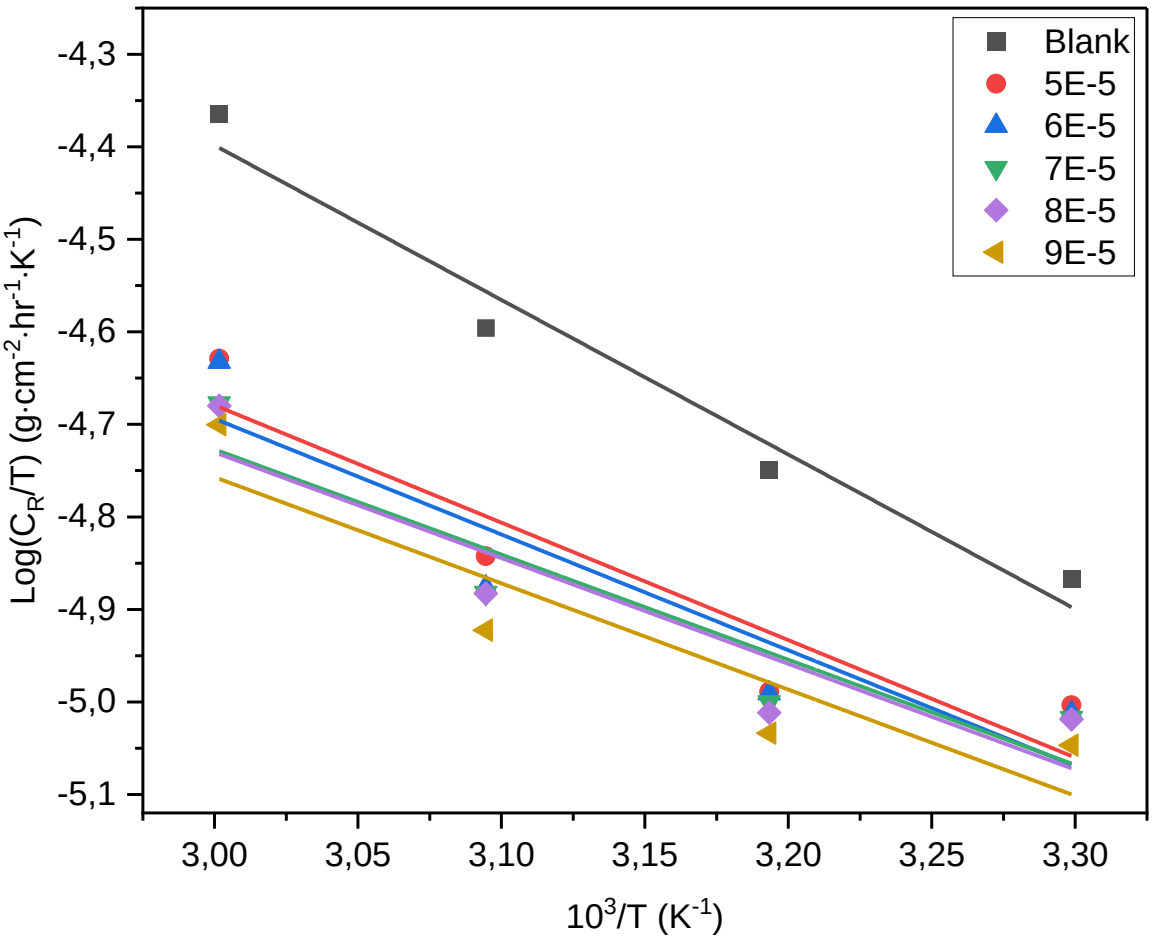

Figure 4.118: B2 Transition state plots (zinc).

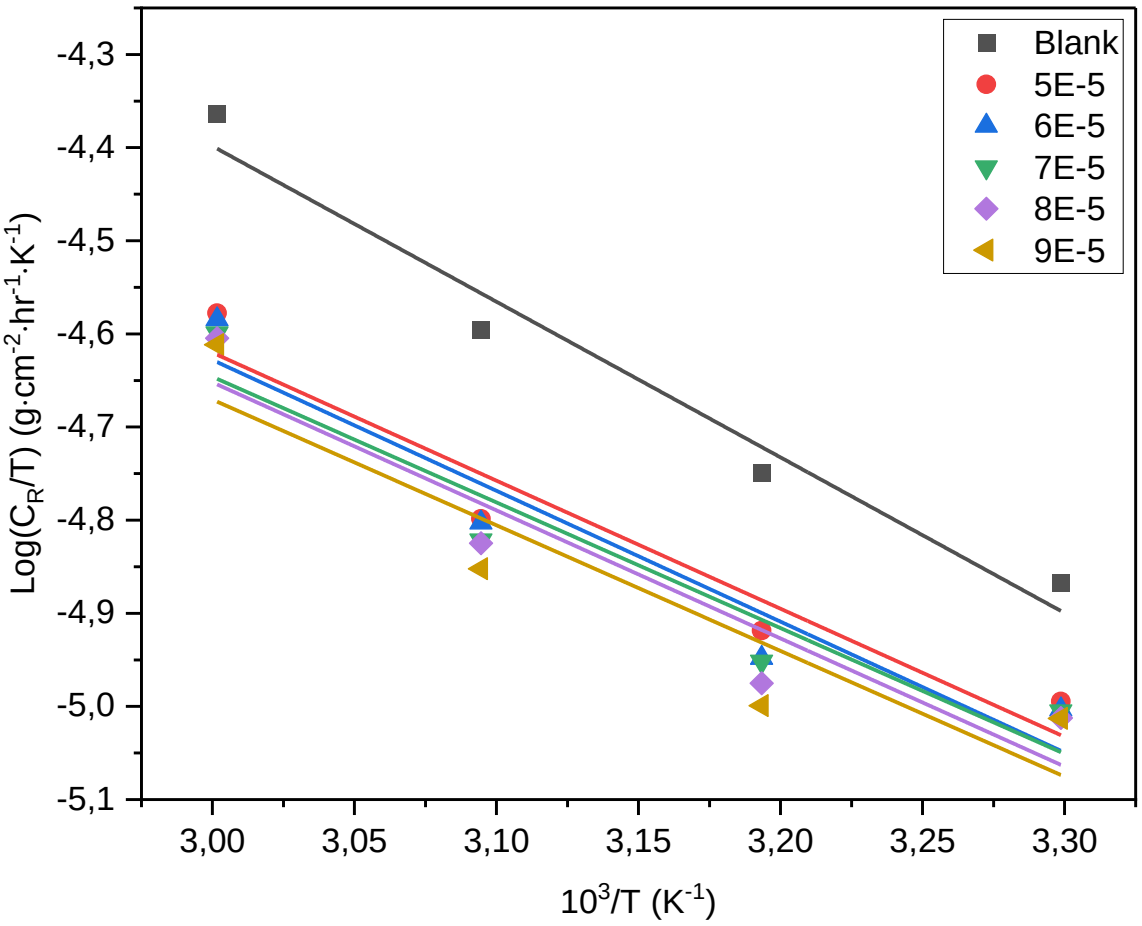

Figure 4.119: G1 Transition state plots (zinc).

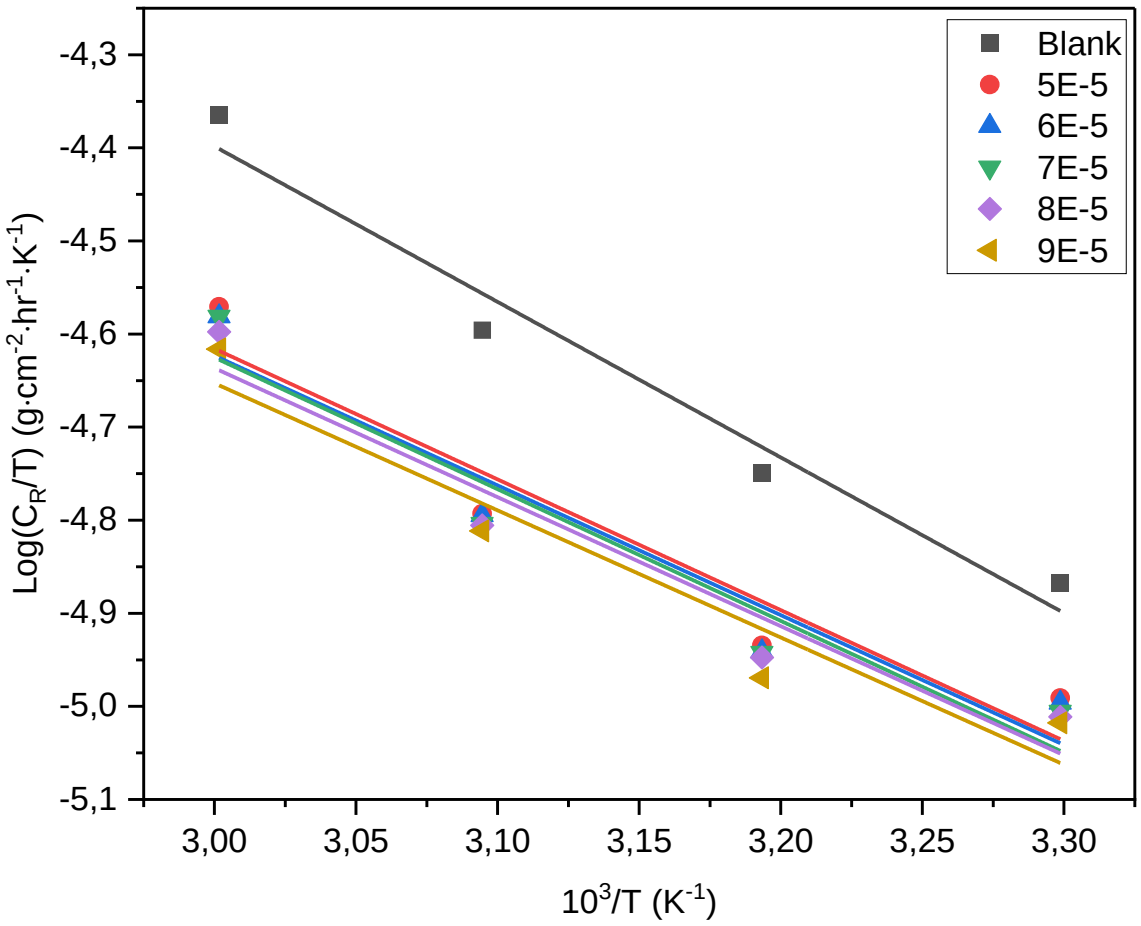

Figure 4.120: G2 Transition state plots (zinc).

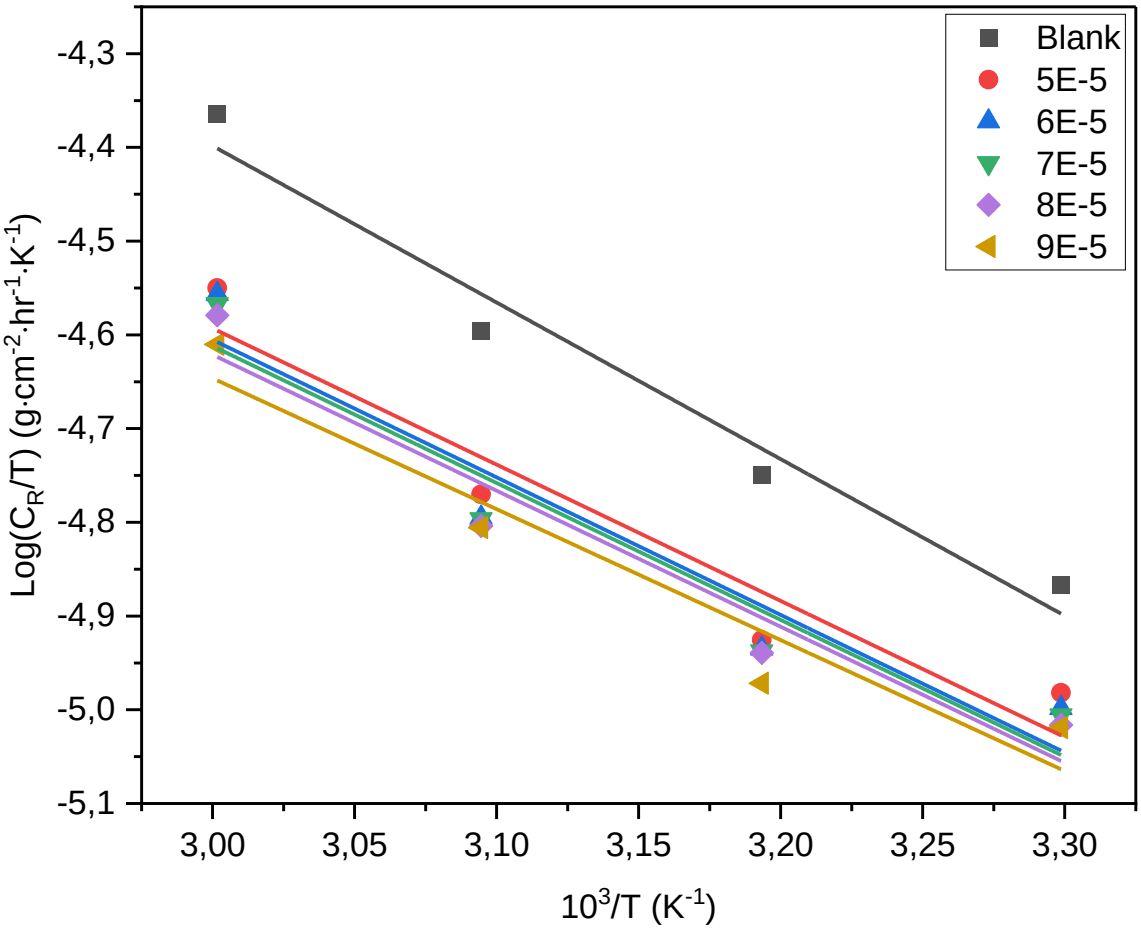

Figure 4.121: G3 Transition state plots (zinc).

As C_{inh} is increased, the E_a generally decreases for all TZDs (Table 4.9). This trend is observed when $\%IE_{WL}$ increases with increasing temperature (chemisorption) [232]. All E_a data is greater than $\Delta H°_{act}$ data, showing that the corrosion process involves a gaseous reaction, that is, the evolution of H_2(g) [233]. Equation 24 is also satisfied by the activation data obtained, an indication that the corrosion process is a unimolecular process [233]:

$$E_a - \Delta H^{\circ}_{act} = RT \qquad (24)$$

The large negative $\Delta S°_{act}$ data show a transition from disorder to order with the formation of an activated complex between the TZDs and the metal surface [234]. The general decrease in $\Delta S°_{act}$ with an increase in C_{inh} is because of the formation of more

dative covalent bonds between the TZDs and the metal surface, a conclusion also drawn by Betti *et al.* [235] when they stated that the decrease in $\Delta S°_{act}$ with increasing C_{inh} is because of the formation of an activated complex between a corrosion inhibitor and a metal surface. All $\Delta H°_{act}$ data is positive, indicating the endothermic nature of the zinc dissolution process in 1 M HCl [236].

Table 4.9: TZD activation parameters (zinc).

TZD/Blank	Concentration (M)	E_a (kJ·mol^{-1})	$\Delta H°_{act}$ (kJ·mol^{-1})	$\Delta S°_{act}$ (J·mol^{-1}·K^{-1})
Blank	-	34.64	32.00	−185.80
A1	5.00E−05	28.54	25.90	−208.52
	6.00E−05	27.37	24.73	−212.57
	7.00E−05	26.92	24.28	−214.16
	8.00E−05	26.91	24.27	−214.43
	9.00E−05	26.94	24.30	−214.64
A2	5.00E−05	25.28	22.64	−219.07
	6.00E−05	25.12	22.48	−219.85
	7.00E−05	24.66	22.02	−221.41
	8.00E−05	24.38	21.74	−222.45
	9.00E−05	25.44	22.80	−219.35
A3	5.00E−05	31.36	28.72	−199.17
	6.00E−05	31.60	28.96	−198.60
	7.00E−05	32.35	29.71	−196.53
	8.00E−05	31.35	28.71	−200.02
	9.00E−05	31.05	28.41	−201.30
B1	5.00E−05	25.97	23.33	−217.11
	6.00E−05	25.21	22.57	−219.77
	7.00E−05	24.40	21.76	−222.60
	8.00E−05	24.14	21.50	−223.61
	9.00E−05	24.26	21.62	−223.47
B2	5.00E−05	26.95	24.31	−214.23
	6.00E−05	26.61	23.97	−215.55
	7.00E−05	24.41	21.77	−222.78
	8.00E−05	24.53	21.89	−222.47

	9.00E−05	24.63	21.98	−222.71
G1	5.00E−05	28.97	26.33	−207.04
	6.00E−05	29.54	26.90	−205.48
	7.00E−05	28.48	25.84	−209.02
	8.00E−05	28.97	26.33	−207.65
	9.00E−05	28.48	25.84	−209.50
G2	5.00E−05	29.54	26.89	−205.27
	6.00E−05	29.33	26.69	−206.03
	7.00E−05	29.73	27.09	−204.87
	8.00E−05	29.18	26.54	−206.73
	9.00E−05	28.79	26.15	−208.21
G3	5.00E−05	30.48	27.84	−201.99
	6.00E−05	30.74	28.10	−201.46
	7.00E−05	30.61	27.97	−201.96
	8.00E−05	30.42	27.78	−202.71
	9.00E−05	29.38	26.74	−206.31

4.3.2 Potentiodynamic polarization

All Tafel plots shown (Figures 4.122 to 4.138) show that Log_{icorr} decreases with an increase in C_{inh}, an indication of the formation of an adsorption film on the metal surface [237]. In addition, all Tafel plots for the inhibited solutions are shifted to more anodic potentials (E_{corr} becomes more positive), an indication that the TZDs primarily inhibit corrosion of zinc by directly preventing metal dissolution [238]. Figures 4.127 and 4.131 show a distinct U-shaped anodic curve as WE potential becomes more positive, showing passivation (sudden drop in i_{corr}) and after a short while, pitting (at the pitting potential (E_{pit})) shown by a sudden increase in i_{corr} due to pitting susceptibility to Cl^- ions [239-241]. All Tafel plots shown become rough at more anodic potentials, an indication of metastable pitting of the ZnO passive film [242].

Figure 4.136 shows a Tafel plot with three E_{corr}. A similar Tafel plot has been observed elsewhere [240]. Li *et al.* [240] attributed such a Tafel plot to two things: the magnitude of the scan rate (specifically low scan rates) and the metal's microstructure. At low scan rates, the frequency of the potential supplied to the WE is much lower [243], allowing sufficient time for equilibrium to be established between the two redox half-reactions, enabling E_{corr} to be achieved. Three separate studies on zinc passivation stated that most passive films consist of two layers, one of which is an inner defective compact oxide [244-246]. Any microstructural defects in a metal will exacerbate the flaws in what already would have been a defective inner oxide layer in a metal with less microstructural defects, leading to a further decline in the protective abilities of a passive film [247]. More of the metal surface would then be exposed to the corrosive environment for longer periods, allowing equilibrium between the two redox half-reactions to be much more easily attained. This is what Li *et al.* [240] were referring to when they noted the influence of microstructure defects in metals on corrosion resilience.

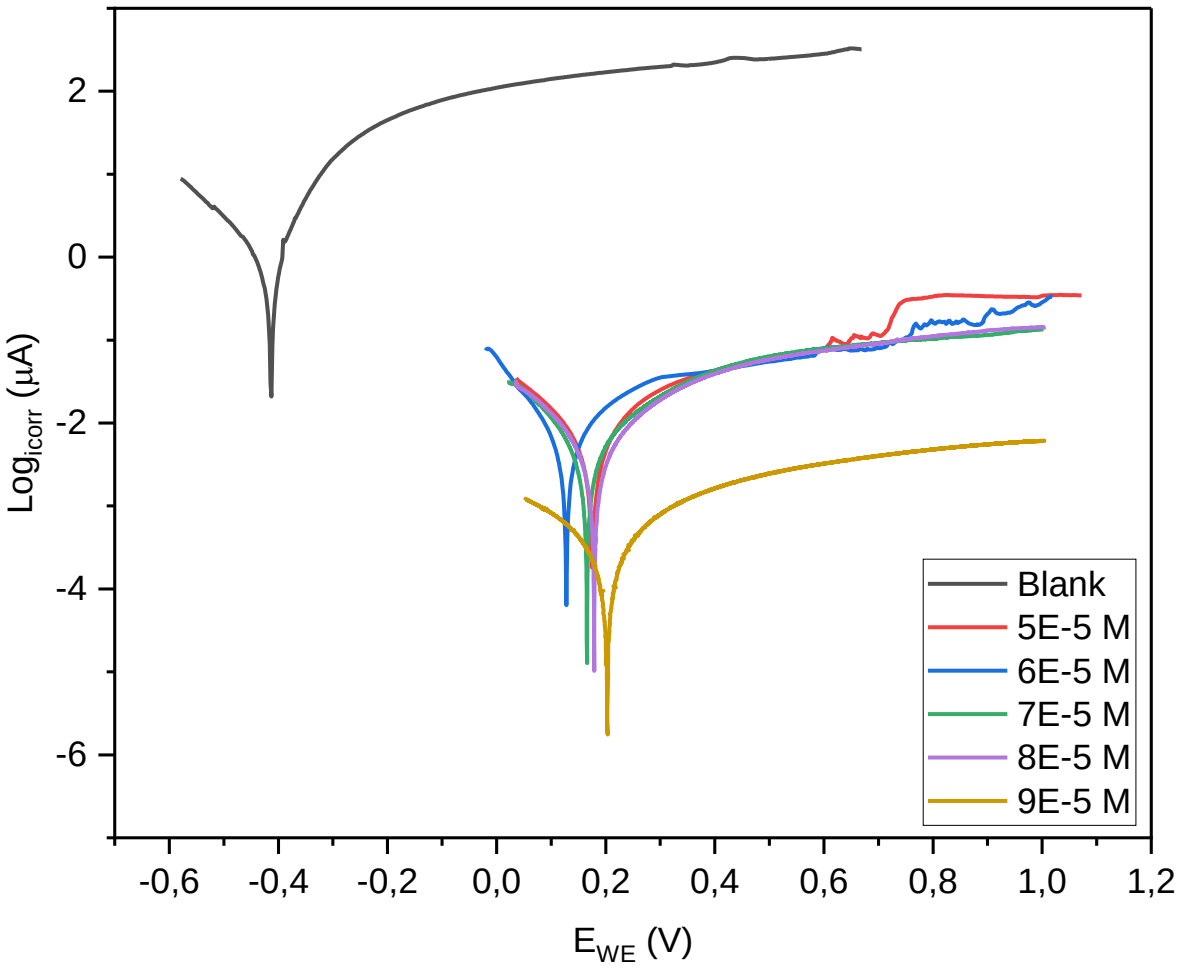

Figure 4.122: Full Tafel plots for A1 (zinc).

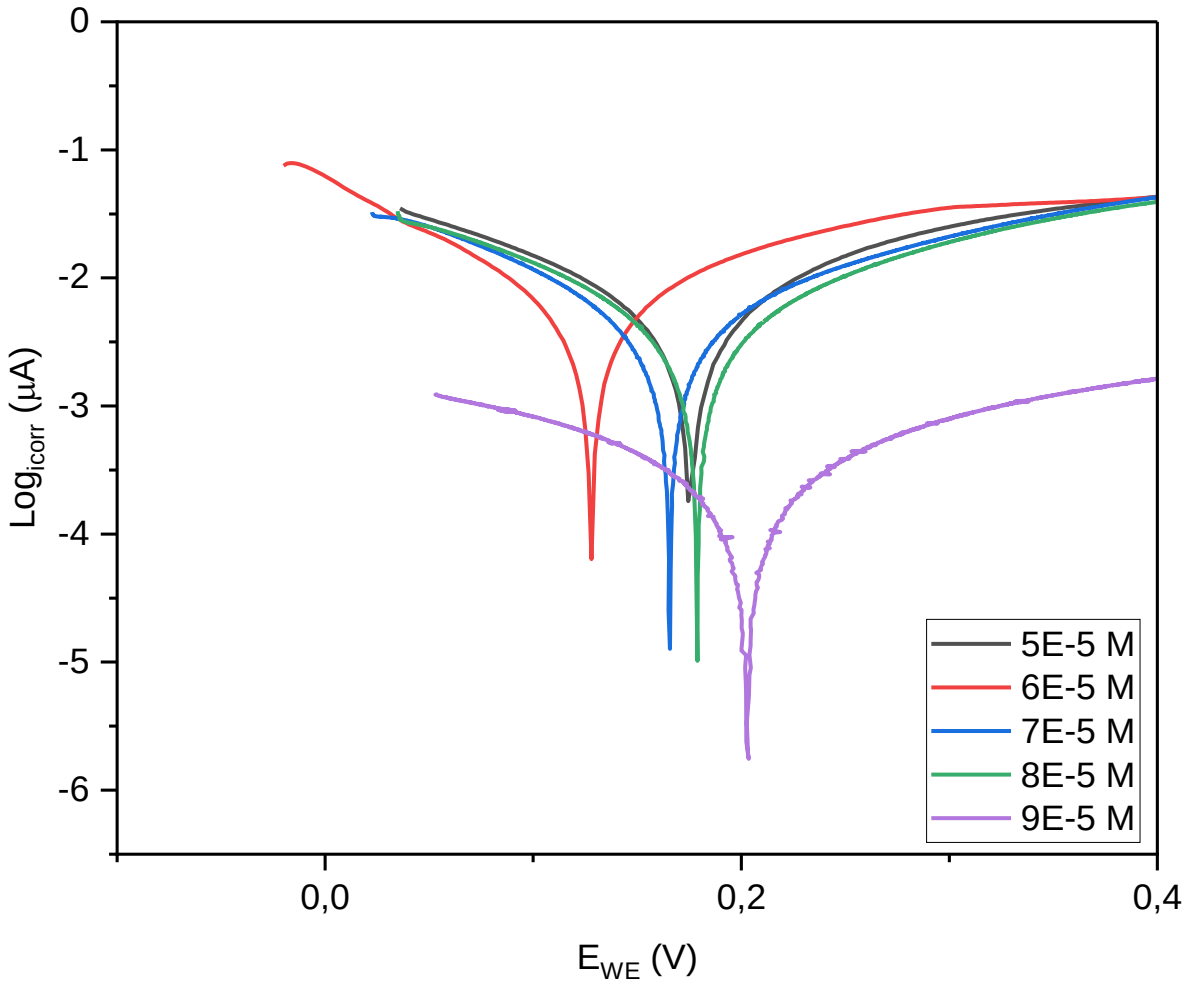

Figure 4.123: Expanded Tafel plots for A1 (zinc).

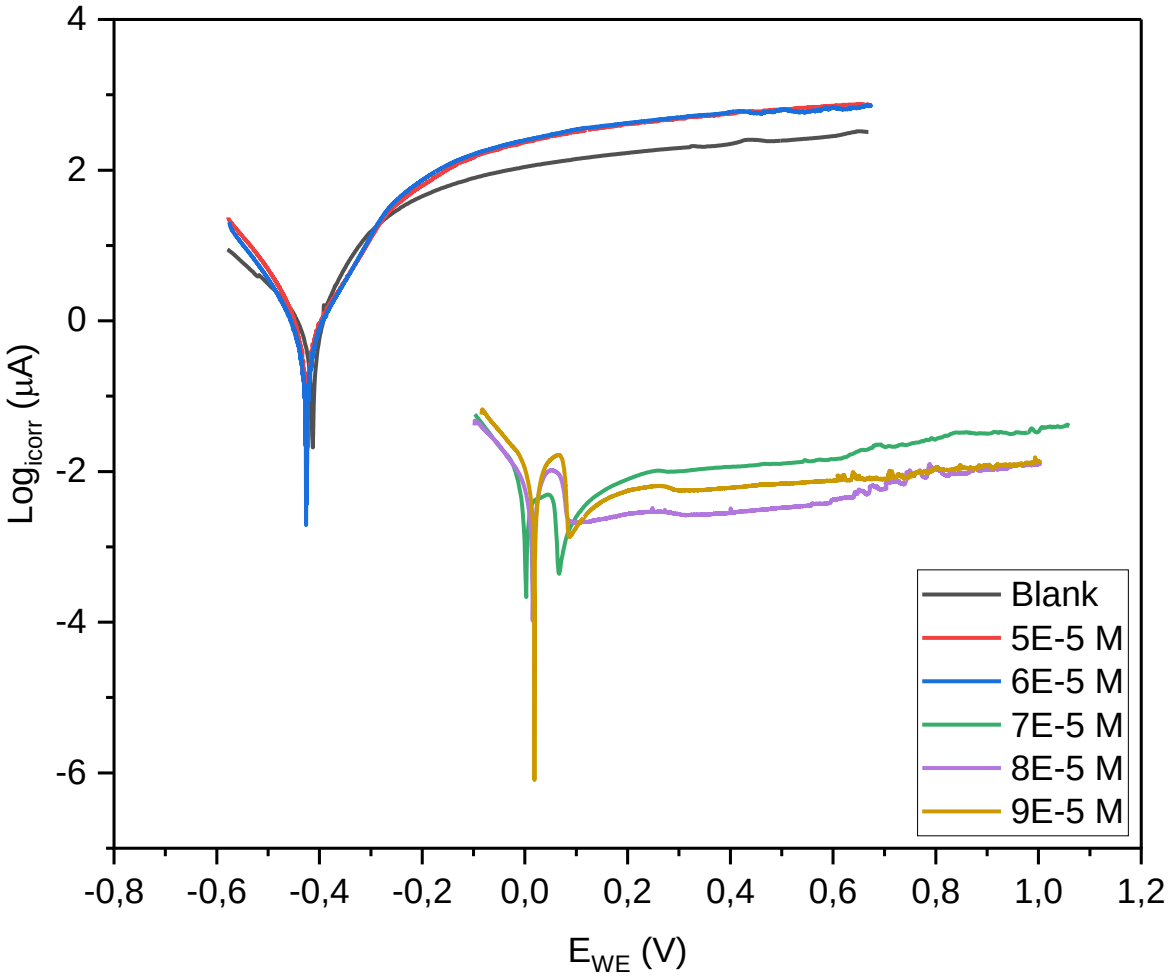

Figure 4.124: Full Tafel plots for A2 (zinc).

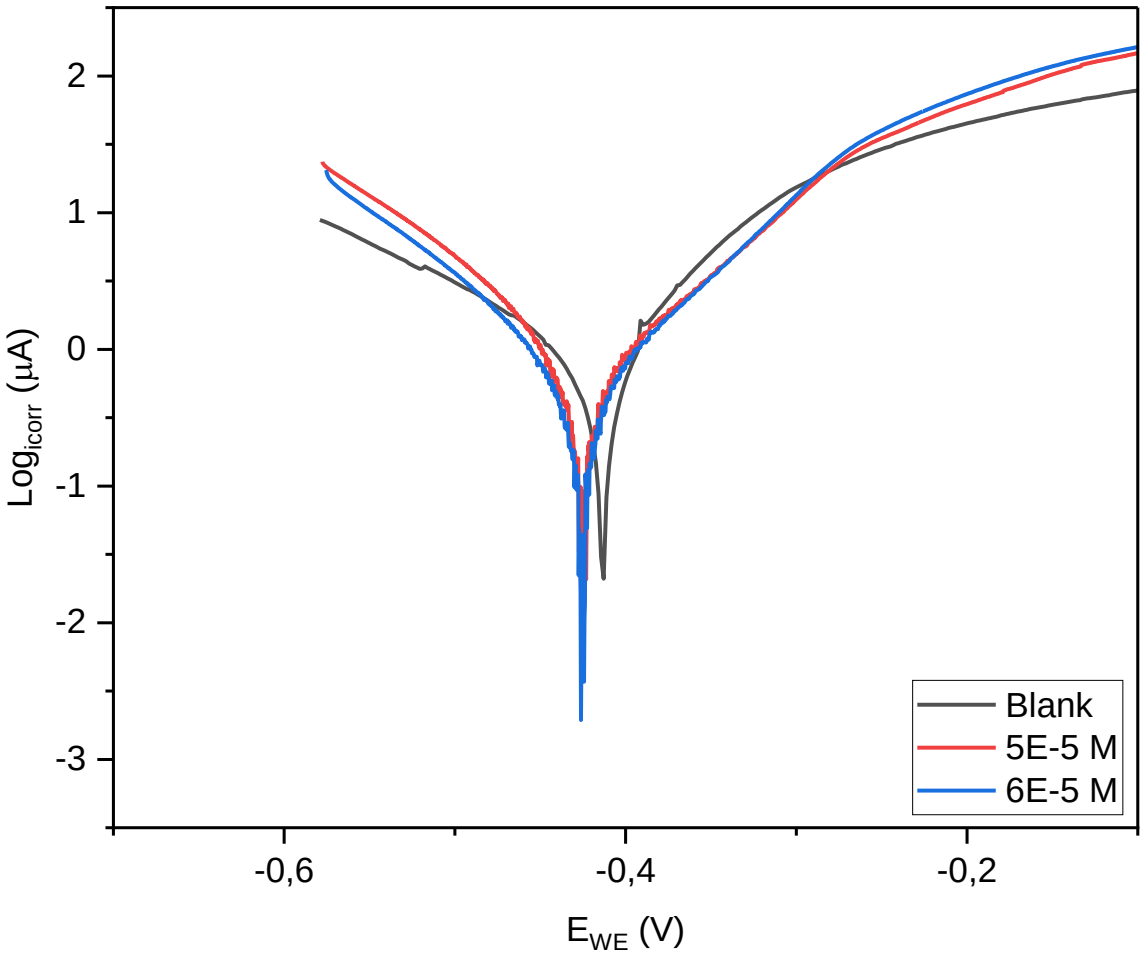

Figure 4.125: First expanded Tafel plots for A2 (zinc).

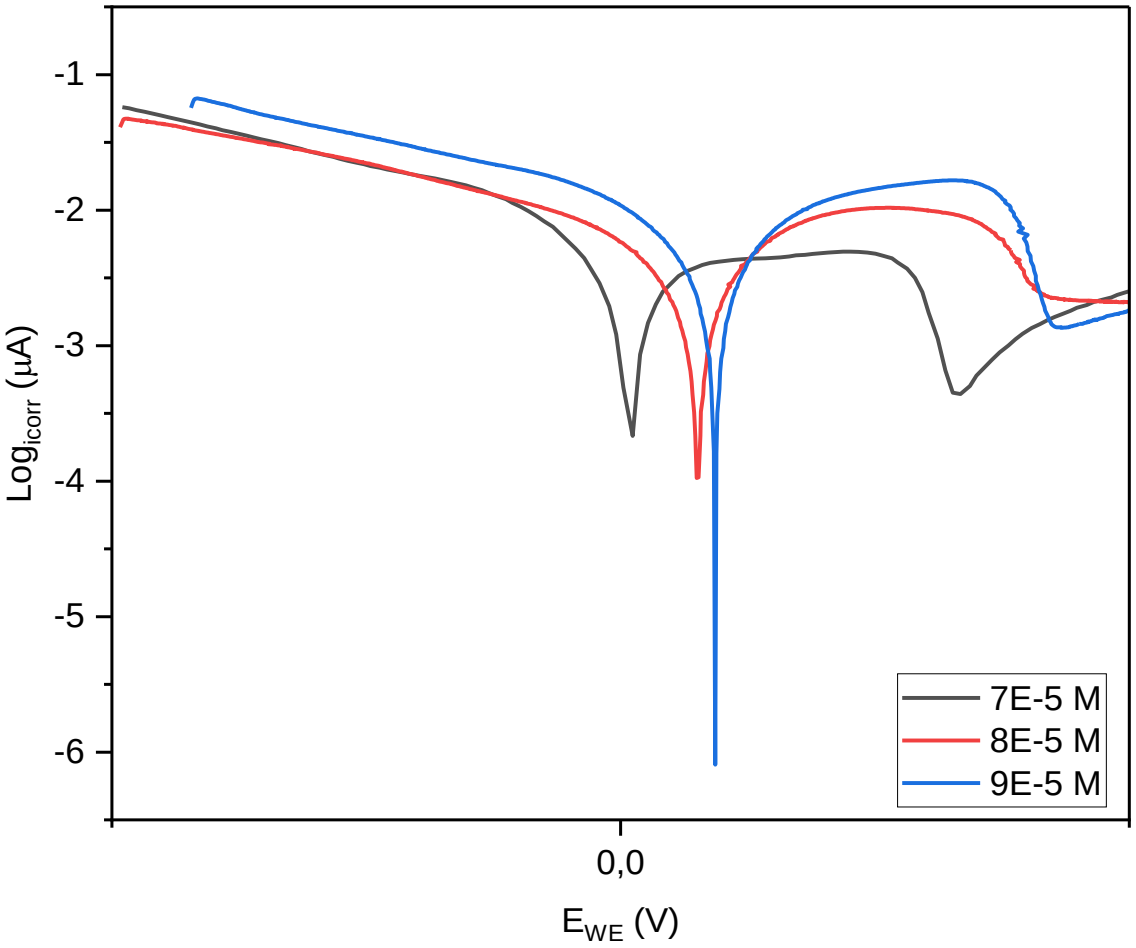

Figure 4.126: Second expanded Tafel plots for A2 (zinc).

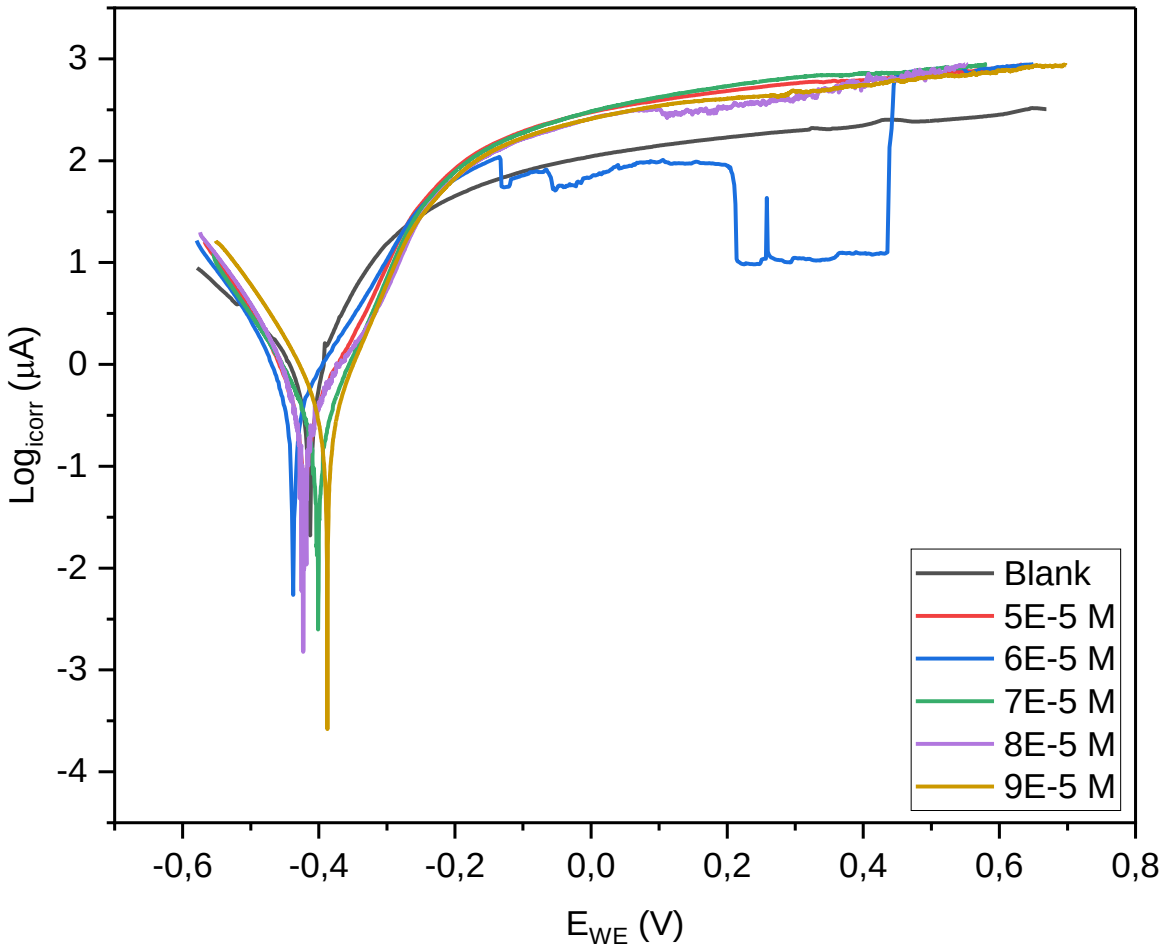

Figure 4.127: Full Tafel plots for A3 (zinc).

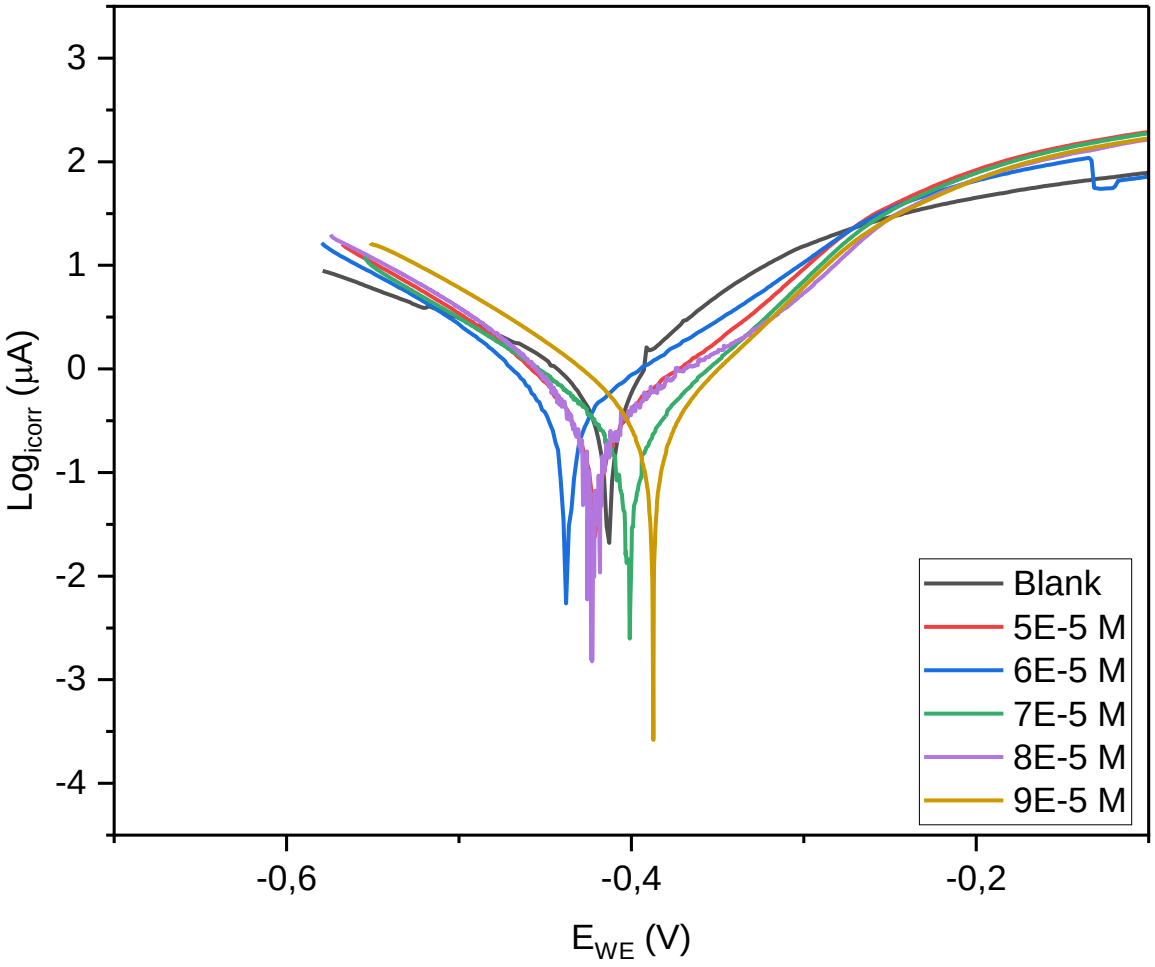

Figure 4.128: Expanded Tafel plots for A3 (zinc).

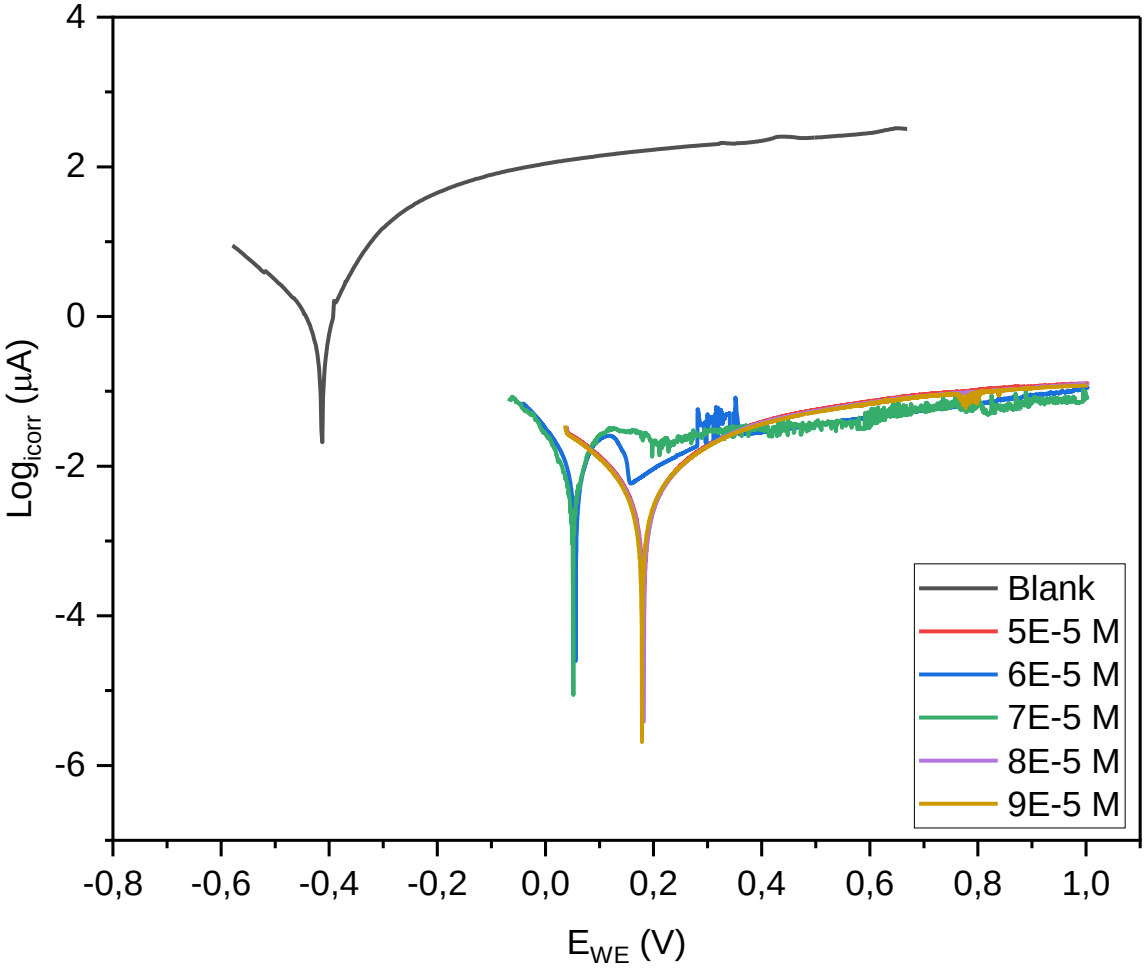

Figure 4.129: Full Tafel plots for B1 (zinc).

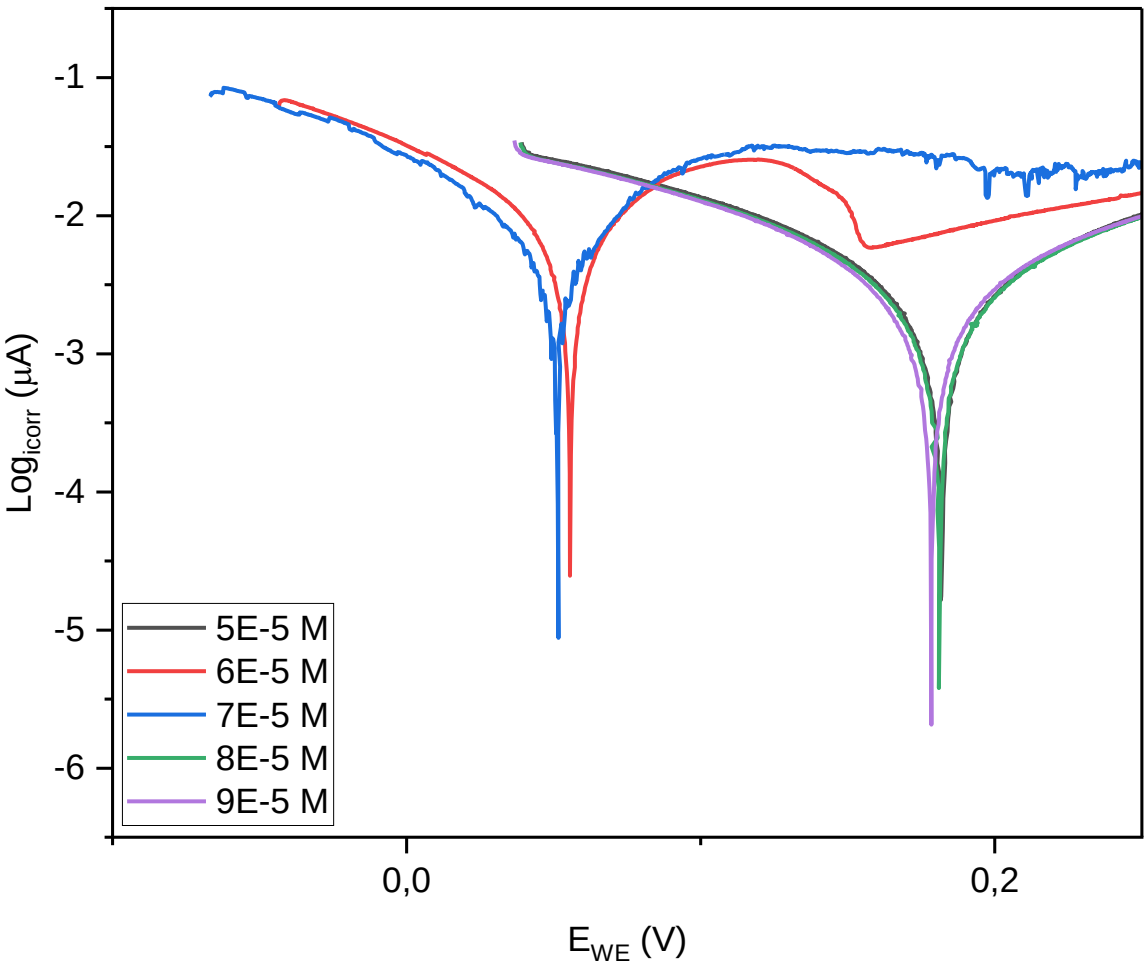

Figure 4.130: Expanded Tafel plots for B1 (zinc).

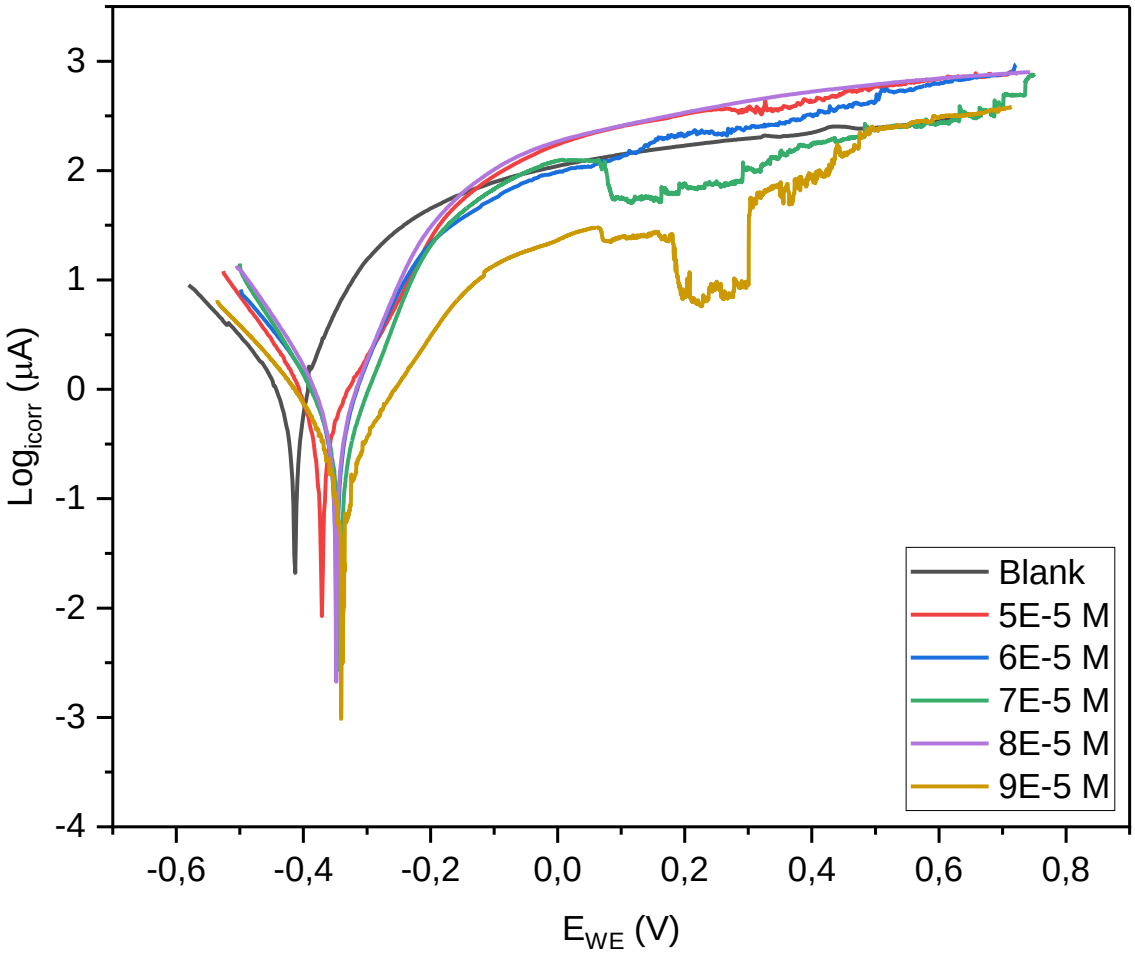

Figure 4.131: Full Tafel plots for B2 (zinc).

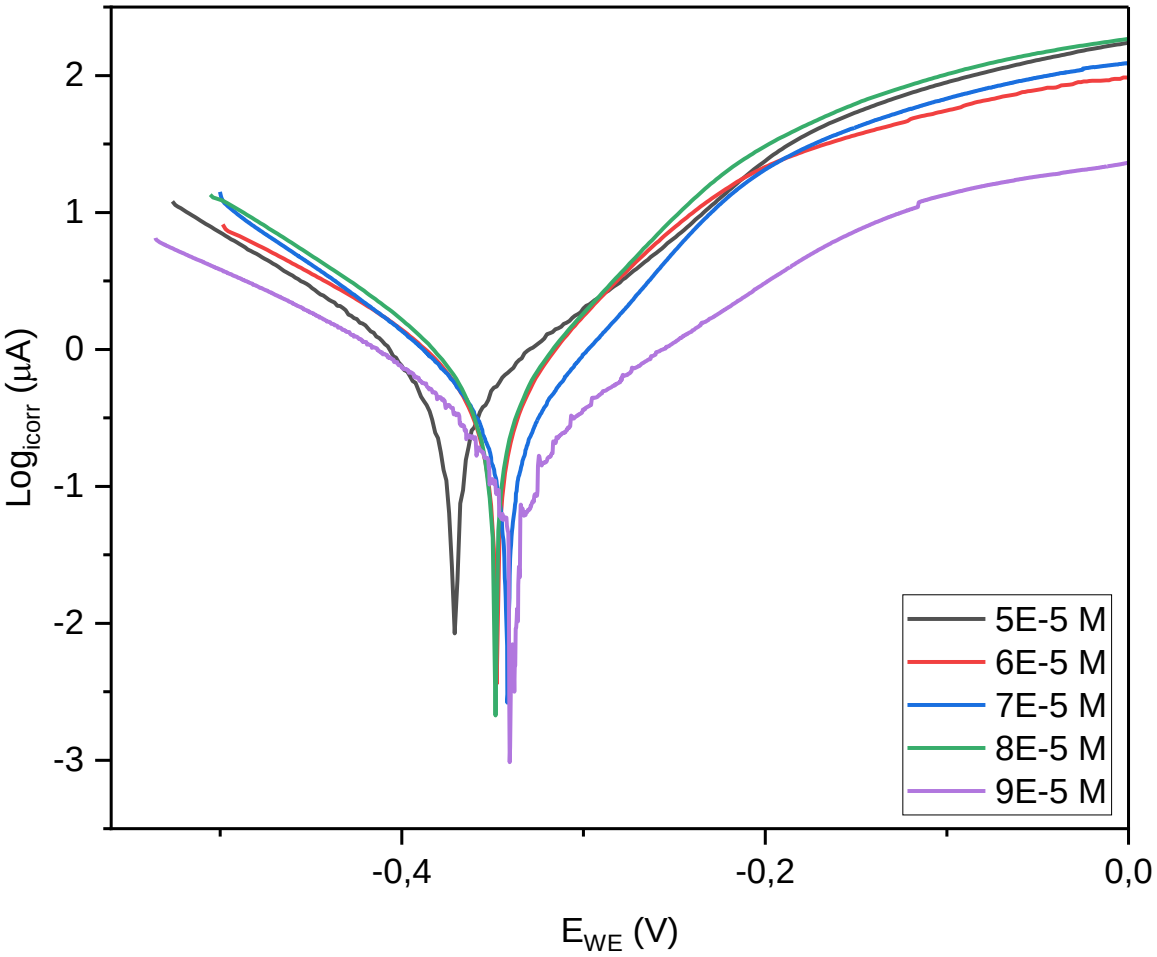

Figure 4.132: Expanded Tafel plots for B2 (zinc).

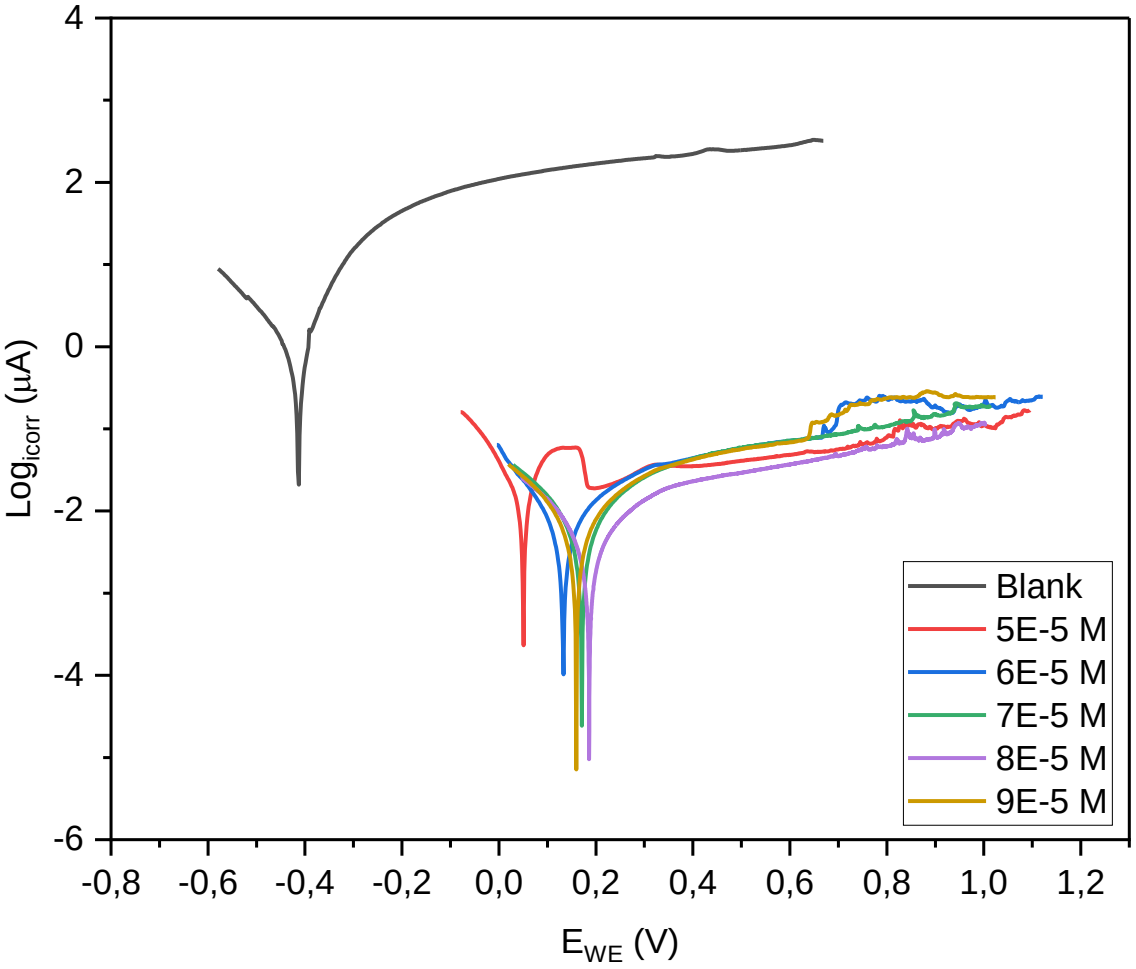

Figure 4.133: Full Tafel plots for G1 (zinc).

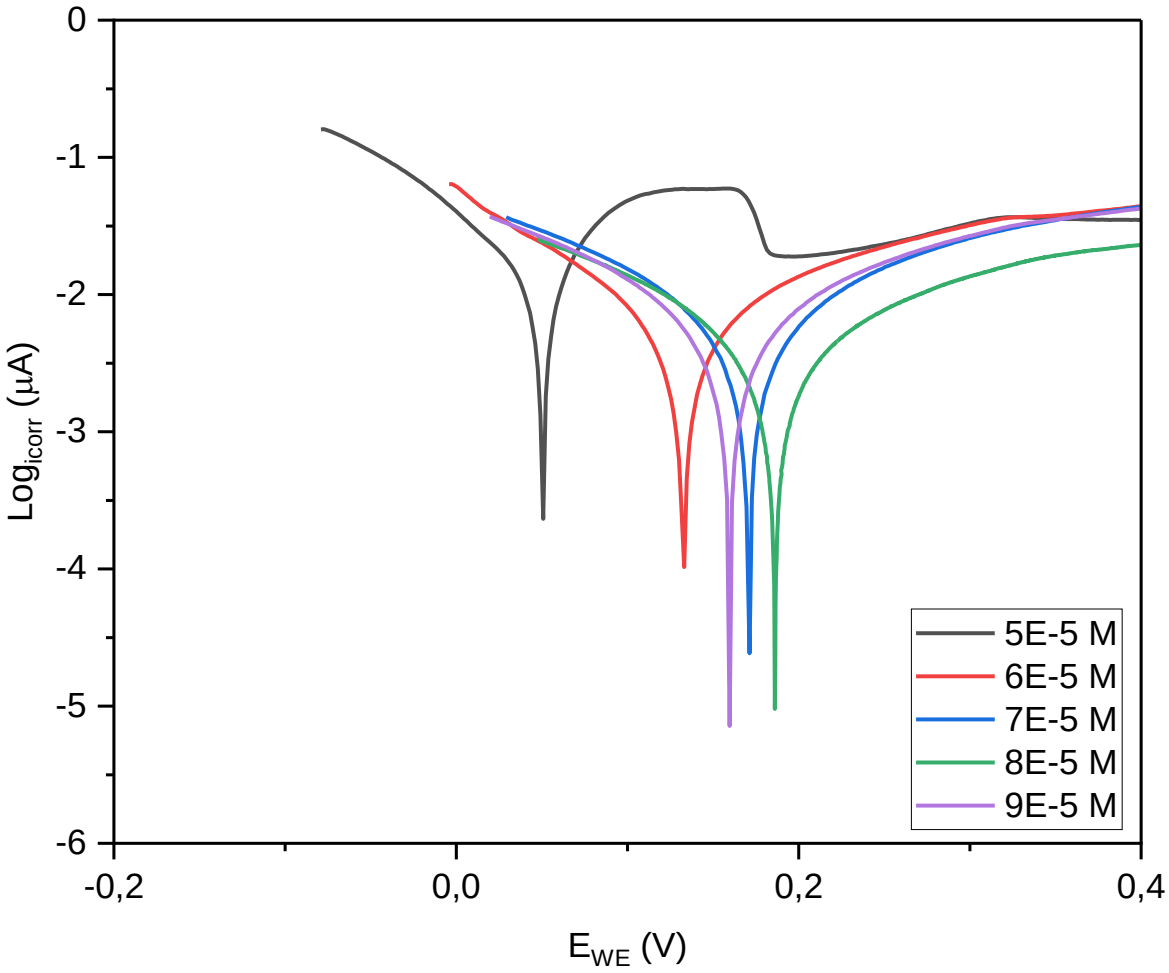

Figure 4.134: Expanded Tafel plots for G1 (zinc).

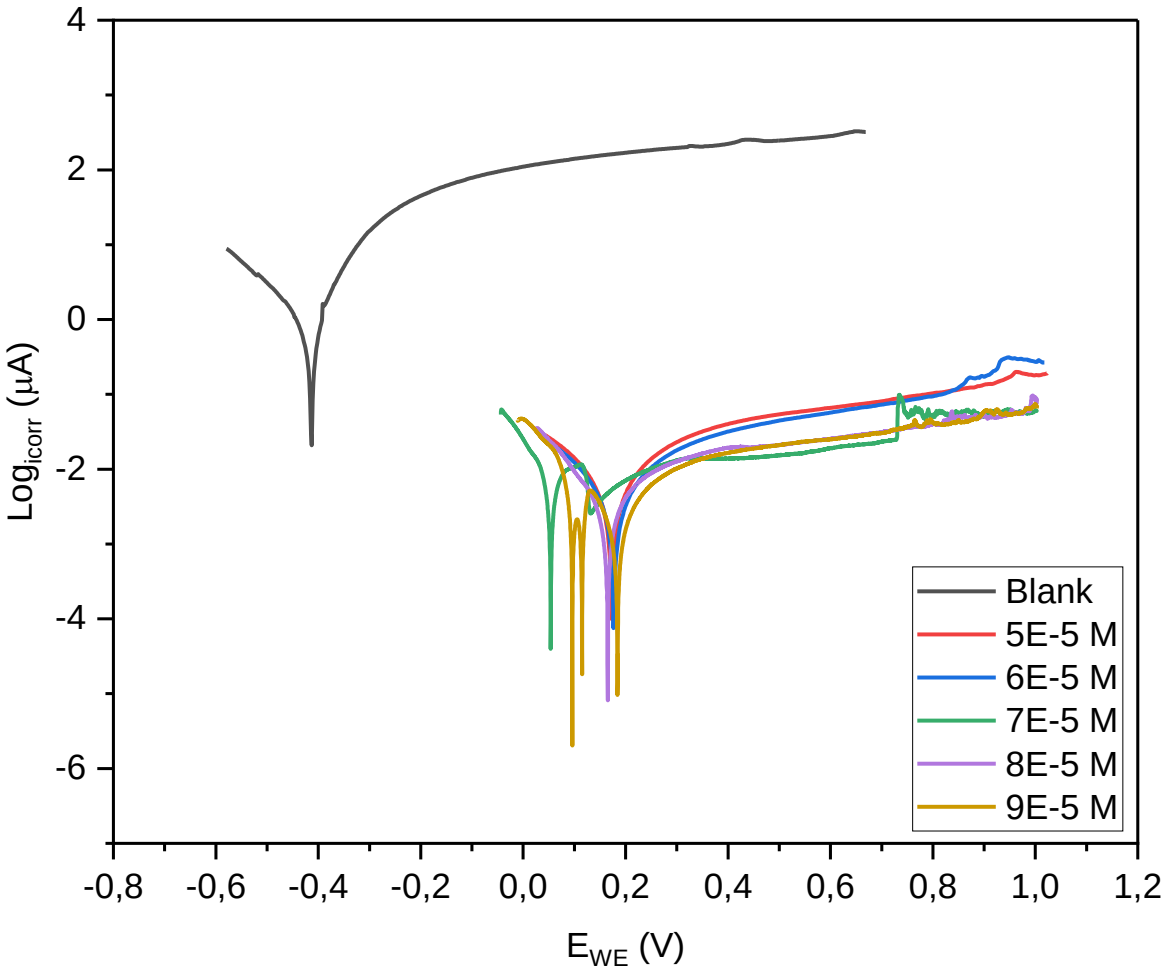

Figure 4.135: Full Tafel plots for G2 (zinc).

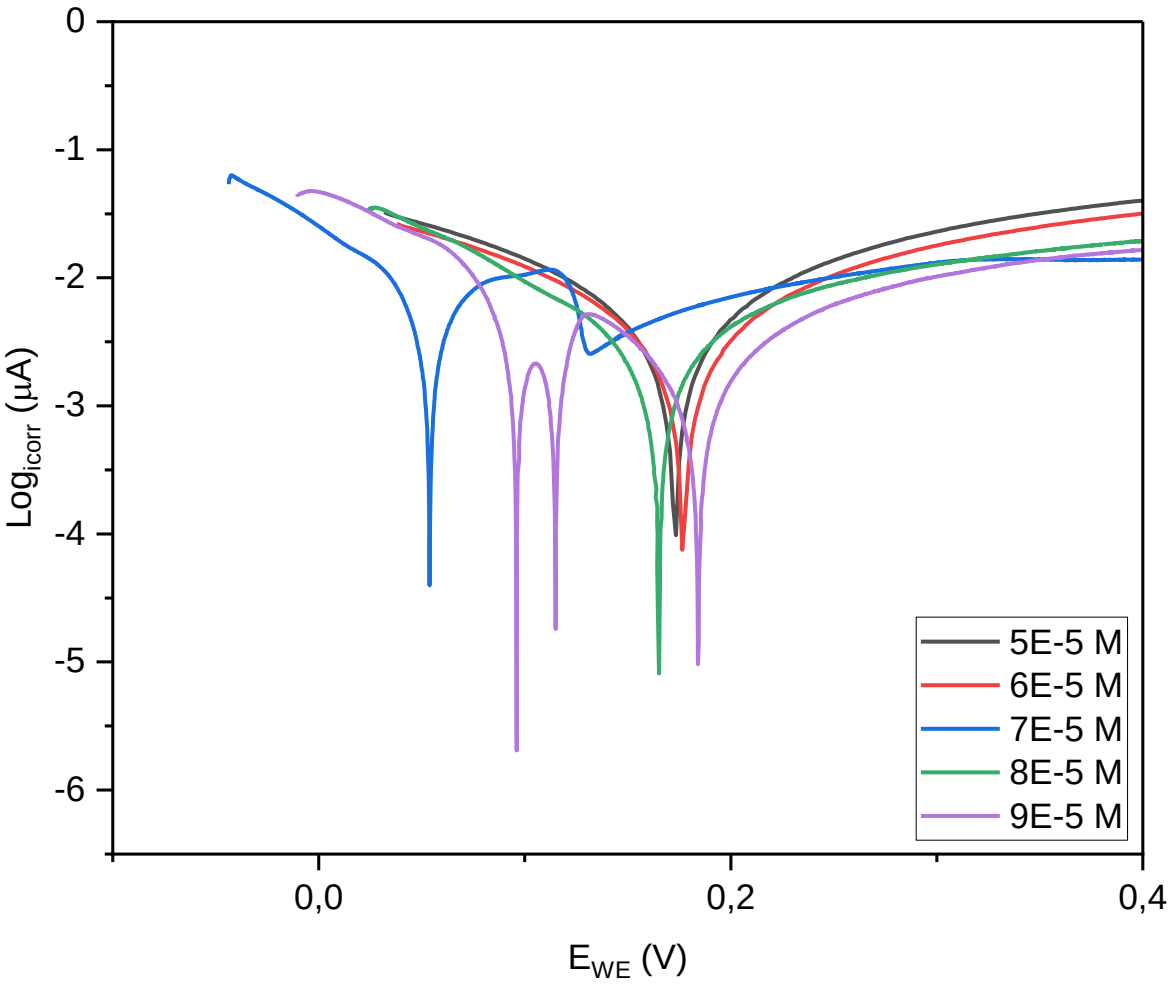

Figure 4.136: Expanded Tafel plots for G2 (zinc).

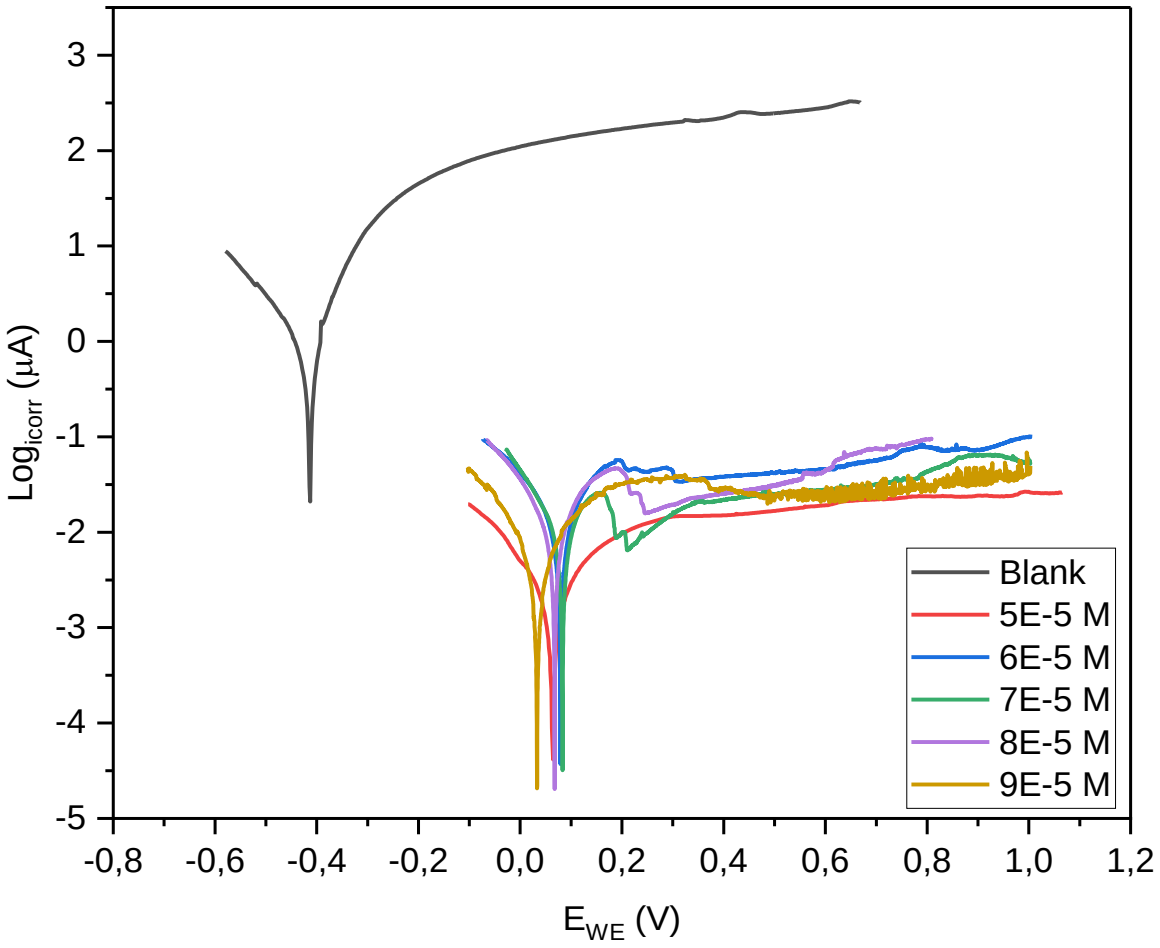

Figure 4.137: Full Tafel plots for G3 (zinc).

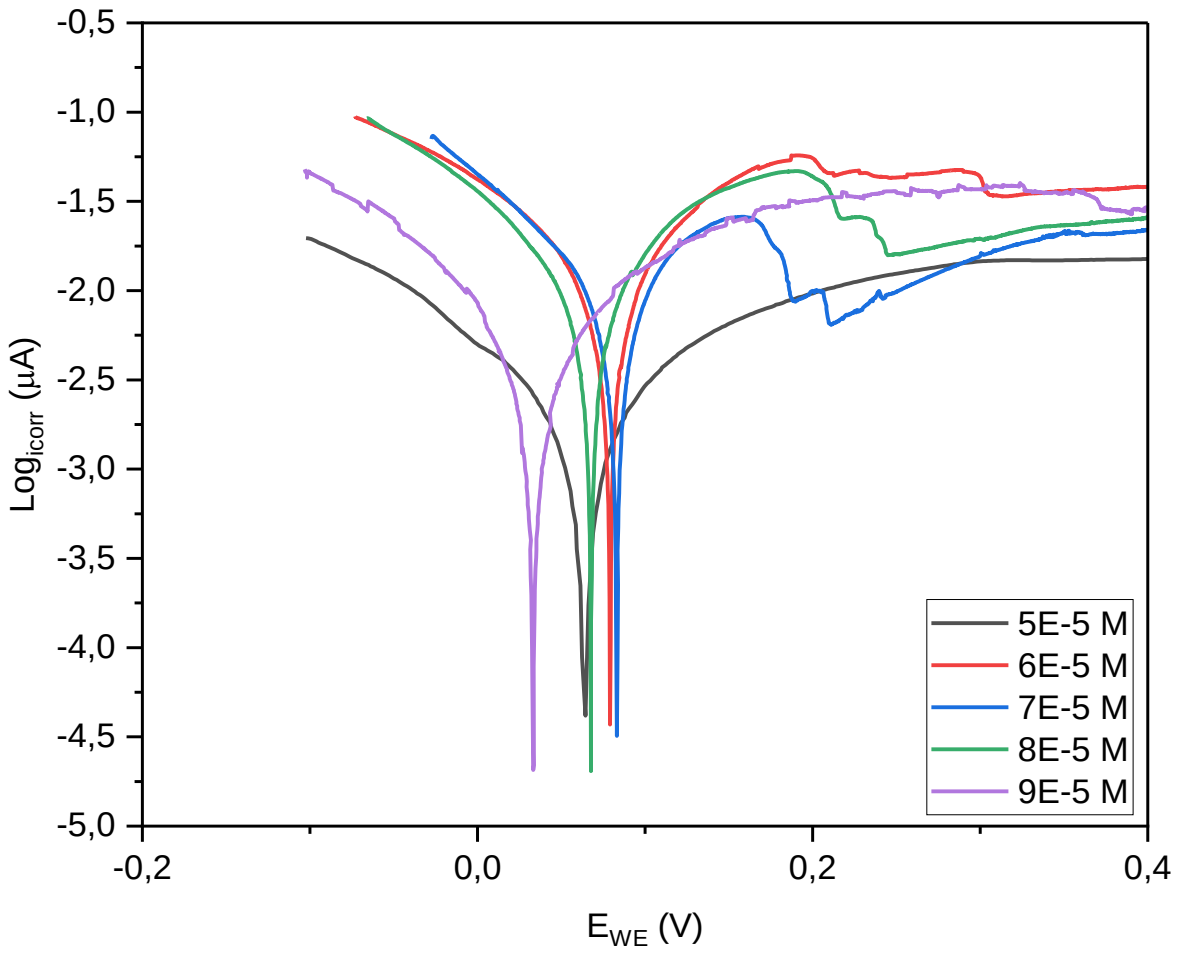

Figure 4.138: Expanded Tafel plots for G3 (zinc).

The parameters shown in Table 4.10 were obtained using Biologic EC-Lab software (see Section 4.2.2). As C_{inh} is increased, C_R, i_{corr}, R_p and $\%IE_{PDP}$ decrease, decrease, increase, and increase respectively [248]. This can be explained by an increase in θ, indicating the formation of an adsorption film on the metal surface [248].

Apart from A3 and B2, the deviation from the E_{corr} of the uninhibited solution is >85mV, an indication that the TZDs inhibit corrosion by acting at either the anodic or cathodic sites on the metal surface, not both [249]. Given the distinct shift in the Tafel plots towards more anodic potentials, it can be said that the TZDs inhibit zinc corrosion in 1 M HCl by inhibiting the oxidation half-reaction (see Equation 10).

Table 4.10: TZD PDP parameters (zinc).

TZD/Blank	Concentration (M)	C_R (mpy)	E_{corr} (mV)	R_p (Ω)	β_a (mV·dec^{-1})	β_c (mV·dec^{-1})	i_{corr} (µA)	%IE_{PDP}
Blank	-	568.05	−420.08	0.03	97.00	161.60	961.94	-
A1	5.00E−05	1.64	127.46	6.04	83.70	72.00	2.78	99.71
	6.00E−05	1.17	179.48	7.39	67.20	67.30	1.98	99.79
	7.00E−05	0.55	166.21	8.93	37.70	39.40	0.94	99.90
	8.00E−05	0.41	178.92	9.70	30.80	30.60	0.69	99.93
	9.00E−05	0.03	202.95	170.79	41.20	42.20	0.05	99.99
A2	5.00E−05	3.06	−423.61	0.03	88.60	76.60	518.62	46.09
	6.00E−05	1.15	−425.26	0.05	42.50	41.30	194.21	79.81
	7.00E−05	2.61	20.93	2.38	43.70	54.60	4.42	99.54
	8.00E−05	2.42	16.35	3.97	69.30	81.50	4.10	99.57
	9.00E−05	1.60	5.04	4.35	77.80	41.80	2.72	99.72
A3	5.00E−05	1.66	−441.21	0.05	85.90	50.90	281.71	70.71
	6.00E−05	1.54	−383.73	0.06	59.60	78.00	261.15	72.85
	7.00E−05	1.41	−417.55	0.06	76.50	61.60	239.57	75.10
	8.00E−05	1.33	−421.07	0.06	73.80	57.20	224.42	76.67
	9.00E−05	1.00	−400.58	0.08	58.70	68.20	170.17	82.31
B1	5.00E−05	3.37	57.31	2.38	59.10	66.50	5.71	99.41
	6.00E−05	2.53	50.34	2.85	55.10	57.20	4.28	99.55
	7.00E−05	0.93	182.66	9.48	68.20	69.20	1.57	99.84
	8.00E−05	0.79	182.28	9.93	59.80	61.90	1.33	99.86
	9.00E−05	0.70	178.33	10.05	57.50	52.60	1.19	99.88
B2	5.00E−05	284.10	−370.56	0.05	102.10	107.40	481.10	49.99
	6.00E−05	216.67	−347.48	0.04	68.50	83.50	366.91	61.86
	7.00E−05	213.91	−346.30	0.05	68.60	94.40	362.23	62.34
	8.00E−05	141.97	−337.90	0.07	66.00	83.80	240.41	75.01

	9.00E−05	121.19	−341.50	0.12	121.90	107.00	205.23	78.67
G1	5.00E−05	6.28	51.21	1.52	64.00	89.10	10.63	98.90
	6.00E−05	1.57	131.68	5.90	81.00	65.60	2.67	99.72
	7.00E−05	0.99	160.30	6.87	52.40	53.30	1.67	99.83
	8.00E−05	0.89	170.48	6.85	49.10	45.80	1.50	99.84
	9.00E−05	0.75	186.45	10.24	63.20	56.90	1.27	99.87
G2	5.00E−05	2.08	55.24	3.10	55.60	45.90	3.53	99.63
	6.00E−05	1.23	172.19	7.83	78.00	72.00	2.08	99.78
	7.00E−05	0.97	166.31	10.75	86.80	77.20	1.65	99.83
	8.00E−05	0.56	178.32	9.82	40.20	45.20	0.94	99.90
	9.00E−05	0.41	184.91	14.29	44.20	47.00	0.69	99.93
G3	5.00E−05	3.31	82.87	2.83	72.90	73.10	5.60	99.42
	6.00E−05	2.98	79.92	2.48	53.60	62.50	5.05	99.47
	7.00E−05	2.82	68.42	2.74	58.60	62.10	4.78	99.50
	8.00E−05	1.05	33.14	6.52	58.10	49.20	1.78	99.82
	9.00E−05	0.62	63.78	16.72	83.00	78.00	1.04	99.89

4.3.3 Electrochemical impedance spectroscopy

Using OriginPro graphing and analysis software, (Z';-Z'') coordinates were plotted to produce Nyquist plots (Figures 4.140 to 4.148). The Nyquist plot of the blank (Figure 4.139) is not shown in most of the Nyquist plots due to the high R_{ct} values obtained, making it necessary to show it separately for clarity. All the Nyquist plots shown are imperfect because of WE surface roughness [250], appearing to be more depressed than those obtained for MS. The roughness of the zinc WE surface leads to the propagation of a ZnO passive film that is more prone to pitting [251], hence the depressed zinc Nyquist plots. Tang *et al.* [252] and Mitchell *et al.* [253] agreed with Hong and Nagumo [251], all three studies highlighting the increased frequency of pit development on rough metallic surfaces.

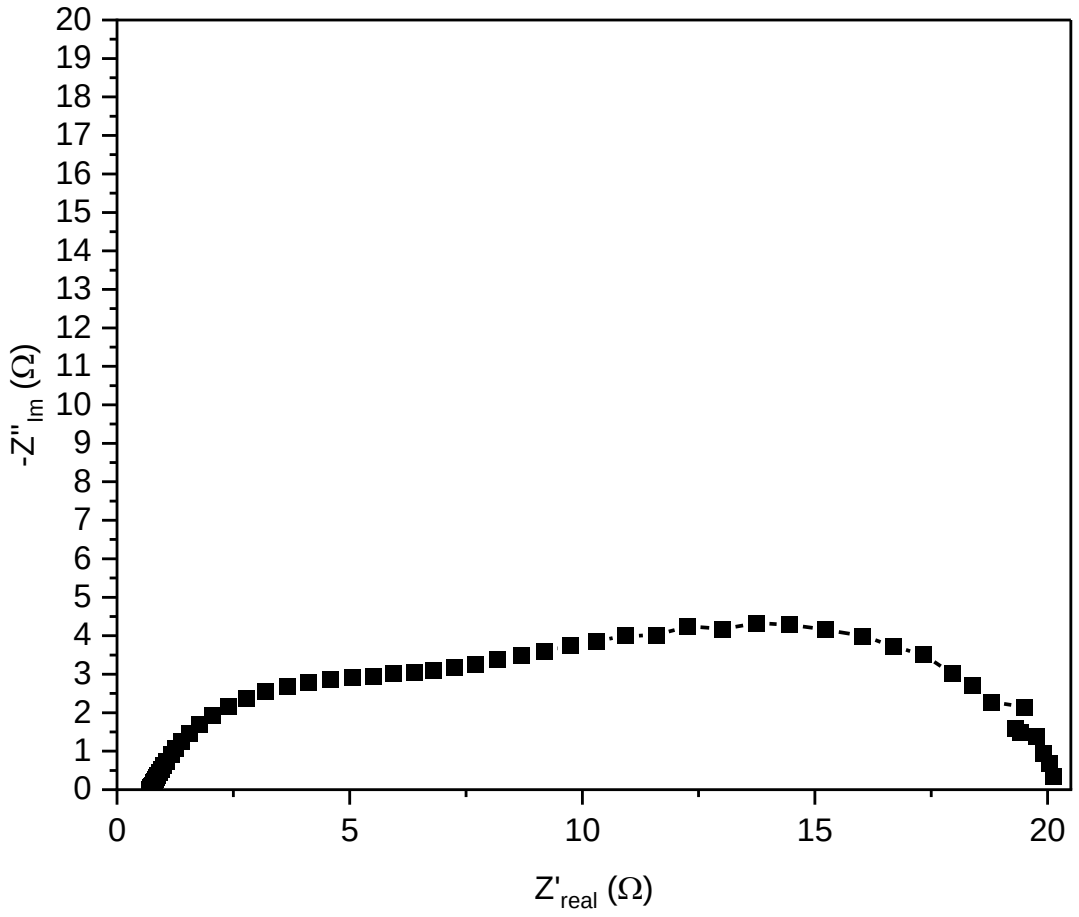

Figure 4.139: Uninhibited (blank) solution Nyquist plot (zinc).

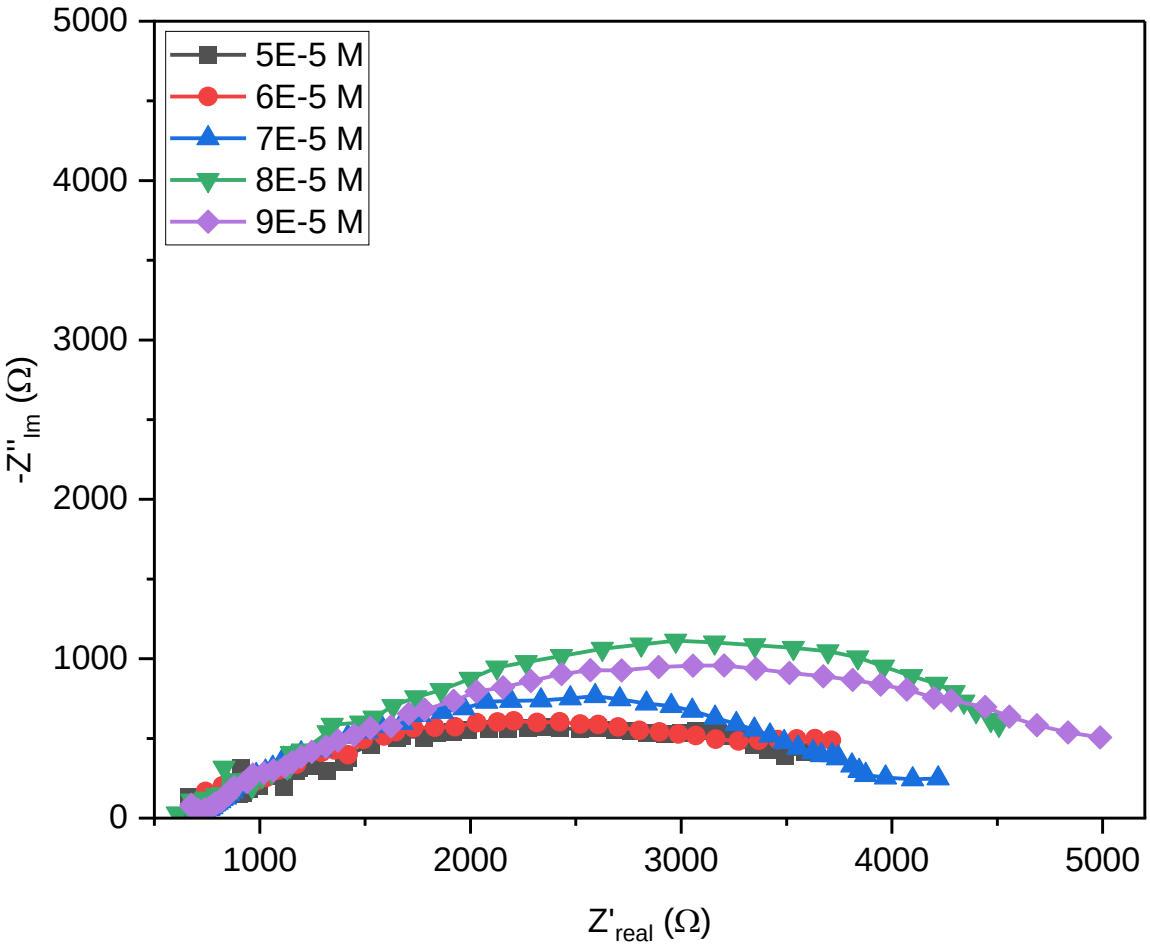

Figure 4.140: Nyquist plots for A1 (zinc).

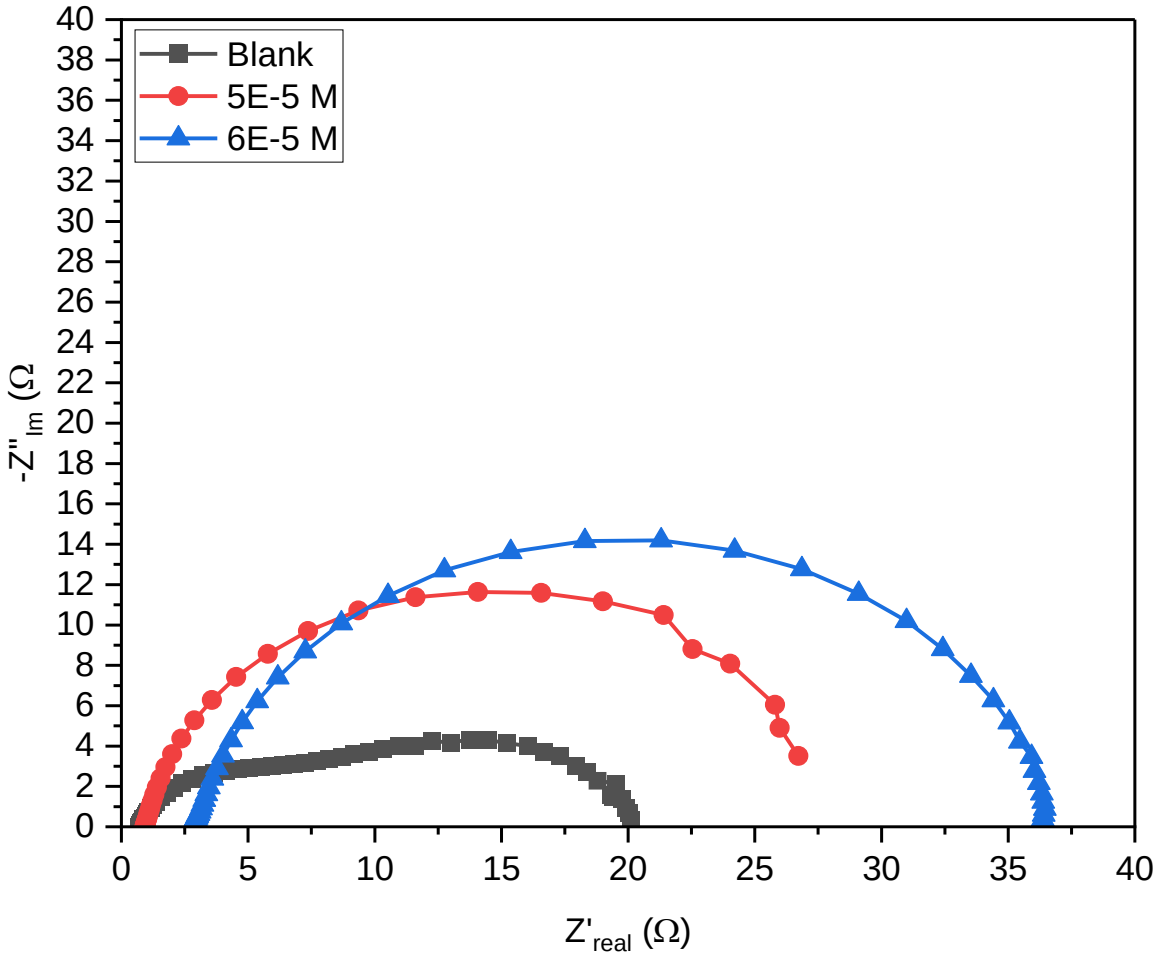

Figure 4.141: Blank to 6E−5 M Nyquist plots for A2 (zinc).

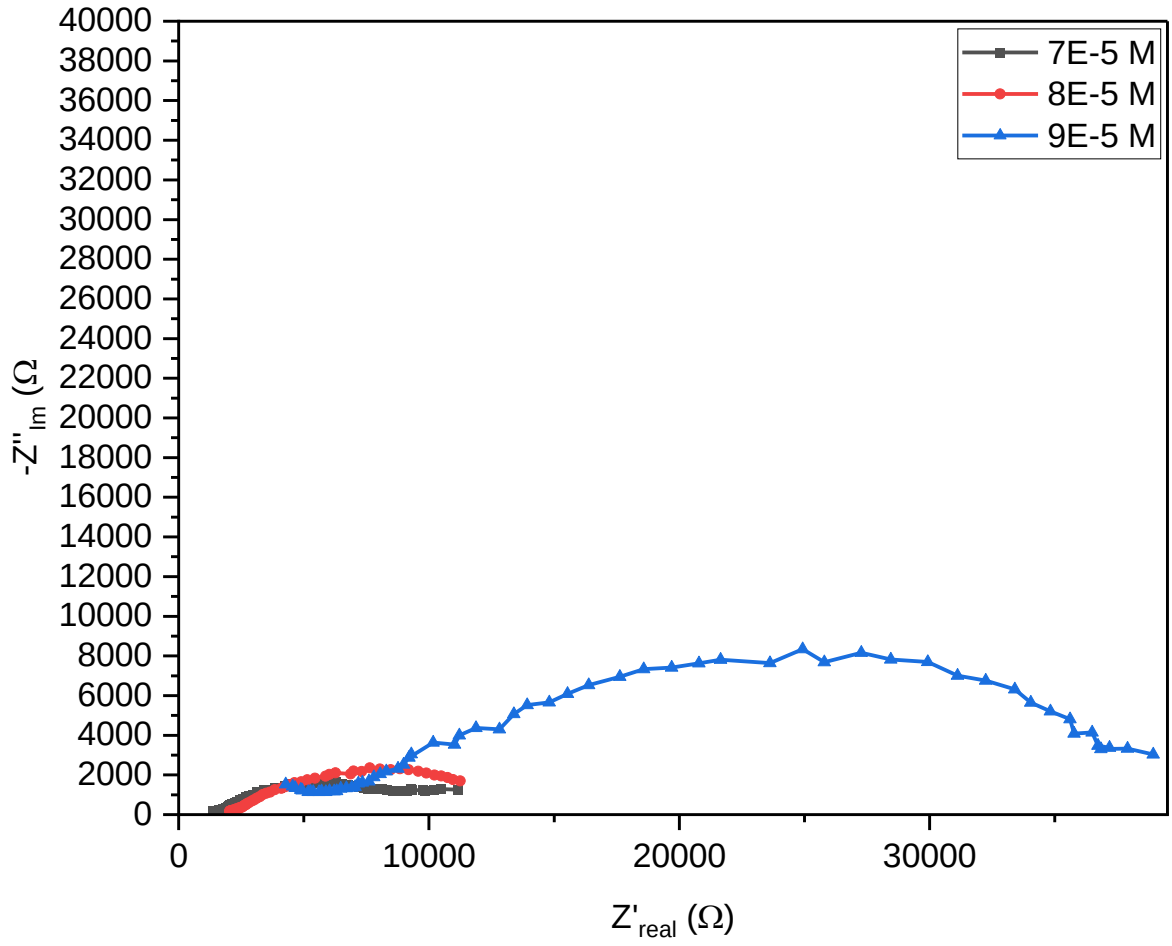

Figure 4.142: 7E−5 M to 9E−5 M Nyquist plots for A2 (zinc).

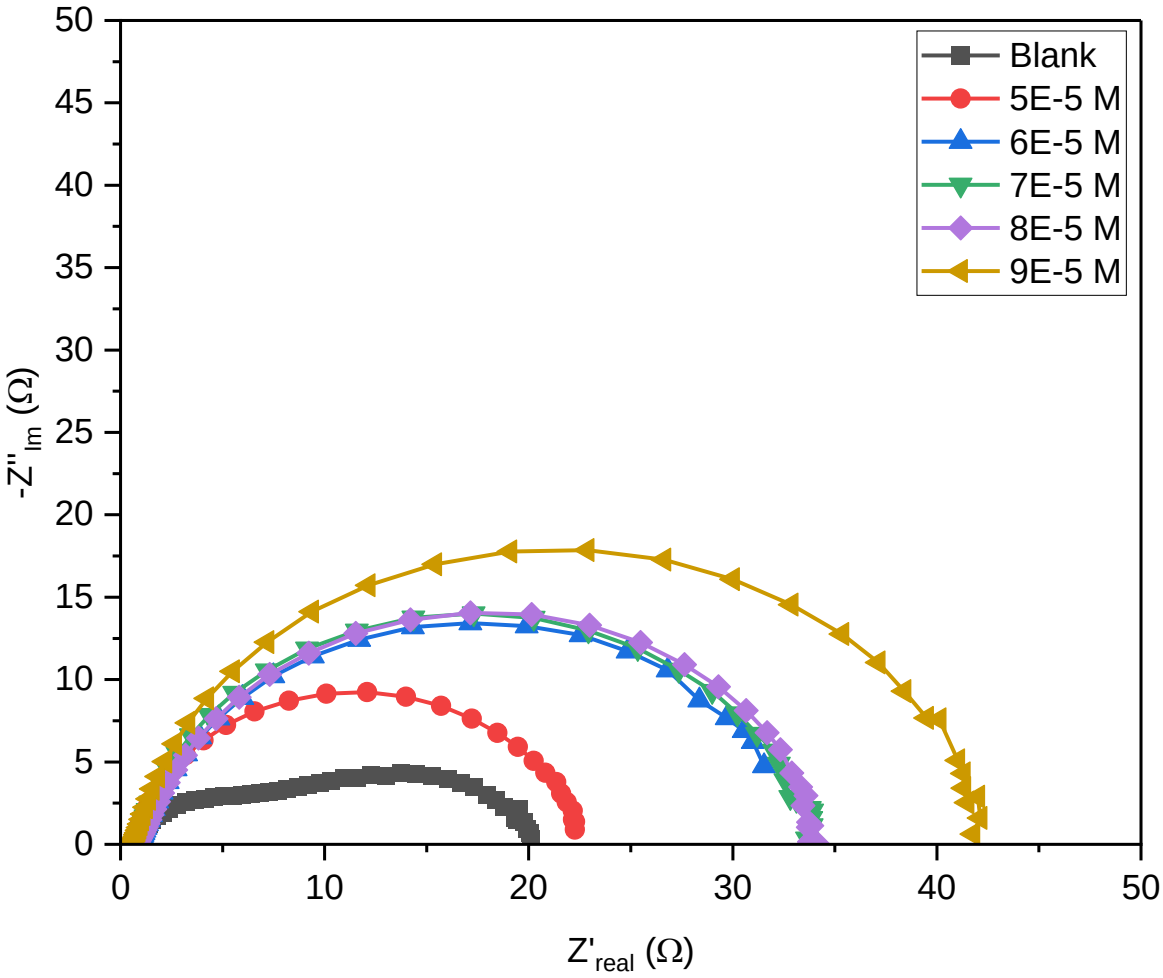

Figure 4.143: Nyquist plots for A3 (zinc).

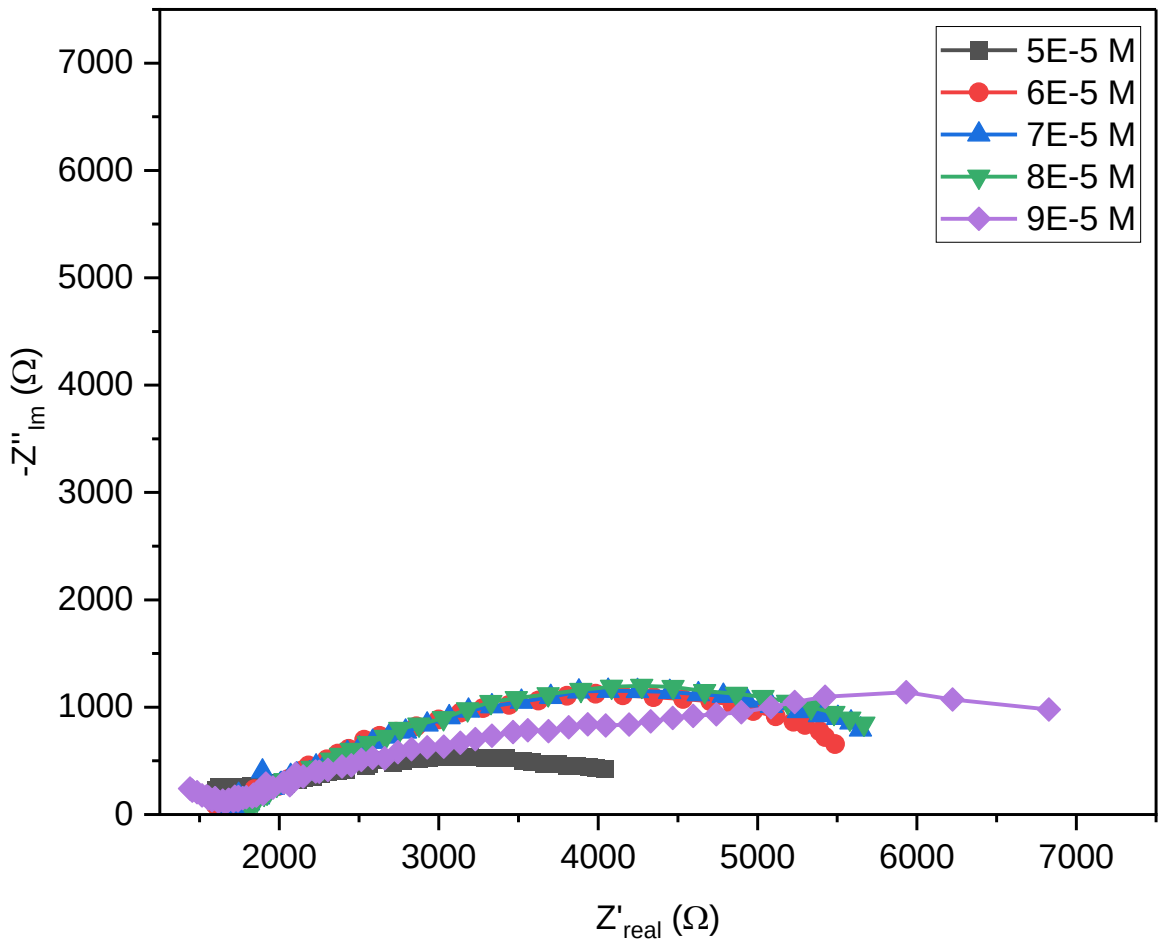

Figure 4.144: Nyquist plots for B1 (zinc).

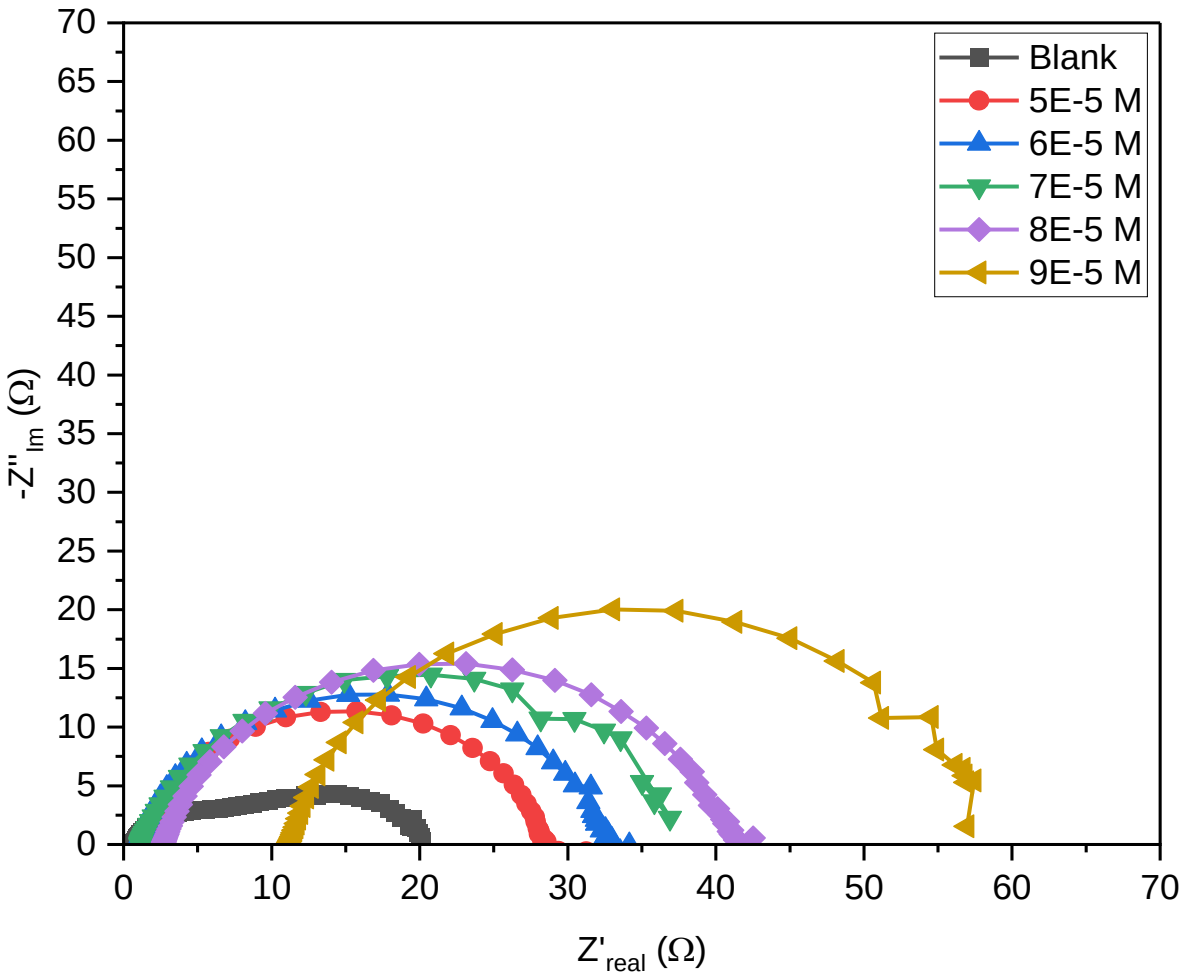

Figure 4.145: Nyquist plots for B2 (zinc).

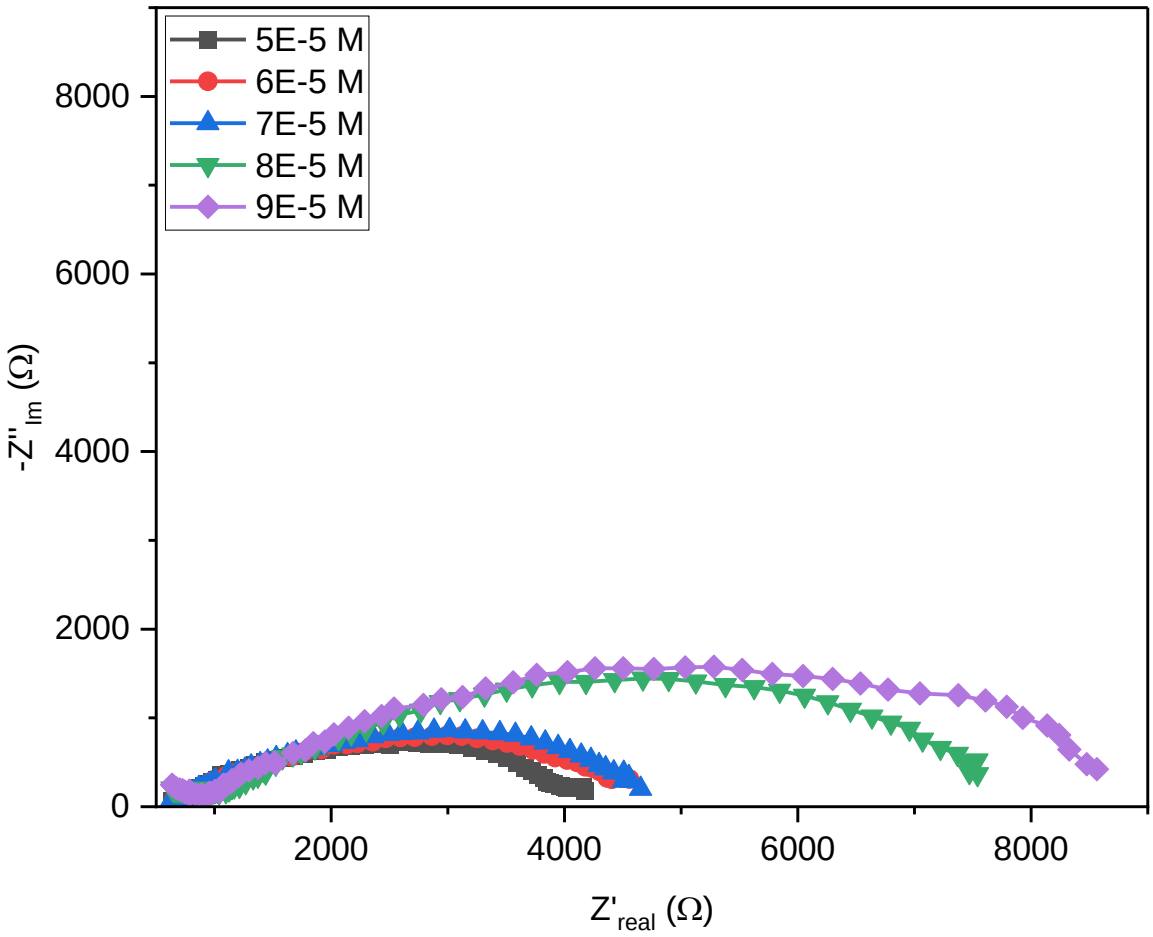

Figure 4.146: Nyquist plots for G1 (zinc).

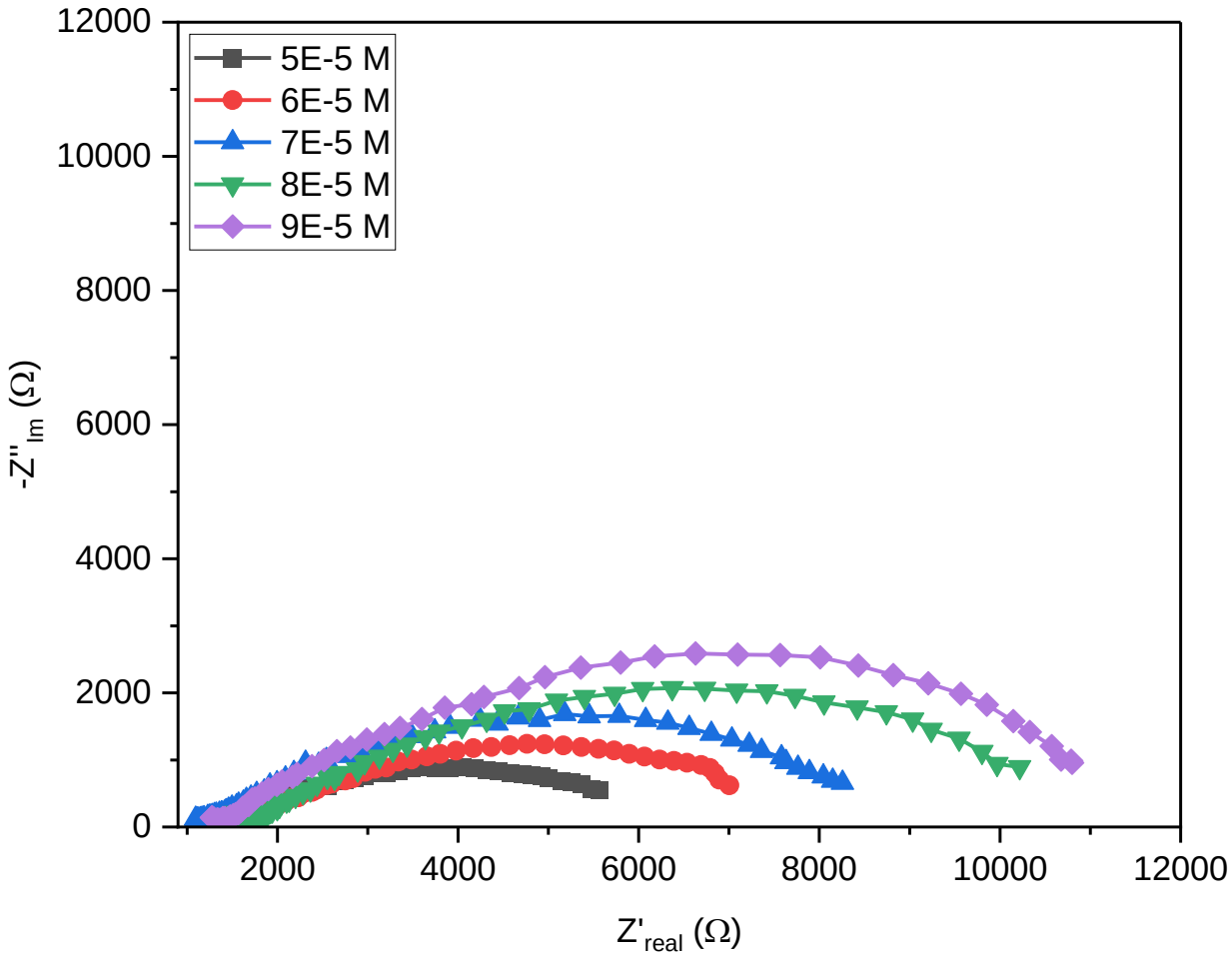

Figure 4.147: Nyquist plots for G2 (zinc).

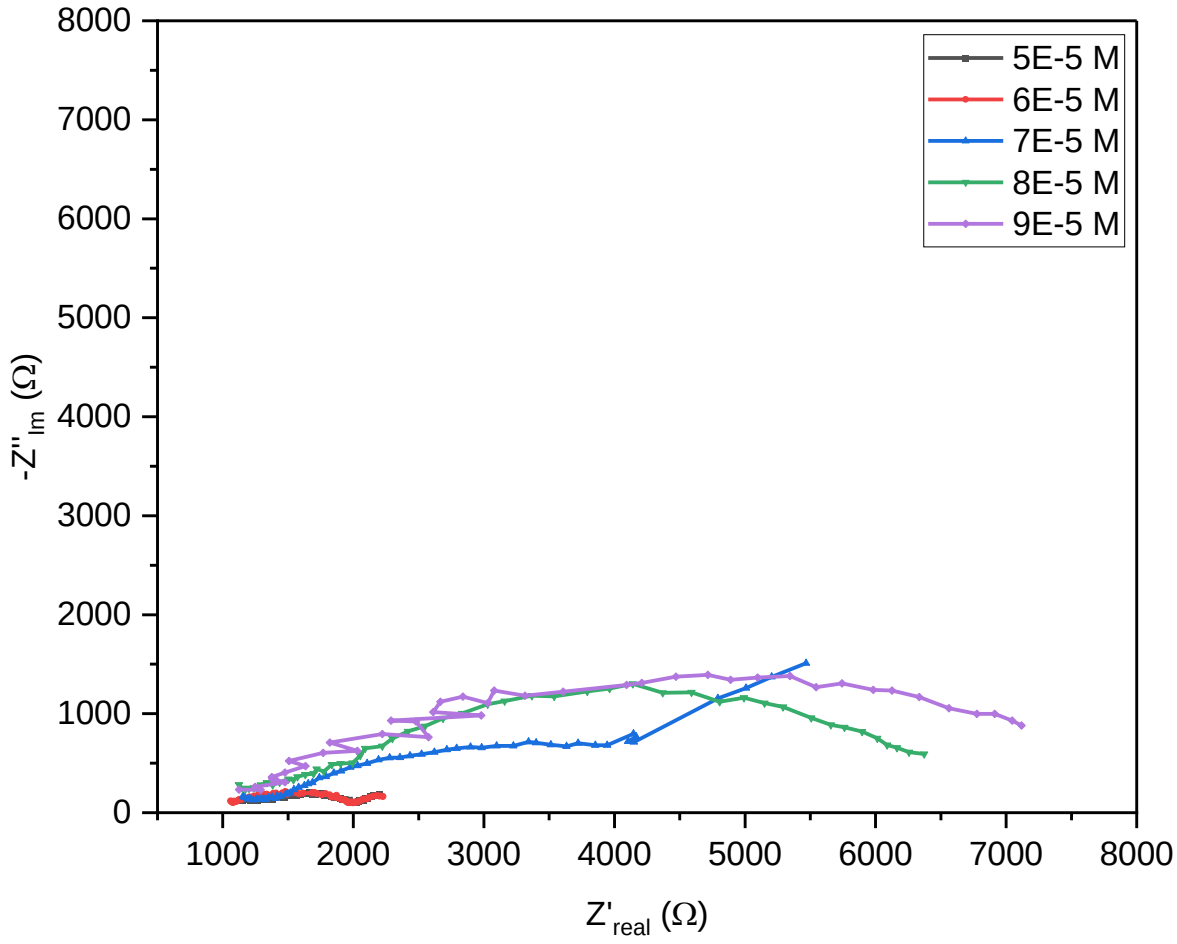

Figure 4.148: Nyquist plots for G3 (zinc).

A modified Randels circuit with a Warburg impedance (W) circuit element (Figure 4.149) was also used to fit some of the impedance data obtained, specifically for the Nyquist plot corresponding to a C_{inh} of 7E−5 M (see Figure 4.148). The fit was done using ZSimDemo 3.30d software.

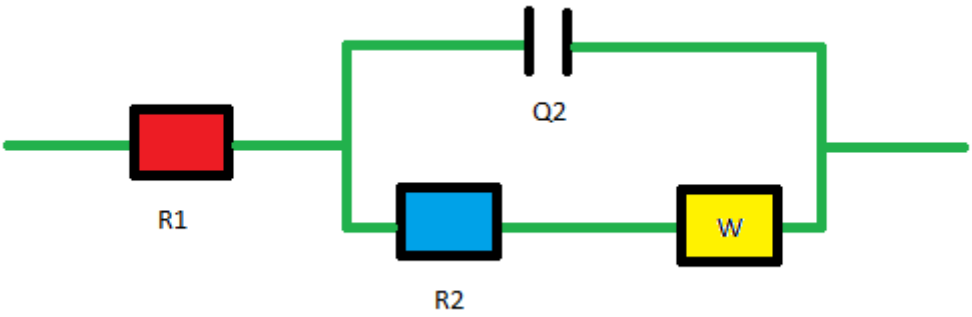

Figure 4.149: Modified Randels circuit with Warburg impedance.

Warburg impedance is associated with diffusion [254]. Typically, W shows itself as a straight line at an angle of 45° (sometimes there are deviations from 45°) to the real impedance axis (semi-infinite W) at low voltage frequencies [254, 255]. This is because at low voltage frequencies, the potential at the WE is held at a particular value for an extended period of time, affording slow diffusing chemical species in the electrolyte enough time to not only reach the WE surface but also to be consumed by one of the redox half-reactions [254]. The disappearance of these chemical species in the electrolyte adjacent to the WE surface results in a reduction in i_{corr}. The software interprets this reduction in i_{corr} as an increase in the impedance of the system, resulting in W. Electrochemical impedance spectroscopy experiments are not long enough to allow the system to reach steady state hence the semi-infinite form of W. If, however, the system was to be allowed to reach steady state, W would present itself in one of two forms (Figure 4.150): finite length Warburg (FLW) and finite space Warburg (FSW) [256].

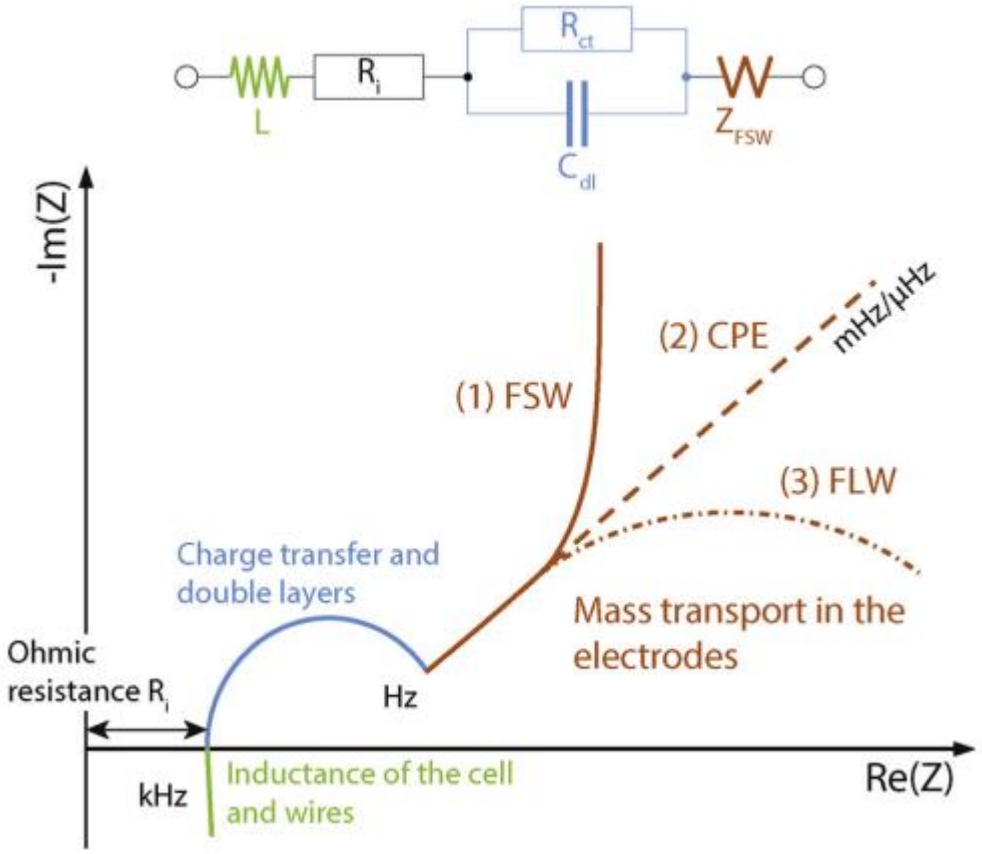

Figure 4.150: Different types of Warburg impedance [256].

Apart from A3 and B2, all TZDs achieve very high R_{ct} values (Table 4.11). In addition, for all TZDs, an increase in C_{inh} results in an increase in R_{ct}. This is consistent with the formation of a protective film on the metal surface [257]. This assertion is bolstered by the fact that the R_{ct} for the uninhibited 1 M HCl solution is ≈20Ω, an indication that the large R_{ct} values achieved in the inhibited solutions are because of the presence of the TZDs. The low n values also show that the surface of the WE has pseudo-resistive behaviour [258]. This explains the high R_{ct} data achieved by most of the TZDs. On the other hand, the n values for A3 and B2 show pseudo-capacitive behaviour, explaining the low R_{ct} values achieved by both TZDs [258].

Amongst the TZDs containing a furan ring (A3, B2 and G3), G3 achieves the highest R_{ct} values. The alkyl groups that confer an advantage to A3 and B2 in their adsorption onto MS clearly act as a hinderance to their adsorption onto zinc, giving G3 a distinct advantage in this regard. Amongst the TZDs with a (-OCH_3) group, G1 shows larger R_{ct} data compared to A1 and B1 for most concentrations. This shows yet again that the presence of alkyl groups in the molecular structures of these TZDs may be a

hinderance to their adsorption onto zinc. Therefore, EIS and WL experiments are both consistent in pointing to the glycinates as being better than the alaninates and butanoates at protecting zinc from corrosion in 1 M HCl.

The TZDs with a (-NO_2) group (A2 and G2) are the only TZDs that achieve R_{ct} values above 10000Ω. This is most likely because the additional O heteroatoms in their molecular structures facilitate the formation of dative covalent bonds with the zinc surface, facilitating chemisorption (Figures 4.151 and 4.152). Whilst G2 outperforms A2 at lower concentrations (5E−5 M and 6E−5 M), A2 achieves larger R_{ct} data at higher concentrations (7E−5 M to 9E−5 M), with the dative covalent bonds formed by the (-NO_2) group overriding any hinderance to adsorption caused by the alkyl group on A2.

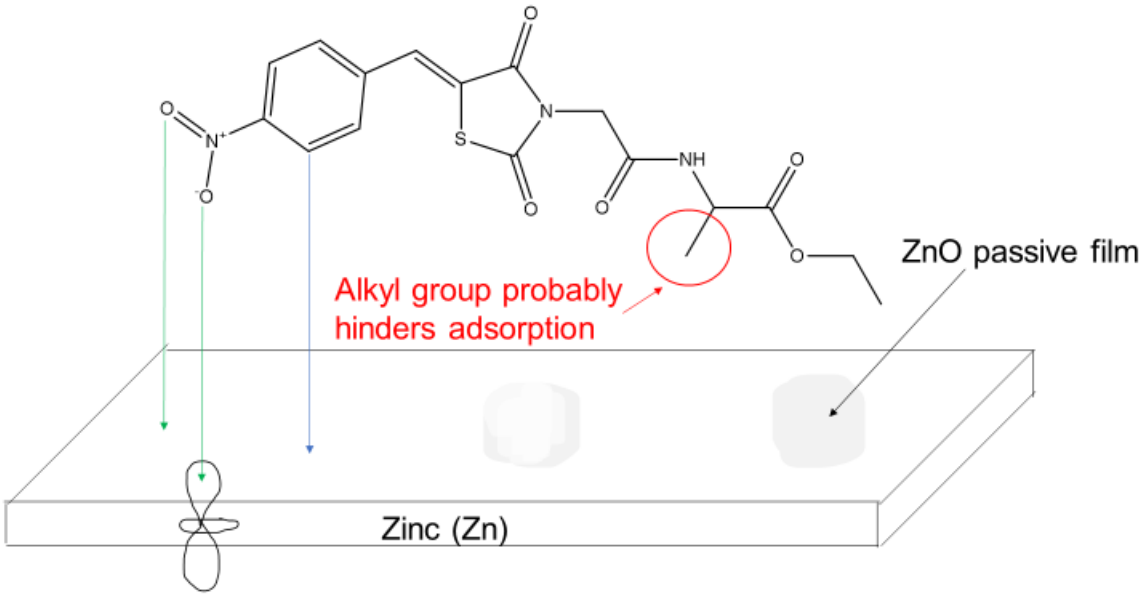

Figure 4.151: Adsorption of A2 onto zinc.

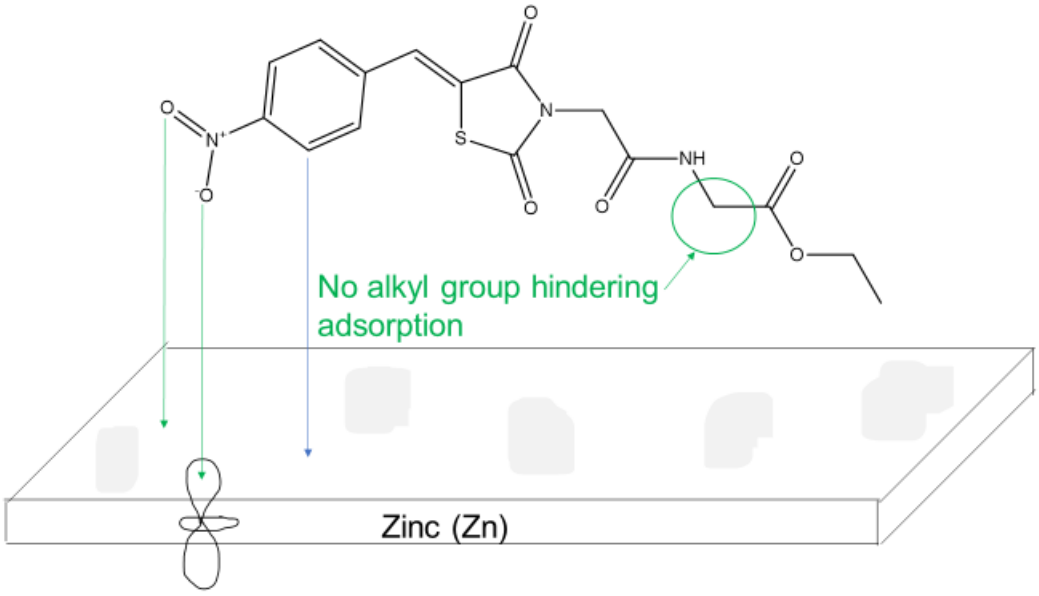

Figure 4.152: Adsorption of G2 onto zinc.

Whilst some of the C_{dl} values of the alaninates and butanoates are smaller than that of the uninhibited solution, many of them are larger (red blocks) whilst some are not that much smaller (orange blocks) (Table 4.11). This shows that the alaninates and butanoates don't adsorb onto the zinc metal surface as efficiently as the glycinates, whose C_{dl} data is consistently smaller than that of the uninhibited solution. Despite fluctuating C_{dl} data as C_{inh} is increased (such as that presented in Table 4.11), Bedair *et al.* [259] stated that an increase in C_{inh} resulted in a decrease in C_{dl}, a trend they attributed to the displacement of H_2O molecules from the metal surface by adsorption of inhibitor molecules onto it. This shows that the alkyl groups in the molecular structures of the alaninates and butanoates act as a hinderance to their adsorption onto the zinc metal surface. This explains why, for the most part, the glycinates show larger R_{ct} and therefore higher %IE data relative to the alaninates and butanoates.

Table 4.11: TZD EIS parameters (zinc).

TZD/Blank	Concentration (M)	R_{ct} (Ω)	R_s (Ω)	X^2	n	C_{dl} (µF)	%IE
Blank	-	19.88	2.92	0.000166	0.8090/0.6851	141	-
A1	5.00E−05	3325	3219	0.00004748	0.4556	136	99.40
	6.00E−05	3501	677	0.0001537	0.5029	24.92	99.43
	7.00E−05	3706	2377	0.0001523	0.3686	110.09	99.46
	8.00E−05	4706	3209	0.0001458	0.5299	181.74	99.58
	9.00E−05	4907	1083	0.00009836	0.4718	112.85	99.59
A2	5.00E−05	24.20	0.82	0.002068	0.8454	184.64	17.86
	6.00E−05	27.52	0.93	0.001055	0.9007	138.12	27.77
	7.00E−05	9537	1313	0.0009108	0.4098	7.08	99.79
	8.00E−05	12840	1948	0.000397	0.4246	6.94	99.85
	9.00E−05	36660	5942	0.000535	0.5010	1.12	99.95
A3	5.00E−05	21.97	7.80	0.00003539	0.8888	96.58	9.52
	6.00E−05	33.22	0.80	0.001402	0.8881	138.37	40.16
	7.00E−05	33.62	0.89	0.001917	0.8474	183.51	40.87
	8.00E−05	34.21	0.86	0.002902	0.8373	294.02	41.89
	9.00E−05	41.99	0.64	0.001931	0.8857	162.14	52.66
B1	5.00E−05	3570	1432	0.00006406	0.3574	4.34	99.44
	6.00E−05	4750	3063	0.0001087	0.5364	233.40	99.58
	7.00E−05	5186	3079	0.00007649	0.5141	327.55	99.62

	8.00E−05	5230	3087	0.00004969	0.5321	409.92	99.62
	9.00E−05	8533	1446	0.0001687	0.3045	450.57	99.77
B2	5.00E−05	26.70	1.62	0.0004543	0.9131	96.96	25.55
	6.00E−05	31.77	0.98	0.001003	0.8620	165.36	37.43
	7.00E−05	37.94	1.14	0.00122	0.8251	183.67	47.61
	8.00E−05	38.53	2.68	0.0001132	0.8568	136.06	48.41
	9.00E−05	47.22	11.27	0.00009009	0.8950	133.79	57.90
G1	5.00E−05	3754	618	0.0001571	0.4620	11.39	99.47
	6.00E−05	4387	1040	0.0001217	0.4372	60.90	99.55
	7.00E−05	4809	1030	0.00008637	0.4294	48.40	99.59
	8.00E−05	7291	1633	0.0001324	0.4831	30.41	99.73
	9.00E−05	8619	1976	0.0001876	0.4603	40.03	99.77
G2	5.00E−05	5077	1334	0.0001038	0.4234	113.90	99.61
	6.00E−05	6710	1588	0.0001001	0.4392	88.94	99.70
	7.00E−05	8288	1123	0.0005999	0.4681	9.37	99.76
	8.00E−05	9395	1918	0.0002229	0.5275	22.37	99.79
	9.00E−05	11320	1366	0.0005426	0.5234	15.82	99.82
G3	5.00E−05	924.40	1155	0.0001227	0.4697	1.68	97.85
	6.00E−05	1113	933.20	0.0001128	0.4434	0.13	98.21
	7.00E−05	3152	1236	0.0003057	0.4584	4.48	99.37
	8.00E−05	5494	1937	0.00006508	0.5398	1.01	99.64

	9.00E−05	7849	6663	0.0001718	0.4232	11.06	99.75

4.3.4 Adsorption film analysis

Figures 4.153 to 4.160 show that the same functional groups involved in the formation of an adsorption film on MS are also involved in the formation of an adsorption film on zinc: (-N-H) functional group, (-C-H) aromatic and alkyl functional group, the (-C=O) functional group, and the ($-NO_2$) functional group (see Section 4.2.4). The disappearance of most of the peaks in the spectra of the adsorption films (red) when the TZDs (black spectra) adsorb onto zinc is an indication that indeed all TZDs adsorbed onto the zinc metal surface [260].

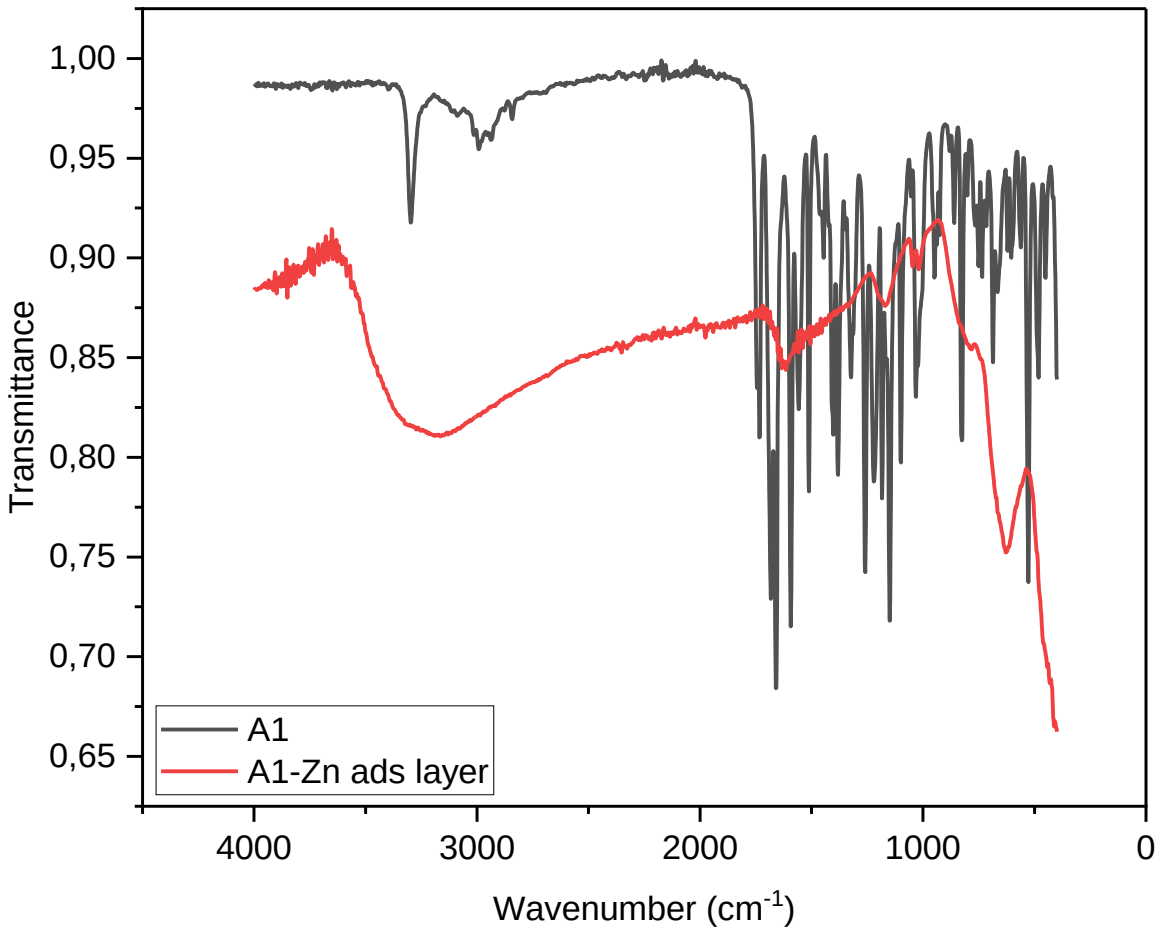

Figure 4.153: A1 FTIR plots (zinc).

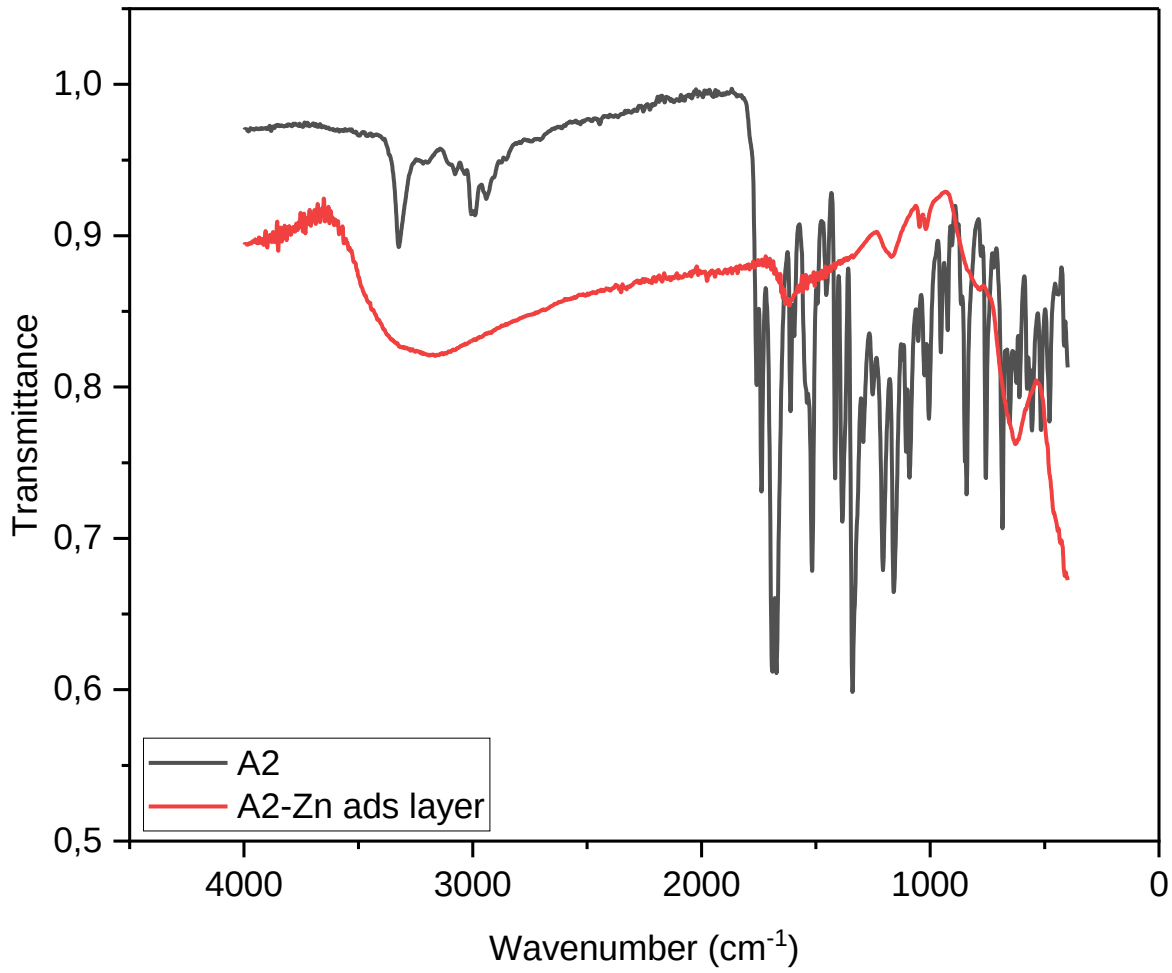

Figure 4.154: A2 FTIR plots (zinc).

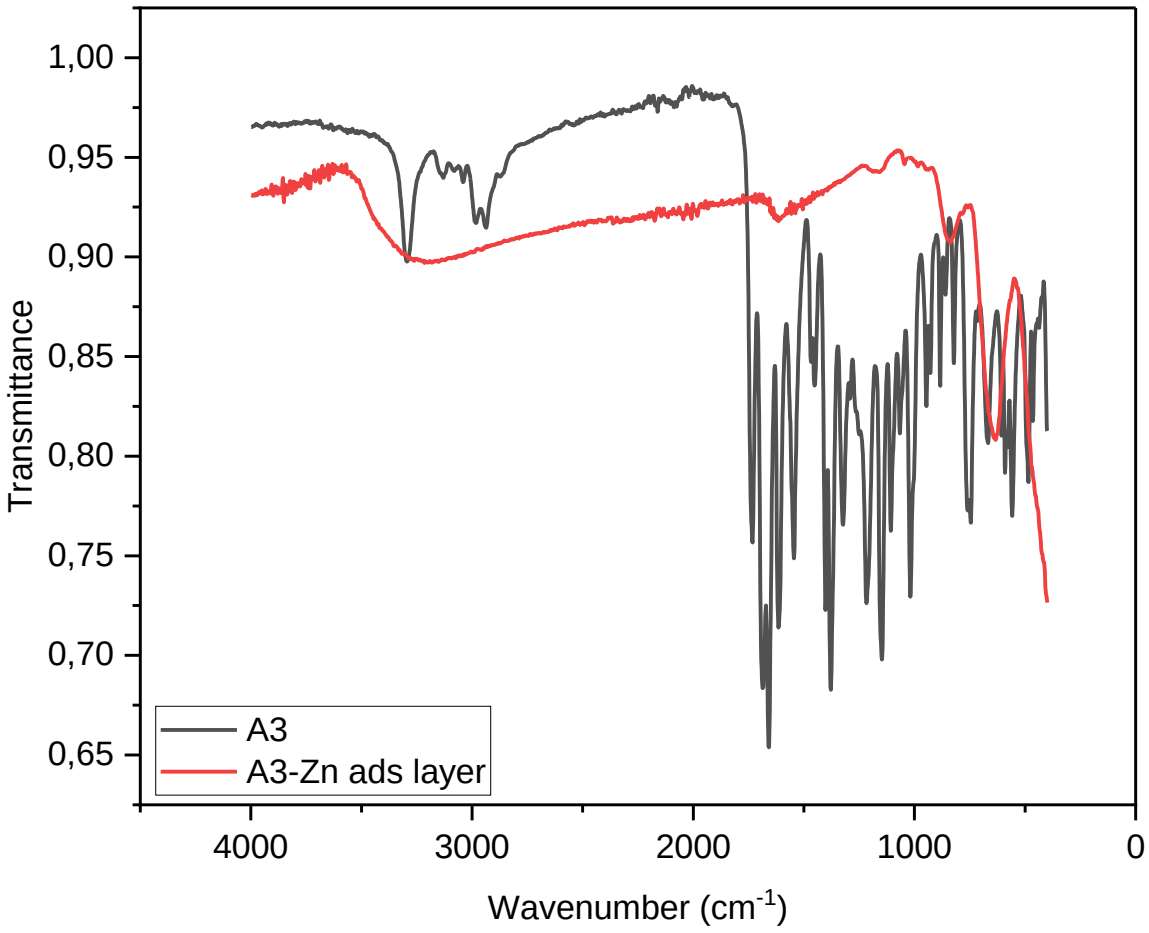

Figure 4.155: A3 FTIR plots (zinc).

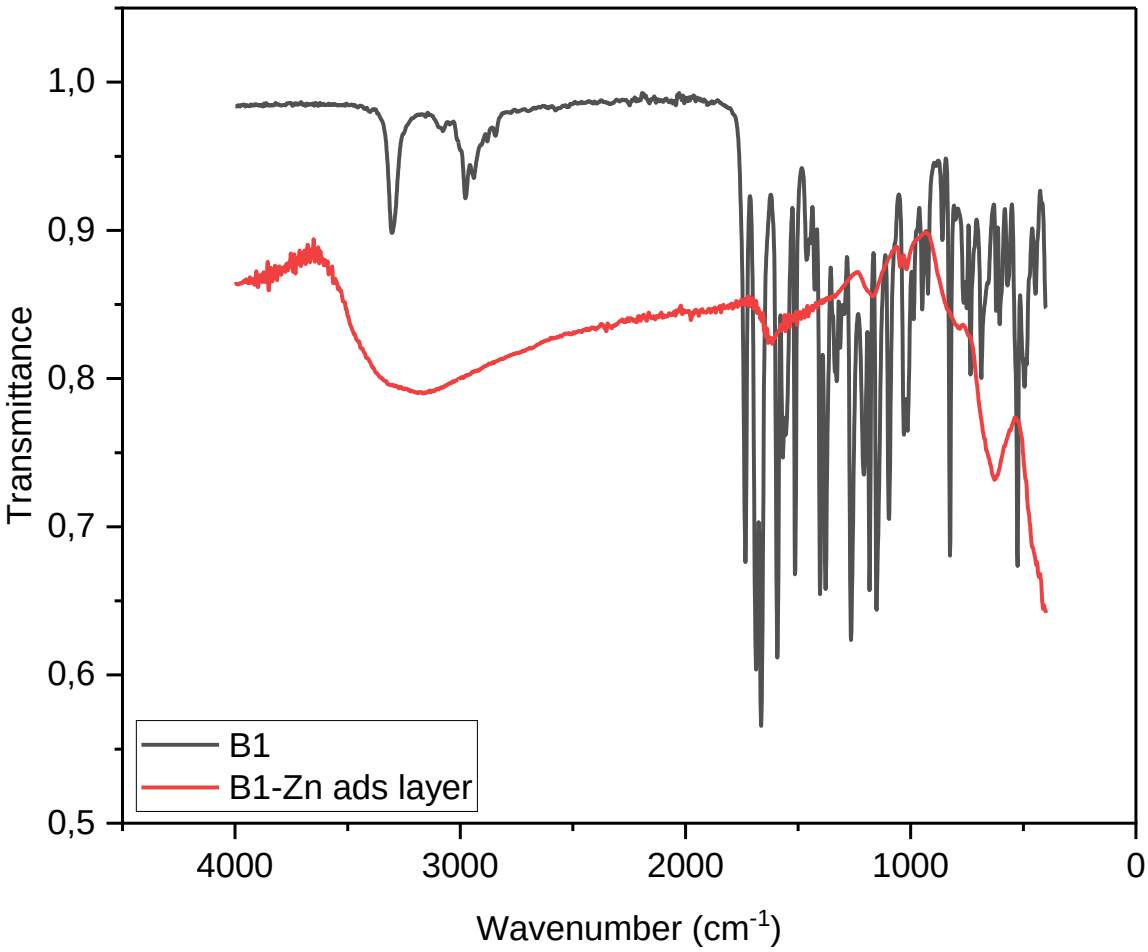

Figure 4.156: B1 FTIR plots (zinc).

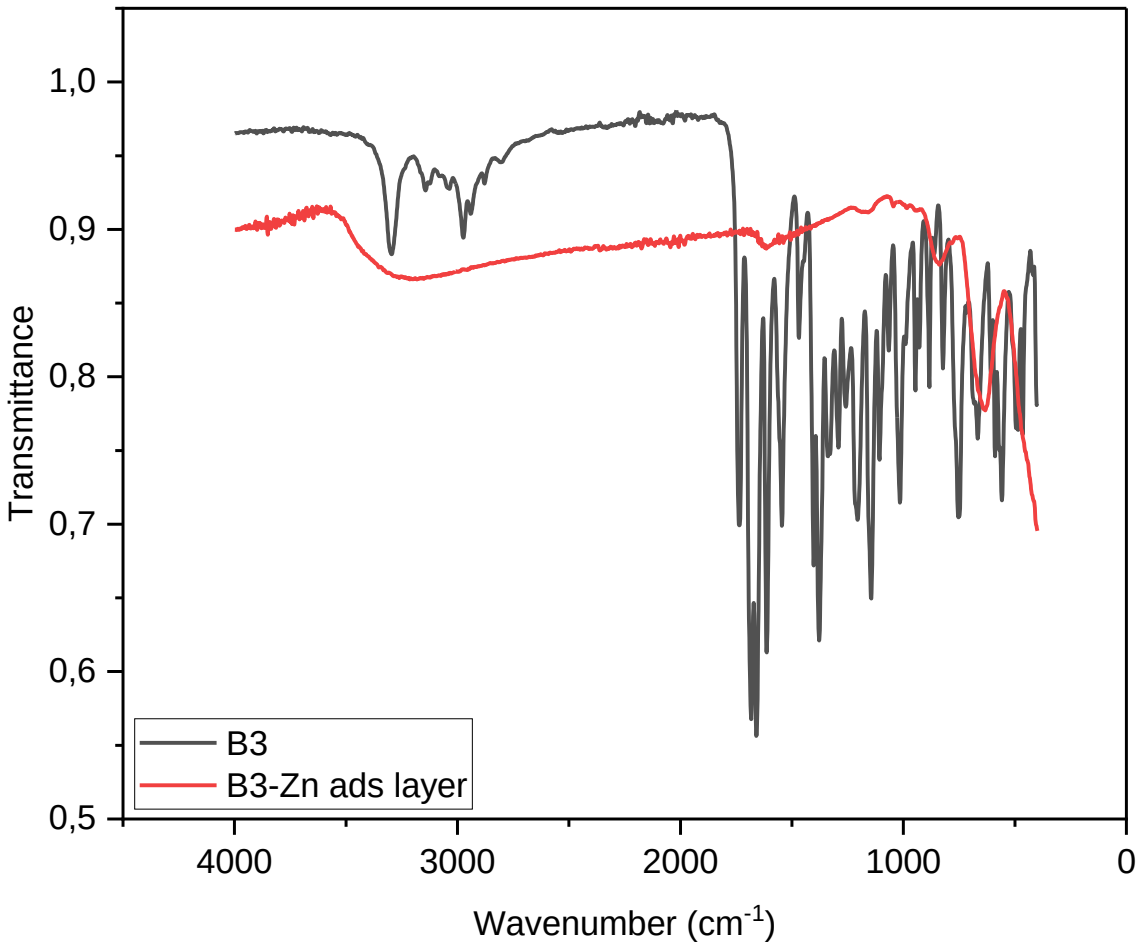

Figure 4.157: B2 FTIR plots (zinc).

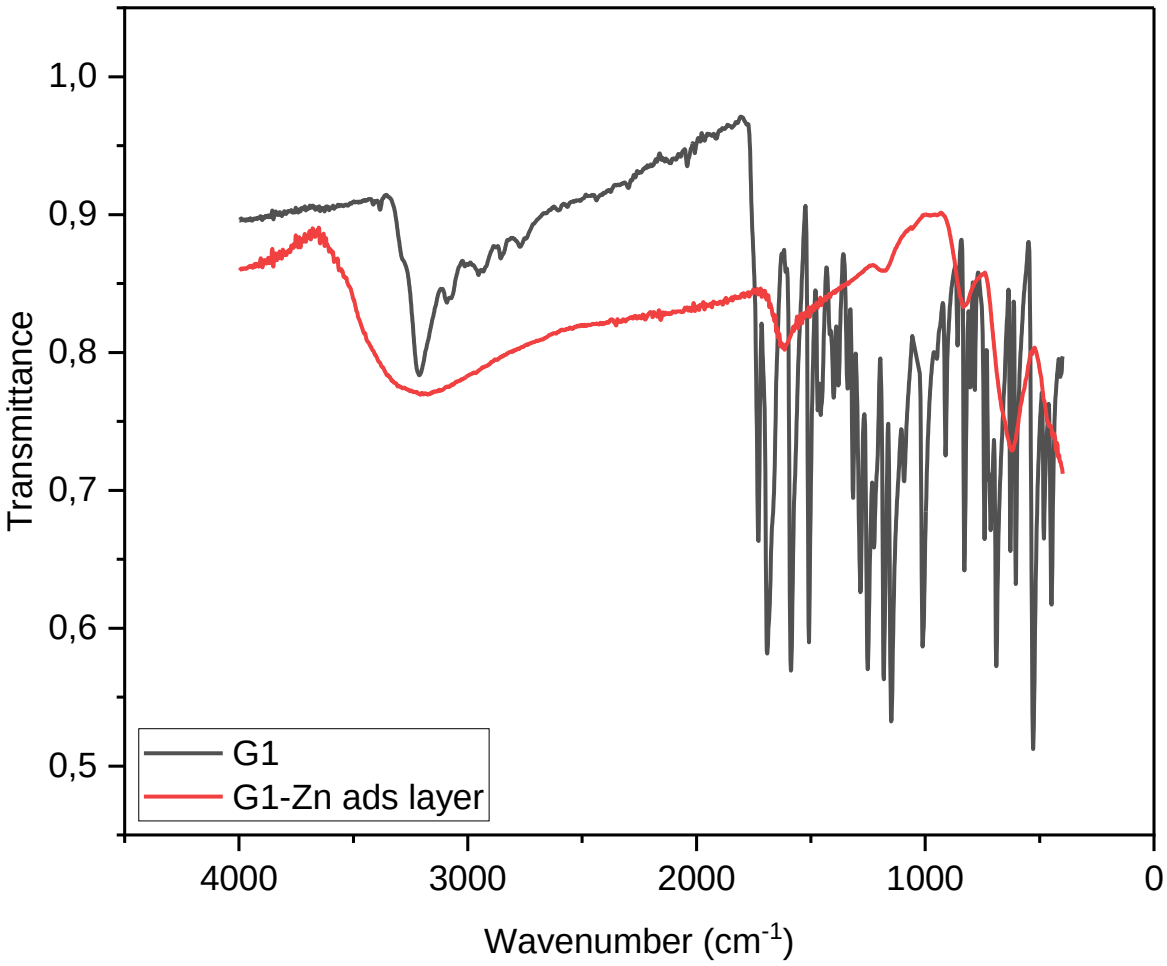

Figure 4.158: G1 FTIR plots (zinc).

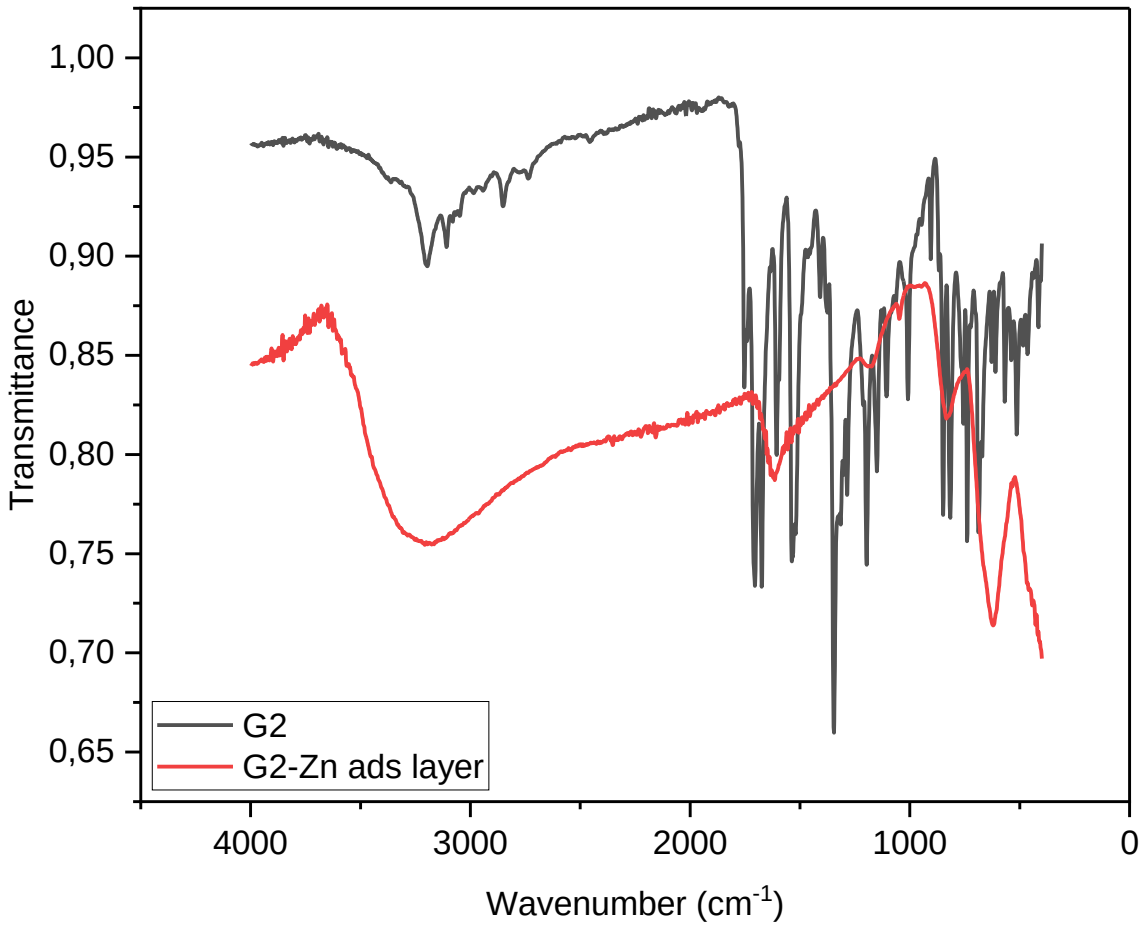

Figure 4.159: G2 FTIR plots (zinc).

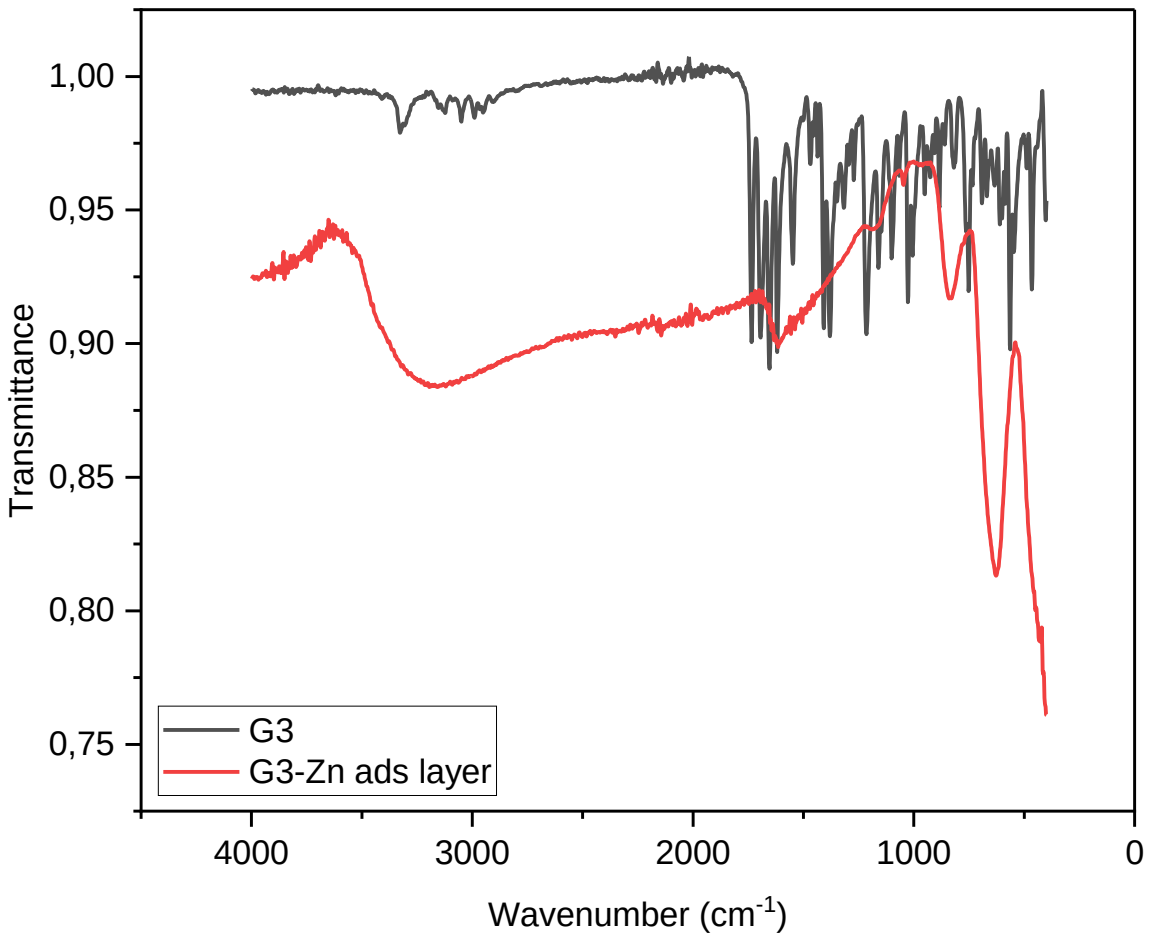

Figure 4.160: G3 FTIR plots (zinc).

CHAPTER FIVE

CONCLUSIONS

Chapter summary

This chapter summarizes the findings obtained in the study according to the aims and objectives of the study. All TZDs were shown to be effective corrosion inhibitors for both MS and zinc in 1 M HCl.

5.1 Conclusions

Eight novel thiazolidinedione derivatives (TZDs) were synthesized and characterized using nuclear magnetic resonance (NMR) spectroscopy. All the NMR spectra obtained corresponded correctly to the molecular structures of the TZDs. The corrosion inhibition potential of the TZDs was ascertained using weight loss (WL) studies, potentiodynamic polarization (PDP), electrochemical impedance spectroscopy (EIS) and, Fourier transform infrared spectroscopy (FTIR). Specifically, FTIR was used to investigate the functional groups involved in the formation of an adsorption film on MS and zinc.

Weight loss percentage inhibition efficiency ($\%IE_{WL}$) data showed that all TZDs adsorb onto zinc via chemisorption. The highest $\%IE_{WL}$ were achieved when the TZDs adsorbed onto MS at 303.15K. Whilst the $\%IE_{WL}$ data for zinc is much lower than that obtained for MS, it is observed at much higher temperatures, predominantly 333.15K. The low zinc $\%IE_{WL}$ data was most likely a function of low C_{inh}. An increase in C_{inh} resulted in a corresponding increase and decrease in $\%IE_{WL}$ and metal corrosion rate (C_R) respectively, an indication of the formation of an adsorption film by the TZDs on both metal surfaces. The Langmuir adsorption isotherm was the best model for the adsorption of the TZDs onto both metal surfaces, despite deviations observed for the adsorption of the TZDs onto MS. Gibbs free energy ($\Delta G°_{ads}$) data showed that all TZDs adsorb spontaneously onto both metal surfaces in either a mixed type fashion (at lower temperatures) or chemisorption (at higher temperatures).

Corrosion potential (E_{corr}) data from PDP analysis showed that on MS, the TZDs inhibited corrosion at both the anodic and cathodic sites, with a prevalence of cathodic action. However, on zinc, six of the TZDs inhibited corrosion exclusively at the anodic sites, preventing metal dissolution. The other two (A3 and B2) showed mixed action corrosion inhibition, acting at both anodic and cathodic sites. The formation of a protective film on both metals was confirmed by a decrease in i_{corr}, a decrease in C_R, an increase in %IE and an increase in polarization resistance (R_p) when C_{inh} was increased. Data from EIS analysis showed that the corrosion of both metals in 1M HCl was a charge transfer driven process given that the impedance data obtained was in the form of imperfect semi-circles. Zinc Nyquist plots were largely depressed, an indication that capacitance played less of a role in TZD adsorption onto zinc. This is

why the n data for zinc was generally much lower than that observed for MS. Zinc double layer capacitance (C_{dl}) data for alaninates and butanoates increased in certain instances with an increase in C_{inh}, an indication that adsorption of these TZDs onto zinc was inadequate. This is further confirmed by the low $\%IE_{WL}$ data obtained for zinc. However, C_{dl} data for MS decreased with an increase in C_{inh} for all TZDs, an indication that adsorption for all TZDs onto MS was adequate. An increase in charge transfer resistance (R_{ct}), together with an increase in %IE as C_{inh} was increased, was an indication of the formation of an adsorption film on both metal surfaces.

Spectra obtained from FTIR analysis showed that all TZDs were able to adsorb onto both metal surfaces, forming protective films on both MS and zinc. Functional groups such as carbonyl (-C=O), aromatic, alkyl, amine (-N-H) and nitro ($-NO_2$) groups were all involved in the formation of an adsorption film on both metal surfaces.

5.2 Recommendations for future studies

The present study focused on two metals (MS and zinc) and 1 M HCl as the corrosive environment. Future studies could include different metals and corrosive environments. In addition, future studies could incorporate theoretical studies to determine the most likely/least energy molecular orientation that the TZDs adopt when adsorbing onto a metal surface. This would more precisely determine the functional groups involved in the formation of an adsorption film on a metal surface and therefore the most likely mode of adsorption, that is, physisorption, chemisorption or mixed type adsorption. With regards to WL studies, future experiments could also investigate the effect of longer immersion times of metal coupons in inhibited aggressive environments.

REFERENCES

1. Christ R.D., Wernli Sr. R.L. (2014) *The ROV manual*. Butterworth Heinemann, Oxford.
2. Dorfman M.R. (2018) *Handbook of environmental degradation of materials*. William Andrew, New York.
3. Miransari M. (2016) *Soybean tillage stress*. Academic Press, Massachusetts.
4. Kazmi B., Taqvi S.A.A., Juchelkova D. (2023) State-of-the-art review on the steel decarbonization technologies based on process system engineering perspective, *Fuel, 347*, 128459.
5. Yuyu X., Hongxiang G., Datin M.N., Andong S., Li D. (2023) Mineral resources depletion, environmental degradation, and exploitation of natural resources: COVID-19 aftereffects, *Resources Policy, 85 Part A*, 103907.
6. Hou B., Li X., Ma X., Du C., Zhang D., Zheng M., Xu W., Lu D., Ma F. (2017) The cost of corrosion in China, *Materials Degradation, 1*, 1-10.
7. Chanson H. (2004) *Hydraulics of open channel flow*. Butterworth Heinemann, Oxford.
8. Olomola T.O., Durodola S.S., Olasunkanmi L.O., Adekunle A.S. (2022) Effect of selected 3-chloromethylcoumarin derivatives on mild steel corrosion in acidic medium: experimental and computational studies, *Journal of Adhesion Science and Technology, 36*, 2547-2561.
9. Nesane T., Mnyakeni-Moleele S.S., Murulana L.C. (2020) Exploration of synthesized quaternary ammonium ionic liquids as unharmful anti-corrosives for aluminium utilizing hydrochloric acid medium, *Heliyon, 6*, 1-11.
10. Sithuba T., Masia N.D., Moema J., Murulana L.C., Masuku G., Bahadur I., Kabanda M.M. (2022) Corrosion inhibitory potential of selected flavonoid derivatives: electrochemical, molecular-Zn surface interactions and quantum chemical approaches, *Results in Engineering, 16*, 1-12.
11. Diki N., Coulibaly N.H., Kassi K.F., Trokourey A. (2021) Mild steel corrosion inhibition by 7-(ethylthiobenzimidazolyl) theophylline, *Journal of Electrochemical Science and Engineering, 11*, 97-106.
12. Akinbulumo O.A., Odejobi O.J., Odekanle E.L. (2020) Thermodynamics and adsorption study of the corrosion inhibition of mild steel by *Euphorbia heterophylla L.* extract in 1.5M HCl, *Results in Materials, 5*, 1-7.

13. Thoume A., Elmakssoudi A., Left B.D., Achagar R., Irahal I.N., Dakir M., Azzi M., Zertoubi M. (2021) Dibenzylidenecyclohexanone as a new corrosion inhibitor of carbon steel in 1M HCl, *Journal of Bio-and Tribo-Corrosion, 7*, 1-12.
14. Umoren S.A., Solomon M.M., Saji V.S. (2022) *Polymeric materials in corrosion inhibition*. Elsevier, Amsterdam.
15. Calle L.M., Li W. (2014) *Handbook of smart coatings for materials protection*. Woodhead Publishing, Sawston.
16. De Damborenea J., Conde A., Arenas M.A. (2014) *Corrosion inhibition with rare earth metal compounds in aqueous solutions*. Elsevier, Amsterdam.
17. Chaouiki A., Chafiq M., Ko Y-G., Al-Moubaraki A.H., Thari F.Z., Salghi R., Karrouchi K., Bougrin K., Ali I.H., Lgaz H. (2022) Adsorption mechanism of eco-friendly corrosion inhibitors for exceptional corrosion protection of carbon steel: electrochemical and first principles DFT evaluations, *Metals, 12*, 1-19.
18. Lgaz H., Saha S.K., Lee H-S., Kang N., Thari F.Z., Karrouchi K., Salghi R., Bougrin K., Ali I.H. (2021) Corrosion inhibition properties of thiazolidinedione derivatives for copper in 3.5 wt.% NaCl medium, *Metals, 11*, 1-13.
19. Alamry K.A., Aslam R., Khan A., Hussein M.A., Tashkandi N.Y. (2022) Evaluation of corrosion inhibition performance of thiazolidine-2,4-diones and its amino derivative: gravimetric, electrochemical, spectroscopic, and surface morphological studies, *Process Safety and Environmental Protection, 159*, 178-197.
20. Letsoalo S.S., Van Averbeke W. (2006) Infrastructural maintenance on smallholder canal irrigation schemes in the north of South Africa, *International Symposium on Water and Land Management for Sustainable Irrigated Agriculture, Cukurova University,* 4-8.
21. Prins F.X., Etale A., Ablo A.D., Thatcher A. (2022) Water scarcity and alternative water sources in South Africa: can information provision shift perceptions? *Urban Water Journal, 20*, 1438-1449.
22. Bhaskar A., Abhishek R., Assadi M., Somehesaraei H.N. (2022) Decarbonizing primary steel production: techno-economic assessment of a hydrogen based green steel production plant in Norway, Journal of Cleaner Production, 350, 131339.
23. Liu X., Li H., Huang S., An H., Santagata R., Ulgiati S. (2020) Environmental and economic-related impact assessment of iron and steel production. A call

for shared responsibility in global trade, *Journal of Cleaner Production, 269*, 122239.

24. Shipilov S.A. (2009) *Materials development and performance of sulphur capture plants*. Canadian Institute of Mining, Metallurgy and Petroleum, Montreal.
25. Biezman M.V., San Cristobal J.R. (2005) Methodology to study cost of corrosion, *Corrosion Engineering, Science and Technology*, *40*, 344-352.
26. Bhaskaran R., Palaniswamy N., Rengaswamy N.S., Jayachandran M., Raghavan M. (2005) Cost of corrosion in Indian pulp and paper industry-a case study, *Corrosion Engineering, Science and Technology*, *40*, 75-80.
27. Eeshanpriya M.S. (2019) *Damage that wasn't controlled: Mumbai civic body expert points at corrosion at bridge that collapsed.* Hindustan Times, New Dehli.
28. Salem H.M., Helmy H.M. (2014) Numerical investigation of collapse of the Minnesota I-35W bridge, *Engineering Structures*, *59*, 635-645.
29. Ghuzali N.A.M., Noor M., Zakaria F.A., Hamidon T.S., Husin M.H. (2021) Study on *Clitoria ternatea* extracts doped sol-gel coatings for the corrosion mitigation of mild steel, *Applied Surface Science Advances, 6,* 1-16.
30. Ansari K.R., Quraishi M.A., Singh A. (2015) Corrosion inhibition of mild steel in hydrochloric acid by some pyridine derivatives: an experimental and quantum chemical study, *Journal of Industrial and Engineering Chemistry, 25*, 89-98.
31. Bahlakeh G., Ramezanzadeh B., Dehghani A., Ramezanzadeh M. (2019) Novel cost-effective and high-performance green inhibitor based on aqueous *Peganum harmala* seed extract for mild steel corrosion in HCl solution: detailed experimental and electronic/atomic level computational explorations, *Journal of Molecular Liquids, 283*, 174-195.
32. Doner A., Kardas G. (2011) *N*-Aminorhodanine as an effective corrosion inhibitor for mild steel in 0.5 M H_2SO_4, *Corrosion Science, 53*, 4223-4232.
33. Sabirneeza A.A.F., Subhashini S. (2012) A novel water-soluble, conducting polymer composite for mild steel acid corrosion inhibition, *Journal of Applied Polymer Science, 127*, 1-9.
34. Marhamati F., Mahdavian M., Bazgir S. (2021) Corrosion mitigation of mild steel in hydrochloric acid solution using grape seed extract, *Scientific Reports, 11*, 1-16.

35. Lunder O., Lapique F., Johnsen B., Nisancioglu K. (2004) Effect of pre-treatment on the durability of epoxy bonded AA6060 aluminium joints, *International Journal of Adhesion and Adhesives, 24*, 107-117.
36. Oguzie E.E. (2008) Evaluation of the inhibitive effect of some plant extracts on the acid corrosion of mild steel, *Corrosion Science, 50*, 2993-2998.
37. Saeed M.T., Saleem M., Usmani S., Malik I.A., Al-Shammari F.A., Deen K.M. (2019) Corrosion inhibition of mild steel in 1 M HCl by sweet melon peel extract, *Journal of King Saud University-Science, 31*, 1344-1351.
38. Obaid A.Y., Ganash A.A., Qusti A.H., Elroby S.A., Hermas A.A. (2017) Corrosion inhibition of type 430 stainless steel in an acidic solution using a synthesized tetra-pyridinium ring-containing compound, *Arabian Journal of Chemistry, 10*, 1276-1283.
39. Deng S., Li X. (2012) Inhibition by *Jasminum nudiflorum* Lindl. leaves extract of the corrosion of aluminium in HCl solution, *Corrosion Science, 64*, 253-262.
40. Anwar S., Khan F., Zhang Y. (2021) Corrosion behaviour of Zn-Ni alloy and Zn-Ni-nano-TiO2 composite coatings electrodeposited from ammonium citrate baths, *Process Safety and Environmental Protection, 141*, 1-34.
41. Foorginezhad S., Mohseni-Dargah M., Firoozirad K., Aryai V., Razmjou A., Abbassi R., Garaniya V., Beheshti A., Asadnia M. (2021) Recent advances in sensing and assessment of corrosion in sewage pipelines, *Process Safety and Environmental Protection, 147*, 192-213.
42. Liu Z., Liao W., Wu W., Du C., Li X. (2017) Failure analysis of leakage caused by perforation in an L415 steel gas pipeline, *Case Studies in Engineering Failure Analysis, 9*, 63-70.
43. Sarkar T.K., Saraswat V., Mitra R.K., Obot I.B., Yadav M. (2021) Mitigation of corrosion in petroleum oil well/tubing steel using pyrimidines as efficient corrosion inhibitor: experimental and theoretical investigation, *Materials Today Communications, 26*, 101862.
44. Yadav M., Sarkar T.K., Obot I.B. (2016) Carbohydrate compounds as green corrosion inhibitors: electrochemical, XPS, DFT and molecular dynamics simulation studies, *Royal Society of Chemistry Advances, 6*, 110053-110069.
45. Abdallah M., Soliman K.A., Alfattani R., Al-Gorair A.S., Fawzy A., Ibrahim M.A.A. (2022) Insight of corrosion mitigation performance of SABIC iron in 0.5

M HCl solution by tryptophan and histidine: experimental and computational approaches, *International Journal of Hydrogen Energy, 47*, 12782-12797.

46. Razali N.Z.K., Ghazali Mohd Sheikh S.A.I., Sharif I., Sapari S., Abdul Razak F.I., Dzulkifli N.N. (2022) Synthesis, characterization, and corrosion inhibition screening on 2-chloroacetophenone 4-ethyl-3-thiosemicarbazone: morphology, weight loss and DFT studies, *Chemical Papers, 76*, 5955-5966.
47. Khanra A., Srivastava M., Rai M.P., Prakash R. (2018) Application of unsaturated fatty acid molecules derived from microalgae toward mild steel corrosion inhibition in HCl solution: a novel approach for metal-inhibitor association, *ACS Omega, 3*, 12369-12382.
48. Bradford S.A. (2003) *Encyclopaedia of physical science and technology*. Academic Press, Massachusetts.
49. Noor E.A., Al-Moubaraki A.H. (2008) Corrosion behaviour of mild steel in hydrochloric acid solutions, *International Journal of Electrochemical Science, 3*, 806-818.
50. Obeyesekere N.U. (2017) *Trends in oil and gas corrosion research and technologies*. Woodhead Publishing, Sawston.
51. Ezuber H., Newman R.C. (1992) Growth-rate distribution of metastable pits, *Journal of the Electrochemical Society, 92-9*, 120-133.
52. Maller R.R. (2007) Passivation of stainless steel, *Trends in Food Science and Technology, 18*, S112-S115.
53. Pagitsas M., Diamantopoulou A., Sazou D. (2001) Distinction between general and pitting corrosion based on the nonlinear dynamical response of passive iron surfaces perturbed chemically by halides, *Electrochemistry Communications, 3*, 330-335.
54. Papavinasam S. (2013) *Corrosion control in the oil and gas industry*. Elsevier, Amsterdam.
55. Vargel C. (2020) *Corrosion of aluminium*. Elsevier, Amsterdam.
56. Madhlopa A. (2022) *Solar receivers for thermal power generation*. Academic Press, Massachusetts.
57. Tait W.S. (2018) *Handbook of environmental degradation of materials*. William Andrew, New York.
58. James B., Hudgins A. (2016) *Handbook of materials failure analysis with case studies from the oil and gas industry*. Butterworth Heinemann, Oxford.

59. Makhlouf A.S.H. (2015) *Intelligent coatings for corrosion control*. Butterworth Heinemann, Oxford.
60. Wang G., Spencer J.S., Saidarasamoot S., Thuanboon S., Olson D.L., Mishra B. (2012) *Handbook of environmental degradation of materials*. Elsevier, Amsterdam.
61. Couvant T. (2013) *Materials ageing and degradation in light water reactors*. Woodhead Publishing, Sawston.
62. Karlsdottir S.N. (2012) *Earth systems and environmental sciences*. Elsevier, Amsterdam.
63. Mills T., Domasky-Prost S., Honeycutt K., Brooks C. (2009) *Corrosion control in the aerospace industry*. Woodhead Publishing, Sawston.
64. Lambert P. (2016) *Sustainability of construction materials*. Woodhead Publishing, Sawston.
65. Popoola L.T., Grema A.S., Latinwo G.K., Gutti B., Balogun A.S. (2013) Corrosion problems during oil and gas production and its mitigation, *International Journal of Industrial Chemistry, 4*, 1-15.
66. Obot I.B., Sorour A.A., Verma C., Al-Khaldi T.A., Rushaid A.S. (2023) Key parameters affecting sweet and sour corrosion: impact on corrosion risk assessment and inhibition, *Engineering Failure Analysis, 145*, 107008.
67. Aslam J., Aslam R., Zehra S., Rizvi M. (2022) *Environmentally sustainable corrosion inhibitors*. Elsevier, Amsterdam.
68. Obot I.B., Onyeachu I.B., Umoren S.A., Quraishi M.A., Sorour A.A., Chen T., Aljeaban N., Wang Q. (2020) High temperature sweet corrosion and inhibition in the oil and gas industry: progress, challenges and future perspectives, *Journal of Petroleum Science and Engineering, 185*, 106469.
69. Chauhan D.S., Quraishi M.A., Qurashi A. (2021) Recent trends in environmentally sustainable sweet corrosion inhibitors, *Journal of Molecular Liquids, 326*, 115117.
70. Usman B.J., Ali S.A. (2018) Carbon dioxide corrosion inhibitors: a review, *Arabian Journal for Science and Engineering, 43*, 1-22.
71. Mazumder M.A., Al-Muallem H.A., Ali S.A. (2015) The effects of N-pendants and electron rich amidine motifs in 2-(p-alkoxyphenyl)-2-imidazolines on mild steel corrosion in CO2-saturated 0.5 M NaCl, *Corrosion Science, 90*, 54-68.

72. Mazumder M.A., Al-Muallem H.A., Faiz M., Ali S.A. (2014) Design and synthesis of a novel class of inhibitors for mild steel corrosion in acidic and carbon dioxide-saturated saline media, *Corrosion Science, 87*, 187-198.
73. Zhu Z., Teevens P.J., Xue H., Cheng F.Y. (2022) Numerical simulation and experimental verification of pitting corrosion propagation in sweet pipeline service, *Journal of Pipeline Science and Engineering, 2*, 78-86.
74. Al-Moubaraki A.H., Obot I.B. (2021) Corrosion challenges in petroleum refinery operations: sources, mechanisms, mitigation, and future outlook, *Journal of Saudi Chemical Society, 25*, 101370.
75. Guruprasad A.M., Sachin H.P., Swetha G.A. (2020) Corrosion inhibition of zinc in 0.1 M hydrochloric acid medium with clotrimazole: experimental, theoretical and quantum studies, *Surfaces and Interfaces, 19*, 100478.
76. Vashi R.T., Desai K. (2013) Aniline as corrosion inhibitor for zinc in hydrochloric acid, *Chemical Science Transactions, 2*, 670-676.
77. Chaudhari H.G., Mahida M.M. (2012) Aliphatic amines as corrosion inhibitors for zinc in hydrochloric acid, *Der Pharma Chemica, 4*, 2305-2312.
78. Guruprasad A.M., Sachin H.P., Swetha G.A., Prasanna B.M. (2019) Adsorption and inhibitive properties of Seroquel drug for the corrosion of zinc in 0.1 M hydrochloric acid solution, *International Journal of Industrial Chemistry, 10*, 17-30.
79. Kuklik V., Kudlacek J. (2016) *Hot-dip galvanizing of steel structures*. Butterworth Heinemann, Oxford.
80. Loto C.A., Loto R.T., Popoola A.P. (2019) Performance evaluation of zinc anodes for cathode protection of mild steel corrosion in HCl, *Chemical Data Collections, 24*, 100280.
81. Singh S., Paswan S.K., Kumar P., Singh R.K., Kumar L. (2023) *Metals in water*. Elsevier, Amsterdam.
82. Gad S.C. (2024) *Encyclopaedia of Toxicology*. Elsevier, Amsterdam.
83. Thierry D., Persson D., Le Bozec N. (2018) *Encyclopaedia of Interfacial Chemistry*. Elsevier, Amsterdam.
84. Porkony P., Kolisko J., Balik L., Novak P. (2015) Description of structure of Fe-Zn intermetallic compounds present in hot-dip galvanized coatings on steel, *Metalurgija, 54*, 707-710.

85. Yang H., Zhang S., Li J., Wang H. (2014) Effect of strip entry temperature on the formation of interfacial layer during hot-dip galvanizing of press-hardened steel, *Surface and Coatings Technology, 240*, 269-274.
86. Marder A.R. (2000) The metallurgy of zinc-coated steel, *Progress in Materials Science, 45*, 191-271.
87. International Organization for Standardization (2010) *Petroleum, petrochemical, and natural gas industries – Materials selection and corrosion control for oil and gas production systems* ISO 21457.
88. American National Standards Institute/American Petroleum Institute (2020) *Damage mechanisms affecting fixed equipment in the refining industry* ANSI/API RP 571.
89. American National Standards Institute/National Association of Corrosion Engineers/International Organization for Standardization (2015) *Petroleum, petrochemical, and natural gas industries – Materials for use in H_2S-containing environments in oil and gas production – Part 1: General principles for selection of cracking-resistant materials* ANSI/NACE MR0175/ISO 15156-1.
90. American National Standards Institute/National Association of Corrosion Engineers/International Organization for Standardization (2015) *Petroleum, petrochemical, and natural gas industries – Materials for use in H_2S-containing environments in oil and gas production – Part 2: Cracking-resistant carbon and low-alloy steels, and the use of cast irons* ANSI/NACE MR0175/ISO 15156-2.
91. Page C.L. (2007) Durability of concrete and cement composites. Woodhead Publishing, Sawston.
92. Monticelli C. (2018) *Encyclopaedia of interfacial chemistry*. Elsevier, Amsterdam.
93. Shehnazdeep., Pradhan B. (2022) A study on effectiveness of inorganic and organic corrosion inhibitors on rebar corrosion in concrete: a review, *Materials Today: Proceedings, 65*, 1360-1366.
94. Praveen B., Venkatesha T. (2009) Metol as corrosion inhibitor for steel, *International Journal of Electrochemical Science, 4*, 267-275.
95. Ahmed M.H.O., Al-Amiery A.A., Al-Majedy Y.K., Kadhum A.A.H., Mohamad A.B., Gaaz T.S. (2018) Synthesis and characterization of a novel organic corrosion inhibitor for mild steel in 1M hydrochloric acid, *Results in Physics, 8*, 728-733.

96. Kadhim A., Al-Okbi A.K., Jamil D.M., Qussay A., Al-Amiery A.A., Gaaz T.S., (2017) Experimental and theoretical studies of benzoxazines corrosion inhibitors, *Results in Physics, 7*, 4013-4019.
97. Assad H., Kumar A. (2021) Understanding functional group effect on corrosion inhibition efficiency of selected organic compounds, *Journal of Molecular Liquids, 344*, 117755.
98. Tshiluka N.R., Bvumbi M.V., Ramaite I.I., Mnyakeni-Moleele S.S. (2021) Synthesis of some new 5-arylidene-2,4-thiazolidinedione esters, *Archive for Organic Chemistry, 5*, 1-16.
99. Al-Majed A., Bakheit A.H.H., Abdel Aziz H.A., Alharbi H., Al-jenoobi F.I. (2016) *Profiles of drug substances, excipients, and related methodology*. Elsevier, Amsterdam.
100. Day C., Bailey C.J. (2016) *Biomedical Sciences*. Elsevier, Amsterdam.
101. Haque J., Verma C., Srivastava V., Quraishi M.A., Ebenso E.E. (2018) Experimental and quantum chemical studies of functionalized tetrahydropyridines as corrosion inhibitors for mild steel in 1 M hydrochloric acid, *Results in Physics, 9*, 1481-1493.
102. Verma D.K., Khan F., Bahadur I., Salman M., Quraishi M.A., Verma C., Ebenso E.E. (2018) Inhibition performance of *Glycine* max, *Cuscuta reflexa* and *Spirogyra* extracts for mild steel dissolution in acidic medium: density functional theory and experimental studies, *Results in Physics, 10*, 665-674.
103. Verma C., Haque J., Ebenso E.E., Quraishi M.A. (2018) Melamine derivatives as effective corrosion inhibitors for mild steel in acidic solution: chemical, electrochemical, surface and DFT studies, *Results in Physics, 9*, 100-112.
104. Thangarasu V., Anand R. (2019) *Advanced biofuels*. Woodhead Publishing, Sawston.
105. Zhang T., Jiang W., Wang H., Zhang S. (2019) Synthesis and localized inhibition behavior of new triazine-methionine corrosion inhibitor in 1 M HCl for 2024-T3 aluminium alloy, *Materials Chemistry and Physics, 237*, 1-10.
106. Loto R.T., Loto C.A. (2018) Anti-corrosion properties of the symbiotic effect of *Rosmarinus officinalis* and trypsin complex on medium carbon steel, *Results in Physics, 10*, 99-106.

107. Saeed M.T., Saleem M., Usmani S., Malik I.A., Al-Shammari F.A., Deen K.M. (2019) Corrosion inhibition of mild steel in 1M HCl by sweet melon peel extract, *Journal of King Saud University-Science, 31*, 1344-1351.

108. Ansari K.R., Quraishi M.A., Singh A. (2017) Chromenopyridin derivatives as environmentally benign corrosion inhibitors for N80 steel in 15% HCl, *Journal of the Association of Arab Universities for Basic and Applied Sciences, 22*, 45-54.

109. Salman T.A., Al-Azawi K.F., Mohammed I.M., Al-Baghdadi S.B., Al-Amiery A.A., Gaaz T.S., Kadhum A.A.H. (2018) Experimental studies on inhibition of mild steel corrosion by novel synthesized inhibitor complemented with quantum chemical calculations, *Results in Physics, 10*, 291-296.

110. Al-Azawi K.F., Mohammed I.M., Al-Baghdadi S.B., Salman T.A., Issa H.A., Al-Amiery A.A., Gaaz T.S., Kadhum A.A.H. (2018) Experimental and quantum chemical simulations on the corrosion inhibition of mild steel by 3-((5-(3,5-dinitrophenyl)-1,3,4-thiadiazol-2-yl) imino) indolin-2-one, *Results in Physics, 9*, 278-283.

111. Singh K.A., Chugh B., Saha S.K., Banerjee P., Ebenso E.E., Thakur S., Pani B. (2019) Evaluation of anti-corrosion performance of an expired semi synthetic antibiotic cefdinir for mild steel in 1 M HCl medium: an experimental and theoretical study, *Results in Physics, 14*, 1-14.

112. Obaid A.Y., Ganash A.A., Qusti A.H., Elroby S.A., Hermas A.A. (2017) Corrosion inhibition of type 430 stainless steel in an acidic solution using a synthesized tetra-pyridinium ring-containing compound, *Arabian Journal of Chemistry, 10*, 1276-1283.

113. Olawale O., Bello J.O., Ogunsemi B.T., Uchella U.C., Oluyori A.P., Oladejo N.K. (2019) Optimization of chicken nail extracts as corrosion inhibitor on mild steel in 2M H_2SO_4, *Heliyon, 5*, 1-9.

114. Karthik G., Sundaravadivelu M. (2013) Inhibition of mild steel in sulphuric acid using esomeprazole and the effect of iodide ion addition, *International Scholarly Research Notices, 2013*, 1-10.

115. Karthik G., Sundaravadivelu M., Rajkumar P. (2015) Corrosion inhibition and adsorption properties of pharmaceutically active compound esomeprazole on mild steel in hydrochloric acid solution, *Research on Chemical Intermediates, 41*, 1543-1558.

116. Nan L., Xu D., Gu T., Song X., Yang K. (2015) Microbiological influenced corrosion resistance characteristics of a 304L-Cu stainless steel against *Escherichia coli*, *Materials Science and Engineering, 48*, 228-234.

117. Beese P., Venzlaff H., Srinivasan J., Garrelfs J., Stratmann M., Mayrhofer K.J.J. (2013) Monitoring of anaerobic microbially influenced corrosion via electrochemical frequency modulation, *Electrochimica Acta, 105*, 239-247.

118. Yuan S., Liang B., Zhao Y., Pehkonen S. (2013) Surface chemistry and corrosion behaviour of 304 stainless steel in simulated seawater containing inorganic sulphide and sulphate-reducing bacteria, *Corrosion Science, 74*, 353-366.

119. Murulana L.C., Kabanda M.M., Ebenso E.E. (2015) Experimental and theoretical studies on the corrosion inhibition of mild steel by some sulphonamides in aqueous HCl, *Royal Society of Chemistry Advances, 5*, 28743-28761.

120. Fernandes C.M., de Mello M.V.P., dos Santos N.E., de Souza A.M.T., Lanznaster M., Ponzio E.L. (2019) Theoretical and experimental studies of a new aniline derivative corrosion inhibitor for mild steel in acid medium, *Materials and Corrosion, 71*, 1-12.

121. Jalab R., Saad M.A., Sliem M.H., Abdullah A.M., Hussein I.A. (2022) An eco-friendly quaternary ammonium salt as a corrosion inhibitor for carbon steel in 5M HCl solution: theoretical and experimental investigation, *Molecules, 27*, 1-21.

122. El-Haddad M.A.M., Radwan A.B., Sliem M.H., Hassan W.M.I., Abdullah A.M. (2019) Highly efficient eco-friendly corrosion inhibitor for mild steel in 5M HCl at elevated temperatures: experimental and molecular dynamics study, *Scientific Reports, 9*, 1-15.

123. Usman A.D., Victoria A.F., Okoro L.N. (2015) Weight loss corrosion study of some metals in acid medium, *Journal of Advances in Chemistry, 11*, 3434-3440.

124. Murulana L.C. (2015) *Adsorption, thermodynamic and density functional theory investigation of some sulphonamides as corrosion inhibitors for some selected metals in acidic medium*. PhD thesis, North-West University (Mafikeng Campus), South Africa.

125. Ugi B.U., Obeten M.E., Magu T.O. (2018) Phytochemical constituents of *Taraxacum officinale* leaves as eco-friendly and nontoxic organic inhibitors for stainless steel corrosion in 0.2M HCl acid medium, *International Journal of Chemical Science, 2*, 35-43.

126. Talukdar A., Rajaraman P.V. (2020) Investigation of acetic acid effect on carbon steel corrosion in CO2-H2S medium: mechanistic reaction pathway and kinetics, *American Chemical Society Omega, 5*, 11378-11388.

127. Pingarron J.M., Labuda J., Barek J., Brett C.M.A. (2020) Terminology of electrochemical methods of analysis (IUPAC recommendations 2019), *Pure and Applied Chemistry, 92*, 641-694.

128. Kakaei K., Esrafili M.D., Ehsani A. (2019) *Interface Science and Technology*. Elsevier, Amsterdam.

129. Ehsani A., Mahjani M.G., Hosseini M., Safari R., Moshrefi R, Shiri H.M. (2017) Evaluation of Thymus vulgaris plant extract as an eco-friendly corrosion inhibitor for stainless steel 304 in acidic solution by means of electrochemical impedance spectroscopy, electrochemical noise analysis and density functional theory, *Journal of Colloid and Interface Science, 490*, 444-451.

130. Ehsani A., Mahjani M.G., Naseri M., Jafarian M. (2014) Influence of electrosynthesis conditions and Al2O3 nanoparticles on corrosion protection effect of polypyrrole films, *Anti-Corrosion Methods and Materials, 61*, 146-152.

131. Obot I.B., Onyeachu I.B. (2018) Electrochemical frequency modulation (EFM) technique: theory and recent practical applications in corrosion research, *Journal of Molecular Liquids, 249*, 83-96.

132. Nossol E., Munoz R.A.A., Richter E.M., de Souza Borges P.H., Silva S.C., Rocha D.P. (2023) *Encyclopaedia of sensors and biosensors*. Elsevier, Amsterdam.

133. Poursaee A. (2023) *Corrosion of steel in concrete structures*. Woodhead Publishing, Sawston.

134. Vyas R.N., Li K., Wang B. (2010) Modifying Randles circuit for analysis of polyoxometalate layer-by-layer films, *Journal of Physical Chemistry B, 114*, 15818-15824.

135. Princeton Applied Research (2006) *Basics of electrochemical impedance spectroscopy* Application Note AC-1.

136. Dinh T., Thong N.M., Huong D.Q., Le Huyen T., Manh T.D., Quy P.T., Mau T.X., Nam P.C. (2021) Insight into anticorrosion mechanism of ampicillin on mild steel in acidic environment: a combined experimental and theoretical approach, *Journal of Chemistry, 2021*, 1-12.

137. Liu Z., Fan B., Zhao J., Yang B., Zheng X. (2023) Benzothiazole derivatives-based supramolecular assemblies as efficient corrosion inhibitors for copper in artificial seawater: formation, interfacial release and protective mechanisms, *Corrosion Science, 212*, 110957.

138. Liu H., Meng G., Gu T., Li W. (2019) Microbiologically influenced corrosion of carbon steel beneath a deposit in CO_2-saturated formation water containing *Desulfotomaculum nigrificans*, Frontiers in Microbiology, 10, 1-13.

139. Zhang X., Xiao K., Dong C., Wu J., Li X., Huang Y. (2011) In situ Raman spectroscopy study of corrosion products on the surface of carbon steel in solution containing Cl^- and SO_4^{2-}, *Engineering Failure Analysis, 18*, 1981-1989.

140. Omidi M., Fatehinya A., Farahani M., Akbari Z., Shahmoradi S., Yazdian F., Tahriri M., Moharamzadeh K., Tayebi L., Vashaee D. (2017) Biomaterials for oral and dental tissue engineering. Woodhead Publishing, Sawston.

141. Gu B., Burgess D.J. (2014) *Natural and synthetic biomedical polymers*. Elsevier, Amsterdam.

142. Boyd R.W. (2020) *Nonlinear optics*. Academic Press, Massachusetts.

143. Petit S., Madejova J. (2013) *Developments in clay science*. Elsevier, Amsterdam.

144. Daeid N.N. (2005) *Encyclopaedia of analytical science*. Elsevier, Amsterdam.

145. Adeloju S.B. (2005) *Encyclopaedia of analytical science*. Elsevier, Amsterdam.

146. Song K. (2017) *Progress in rubber nanocomposites*. Woodhead Publishing, Sawston.

147. Nandiyanto A.B.D., Oktiani R., Ragadhita R. (2019) How to read and interpret FTIR spectroscope of organic material, *Indonesian Journal of Science and Technology, 4*, 97-118.

148. Dutta A. (2017) *Spectroscopic methods for nanomaterials characterization-Micro and nano technologies*. Elsevier, Amsterdam.

149. Titus D., Samuel E.J.J., Roopan S.M. (2019) *Green synthesis, characterization and applications of nanoparticles-Micro and nano technologies*. Elsevier, Amsterdam.

150. Oluwafemi O.S., Sakho E-H.M., Parani S., Lebepe T.C. (2021) *Ternary quantum dots-Synthesis, properties, and applications*. Woodhead publishing, Sawston.

151. Prabakaran M., Seung-Hyun K., Hemapriya V., Gopiraman M., Ick Soo K., Ill-Min C. (2016) *Rhus verniciflua* as a green corrosion inhibitor for mild steel in 1 M H_2SO_4, *Royal Society of Chemistry Advances, 6*, 57144-57153.

152. Abd-El-Nabey B.A., El-Housseiny S., Abd-El-Fatah M.A. (2022) Trizma as an eco-friendly efficient inhibitor for the acidic corrosion of steel: experimental and computational studies, *Scientific Reports, 12*, 1-16.

153. Wang D., Yue Y., Xie Z., Mi T., Yang S., McCague C., Qian J., Bai Y. (2022) Chloride-induced depassivation and corrosion of mild steel in magnesium potassium phosphate cement, *Corrosion Science, 206*, 1-18.

154. Udensi S.C., Ekpe O.E., Nnanna L.A. (2021) Corrosion inhibition performance of low cost and eco-friendly *Treculia Africana* leaves extract on aluminium alloy AA7075-T7351 in 2.86% NaCl solutions, *Scientific African, 12*, e00791.

155. Chaouiki A., Lgaz H., Salghi R., Gaonkar S.L., Bhat K.S., Jodeh S., Toumiat K., Oudda H. (2019) New benzohydrazide derivative as corrosion inhibitor for carbon steel in a 1M HCl solution: electrochemical, DFT and Monte Carlo simulation studies, *Portugaliae Electrochimica Acta, 37*, 147-165.

156. Ouakki M., Galai M., Rbaa M., Abousalem A.S., Lakhrissi B., Rifi E.H., Cherkaoui M. (2019) Quantum chemical and experimental evaluation of the inhibitory action of two imidazole derivatives on mild steel corrosion in sulphuric acid medium, *Heliyon, 5*, 1-18.

157. Zhang C., Duan H., Zhao J. (2016) Synergistic inhibition effect of imidazoline derivative and L-cysteine on carbon steel corrosion in a CO_2-saturated brine solution, *Corrosion Science, 112*, 160-169.

158. Nishiwaki N. (2014) *Comprehensive organic synthesis*. Elsevier, Amsterdam.

159. Zhou X., Yang H., Wang F. (2011) [BMIM]BF4 ionic liquids as effective inhibitor for carbon steel in alkaline chloride solution, *Electrochimica Acta, 56*, 4268-4275.

160. Rahiman A.F.S.A., Sethumanickam S. (2017) Corrosion inhibition, adsorption and thermodynamic properties of poly(vinyl alcohol-cysteine) in molar HCl, *Arabian Journal of Chemistry, 10*, S3358-S3366.

161. Beniken M., Salim R., Ech-Chihbi E., Sfaira M., Hammouti B., Ebn Touhami M., Mohsin M.A., Taleb M. (2022) Adsorption behaviour and corrosion inhibition mechanism of a polyacrylamide on C-steel in 0.5 M H2SO4: electrochemical assessments and molecular dynamic simulation, *Journal of Molecular Liquids, 348*, 118022.

162. Saleh T.A. (2022) *Interface science and technology*. Elsevier, Amsterdam.

163. Stauffer E., Dolan J.A., Newman R. (2008) Fire debris analysis. Academic Press, Massachusetts.

164. Verma C., Ebenso E.E., Quraishi M.A. (2020) Molecular structural aspects of organic corrosion inhibitors: influence of -CN and -NO_2 substituents on designing of potential corrosion inhibitors for aqueous media, *Journal of Molecular Liquids, 316*, 1-21.

165. Roos Y.H. (1995) *Phase transitions in foods*. Academic Press, Massachusetts.

166. Yurt A., Ulutas S., Dal H. (2006) Electrochemical and theoretical investigation on the corrosion of aluminium in acidic solution containing some Schiff bases, *Applied Surface Science, 253*, 919-925.

167. Nwosu F.O., Muzakir M.M. (2016) Thermodynamic and adsorption studies of corrosion inhibition of mild steel using lignin from siam weed (Chromolaena odorata) in acid medium, *Journal of Materials and Environmental Science, 7*, 1663-1673.

168. Tiwari N., Mitra R.K., Yadav M. (2021) Corrosion protection of petroleum oil well/tubing steel using thiazolidines as efficient corrosion inhibitor: experimental and theoretical investigation, *Surfaces and Interfaces, 22*, 1-19.

169. Diki N., Coulibaly N.H., Kassi K.F., Trokourey A. (2021) Mild steel corrosion inhibition by 7-(ethylthiobenzimidazolyl) theophylline, *Journal of Electrochemical Science and Engineering, 11*, 97-106.

170. Fouda AEAS., El-Askalany A.H., Molouk A.F.S., Elsheikh N.S., Abousalem A.S. (2021) Experimental and computational chemical studies on the corrosion inhibitive properties of carbonitrile compounds for carbon steel in aqueous solutions, *Scientific Reports, 11*, 21672.

171. Pepper I.L. (2019) *Environmental and pollution science*. Academic Press, Massachusetts.

172. Vinutha M.R., Venkatesha T.V. (2018) Anticorrosive ability of electrochemically synthesized 2,2'-disulfanediyldianiline for mild steel corrosion: electrochemical and thermodynamic studies, *International Journal of Industrial Chemistry, 9*, 185-197.

173. Inglezakis V.J., Poulopoulos S.G. (2006) *Adsorption, ion exchange and catalysis*. Elsevier, Amsterdam.

174. Arshadi M.R., Lashgari M., Parsafar G.A. (2004) Cluster approach to corrosion inhibition problems: interaction studies, *Materials Chemistry and Physics, 86*, 311-314.

175. Usman B.J., Gasem Z.M., Umoren S.A., Solomon M.M. (2019) Eco-friendly 2-thiobarbituric acid as a corrosion inhibitor for API 5L X60 steel in simulated sweet oilfield environment: electrochemical and surface analysis studies, *Scientific Reports, 9*, 1-17.

176. Go L.C., Depan D., Holmes W.E., Gallo A., Knierim K., Bertrand T., Hernandez R. (2020) Kinetic and thermodynamic analyses of the corrosion inhibition of synthetic extracellular polymeric substances, *PeerJ Materials Science, 4*, 1-22.

177. Husaini M., Ibrahim M.B. (2019) Thermodynamic and kinetic study on the corrosion of aluminium in hydrochloric acid using benzaldehyde as corrosion inhibitor, *International Journal of Engineering and Manufacturing, 6*, 53-64.

178. Udensi S.C., Ekpe O.E., Nnanna L.A. (2021) Corrosion inhibition performance of low cost and eco-friendly *Treculia Africana* leaves extract on aluminium alloy AA7075-T7351 in 2.86% NaCl solutions, *Scientific African, 12*, 1-10.

179. Deyab M.A., Mohsen Q., Guo L. (2022) Theoretical, chemical, and electrochemical studies of *Equisetum arvense* extract as an impactful inhibitor of steel corrosion in 2M HCl electrolyte, *Scientific Reports, 12*, 1-14.

180. Quraishi M.A., Singh A., Singh V.K., Yadav D.K., Singh A.K. (2010) Green approach to corrosion inhibition of mild steel in hydrochloric acid and sulphuric acid solutions by the extract of *Murrayakoenigii* leaves, *Materials Chemistry and Physics, 122*, 114-122.

181. Preethi K.P., Rao S.A., Shetty P. (2014) Corrosion inhibition of mild steel in 2 M HCl by a Schiff base derivative, *Procedia Materials Science, 5*, 499-507.

182. Assad H., Kumar S., Saha S.Kr., Kang N., Fatma I., Dahiya H., Sharma P.K., Thakur A., Sharma S., Ganjoo R., Kumar A. (2023) Evaluating the adsorption and corrosion inhibition capabilities of pyridinium-p-toluene sulphonate on MS in 1 M HCl medium: an experimental and theoretical study, *Inorganic Chemistry Communications, 153*, 110817.

183. Cao S., Liu D., Ding H., Wang J., Lu H., Gui J. (2019) Task-specific ionic liquids as corrosion inhibitors on carbon steel in 0.5 M HCl solution: an experimental and theoretical study, *Corrosion Science, 153*, 301-313.

184. Virtanen S. (2009) *Encyclopaedia of electrochemical power sources*. Elsevier, Amsterdam.

185. Virtanen S. (2011) *Tribocorrosion of passive metals and coatings*. Woodhead Publishing, Sawston.

186. Metrohm AG. (2019) *Electrochemical corrosion studies of various metals*. Metrohm AG, Herisau.

187. Qiang Y., Zhang S., Tan B., Chen S. (2018) Evaluation of *Ginkgo* leaf extract as an eco-friendly corrosion inhibitor of X70 steel in HCl solution, *Corrosion Science, 133*, 6-16.

188. Goel R., Siddiqi W.A., Ahmed B., Hussan J. (2010a) Corrosion inhibition of mild steel in HCl by isolated compounds of *Riccinus Communis* (L.), *Journal of Chemistry, 7*, 1-12.

189. Yildiz R. (2015) An electrochemical and theoretical evaluation of 4,6-diamino-2-pyrimidinethiol as a corrosion inhibitor for mild steel in HCl solutions, *Corrosion Science, 90*, 544-553.

190. Mahalakshmi D., Hemapriya V., Subramaniam E.P., Chitra S. (2019) Synergistic effect of antibiotics on the inhibition property of aminothiazolyl coumarin for corrosion of mild steel in 0.5 M H_2SO_4, *Journal of Molecular Liquids, 284*, 316-327.

191. Verma C., Quraishi M.A., Rhee K.Y. (2022) *Advances in Colloid and Interface Science*. Elsevier, Amsterdam.

192. Wang S., Jia H., Wang Q., Yan H., Wei Z., Wen X., Wang Q., Fan F., Wen S., Huang P., Kang W. (2022) Experimental and theoretical studies of the corrosion inhibition performance of fatty acid-based ionic liquids for mild steel in 1 M HCl: effects of the varied alkyl chain length in the anionic group, *American Chemical Society Sustainable Chemistry and Engineering, 10*, 17151-17166.

193. Liu R., Han X., Wang F., Tan B., Zhang N., Li W., Zhang S. (2024) Enhancing performance in copper corrosion inhibitors through molecular structural modifications: mechanisms, design, and future pathways, *Journal of Molecular Liquids, 394*, 123750.

194. Mohsen Q., Deyab M.A. (2022) Utilizing birch leaf extract in pickling liquid as a sustainable source of corrosion inhibitor for pipeline steel, *Scientific Reports, 12*, 1-11.

195. Umasankareswari T., Dorothy R., Jeyasundari J., Singh G., Rajendran S., Subramania A., Al-Hashem A., Aslam J. (2023) *Electrochemical and analytical techniques for sustainable corrosion monitoring*. Elsevier, Amsterdam.

196. Zaher A., Chaouiki A., Salghi R., Boukhraz A., Bourkhiss B., Ouhssine M. (2020) Inhibition of mild steel corrosion in 1M hydrochloric medium by the methanolic extract of *Ammi visnaga* L. Lam seeds, *International Journal of Corrosion, 2020*, 1-11.

197. Ahmad Z. (2006) *Principles of corrosion engineering and corrosion control*. Butterworth Heinemann, Oxford.

198. Keshk A.A., Elsayed N.H., Almutairi F.M., Al-Anazi M., Said S., Althurwi H.M., Albalawi R.K., El-Aassar M.R. (2023) *Biomass conversion and biorefinery*. Springer, New York.

199. Lai C-Y., Huang W-C., Weng J-H., Chen L-C., Chou C-F. (2020) Impedimetric aptasensing using a symmetric Randels circuit model, *Electrochimica Acta, 337*, 1-11.

200. Lemine A.S., Fayyaz O., Shakoor R.A., Ahmad Z., Bhadra J., Al-Thani N.J. (2023) Effect of cold and hot compactions on corrosion behaviour of p- and

n-type bismuth telluride-based alloys developed through microwave sintering process, *Journal of Alloys, and Compounds, 939*, 168763.

201. Gangan A., El-Sabbagh M., Bedair M.A., Ahmed H.M., El-Sabbah M., El-Bahy S.M., Fahmy A. (2021) Influence of pH values on the electrochemical performance of low carbon steel coated by plasma thin SiO_xC_y films, *Arabian Journal of Chemistry, 14*, 103391.

202. Al-Amiery A.A., Mohamad A.B., Kadhum A.A.H., Shaker L.M., Isahak W.N.R.W., Takriff M.S. (2022) Experimental and theoretical study on the corrosion inhibition of mild steel by nonanedioic acid derivative in hydrochloric acid solution, *Scientific Reports, 12*, 1-21.

203. Namrata C.S., Singh V.K., Quraishi M.A. (2017) Corrosion inhibition performance of different bark extracts on aluminium in alkaline solution, *Journal of the Association of Arab Universities for Basic and Applied Sciences, 22*, 38-44.

204. De Ketelaere E., Moed D., Vanoppen M., Verliefde A.R.D., Verbeken K., Depover T. (2023) Sodium silicate corrosion inhibition behaviour for carbon steel in a dynamic saltwater environment, *Corrosion Science, 217*, 111119.

205. Safak S., Duran B., Yurt A., Turkoglu G. (2012) Schiff bases as corrosion inhibitors for aluminium in HCl solution, *Corrosion Science, 54*, 251-259.

206. Azzeddine H., Hanna A., Dakhouche A., Luthringer-Feyerabend B. (2021) Corrosion behaviour and cytocompatibility of selected binary magnesium-rare earth alloys, *Journal of Magnesium and Alloys, 9*, 581-591.

207. Padhi S., Behera A. (2022) *Agri-waste and microbes for production of sustainable nanomaterials*. Elsevier, Amsterdam.

208. Sindhu R., Binod P., Pandey A. (2015) *Industrial biorefineries and white biotechnology*. Elsevier, Amsterdam.

209. Khan S.A., Khan S.B., Khan L.U., Farooq A., Akhtar K., Asiri M.A. (2018) *Handbook of materials characterization*. Springer, New York.

210. Naghshbandi M.P., Moghimi H. (2020) *Methods of Enzymology*, Elsevier, Amsterdam.

211. Gupta D., Mahajani S.M., Garg A. (2020) Investigation on hydrochar and macromolecules recovery opportunities from food waste after hydrothermal carbonization, *Science of the Total Environment, 749*, 1-11.

212. Jisha M., Zeinul Hukuman N.H., Leena P., Abdussalam A.K. (2019) Electrochemical, computational and adsorption studies of leaf and floral extracts of *Pogostemon quadrifolius* (*Benth.*) as corrosion inhibitor for mild steel in hydrochloric acid, *Journal of Materials and Environmental Sciences, 10*, 840-853.

213. Fumoto E., Sato S., Takanohashi T. (2020) Determination of carbonyl functional groups in heavy oil using infrared spectroscopy, *Energy and Fuels, 34*, 5231-5235.

214. Okewale A.O., Adesina O.A. (2020) Kinetics and thermodynamic study of corrosion inhibition of mild steel in 1.5 M HCl medium using cocoa leaf extract as inhibitor, *Journal of Applied Sciences and Environmental Management, 24*, 37-47.

215. Salman H.E., Balakit A.A., Mahmood A. (2019) Study of the corrosion inhibitive effect and adsorption process of two azo aldehydes on carbon steel in 1M H_2SO_4, *Materials Science and Engineering, 571*, 1-18.

216. Subasree N., Arockia-Selvi J. (2020) Imidazolium based ionic liquids derivatives; synthesis and evaluation of inhibitory effect on mild steel corrosion in hydrochloric acid solution, *Heliyon, 6*, 1-12.

217. Beal R.W., Brill T.B. (2005) Vibrational behaviour of the -NO_2 group in energetic compounds, *Applied Spectroscopy, 59*, 1194-1202.

218. Mahdi B.S., Abbass M.K., Mohsin M.K., Al-azzawi W.K., Hanoon M.M., Al-Kaabi M.H.H., Shaker L.M., Al-Amiery A.A., Isahak W.N.R.W., Kadhum A.A.H., Takriff M.S. (2022) Corrosion inhibition of mild steel in hydrochloric acid environment using terephthaldehyde based on Schiff base: gravimetric, thermodynamic, and computational studies, *Molecules, 27*, 4857.

219. Shukla S.K., Ebenso E.E. (2011) Corrosion inhibition, adsorption behaviour and thermodynamic properties of streptomycin on mild steel in hydrochloric acid medium, *International Journal of Electrochemical Science, 6*, 3277-3291.

220. Nahle A., Abu-Abdoun I.I., Abdel-Rahman I. (2012) Effect of temperature on the corrosion inhibition of trans-4-hydroxy-4-stilbazole on mild steel in HCl solutions, *International Journal of Corrosion, 2012*, 1-8.

221. Oubaaqa M., Ouakki M., Rbaa M., Abousalem A.S., Maatallah M., Benhiba F., Jarid A., Ebn Touhami M., Zarrouk A. (2021) Insight into the

corrosion inhibition of new amino-acids as efficient inhibitors for mild steel in HCl solution: experimental studies and theoretical calculations, *Journal of Molecular Liquids, 334*, 116520.

222. Deng Q., Jeschke S., Mishra R.K., Spicher S., Darouich S., Schreiner E., Eiden P., Deglmann P., Gorges J.N., Chen X-B., Keil P., Cole I. (2024) Design of alkyl substituted aminothiazoles to optimise corrosion inhibition for galvanised steel: a combined experimental and molecular modelling approach, *Corrosion Science, 227*, 111733.

223. Azizian S., Setareh E. (2021) *Interface science and technology*. Elsevier, Amsterdam.

224. Liu L., Luo X-B., Ding L., Luo S-L. (2019) *Nanomaterials for the removal of pollutants and resource reutilization*. Elsevier, Amsterdam.

225. Ballantine Jr D.S., Martin S.J., Ricco A.J., Frye G.C., Wohltjen H., White R.M., Zellers E.T. (1997) *Acoustic wave sensors*. Academic Press, Massachusetts.

226. Coote M.L. (2012) *Polymer science: a comprehensive reference*. Elsevier, Amsterdam.

227. El Basiony N.M., Elgendy A., Nady H., Migahed M.A., Zaki E.G. (2019) Adsorption characteristics and inhibition effect of two Schiff base compounds on corrosion of mild steel in 0.5M HCl solution: experimental, DFT studies, and Monte Carlo simulation, *Royal Society of Chemistry Advances, 9*, 10473-10485.

228. Huong D.Q., Huong N.T.L., Nguyet T.T.A., Duong T., Tuan D., Thong N.M., Nam P.C. (2020) Pivotal role of heteroatoms in improving the corrosion inhibition ability of thiourea derivatives, *American Chemical Society Omega, 5*, 27655-27666.

229. Singh A., Ansari K.R., Ali I.H., El-Ibrahimi B., Sharma N.R., Bansal A., Alanazi A.K., Younas M., Alamri A.H., Lin Y. (2023) *Colloids and surfaces A: physicochemical and engineering aspects*. Elsevier, Amsterdam.

230. Arellanes-Lozada P., Olivares-Xometi O., Guzman-Lucero D., Likhanova N.V., Dominguez-Aguilar M.A., Lijanova I.V., Arce-Estrada E. (2014) The inhibition of aluminium corrosion in sulphuric acid by poly(1-vinyl-3-alkyl-imidazolium hexafluorophosphate), *Materials, 7*, 5711-5734.

231. Denis L., Grzeskowiak H., Trias D., Delaux D. (2017) *Reliability of high-power mechatronic systems 2*. Elsevier, Amsterdam.

232. Yadav M., Behera D., Kumar S., Yadav P. (2014) Experimental and quantum chemical studies on corrosion inhibition performance of thiazolidinedione derivatives for mild steel in hydrochloric acid solution, *Chemical Engineering Communications, 202*, 303-315.

233. Noor E.A. (2007) Temperature effects on the corrosion inhibition of mild steel in acidic solutions by aqueous extract of fenugreek leaves, *International Journal of Electrochemical Science, 2*, 996-1017.

234. El-Wanees S.A., Kamel M.M., Ibrahim M., Rashwan S.M., Atef Y., El-Sadek M.G.A. (2023) Corrosion inhibition and synergistic effect of ionic liquids and iodide ions on the corrosion of C-steel in formation water associated with crude oil, *Journal of Umm Al-Qura University for Applied Sciences*, 1-13.

235. Betti N., Al-Amiery A.A., Al-Azzawi W.K., Isahak W.N.R.W. (2023) Corrosion inhibition properties of Schiff base derivative against mild steel in HCl environment complemented with DFT investigations, *Scientific Reports, 13*, 8979.

236. Mohsenifar F., Jafari H., Sayin K. (2016) Investigation of thermodynamic parameters for steel corrosion in acidic solution in the presence of N,N'-Bis(phloroacetophenone)-1,2 propanediamine, *Journal of Bio- and Tribo-Corrosion, 2*, 1-13.

237. Patel N.S., Jauhari S., Mehta G.N. (2009) Inhibitor for the corrosion of mild steel in H_2SO_4, *South African Journal of Chemistry, 62*, 200-204.

238. Hiromoto S. (2010) *Metals for biomedical devices*. Woodhead Publishing, Sawston.

239. Bansod A.V., Patil A., Verma J., Shukla S. (2019) Microstructure, mechanical and electrochemical evaluation of dissimilar low Ni SS and 304 SS using different filler materials, *Materials Research, 22*, 1-15.

240. Li Y.J., Wang Y.G., An B., Xu H., Liu Y., Zhang L.C., Ma H.Y., Wang W.M. (2016) A practical anodic and cathodic curve intersection model to understand multiple corrosion potentials of Fe-based glassy alloys in OH^- contained solutions, *PLOS One, 11*, 1-20.

241. Loto R.T. (2016) Inhibition effect of butan-1-ol on the pitting corrosion of austenitic stainless steel (type 304), *Gazi University Journal of Science, 29*, 19-25.

242. Kang D.H., Lee H.W. (2013) Study of the correlation between pitting corrosion and the component ratio of the dual phase in duplex stainless-steel welds, *Corrosion Science, 74*, 396-407.

243. Schalenbach M., Durmus Y.E., Tempel H., Kungl H., Eichel R-A. (2021) Double layer capacitances analysed with impedance spectroscopy and cyclic voltammetry: validity and limits of the constant phase element parameterization, *Physical Chemistry Chemical Physics, 23*, 21097-21105.

244. Macdonald D.D. (1999) Passivity-the key to our metals-based civilization, *Pure and Applied Chemistry*, 71, 951-978.

245. Macdonald D.D., Ismail K.M., Sikora E.J. (1998) Characterization of the passive state on zinc, *Journal of the Electrochemical Society, 145*, 3141-3149.

246. Macdonald D.D. (2011) The history of the point defect model for the passive state: a brief review of film growth aspects, *Electrochimica Acta, 56*, 1761-1772.

247. Yilmaz A., Traka K., Pletincx S., Hauffman T., Sietsma J., Gonzalez-Garcia Y. (2021) Effect of microstructural defects on passive layer properties of interstitial free (IF) ferritic steels in alkaline environment, *Corrosion Science, 182*, 109271.

248. Shaban M. (2016) N-(3-(Dimethyl benzyl ammonio)propyl)alkanamide chloride derivatives as corrosion inhibitors for mild steel in 1M HCl solution: experimental and theoretical investigation, *Royal Society of Chemistry Advances, 6*, 1-18.

249. Loto R.T., Loto C.A., Popoola A.P. (2015) Inhibition effect of Deanol on mild steel corrosion in dilute sulphuric acid, *South African Journal of Chemistry, 68*, 105-114.

250. Singh A.K., Ebenso E.E. (2012) Effect of Ceftezole on the corrosion of mild steel in HCl solution, *International Journal of Electrochemical Science, 7*, 2349-2360.

251. Hong T., Nagumo M. (1997) Effect of surface roughness on early stages of pitting corrosion of Type 301 stainless steel, *Corrosion Science, 39*, 1665-1672.

252. Tang Y., Dai N., Wu J., Jiang Y, Li J. (2019) Effect of surface roughness on pitting corrosion of 2205 duplex stainless steel investigated by electrochemical noise measurements, *Materials, 12*, 1-20.

253. Mitchell J., Crow N., Nieto A. (2020) Effect of surface roughness on pitting corrosion of AZ31 Mg alloy, *Metals, 10*, 1-12.

254. Nguyen T.Q., Breitkopf C. (2018) Determination of diffusion coefficients using impedance spectroscopy data, *Journal of the Electrochemical Society, 165*, E826-E831.

255. Huang J. (2018) Diffusion impedance of electroactive materials, electrolytic solutions and porous electrodes: Warburg impedance and beyond, *Electrochimica Acta, 281*, 170-188.

256. Oldenburger M., Bedurftig B., Gruhle A., Grimsmann F., Richter E., Findeisen R., Hintennach A. (2019) Investigation of the low frequency Warburg impedance of Li-ion cells by frequency domain measurements, *Journal of Energy Storage, 21*, 272-280.

257. Pandimuthu G., Muthukrishnan P., Rameshkumar S., Paramasivaganesh K., Sankar A. (2021) Charge transfer resistance and adsorption performance of a new pyrrole derivative on mild steel in acidic media: antibacterial studies, *Oriental Journal of Chemistry, 37*, 779-790.

258. Shahzad K., Sliem M.H., Shakoor R.A., Radwan A.B., Kahraman R., Umer M.A., Manzoor U., Abdullah A.M. (2020) Electrochemical and thermodynamic study on the corrosion performance of APIX120 steel in 3.5% NaCl solution, *Scientific Reports, 10*, 1-15.

259. Bedair M.A., El-Aryian H.M., Gad E.S., Al-Shareef M., Bedair A.H., Aboushahba R.M., Abd El-Aziz S.F. (2023) Insights into the adsorption and corrosion inhibition properties of newly synthesized diazinyl derivatives for mild steel in hydrochloric acid: synthesis, electrochemical, SRB biological resistivity and quantum chemical calculations, *Royal Society of Chemistry Advances, 13*, 478-498.

260. Alaneme K.K., Olusegun S.J., Adelowo O.T. (2016) Corrosion inhibition and adsorption mechanism studies of *Hunteria umbellata* seed husk extracts on mild steel immersed in acidic solutions, *Alexandria Engineering Journal, 55*, 673-681.